

THE WORLD'S MOST FUEL EFFICIENT VEHICLE

DESIGN AND DEVELOPMENT OF **pac_{car} II**

J.J. Santin, C.H. Onder, J. Bernard, D. Isler,
P. Kobler, F. Kolb, N. Weidmann, L. Guzzella



vdf Hochschulverlag AG an der ETH Zürich

Warning – Important safety notice

The information in this book represents a general summary of engineering principles involved in fuel economy vehicle design and construction. Some of these design practices may be dangerous unless undertaken and implemented by experienced people who are trained in vehicle engineering, design, and construction. The authors and publisher have endeavored to ensure the accuracy of this book. However, all information should be read with the potential risks of racing and vehicle modification in mind. Racing and vehicle design and construction are risky undertakings – both for yourself and for others. No book can teach all aspects of racing and vehicle design and construction. There is no substitute for appropriate engineering credentials and experience. For these reasons, the authors and publisher make no warranties, express or implied, that the information in this book is free of error, or that it will meet requirements for any particular application. The authors and publisher expressly disclaim the implied warranties of merchantability and of fitness for any particular purpose, even if the authors and publisher have been advised of a particular purpose, and even if a particular purpose is described in the book. The authors and publisher also disclaim all liability for direct, indirect, incidental, or consequential damages that result from any use of the examples, instructions, or other information in this book.

(Text based on the safety notice of Tamai [18])

Cover photograph courtesy of Philippe Ricoux, Michelin

Bibliographic information published by the Deutsche Nationalbibliothek

The Deutsche Nationalbibliothek lists this publication in the Deutsche Nationalbibliografie; detailed bibliographic data are available in the Internet at <http://dnb.d-nb.de>.

ISBN 978-3-7281-3134-8

© 2007, vdf Hochschulverlag AG an der ETH Zürich, Zürich/Singen

All rights reserved. Nothing from this publication may be reproduced, stored in computerized systems or published in any form or in any manner, including electronic, mechanical, reprographic or photographic, without prior written permission from the publisher.

Preface

Created more than 20 years ago to promote fuel efficiency, the Shell Eco-marathon has embraced – and anticipated – the challenges raised by energy use in the transportation sector. Energy companies like Shell face these challenges daily in their business; by sharing them with students and their teachers as part of the Shell Eco-marathon project, we hope to help them prepare their careers as future engineers, technicians or scientists.

This opportunity to gain hands-on experience working on a project that is environmental, economic and social in nature is an invitation to contribute to sustainable mobility. This tripartite equation has several unknowns, including the future role that alternative energy sources will play in the transport sector. Hydrogen, used in fuel cells like the one used in the PAC-Car II, is one possible alternative response that would represent a major technological leap forward.

The capacity for innovation – the primary quality demanded of Shell Eco-marathon participants – is what drove the PAC-Car II project, managed by the Swiss Federal Institute of Technology (ETH) in Zurich. In 2005, their vehicle set a new race record at the Nogaro motor circuit in France: 3,836 km/l* with a fuel cell system driving an electric motor! Two months later, they confirmed and exceeded this accomplishment at the Michelin Technology Centre, setting a new record of 5,385 km/l*.

The Shell Eco-marathon's reputation has been built largely on such legendary performances by the top performing teams, which are generally based on partnerships between teachers, students and industry – a key value of this event. The PAC-Car team demonstrated the heights that can be reached by such educational projects, and now they share their experience in another demonstration of team spirit, sportsmanship and openness.

This is the first time that a book has been published telling the steps taken for the development, construction and successful performance of a vehicle designed

* Distance that would have been covered with one litre of petrol, equivalent consumption calculated using the lower heating values of hydrogen and gasoline.

specifically for the Shell Eco-marathon. In general, the secrets of a winning and record-breaking vehicle are jealously guarded, but this exceptional team would like to make the findings of their adventure available to those who share an interest in developing a similar project. The spirit of the Shell Eco-marathon is one of innovation and creativity; by sharing their experience, the PAC-Car team provides experiments, results, models and ideas for comparison, which will stimulate further innovation by the next generation.

Bravo to this pan-European team, which is a perfect reflection of the Shell Eco-marathon's international scope. They deserve our warmest congratulations for having built the PAC-Car II, a fantastic vehicle that incites us to think about sustainable mobility and how to use the planet's precious energy resources. But, beyond the vehicle itself, we should also congratulate the team for putting this educational project together in order to achieve their ambition, for demonstrating real teamwork in doing so and for sharing the knowledge acquired.

I am certain that the experience acquired by all the team members will be very useful to them in their future careers and that the positive values that drove this project will continue to guide them in their search for innovative solutions in all fields.

*Serge Giacomo
Director, European Shell Eco-marathon 2005.*

Acknowledgments

As the initiator of, and coordinator for, the writing of this book, it gives me great pleasure to be able to thank all those who have contributed to its development.

Firstly, I would like to thank Professor Lino Guzzella, the Director of both the *Institut für Mess-und Regeltechnik* (Measurement and Control Laboratory) at the *Eidgenössische Technische Hochschule Zürich* (Swiss Federal Institute of Technology Zurich) and the PAC-Car projects, for having given us the freedom to write this book as we saw fit, and at the same time for making sure that we always had the means to complete the project in the best of conditions – his Golden Rule!

Next, I would like to thank the authors, in particular the five students at the heart of the PAC-Car II project: Dominik Isler, Pius Kobler, Florian Kolb, Nicolas Weidmann and Jérôme Bernard. It's true to say that after working on such a demanding project, we were all ready to turn the page; but the five of you found the energy to dive back in again by writing one or more chapters. Without your individual contributions, this book wouldn't have been complete.

My thanks also go to Mr. Serge Giacomo, the Director of the European Shell Eco-Marathon 2005, for agreeing to write the preface to this book.

I would also like to thank the people whose participation so improved the quality of the final product: Jan Hailwood and Lisa Helen Spencer, for their English language work; the individuals and companies who gave permission for their illustrations to be used; Nicolas Weidmann, for all his work on the 307 figures found throughout the book.

More generally, I would like to thank all those who contributed in some way to the PAC-Car II project: this book would not exist had PAC-Car II not been such a great collective success.

And finally, my heartfelt thanks go to my colleagues, friends and family, and in particular, Karine, Léa and Luc, for their patience and support.

Jean-Jacques Santin

Introduction

"If you want to build a ship, don't herd people together to collect wood and don't assign them tasks and work, but rather teach them to long for the endless immensity of the sea."

Antoine de Saint-Exupéry

Why PAC-Car?

The PAC-Car project began in 2002 at the *Eidgenössische Technische Hochschule Zürich* (ETH Zurich, Swiss Federal Institute of Technology Zurich). At that time, our laboratory had been involved in research in the field of advanced vehicle propulsion systems for almost twenty years, working primarily to reduce the pollution emissions and improve the fuel economy of passenger cars. Amazing progress was made during this period: passenger car pollution emissions were reduced by two orders of magnitude and prototype IC engines and hybrid-electric propulsion systems with the potential to reduce fuel consumption by a factor of two were constructed. Low-temperature fuel cell systems were a "hot topic" at the time, and our laboratory acquired expertise in such systems by cooperating on a fuel cell vehicle and a fuel cell auxiliary power unit project.

Amazingly, despite these achievements, a somewhat melancholic feeling permeated the laboratory because the ongoing research projects did not constitute a really exciting challenge. As often happens, it was at that moment that serendipity struck: Gino Paganelli – at that time a post-doctoral associate in our lab – came into my office one day and told me about the Shell Eco-marathon. He wanted to check with the organizers to see if they would let us race with a fuel cell vehicle, and if so, would they allow us to participate in the next Shell Eco-marathon using a new fuel cell propulsion system embedded in an existing vehicle, built by the French *Université de Valenciennes* (UVHC – University of Valenciennes).

With the approval of the organizers of the Nogaro Shell Eco-marathon, the PAC-Car adventure began. Gino's idea immediately became a full-fledged serious project. From the very beginning, it was clear that a fuel cell driving an ultra-efficient vehicle would have the potential to achieve a level of fuel economy beyond all known limits. In the PAC-Car I project, an innovative fuel cell-based power train was developed to verify this potential, and this power train was tested in the UVHC vehicle on proving grounds and in several Shell Eco-marathons. The second phase of the PAC-Car project – the design and construction of a completely new vehicle – would prove even more exciting and challenging, calling for serious

management skills and more ample resources. Luckily, we were able to persuade Jean-Jacques Santin from UVHC to lead this second phase, and the *Bundesamt für Energie* (BfE – Swiss Federal Office of Energy) and ETH Zurich were generous enough to provide the needed financial support. The results of this second phase are presented in this volume.

The students who worked on the PAC-Car II project, whether for a short or long period, were central to its success, and their names are listed on our website. All of them did a marvellous job, but four students played a special role: Dominik Isler, Pius Kobler, Florian Kolb and Nicolas Weidmann. Opting for a project-oriented major, these students organized their entire graduate curriculum around this project. I would guess that few mechanical engineering students ever learned the fundamentals of mechanical structures, control systems, composite materials and fluid dynamics in a more motivating environment. Many other people, too numerous to mention, contributed in some way or another to the project's successful completion. Among them, the following groups were instrumental in this success: the teams at RUAG Aerospace, Esoro and Tribecraft AG; the colleagues of the *Paul Scherrer Institut* (PSI); and the colleagues in the *Institut für Flüssigdynamik* (Institute of Fluid Dynamics) and *Zentrum für Strukturtechnologien* (Centre of Structure Technologies) at ETH Zurich.

PAC-Car I and II have probed the actual limits of road vehicle fuel economy. They provided an excellent breadboard for testing and then integrating the latest developments in materials, aerodynamics, structures, systems, and many other disciplines into a single system. I am convinced that some of the ideas generated during this project will eventually show up on the road and, in accordance with our primary mission, will help to save fuel and reduce the harmful pollution emitted by passenger cars.

This said, I think that the most important reason why our team was captivated by this project from the very first moment is simply that we had a lot of fun working on it. For this reason, in the name of all the team members, I would like to express our gratitude to our sponsors, who made this adventure possible. My personal “thank you” goes out to all the members of the PAC-Car I and II teams. Without their enthusiasm, endurance and creativity, this adventure would not have been possible.

*Professor Dr. Lino Guzzella
Head of the Institut für Mess- und Regeltechnik
(Measurement and Control Laboratory)
ETH Zürich*

Contents

Chapter 1: Fuel economy competitions.....	1
1.1. <i>The philosophy behind a fuel economy competition.....</i>	<i>1</i>
1.2. <i>Measuring fuel consumption</i>	<i>4</i>
1.3. <i>A brief summary of the Shell Eco-marathon rules and regulations</i>	<i>10</i>
1.4. <i>World records</i>	<i>13</i>
1.5. <i>The pilot.....</i>	<i>16</i>
Chapter 2: Some design considerations for fuel economy vehicles	19
2.1. <i>Defining the vehicle architecture</i>	<i>19</i>
2.2. <i>Defining the target figures of the vehicle</i>	<i>28</i>
Chapter 3: Tires	41
3.1. <i>Rolling resistance of a tire.....</i>	<i>41</i>
3.2. <i>Ultra-low rolling-resistance tires on the market.....</i>	<i>50</i>
3.3. <i>Relevant tire mechanics basics.....</i>	<i>54</i>
3.4. <i>The mechanical effects of cambered wheels.....</i>	<i>63</i>
3.5. <i>Mechanical effect of toe-in angle</i>	<i>68</i>
Chapter 4: Tire drag when cornering	71
4.1. <i>Vehicle Fixed Coordinate System.....</i>	<i>72</i>
4.2. <i>Steady-state cornering models.....</i>	<i>73</i>
4.3. <i>Comparison of three steering system types</i>	<i>85</i>
4.4. <i>Tire forces and moments when cornering</i>	<i>87</i>
4.5. <i>The optimization of the vehicle architecture parameters</i>	<i>90</i>
Chapter 5: Aerodynamics	93
5.1. <i>Fundamental principles of aerodynamics for low-drag vehicles</i>	<i>93</i>

5.2.	<i>Design process for the PAC-Car II body shape</i>	101
5.3.	<i>Aerodynamics of the PAC-Car II</i>	112
5.4.	<i>Experimental and numerical optimization methods</i>	120
5.5.	<i>Conclusion</i>	127
Chapter 6: Vehicle body structure		129
6.1.	<i>The pilot's field of vision</i>	129
6.2.	<i>Vehicle body design process</i>	133
6.3.	<i>Structural optimization of the body</i>	138
6.4.	<i>Manufacturing Process</i>	145
Chapter 7: Wheels.....		155
7.1.	<i>Wheel bearings</i>	155
7.2.	<i>The wheel criteria</i>	159
7.3.	<i>Design process</i>	162
7.4.	<i>Manufacturing process</i>	173
Chapter 8: Front axle & steering system		183
8.1.	<i>The front axle</i>	183
8.2.	<i>The steering system</i>	188
Chapter 9: Powertrain.....		207
9.1.	<i>An overview of the PAC-Car II powertrain</i>	208
9.2.	<i>The drive motor</i>	210
9.3.	<i>The drive train</i>	215
9.4.	<i>The clutch</i>	228
9.5.	<i>The brakes</i>	232
Chapter 10: Fuel cell system		235
10.1.	<i>Fuel cell fundamentals</i>	235
10.2.	<i>The fuel cell system of PAC-Car II</i>	247
10.3.	<i>The control systems</i>	278
10.4.	<i>System results</i>	290

10.5.	<i>Conclusion</i>	294
Chapter 11: Driving strategy		295
11.1.	<i>The PAC-Car II model</i>	297
11.2.	<i>The driving strategy problem</i>	312
11.3.	<i>Validating the strategy and race results</i>	321
11.4.	<i>Conclusion</i>	324
Chapter 12: Conclusion and outlook.....		325

Chapter 1: Fuel economy competitions

By Jean-Jacques Santin.

This chapter introduces the fuel economy competitions and should provide useful information to the reader who has not yet encountered this specific kind of race. Section 1.1 presents the principles and spirit of these fuel economy challenges and describes the growth of these events around the world over the last several years. Section 1.2 focuses on fuel consumption measurement practices and the calculations that allow an overall ranking of the participating vehicles, whatever the fuel that they use. Like for all car races, the regulations are of primary importance. They define what is technically feasible and guarantee fairness and safety. The key aspects of the regulations that stipulate vehicle design for the European Shell Eco-marathon 2006 are summarized in Section 1.3. Section 1.4 provides a short history of the world records in fuel-efficiency and offers guidance and recommendations for obtaining official recognition of such records. Last but not least, Section 1.5 deals with the pilots and the necessary piloting skills.

1.1. The philosophy behind a fuel economy competition

1.1.1. The basic principles

The goal of fuel economy competitions is to develop and race a vehicle that consumes the least possible amount of fuel. The vehicle's performance is evaluated at a minimum average speed of about 30 km/h for a run of twenty or so kilometers. In general, the vehicles start from full stop and complete the 20-km run alone. The final vehicle ranking is determined by calculating the equivalent gasoline consumption, regardless of the fuel actually used. This calculation is performed using the lower heating value (LHV) of both fuels, and the results are expressed in kilometers per liter. Thus, for example, the fuel consumption in a hydrogen fuel cell vehicle is measured either by using a mass flow meter or by weighing the hydrogen storage system before and after the run. Then this consumption is converted in gasoline consumption as described above. At the time that these lines were written (2006), the record, set by our hydrogen fuel cell vehicle, is a theoretical distance of 5,385 km covered with the equivalent of one liter of gasoline.

1.1.2. The spirit of the competitions

These challenge competitions are open principally to students from a whole range of educational levels (e.g., middle schools, secondary schools, technical colleges, universities and engineering schools) from all around the world. Whatever the level, the challenge for the students and their teachers is to design and produce a vehicle that has the lowest possible fuel consumption and complies with the race regulations, while using only their own means.



*Figure 1-1: Family photo taken during the Shell Eco-marathon in 2004.
(Courtesy of Shell)*

Participating in a fuel economy event is a perfect occasion for students to learn to manage a long-term 1-year project from A to Z. This project touches on a large variety of subjects, ranging from the obvious design and manufacturing, to the less obvious management, communications, and finance. Participation provides a unique opportunity in the context of the school curriculum for students to work on team project that has a firm deadline (the date of the event), a real budget (often quite small), and a chance to compete internationally with other students. The search for technical partners and financial sponsors offers them an excellent initiation into the world of business, which can lead to useful professional contacts.

The project also introduces students to two of the primary topical concerns of the automotive industry: safety and environmental sustainability.

1.1.3. History of fuel economy races in Europe

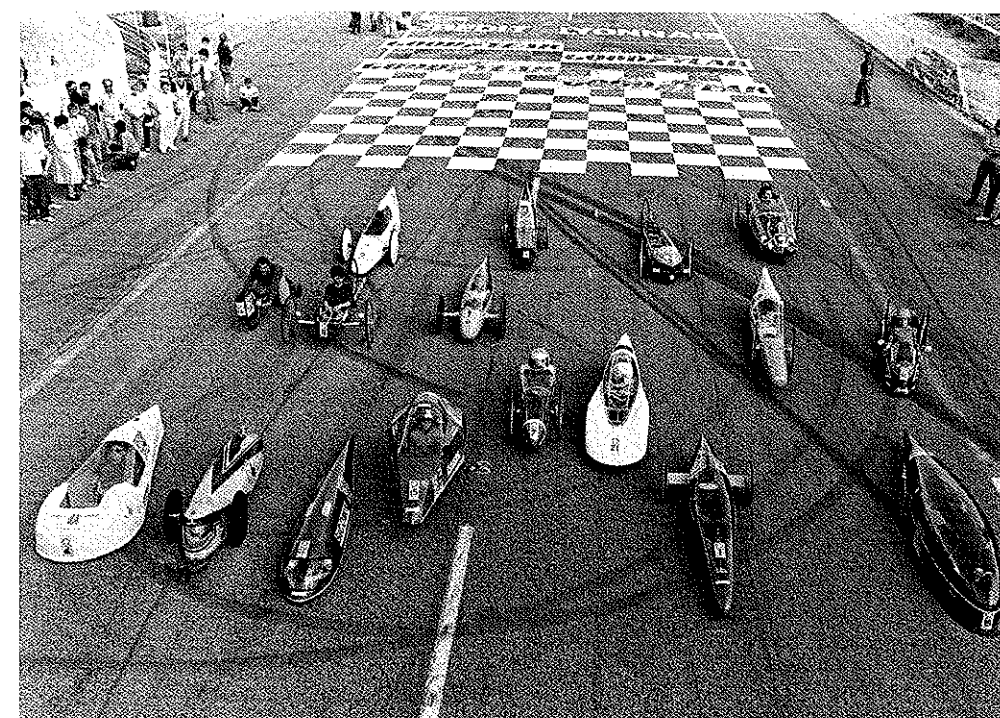


*Figure 1-2: Family photo taken during the French Shell Eco-marathon in 1985.
(Courtesy of Shell)*

According to its UK website, the Shell Eco-marathon “originated at Shell’s research lab in Illinois (USA) with friendly wagers between fellow scientists to see who could get the most miles per gallon from their vehicles. From these humble origins, where the winner scarcely achieved 50 MPG, more organized competitions evolved. In 1977, Shell organized the first competition at Mallory Park, essentially for student teams. In 1978 the competition grew further, and an open class was introduced.” The Finnish Mileage Marathon Club’s website, on the other hand, claims to have organized its thirtieth race in 2005, which would mean that the Finns started a bit earlier. The first Shell Eco-marathon event in France was not held until 1985, with a record of 680 km on a liter of gasoline.

1.1.4. Fuel economy races around the world

Several fuel economy challenges are held around the world, in countries like Finland, France, Japan, Scotland, the United Kingdom and the United States of America. Still others have taken place in other places. The various events all differ in terms of their tracks and their regulations, which have evolved over the years.

Undoubtedly, the best place to break a fuel economy record is the Shell Eco-marathon UK, an annual competition organized by Shell Global Solutions on the tremendous Rockingham Motor Speedway in Corby, Northamptonshire (UK). The principle reasons for this being the best place include: a ring track with large curvature radii (about 200 m), one of the lowest minimum average speeds allowed (24.1 km/h), and no minimum mandatory weight for the pilot.

1.1.5. Technical innovation

A fuel economy race is a propitious environment for technical innovation. Unfortunately, the majority of the teams do not have a strong enough connection to the worlds of research and industry – particularly the automotive or cycling industries – and have very limited financial support. These are the two primary obstacles to the development of true technical innovations. Still, at least three major automobile manufacturers, namely Ford, Honda, and Mercedes-Benz, have participated in these competitions in the past, so there is hope that the links to industry can be encouraged. Honda also organize from several years some fuel economy competitions called Honda Econo Power in countries like Japan, China and Thailand.

The most remarkable and long-lasting of the innovations for fuel-efficient vehicles is probably the so-called “stop-and-go” strategy. This strategy consists of switching off the engine when drive power is not required, and using it when it is most efficient, for example, when the vehicle is going uphill. On one hand, the stop-and-go strategy is becoming widespread, as is proved by the launching on the market of the Citroën “Stop & Start” system or the BMW “Auto Start/Stop” system. On the other hand, using the engine at its most efficient operating point is now possible in hybrid vehicles, thanks to the reversibility of the electric drive motor. A scientific discussion about these ideas can be found in [1].

1.2. Measuring fuel consumption

In this section, two kinds of fuel are considered separately. First (1.2.1), we present the so-called “conventional fuels”, which have been used for many years in fuel economy contests, and for which the fuel consumption measurement protocol is well-established and well known. Then (1.2.2), we move on to the less well-known

case of hydrogen, which is typical in fuel cell powered vehicles. The other fuels are not considered. The next sub-section (1.2.3) explains how the equivalent gasoline consumption is calculated for several kinds of fuel, and the last sub-section (1.2.4) explains how and why the final figure is displayed as the number of kilometers covered per liter of gasoline.

1.2.1. Conventional fuels

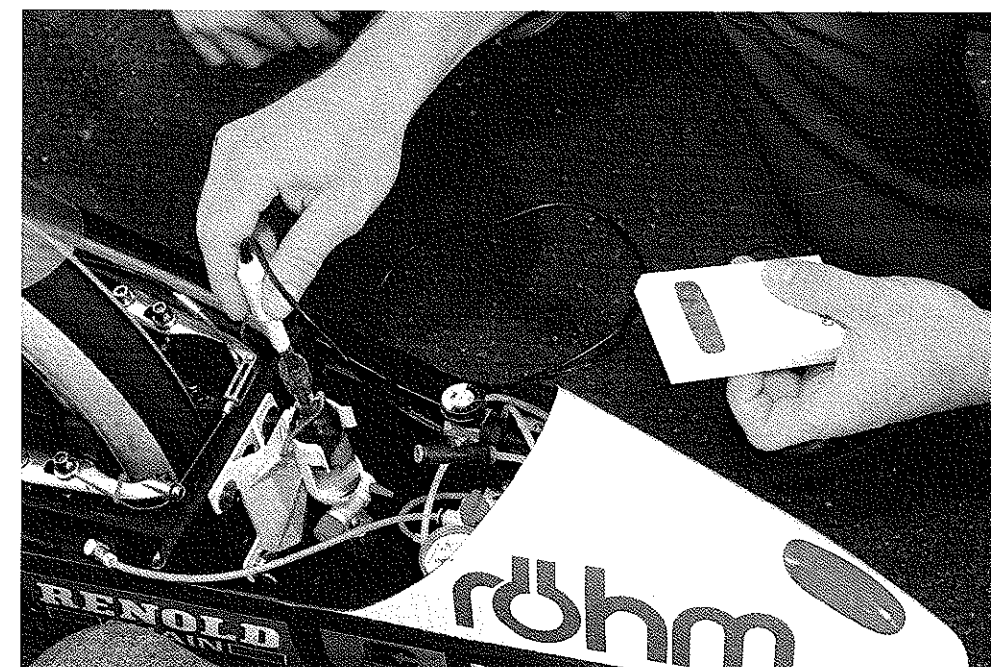


Figure 1-3: Measurement of the fuel temperature after the tank has been refilled, part of the measuring procedure by volume of the fuel consumption during the European Shell Eco-marathon. (Courtesy of Shell)

The “conventional” fuels include gasoline, diesel fuel, and Liquefied Petroleum Gas (LPG). The consumption of liquid fuels like gasoline and diesel are measured either by volume or by weight. The consumption of LPG, on the other hand, is only measured by weight.

Measurement by volume

Measurement by volume is the standard measuring system used in the competitions. The vehicles used in the competitions are all equipped with a special glass tank,

which has a visible marker on its side, allowing it to always be filled to the same level. A few minutes before departure, the tank is filled to the level of that marker by a race steward. After the run, a steward using a precisely graduated pipette again fills the tank up to that same mark. The quantity of fuel added by the steward is the quantity of fuel used during the run. The temperature of the fuel is also measured, before and after the run, making it possible to take the fuel's thermal expansion into account, and to convert the volume consumed into the actual mass consumed.

Measurement by weight

Measurement by weight is reserved for the top teams. This technique is much more precise, but is a complex procedure that takes much longer. First, the entire fuel supply system – the tank, the flexible gasoline pipe and the injector – is dismantled. The system is then filled, carefully bled of all air bubbles, weighed and then reassembled in the vehicle. After the run, it is again dismantled and weighed. The difference in weight is the weight of fuel consumed. The scales used in this procedure are precise to one hundredth of a gram. Calibrated on the spot, they are used in an air-conditioned room on an anti-vibratory table.

1.2.2. Hydrogen fuel

There are two procedures currently in use for measuring hydrogen fuel consumption. One relies on an embedded flowmeter to measure the mass flow of hydrogen, and the other weighs the hydrogen tank. They are sometimes used together in order to verify the coherence of the results.

Measurement by flowmeter

A flowmeter is a measuring instrument installed in the hydrogen circuit, at the outlet of the pressure regulator situated downstream from the tank. It measures the instantaneous mass flow of hydrogen and calculates the total amount consumed during the entire run. Several sensor technologies that are more or less appropriate for this specific application are available on the market. Sometimes, the flowmeter has a display, allowing a direct reading of the measurement, and a basic keyboard for resetting the display to zero. Alternatively, these operations can be carried out via a computer link and dedicated software.

However, the intrinsic accuracy of such a device is around 5% (full scale), which is insufficient for ranking high-performance teams. Moreover, certain flow levels are not detected, such as those that are too slight or too short and high. For example, the diffusion of hydrogen through the membranes when the stack is pressurized but no electric power is delivered can lead to a very slight flow, around 3 S₁ (Standard liter) of hydrogen per hour and per square meter of active surface of the membrane.

On the other hand, purging the hydrogen circuit can generate a very short flow peak, equal to around 3 S₁ of hydrogen per second during a tenth of a second. Of course, those two figures are fairly approximative as they both depend on many parameters, such as, in case of the hydrogen diffusion flow rate, the type of membrane or the differential pressure on both sides of the membrane. For all these reasons, weighing the tank is preferable to using a flowmeter.

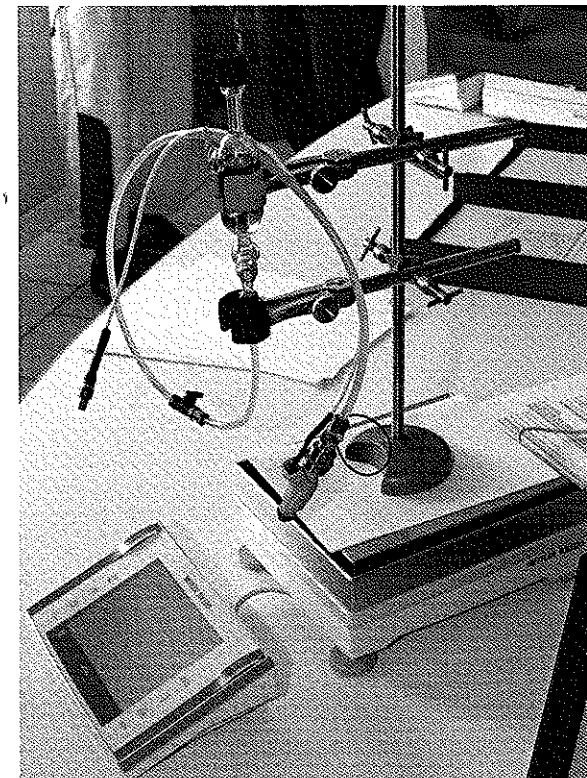


*Figure 1-4: Measurement by weight of the fuel consumption during the European Shell Eco-marathon. The entire fueling system has been put on the scale.
(Courtesy of Shell)*

Measurement by weight

In principle, the procedure for measuring hydrogen consumption by weight is nearly identical to the one used for the standard fuels (Section 1.2.1). Still, some differences do exist, and they are described below.

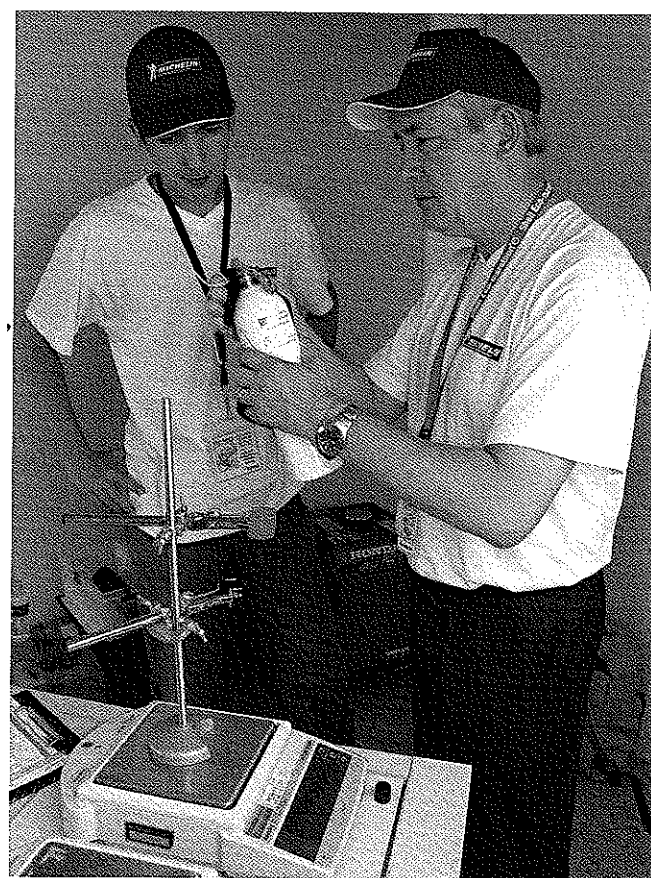


Figure 1-5: Measurement by weight of the hydrogen consumption of PAC-Car II during the Shell Eco-marathon at the Michelin Technology Center in 2005.

Unlike a conventional fuel engine, the fueling system of a FCS cannot be separated: the hydrogen circuit is constituted of many inter-connected components, including the stack. Therefore, the tank itself must be dismounted in order to weigh it. The consequences of this reality are two-fold:

- the tank must be equipped with a double-end shutoff connector, which makes it possible to disconnect the tank from the hydrogen circuit without a pressure drop on both sides, and without any hydrogen leaking. However, before connecting the full tank after weighing, the hydrogen circuit must first be pressurized at the same pressure as the full tank, using a separate bottle;
- the tank must not weigh more than the maximal load of the scale, which is generally a few hundred grams. If the tank exceeds this maximal weight, it is

impossible to obtain the necessary accuracy (i.e., at least one hundredth of a gram) for measuring the consumption of only a few grams of hydrogen. For this reason, we strongly recommend contacting the organizers of the competition at an early date to find out the exact type of scale that will be used.

1.2.3. Calculating the equivalent gasoline consumption

Since 2004, regardless of the fuel really used, the overall ranking of the competitors in the Shell Eco-marathon in France is based on the equivalent consumption of Shell Unleaded 95 gasoline. This regulation was made inevitable by the growing diversity of fuels used for the competition. Up to that point, gasoline consumption was compared to LPG consumption, for example, without even considering whether the two fuels had the same energy value! This kind of inapt comparison, which is widespread among the general public (After all, who has not compared the consumption of a gasoline vehicle with a diesel vehicle?), was brought into question when the competition began to register vehicles using a fuel that, whatever its pressure, can only be in a gaseous state at the ambient temperature: hydrogen.

Beginning in 2004, the calculations of equivalent gasoline consumption has been based on the lower heating value (LHV, also known as “net calorific value”) of the different fuels. The LHV, expressed in MJ/kg, represents the quantity of heat given off by the complete combustion of 1 kg of this fuel in air, under certain well-defined initial and final conditions of temperature, pressure and state of byproducts. This value provides an index of the energy content of different fuels. The following table collects the LHV and the densities of the most generally used fuels.

Table 1-1: Lower heating value (LHV) and density values for a few fuels.

Fuel	LHV [kJ/g] [2]	density [g/ml] [3]
Shell Unleaded 95 gasoline	42.9	0.730...0.780
LPG “Gepel-Butagaz”	46.0	0.54
Diesel “Shell Formula Diesel Plus”	42.6	0.815...0.855
Rapeseed methyl ester	37.7	
Dimethyl ether	28.43	
Ethanol	26.9	0.79
Hydrogen	119.93	

To provide a concrete application of the above information, consider the PAC-Car II performance. The PAC-Car II consumed 1.02 grams of hydrogen during its run for the Shell Eco-marathon at the Michelin Technology Center in

Ladoux, France, on 26 June 2005. The following formula can be used to convert this amount of fuel into the equivalent volume of gasoline, $v_{gas\ eq.}$:

$$v_{gas\ eq.} = \frac{119.93 \times 1.02}{42.9 \times 0.74262} = 3.8397 \text{ ml} \quad (1.1)$$

1.2.4. Expressing of the final result

Usually, the fuel consumption of a ground transport vehicle is expressed as the number of liters consumed to cover a distance of 100 km under standardized conditions (i.e., speed profiles called driving cycles). However, in the fuel economy competitions, the final result is expressed as the number of kilometers covered per liter of gasoline. This commonly causes confusion among the general public, who assume that the vehicles have really covered the distance indicated. Still, in deciding to express the results in this way, the organizers of the event made a deliberate choice since they felt that a result in liters consumed per 100 km wasn't meaningful enough for the average person. Certainly, 5,385 km per liter is more evocative than 0.01857 l per 100 km! Furthermore, expressing the results in liters per hundred kilometers would make the difference between the best vehicles appear to be narrow and insignificant.

In reality, for example, the PAC-Car II covered 20.678 km using an amount of fuel equivalent to 3.8398 ml of gasoline. Given that real consumption, the pro rata distance that would have been covered if one liter of fuel had really been consumed can be calculated as follows:

$$d_{1\ litre} = \frac{20.678}{3.8398} \times 1,000 = 5,385 \text{ km} \quad (1.2)$$

1.3. A brief summary of the Shell Eco-marathon rules and regulations

The information given below is taken from the regulations of the European Shell Eco-marathon 2006 (prototype group). This is partial summary designed to provide general guidance. This section reviews some of the rules related to the vehicles, but the rules governing the organization or the traffic on the track, for example, have not been mentioned. Please remember that this is a summary, and that only the official regulations are valid!

The rules of the competition have been established with the dual purpose of maintaining safety and fairness, with the two ideas sometimes overlapping. Some of the rules pertaining to safety are presented in Section 1.3.1. A fuel economy

competition is just like any car race, with its attendant risks of collision or leaving the track. If there have been no accidents or major incidents since the start of these competitions, it is definitely due to the safety regulations, the relatively low vehicle velocity, and the small amount of fuel taken on board. Section 1.3.2 introduces some of the rules designed to make the competitions fair, offering the same chance of success to everyone, while at the same time preventing cheating.

1.3.1. Safety

In the automotive industry, safety systems are divided into three main categories:

- Primary (or active) safety systems, which focus on both the vehicle and its environment, are intended to avoid accidents;
- Secondary (or passive) safety systems focus on the vehicle itself, and are designed to prevent serious injuries to the pilots during a crash;
- Tertiary safety systems also target the vehicle, but they are intended to facilitate the intervention of the rescue teams after an accident.

These three levels of safety can be found in the rules of the competition, and this summary follows that organization.

Primary safety

- Three or four running wheels must be in continuous contact with the road.
- The minimum track width between the two outermost wheels is 50 cm (110 cm at the most).
- The wheelbase must be at least 1m.
- The maximum height measured at the top of the pilots' compartment must be less than 1.25 times the maximum track width.
- Pilots must have direct forward visibility. They must be able to turn their heads 90° on each side of the longitudinal axis of the vehicle. This field of vision must be achieved without help of any optical devices, such as mirrors, prisms, periscopes, etc.
- The vehicle must be equipped with a side-view mirror with a minimum surface area of 25 cm² on each side of the vehicle.
- The cockpit must be properly ventilated and equipped with a sunscreen windscreens.

- The vehicle must be equipped with at least two independent braking devices such that the failure of any one system does not render the other(s) inoperative. Hydraulically-controlled braking systems or disc brakes are required. The effectiveness of each brake systems is tested as follows: the vehicle must remain immobile when it is placed on a 20% incline.
- The vehicle must be equipped with a loud automotive-type horn, which must be used before passing any vehicle.
- The whole fueling system, from the tank to the engine, must be placed in a compartment completely separated from the cockpit. It must be properly ventilated with fresh air drawn from outside the vehicle and then expelled directly from the vehicle. For hydrogen-powered vehicles, this compartment must have a ventilation window measuring 1 cm² situated at the highest point of the compartment.

Secondary safety

- The headfirst driving position is prohibited.
- The pilots must wear a helmet (lightweight motorbike type).
- Synthetic pilots clothing are forbidden.
- Driving barefoot or in socks is prohibited.
- The pilots' seat must be equipped with a four-point safety belt.
- The sides of the cockpit must be sufficiently reinforced to protect the pilots from possible lateral shocks.
- The cockpit must be equipped with an effective roll bar, extending beyond the width of the pilots' shoulders. This bar must be at least 5 cm above the top of the pilots' helmet and must be capable of withstanding a 700 daN static load applied to its center without bending.
- A minimum distance of 10 cm is required between the pilots' feet and the internal front bodywork.

Tertiary safety

- An extinguisher must be placed in the cockpit within the pilots' reach.

- Pilots must be able to vacate their vehicles at any time without assistance. The vehicle must be equipped with a sufficiently large opening for the cockpit.
- The fuel cell system must be equipped with an emergency shutdown valve, easily accessible from the exterior via an opening in the bodywork or an access hatch that can be easily opened or broken.

1.3.2. Fairness

- Mobile aerodynamics appendages are forbidden.
- Stored electrical or pneumatic energy that is not replaced by the engine during the competition may only be used for the self-starter, the ignition and injection systems, and the instrumentation and metering units. Auxiliary energy sources (e.g., solar, chemical) are not permitted.
- For fuel cell vehicles: the use of non-replaced oxygen or compressed air reserves is not authorized.
- The wheels located inside the bodywork must not be accessible to the pilots.
- A bulkhead must be mounted between the engine compartment and the cockpit, preventing any manual access to the engine compartment by the driver.

1.4. World records

1.4.1. A brief history

Given the differences between the race circuits, the regulations and the fuels allowed in the various competitions organized throughout the world, it is very difficult to compare the results obtained. The 2004 introduction of an equivalent gasoline consumption calculation for all fuels (described in Section 1.2.3) has made comparing results less complicated, but it is not likely to become any easier soon.

The background information related to the fuel economy world record presented in Figure 1-6 was reconstructed by gathering together and examining the information available on the Internet: the official results published by the Guinness World Records², the official results appearing on the competition websites, and the results

² www.guinnessworldrecords.com

posted by the individual teams. Vehicles with Internal Combustion Engines (ICE), running on gasoline, are shown in blue, and vehicles powered by fuel cells, which run on hydrogen, in green.

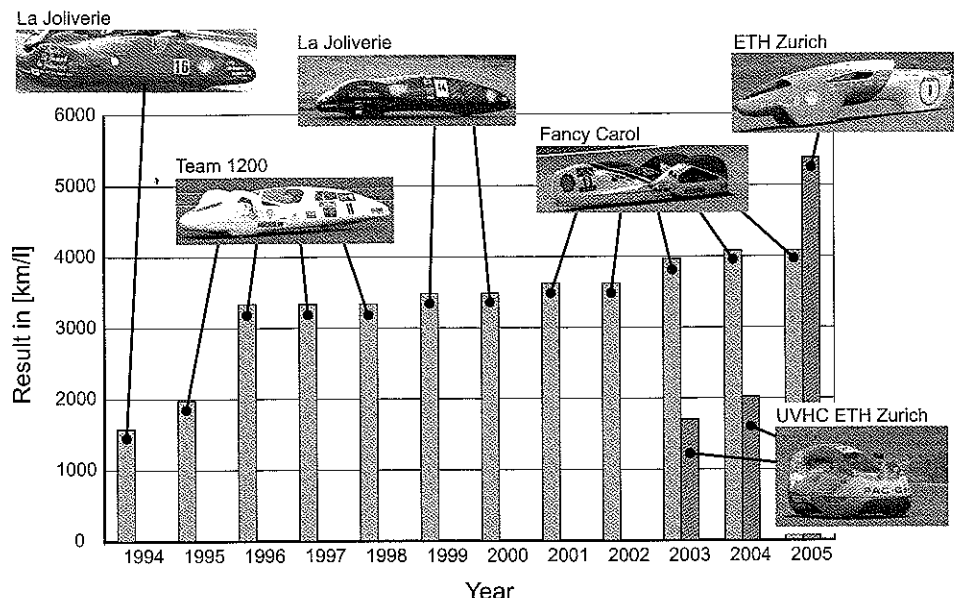


Figure 1-6: History of the world record for the fuel economy vehicle, based on our own investigations.

(Photo of Fancy Carol courtesy of Fancy Carol)

(Photo of PAC-Car I courtesy of Gérard Dechenaud)

(Photo of PAC-Car II courtesy of Dieter Wanke)

The year 1996 appears to have been a turning-point: the world record went from about 2,000 km/liter to 3,000 km/liter. This significant step forward might have been the result of the use of radial-ply tires specifically designed for such a competition instead of cross-ply tires, but this cannot be affirmed categorically. In any case, from 1996 to 2005, the results obtained by gasoline vehicles improved steadily, going from about 3,300 km/l to 4,100 km/l. The first vehicle powered by a hydrogen fuel cell, the PAC-Car I developed by ETH Zurich and University of Valenciennes, appeared in 2003. In 2005, the PAC-Car II, developed solely by ETH Zurich, outclassed the ICE-powered vehicles, improving the fuel economy performance to 5,385 km/l.

1.4.2. Obtaining an official world record

If your ultimate goal is to break the world record of fuel economy, it is necessary to get your result recognized by an official organization, which requires serious preparation. In fact, obtaining official recognition of a performance after the fact is almost always impossible, so one of your team members should be assigned exclusively to this task, beginning some months before the record-breaking attempt.

The recognition procedure may not be free of charge. For instance, the Guinness World Records (GWR) offers a free standard procedure, but the paying procedure offers additional services and dramatically speeds up the feedback and email exchanges, so we strongly suggest using it. Keep in mind that GWR receives hundreds of thousands of record proposals each year! If you want an adjudicator to attend the event, which is generally not necessary, you may have to pay costs, including traveling expenses, accommodation and a daily attendance fee. Though the original certificate is free, any copies requested may accrue additional charges.

The main tasks that you must accomplish include:

Before the attempt

- contact the organization that will register your record;
- prepare all the requested material (e.g., official forms, witness' letters, log books);
- contact the people who might help you get your record recognized (e.g., adjudicators, witnesses, reporters, photographers) and inform them of the role you would like them to play;
- prepare for the arrival of those you have invited (e.g., arranging for their transportation and accommodation).

During the attempt

- accompany your guests and keep them informed about what is going on;
- make sure that the requested information is being properly gathered.

After the attempt

- collect all the requested material (e.g., authentication statements, forms, log books, photographs, videos, newspaper and magazine clippings)

- prepare the material to send to the recording organization;
- update your claim;
- inform your team members and partners that the official record has been obtained and then... celebrate!



Figure 1-7: The PAC-Car II team during the award ceremony of the Shell Eco-marathon at the Michelin Technology Center, on 26 June 2005.

1.5. The pilot

This book deals almost exclusively with technical ideas. As technical experts, our natural tendency is to forget about the human beings involved. Nonetheless, the pilot is one of the key elements of the success of such a project, and as such has a place in this book. We estimate that the difference between a talented and an inept pilot can influence the final result by about 30%. Unfortunately, fuel economy races are so different from speed races that even a talented speed race pilot may not have the necessary skills for a fuel economy competition. So, what then constitutes a talented pilot?

First of all, according to the requirements set in the official event rules, the pilot must be a student at the school registered in the competition. In addition to this mandatory criterion, the ideal pilot is psychologically strong enough to withstand the pressure of the challenge and the media, is not claustrophobic, is calm in all situations, as well as modest and easy to talk to. This person must also be physically strong enough to withstand the heat when sitting for almost an hour in a narrow vehicle exposed to sunshine, while also weighing as little as possible, preferably close to the minimum authorized weight. It can also be a great advantage to have access to two interchangeable pilots, both being either right-handed or left-handed.

It is important to involve the pilot in the vehicle design process from the very beginning. For example, the body shell can be drawn to conform to the pilot's body, making it as tiny as physically possible. But, the pilot should remain focused on the driving task and thus should not be implicated in the technical choices about the vehicle. Having a coach, who can serve as the interface between the pilot and the technical staff and help the pilot to develop a driving strategy, can be an advantage.

Chapter 2: Some design considerations for fuel economy vehicles

By Jean-Jacques Santin.

Because time, money and materials are not infinite, project priorities must be set during the preparatory phase of the project in order to decide where the most effort must be expended to reach the goal. In general, there are two major areas that must be considered. First, early in the project, several major decisions about vehicle architecture must be made in order to eliminate poor or unrealistic solutions. Second, target figures have to be defined. These figures, which serve as preliminary input in the highly iterative design process, help to maintain project coherency while also verifying that the targeted fuel consumption is reachable.

This chapter describes some of the preliminary choices made for the PAC-Car II design. Section 2.1 explains the process used to choose the design with the best potential in terms of fuel economy: three wheels, two in front and one in the back, with the rear wheel being powered and steered. The preliminary calculations presented in Section 2.2 define the minimum vehicle specifications needed to give us a chance of breaking the then world record, for example, the vehicle's maximal weight or minimal tank-to-wheel powertrain efficiency.

2.1. Defining the vehicle architecture

2.1.1. The number of wheels

Generally speaking, two-, three-, and four-wheel vehicles are feasible. However, the two-wheel vehicle architecture is not permitted by the race regulations, which specify that 3 or 4 running wheels must be in continuous contact with the road (Section 1.3). Still, as shown in Figure 2-1 (a), it is possible to finesse this regulation: the vehicle in this photo is basically a two-wheel vehicle to which 2 side wheels were added in order to respect the regulations.

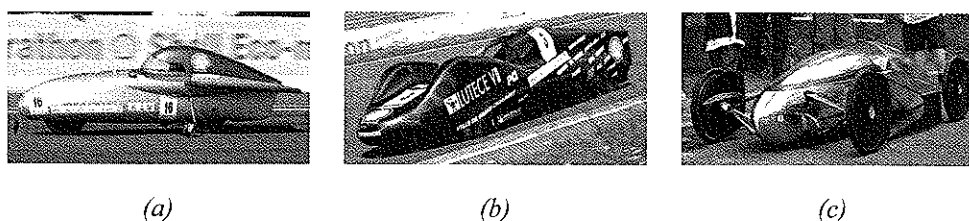


*Figure 2-1: Examples of two-, three-, and four-wheel vehicles.
(Photo (c) courtesy of Jim Shaw, Bentley Motors Limited)*

The four-wheel vehicle, on the other hand, has a more appealing appearance since it looks more like a real automobile. Figure 2-1 (c) shows the four-wheel vehicle designed for gravity race competitions. However, this design is not appropriate for fuel economy competitions for several reasons:

- it increases the vehicle's weight and complexity;
- it requires a suspension system to compensate for the unevenness of the road surface in order to maintain the required tire/road contact; and
- it requires some kind of a differential to distribute the drive torque symmetrically.

This last reason merits a more detailed explanation. In fact, normally, a four-wheel vehicle employs at least two drive wheels. Using a single drive wheel on a four-wheeled vehicle induces yaw torque, which must be balanced somewhere by the steering to allow the vehicle to move in a straight line. This steering compensation generates additional rolling resistance (Chapter 4). Replacing the conventional differential by two overrunning clutches, one in each drive wheel, does not solve the problem since it actually amounts to the same thing as a single drive wheel: the drive torque is transmitted to the inner wheel, which turns slower when cornering. Removing the differential is obviously not an option either, as the difference between the rotational speed of the inner and the outer wheel would lead to tire slip and energy loss. Given the incompatibility of the 2-wheel and 4-wheel vehicle designs, the best number of wheels for a fuel economy vehicle appears to be three (Figure 2-1 (b)).

2.1.2. The number of axles

Once the number of wheels has been chosen, the next step is to decide how many axles the wheels will be mounted on. Given the 3-wheel design selected above, the choice is between two or three axles.

Mounting the three wheels on three different axles set in the same longitudinal plane would be rejected during the technical inspection since the track width would be nil and therefore less than the minimum value requested by the regulations.

A three-axle architecture, in which the wheels are not in the same longitudinal plane, would result in a non-symmetrical vehicle. Such non-symmetrical vehicles have already competed, their designers arguing that this design could lower rolling resistance since the vehicle turns more often in one direction than the other (e.g., more to the right than to the left) due to the looping of the track. However, in reality, non-symmetric geometries imply a drive dissymmetry that would have to be counterbalanced by the tires, which means additional rolling resistance, whatever the vehicle trajectory. Therefore, we chose to design the PAC-Car II with three wheels mounted symmetrically on two axles.

2.1.3. The front wheels

Once the number of wheels and axles and their symmetry/dissymmetry has been decided upon (e.g., three wheels mounted with two symmetrical axles), the next step in defining the vehicle architecture is choosing the wheel configuration. Two configurations are possible:

- a single front wheel and two rear wheels, called the 1+2 layout; or
- two front wheels and a single rear wheel, called the 2+1 layout.

A few examples of 1+2 and 2+1 vehicles are shown in Figure 2-2.

The main criteria for choosing the best wheel configuration are:

- the aerodynamics of the resulting vehicle shape;
- the forward and lateral visibility from the driver's seat; and
- the vehicle's stability and rollover resistance.

The following sections describe these criteria in detail.

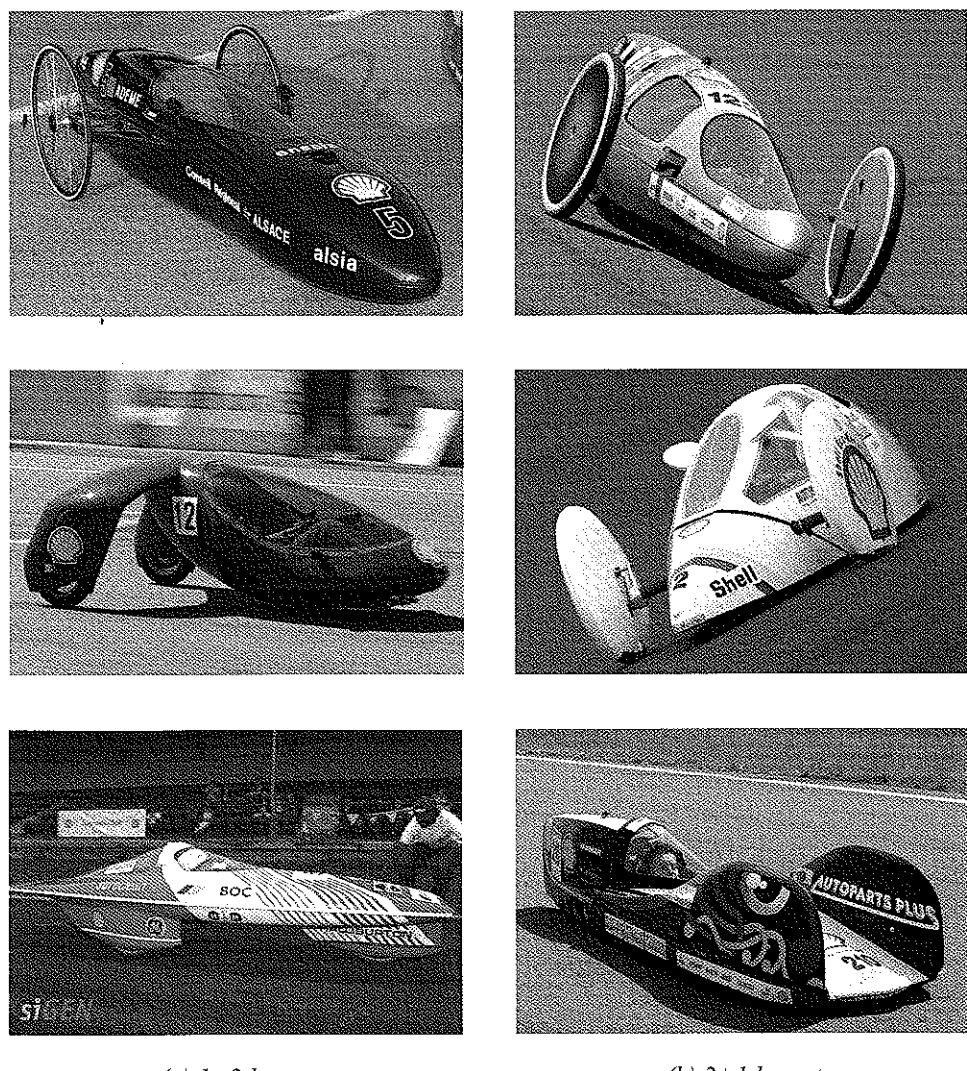


*Figure 2-2: Examples of 2+1 and 1+2 vehicles.
 (Photo of Gh2ost courtesy of siGEN Ltd – Fuel Cell Power Solutions)
 (Photos (b) courtesy of Shell)*

Aerodynamic potential of the vehicle's body

Even at this stage of the vehicle design, decisions concerning the shape of the vehicle must be made. A quick bibliographic search for the aerodynamic drag coefficients of simple geometric shapes [3, 4] shows that a vehicle body whose

cross section is wider in the front than in the rear offers a greater potential for lowering the vehicle's aerodynamic drag. Based on this information, given a vehicle body that covers all of the wheels, the 2+1 layout would provide a lower drag force than the 1+2 layout.

For the complete details of the aerodynamic study of the bodywork, see Chapter 5.

Forward and lateral visibility

The primary visibility problem comes from the wheels themselves, which take up a lot of room inside the vehicle body. As will be explained in Section 3.2, the choice of the tire diameters offered on the market is highly limited. Deciding to use tires with the best rolling resistance values means using a tire with a diameter of about 50 cm. Choosing disk-type wheels (Section 7.2) can reduce the driver's field of vision. In fact, there is really no single best solution: the 2+1 layout limits the driver's lateral field of vision, whereas the 1+2 layout reduces the driver's forward field of vision. Regardless of the wheel configuration ultimately chosen, this visibility issue should be considered as soon as possible in the design process. (More details on the way visibility was dealt with in the PAC-Car II are discussed in Section 6.1.)

Stability and rollover resistance

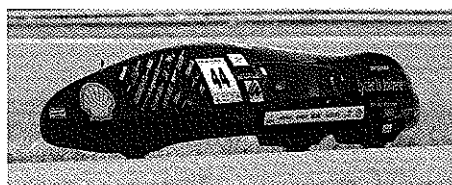
Rollovers are the most frequent accidents during fuel economy competitions, with one or two usually occurring at each race. This tendency to roll is due to the three-wheel configuration, which is less stable than the common four-wheel one, especially under specific traffic conditions, such as a sudden high-speed turn to avoid an obstacle or a turn while braking.

The wheel layout is not the only parameter influencing the rollover resistance of a vehicle. The other fundamental parameters include the track width, the wheelbase, the position of the center of gravity (CG), the tire-road adhesion, and the vehicle's braking capability. Obviously, vehicle velocity and the turn radius also play a role in the level of lateral acceleration that is ultimately responsible for rollovers. Track superelevation and lateral winds can also influence vehicle stability.

A steady-state analytical study of a vehicle's rollover resistance can easily be done by applying the Newton's second law. This method is similar to the one described in Section 4.2. Still, at this stage of the design process, the graphic method suggested by Riley [5] will also provide satisfactory results. Both methods show that, because the acceleration level of a car is higher while braking than accelerating, the 2+1 layout offers a better rollover resistance than the 1+2 layout.

2.1.4. The steer wheel(s)

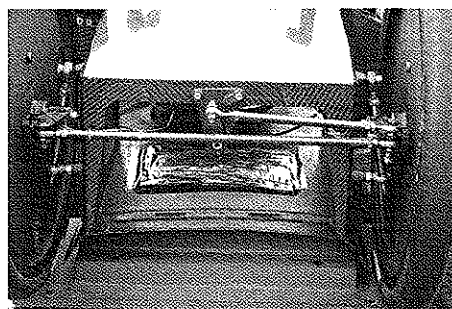
Based on the information presented in section 1.1.3, the 2+1 layout appears to be the better choice for a FEV. Given this choice, there are three possible options for the steer wheel position: front, rear, or both front and rear (i.e., three-wheel steering system). Figure 2-3 shows an example of both a front steer wheel and a rear steer wheel vehicle.



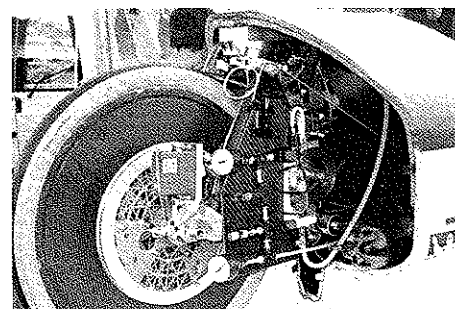
(Courtesy of Shell)



(Courtesy of Shell)



(a) Front steer wheel vehicle



(b) Rear steer wheel vehicle

Figure 2-3: Example of a front and a rear steer wheel vehicle.

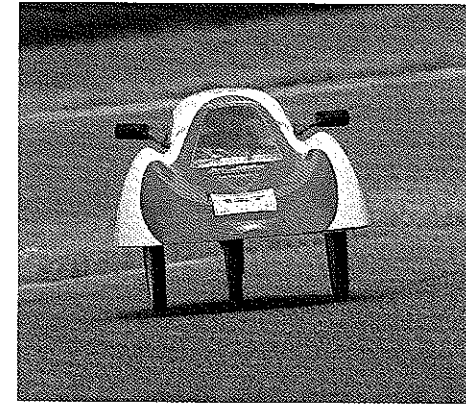
During the design phase of PAC-Car II, the steer wheel choice remained open for a long time. It was impossible to make a simple decision based on theoretical considerations, despite – or maybe because of – the importance of the choice and its extensive consequences.

Steer wheels, after all, require ample room to turn without touching the inside of the vehicle body. Thus, the consequence of choosing a front steer wheel would be a larger frontal area, thus increasing the aerodynamic drag. On the other hand, a rear steer wheel would use the space already available at the back of the vehicle both due to the headspace required by the regulations for the driver's helmet, which is located close to the rear wheel, and due to aerodynamic considerations that impose a gradual decrease in the dimensions of body sections towards the tail. In addition,

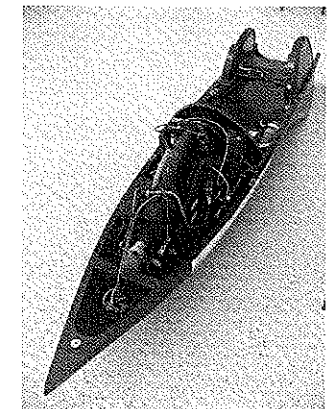
putting the steer wheel at the rear of the vehicle would allow the front wheels to be tilted, thus lowering the frontal area even more (Figure 2-4).



(Courtesy of Shell)



(Courtesy of Shell)



(Courtesy of Ecomobile Team)

(a) Non-tilted front wheels

(b) Tilted front wheels

Figure 2-4: Examples of vehicles with and without tilted front wheels.

Our decision was hampered by a lack of information about vehicles with rear steer wheels. A bibliographic search showed that this configuration had a lot of drawbacks, including difficulties in maintaining the correct heading and steering stability.

However, the three-wheel steering configuration offers one additional degree of freedom: depending on the steering kinematics, the center of turn can be shifted slightly forward or backward, thus changing the level of drivability and comfort. Still, for a FEV, the important question concerned whether or not this steer wheel configuration would lower the rolling resistance when cornering? The results of a steady state cornering analysis (presented in Section 4.3), as well as experiments with PAC-Car I (Section 8.2) indicated that the answer was no. Another advantage of the three-wheel steering configuration is the possibility of turning the body along its yaw axle, setting it to catch the wind like a glider, thus lowering the aerodynamic drag.

In the end, after track-testing a modified version of PAC-Car I, we chose to use a rear steer wheel and tilted front wheels in the PAC-Car II. We must admit that the advantage over the more common front steer wheel solution is fairly minute, and so the success of PAC-Car II is more due to the outstanding work done on the aerodynamics of the vehicle body than the position of the steer wheel.

2.1.5. The drive wheel(s)

As explained in Section 2.1.1, the three-wheel configuration was chosen for our vehicle in order to have a single drive wheel, which makes the vehicle simpler and lighter. Given this logic, it makes sense to drive the single rear wheel.

Still, this logic could be called into question in the case of an electric vehicle – which is, after all, what a fuel cell powered vehicle (FCPV) is. Using two identical motors, each mounted on one of the front wheels and properly current-controlled, would allow the drive torque to be distributed equally, in much the same way that a differential would act with a single motor. This solution would thus be simpler than the single motor with a differential. But, if these motors need a transmission to increase their drive torque, the solution becomes more complicated as well as heavier because two transmissions would be required. In addition, if the electric generator (e.g., a fuel cell system) is installed in the rear of the vehicle, long electrical wires would be necessary, which would lead to undesirable copper losses. Thus, the single rear drive wheel solution remains the best choice.

2.1.6. The brake wheel(s)

In a standard vehicle, all the wheels are equipped with a brake. Due to the increase of the vertical load on the front axle while braking, the brakes are more effective when they act on the front wheels. In case of the 2+1 wheel configuration, this would mean 2 brakes, one for each wheel, with a braking control device to balance braking torque.

However, in the FEV context, the brakes are almost never used, and their effectiveness is only tested under static conditions during the technical inspection (see Section 1.3). Therefore, the best solution is to equip only the single rear wheel with a brake, thus reducing the weight of the vehicle.

2.1.7. Track width, wheelbase and ground-CG distance

The track width is the distance between the two wheels of a vehicle axle. The track width has a large influence on the size of the frontal area of the vehicle, and therefore on the aerodynamic drag. Consequently, the narrower the track width, the lower the drag. On the other hand, a narrower track width also means a less

rollover-resistant vehicle. For this reason, the minimal track width has been officially set to 50 cm in the race regulations (Section 1.3).

The wheelbase is the distance between the front axle and the rear axle of a vehicle. The minimal wheelbase parameter value is also set in the regulations. Obviously, the longer the vehicle, the heavier it will be. For a vehicle with a front steer wheel, the larger the wheelbase, the larger the frontal area must be, since more room is needed to steer the wheels, which in turn provides a given turn radius. From the point of view of aerodynamics, the longer the vehicle, the larger the wetted area and the more friction drag there will be (see Section 5.1). However, a body that is short and blunt may cause aerodynamic drag due to flow separation. Since the wheelbase has no influence on the rolling resistance when cornering (see Section 4.5), it can be chosen in consideration of other criteria, such as stability, weight distribution, or available room.

The ground-CG distance is the distance between the ground and the vehicle's center of gravity. Once the track width and wheel base have been determined, the next step is to decide whether the ground-CG distance should be large or small. In making that decision, several criteria must be considered: the rollover resistance, the rolling resistance when cornering, and the aerodynamic drag. The conclusions related to the first criterion are fairly obvious: the larger the ground-CG distance, the less rollover resistance the vehicle will have. The second criterion is a bit more difficult to analyze. To estimate the rolling resistance when cornering, we used the tri-cycle vehicle model and the optimizing method detailed in Section 4.2.3. For the range of variation studied, the larger the ground-CG distance, the lower the cornering rolling resistance appeared to be. The last criterion, aerodynamic drag, is analyzed in detail in Section 5.3. According to our bibliographic search, the optimal ground clearance is around 20 cm. In light of this optimum, the ground-CG distance should be chosen as high as possible while still preventing rollovers.

2.1.8. Synthesis

At this stage of the design process, it seemed that the best vehicle architecture for fuel economy races is a 3-wheel symmetrical vehicle, with two front wheels and one rear drive wheel that is equipped with brakes. A rear steer wheel also seems to be a good option. However, the advantage provided by tilting the front wheel inside the body (i.e., negative camber angle) is slighter and needs further investigations. The track width should be set to the authorized minimal value (50 cm), but the wheelbase can be defined later. The vehicle CG does not need to be as low as possible, which leaves the option of a vehicle body with a large ground clearance open. As a result of our previous choices, all the wheels in the PAC-Car II are contained inside the vehicle body.

2.2. Defining the target figures of the vehicle

All the teams competing in fuel economy competitions have their own goals. The lowest fuel consumption is just one of the possibilities. Other goals are testing an innovative technical solution, consuming less fuel than the previous year's entry, winning a special award, or training students, to name but a few.

This section focuses on one of the possible goals: lowering fuel consumption. Concretely, this means determining the target number of kilometers to be covered per liter of gasoline. For the PAC-Car II project, our goal was to attain the lowest fuel consumption ever for a ground transport vehicle, whatever the conditions (i.e., vehicle type, event, average speed). We set this figure at 4,500 km/l since the best previous performance was 4,071 km/l, the world record set by FancyCarol during the Supermileage Car Challenge Hiroshima held in Japan in 2004 (Section 1.4.1). This target figure then had to be converted into the technical parameters characterizing the vehicle, which would be used as engineering specifications when designing the vehicle components. These parameters had to be realistic as well as consistent with each other because they determined the work that would have to be done in terms of time, manpower, materials, and money.

In this section, these parameters are presented and explained, along with our best answer to the question of what factors are primarily responsible for the fuel consumption of a vehicle. The three main factors are drag, powertrain efficiency and driving style. The drag and powertrain efficiency factors are discussed in the sub-sections below, while driving style is explained in detail in Chapter 11.

2.2.1. Drag

The general rule holds that the lower the drag, the lower the fuel consumption. Drag is the longitudinal retaining force generated by rolling resistance, aerodynamics, road slope or vehicle acceleration. The physical origin of these forces and the hypotheses linked to their modeling have been widely described in the literature. Several of these notions are briefly presented below, while others, such as tire rolling resistance or aerodynamic drag, are explained in detail in Chapters 3 and 5, respectively.

Tire drag

Tire drag, or the rolling resistance force F_R of a vehicle is obtained using the following equation:

$$F_R = f_r Mg \quad (2.1)$$

where f_r is the rolling resistance coefficient (dimensionless); M is the mass of vehicle, pilot included (kg); and g is the gravitational acceleration ($= 9.81 \text{ m/s}^2 \approx 10 \text{ m/s}^2$).

The rolling resistance coefficient f_r depends on many of the parameters discussed in Section 3.1.2. Table 2-1 provides the orders of magnitude of the rolling resistance coefficient for several specific kinds of vehicles depending on their tire type.

Table 2-1: Orders of magnitude of the rolling resistance coefficient f_r for various kinds of vehicles and their tire type.

Tire type	$f_r [-]$
Car tire on concrete or asphalt [3]	0.013
Bicycle tire [4]	0.006
FEV cross-ply tire (Michelin 44-406)	0.0024
FEV radial-ply tubeless tire (Michelin 45-75R16)	0.00081

The tire's rolling resistance varies, depending on whether the vehicle is driving straight or cornering. The cornering factor is explained in more depth in Chapter 4.

Wheel bearing drag

The resistance force F_B generated by the wheel bearings, called wheel bearing drag, can be obtained using the following equation:

$$F_B = \mu Mg \frac{d}{D} \quad (2.2)$$

where

μ is the bearing coefficient of friction (dimensionless);

M is the mass of vehicle, pilot included (kg);

d is the bearing bore diameter (m, about 0.02) ;

D is the wheel diameter (m, about 0.5); and

g is the gravitational acceleration ($= 9.81 \text{ m/s}^2 \approx 10 \text{ m/s}^2$).

The bearing friction coefficient depends on the bearing type. Its order of magnitude is about 0.0015 [6].

In all cases, the wheel bearing drag represents less than 1% of the total drag (all types included). This value is valid for correctly mounted, properly lubricated and unsealed wheel bearings.

Aerodynamic drag

The aerodynamic drag generated by a vehicle's body moving through air can be obtained using the following equation:

$$F_A = \frac{1}{2} \rho A c_X v^2 \quad (2.3)$$

where

ρ is the air density ($= 1.2 \text{ kg/m}^3$);

v is the relative velocity between the vehicle body and the air (m/s);

c_X is the dimensionless aerodynamic drag coefficient; and

A is the frontal area of the vehicle body (m^2).

In the absence of true wind (i.e., the wind due to the weather), the relative velocity between the vehicle body and the air v is equal to the vehicle speed. The aerodynamic drag force varies with true wind conditions, which influence speed and direction. This influence is explained in depth in Chapter 5.

Table 2-2: Orders of magnitude of the drag area for various kinds of human-powered vehicles [4].

Type of human-powered vehicle	$A c_X [\text{m}^2]$
Touring bike	0.56
Racing bike, cyclist in racing position	0.30
Recumbent bicycle	0.27
Streamline recumbent tricycle	0.05

The aerodynamic drag coefficient c_X and the frontal area A depend on the shape of the vehicle body. Optimizing these parameters for FEVs is discussed in Chapter 5. Table 2-2 provides the various sizes of the drag area (i.e., the product of the body

frontal area A and the aerodynamic drag coefficient c_X) for several specific kinds of human powered vehicles [4].

Uphill drag

The uphill drag is the force F_U induced by gravity when driving on a less than exactly horizontal road. It can be obtained using the following equation (valid gradients up to $p < 20\%$):

$$F_U \approx 0.01 M g p \quad (2.4)$$

where p is the incline gradient of the road (%); M is the mass of vehicle, pilot included (kg); and g is the gravitational acceleration ($= 9.81 \text{ m/s}^2 \approx 10 \text{ m/s}^2$).

Acceleration drag

The acceleration drag is the force generated by vehicle acceleration due to vehicle inertia. It can be obtained using the following equation:

$$F_A \approx M \gamma \quad (2.5)$$

where γ is the magnitude of the vehicle acceleration (m/s^2); and M is the mass of vehicle, pilot included (kg). In this equation, the inertia of the rotating parts inside the vehicle (mainly the wheels) is ignored.

The acceleration of a FEV may be quite low compared to a passenger car. But even on such a FEV vehicle, the acceleration drag defines the maximum drive torque that must be delivered at the wheel. If this drive torque is too low, the launching time lasts too long and the time lost during the launching phase has to be compensated by raising the vehicle velocity during the rest of the attempt, which increases the aerodynamic drag and spoils the performance.

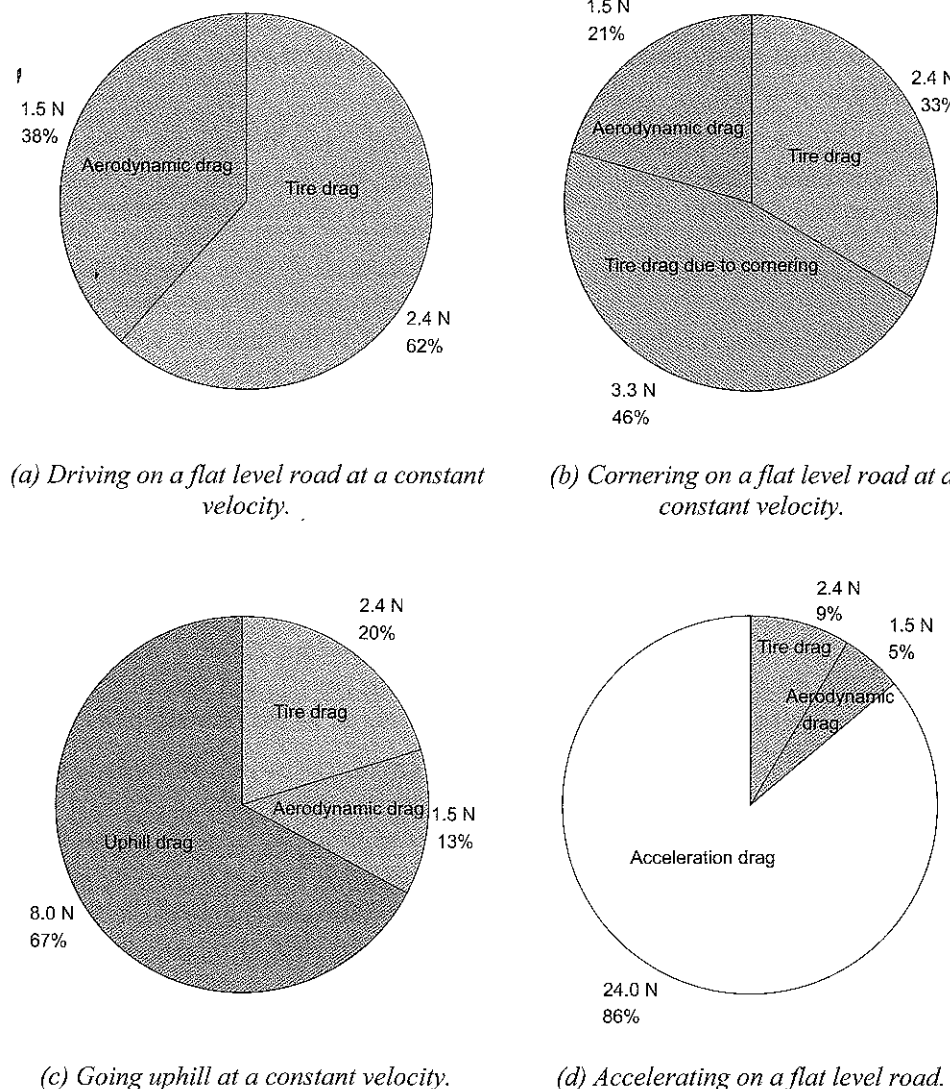


Figure 2-5: The relative orders of magnitude of the external forces applied to a fuel economy vehicle. The wheel bearing resistance force is not shown.

A comparison of orders of magnitude of the various kinds of drag

A comparison of the orders of magnitude of the kinds of drag presented above is provided in Figure 2-5; the values used in the calculations are given in Table 2-3.

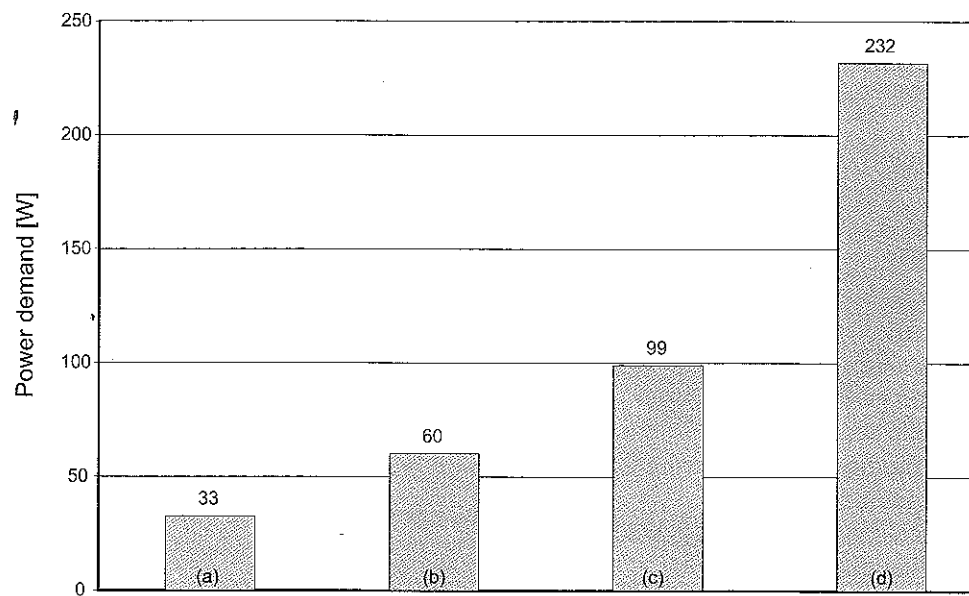
Table 2-3: Values used to calculate the external forces illustrated in Figure 2-5.

Parameter	Value	Unit
Rolling resistance coefficient f_r	0.003	-
Bearing friction coefficient μ	0.0015	-
Bearing bore diameter d	0.02	m
Wheel diameter D	0.5	m
Air density ρ	1.2	kg/m ³
Vehicle velocity v	8.3	m/s
Aerodynamic drag coefficient c_x	0.1	-
Body shell frontal area A	0.3	m ²
Incline gradient of the road p	1	%
Vehicle acceleration γ	0.3	m/s ²
Tire rigidity when cornering C_a	100	N/ ^o
Turn radius R	40	m
Vehicle mass M , pilot included	80	kg
Gravitational acceleration g	10	m/s ²

Based on these graphs, the tire drag of a streamlined FEV that is moving straight on a flat level road is higher than the aerodynamic drag. The tire drag increases sharply when the vehicle is cornering. When the vehicle is accelerating or moving uphill, the acceleration drag or the uphill drag are predominant.

Power demand

The mechanical power demand at the wheel (expressed in Watts) can be calculated by multiplying the sum of drag values presented above (expressed in Newton) by the vehicle velocity (meters per second). Therefore, the power demand varies depending on the driving task (e.g., launching, going uphill...). Its order of magnitude is depicted in Figure 2-6 for four typical driving conditions.

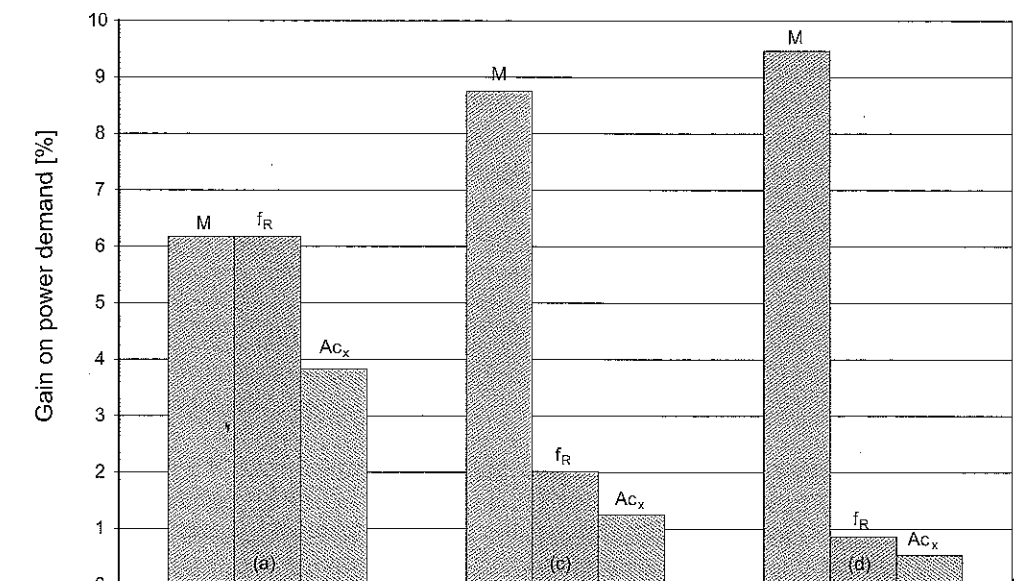


*(a) Driving on a flat level road at a constant velocity
(b) Cornering on a flat level road at a constant velocity
(c) Going uphill at a constant velocity
(d) Accelerating on a flat level road*

Figure 2-6: Mechanical power demand at the wheel under various driving tasks.

A brief sensitivity analysis

To determine the sensitivity of the various parameters [1], we reduced one parameter – either the vehicle mass M , the tire rolling resistance coefficient f_R or the drag area Ac_x – by 10% of the starting values presented in Table 2-3. The resulting reduction of the drag values for three different driving tasks, i.e., (a), (b) and (c), is shown in Figure 2-7. Thus, it appears that reducing the vehicle mass would provide the most significant reduction in the total drag value, whatever the driving task. The advantage of reducing one of the other two parameters would be proportionally much less significant.



*(a) Driving on a flat level road at a constant velocity
(c) Going uphill at a constant velocity
(d) Accelerating on a flat level road*

Figure 2-7: The reduction in the mechanical power demand at the wheel achieved by reducing one parameter – i.e., vehicle mass M , rolling resistance coefficient f_R or drag area Ac_x – by 10%, for 3 different driving tasks.

2.2.2. Powertrain efficiency

In order to discuss powertrain efficiency, the terms “powertrain,” “efficiency” and “operating point” must first be defined.

The powertrain

What we call the “powertrain” of a vehicle is the set of energy converters included in the drive powerpath, from the fuel tank to the drive wheel. These converters are depicted in Figure 2-8 for the case of a fuel cell powered FEV.

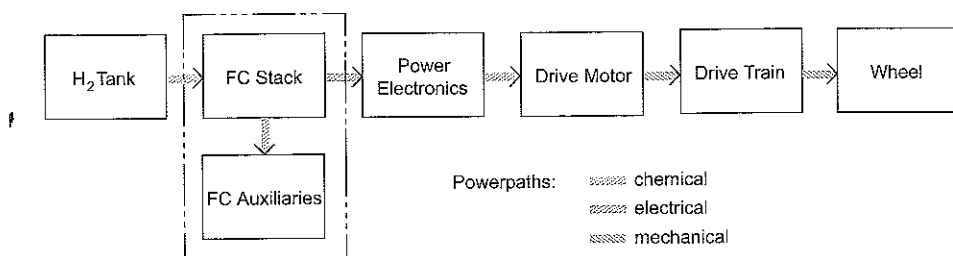


Figure 2-8: Illustration of the components considered in the average operating point approach of a fuel cell powered vehicle.

Efficiency

The powertrain efficiency is the ratio of the useful mechanical power obtained at the wheel to the chemical power expended (i.e., contained in the fuel). Efficiency ratings are dimensionless and always lower than one, and are thus expressed as percentages. The efficiency of a powertrain may be calculated by multiplying the efficiencies of the powertrain components. However, the efficiency of each powertrain component depends on the operating point it is performing.

Operating point

An operating point characterizes the point at which a system is operating; it is defined by the pair of physical quantities that provide the system power when multiplied. For instance, the electrical operating point of a motor is obtained from the voltage (in Volts) and the current (in Amps) that it receives, whereas the mechanical operating point of the same motor is obtained by its torque (in Newton meters) and rotating speed (in radians per second). Thus, the electric power of this motor is the product of its voltage and current, and its mechanical power is the product of its torque and rotating speed. Its efficiency is obtained by dividing the mechanical power (i.e., output power) by the electrical power (i.e., input power).

During a competitive trial, several driving tasks must be undertaken: launching, driving uphill, or coasting downhill, for example. The method often used for a preliminary estimation of the fuel consumption is called the average operating point approach [1]. In this approach, the accumulated value of all powertrain operating points is reduced to one or two representative average operating points, at which fuel consumption is then calculated.

For an ICE FEV, a single average operating point is taken into account. Its torque is close to the maximal motor torque and its regime close to the average vehicle

speed required in the race regulations, taking the transmission speed ratio into account. This hypothesis is justified by the fact that such a vehicle is not equipped with any accelerators: the engine is either off or on, and if on, the accelerator is usually tuned prior to the race and cannot be adjusted by the pilot during the race. Use of this average operating point, which we call the “full-torque operating point”, requires accepting two notions: (1) regardless of the motor’s regime, the motor is most efficient when it is delivering its maximal torque; and (2) a stop-and-go motor strategy will be used. The stop-and-go motor strategy implies that the motor is started when the vehicle speed decreases below a certain speed x (which is generally below the required average speed), and is stopped when the vehicle speed increases above a certain speed y (which is generally above the required average speed). Finding the best motor strategy consists in determining x and y in terms of the vehicle’s location on the track.

For an FC FEV, two average operating points are usually considered: one at full torque (as explained above) and one at a constant vehicle speed (chosen close to the required average speed). This last driving situation, called the “cruise operating point”, implies that the vehicle is moving on a flat-level road, while the “full-torque operating point” is mostly used when launching the vehicle or going up a hill. This “cruise operating point” may be the most efficient powertrain operating point, given the shape of the efficiency curves for a PEM FCS (maximum at about one third of the full power, see Section 10.1.8) and a brush DC motor (maximum at low torque and high speed, see Section 9.2.2).

Unfortunately, since not all of the values in the same column of Table 2-4 can be reached under the same conditions – either they are not physically compatible or they do not correspond to the same operating point – the highest powertrain efficiency can not be calculated by simply multiplying the figures of the “upper bound” column. This calculation would have yielded a 55% tank-to-wheel powertrain efficiency; thus, our experience indicates that a 45% tank-to-wheel powertrain efficiency is an achievable target figure.

Table 2-4: Highest possible efficiency of the powertrain components of a FC FEV.

- (1) PEM FC with an air supply at atmospheric pressure
- (2) Pressurized PEM FC operating with a pure oxygen supply
- (3) Under continuous flow operating conditions
- (4) Using a hub motor may be less efficient
- (5) Without a transmission (hub motor solution)

Highest efficiency	Lower bound	Upper bound
FCS	40% ⁽¹⁾	65% ⁽²⁾
Power electronics	90%	100% ⁽³⁾
Drive motor	70% ⁽⁴⁾	85%
Transmission	95%	100% ⁽⁵⁾

2.2.3. The target characteristics of the winning vehicle

Thanks to the preliminary calculations detailed in the previous sections, the target figures of the winning vehicle can be estimated.

First, please consider the hypotheses:

- H1: the target minimum number of kilometers to be covered per liter of gasoline is set at 4,500 km/l;
- H2: the characteristics of the gasoline used include a PCI of 42.9 kJ/g and a density of 0.75 g/ml, meaning that a single liter of gasoline contains 32.2 MJ (Section 1.2.3);
- H3: the minimum tank-to-wheel powertrain efficiency is 45%; and
- H4: the track is flat and straight (i.e., the potential energy accumulated on the top of the hills is integrally restored and the additional rolling resistance when cornering is neglected); the tire rolling resistance coefficient is 0.003 (which is actually a relatively bad value); there is no wind on the track; and the FEV is running at a constant speed equal to minimum average speed required by the regulations (i.e., 30 km/h).

Given Hypothesis H1 and H2, the drive force that might be delivered at wheel if the entire energy contained in the fuel is converted into mechanical energy is:

$$32.2 \text{ MJ} / 4,500 \text{ km} = 7.16 \text{ N} \quad (2.6)$$

Given Hypothesis H3, the actual drive force at wheel is:

$$7.16 \text{ N} \times 0.45 = 3.22 \text{ N} \quad (2.7)$$

Given Hypothesis H4, the drag repartition between the tires and the aerodynamics (Figure 2-7) is respectively 62% and 38%. Therefore, the target maximal drag values are:

$$\text{Tire drag: } 3.22 \text{ N} \times 0.62 = 2.00 \text{ N} \quad (2.8)$$

$$\text{Aerodynamic drag: } 3.22 \text{ N} \times 0.38 = 1.22 \text{ N} \quad (2.9)$$

From Equations (2.1) and (2.3), it can be deduced that the maximum weight of the vehicle (pilot included) is:

$$2.00 \text{ N} / 0.003 / 10 \text{ N/kg} = 67 \text{ kg} \quad (2.10)$$

and the maximum drag area (i.e., the product of the body frontal area A and the aerodynamic drag coefficient c_x) is:

$$1.22 \text{ N} \times 2 / 1.2 \text{ kg/m}^3 / (8.33 \text{ m/s})^2 = 0.0293 \text{ m}^2 \quad (2.11)$$

Given these figures of the vehicles, the powertrain sizing process (e.g., torque, power at the wheel) can be examined in more detail, which is done in some chapters of this book.

2.2.4. Conclusion

In light of the information presented in this chapter, a vehicle capable of covering more than of 4,500 km on the equivalent of one liter of petrol should have the following characteristics:

- maximum weight: 22 kg (assuming a pilot's weight of 45 kg);
- minimum tire rolling resistance coefficient: 0.003;
- maximum drag area: 0.0293 m²; and
- average powertrain tank-to-wheel efficiency: 45%.

Chapter 3: Tires

By Jean-Jacques Santin.

As mentioned in the second part of the previous chapter, the tire drag of a fuel economy vehicle corresponds to about the half of the energy needed to keep it in motion on a flat level road. The importance of this contribution explains why one entire chapter of this book is devoted to the tire itself. The definitions related to tire drag, the main parameters affecting this force, and a few methods for measuring it are discussed in section 1.1. Then, section 3.2 provides an overview of the ultra-low rolling resistance tires currently available on the market. Section 3.3 introduces the fundamentals of tire mechanics in order to provide the background knowledge needed to understand the mechanical models developed in the chapter about tire drag when cornering (Chapter 4). The last two sections, 3.4 and 3.5, examine the mechanical effect of cambered and non-parallel wheels on tire drag.

3.1. Rolling resistance of a tire

A tire consists on two elements: (1) a rubber covering placed around a wheel to form a flexible contact with the road; and (2) an inflatable inner tube. In this chapter, “tire” is used to refer to this rubber covering and “tube”, obviously, to refer to the inflatable tube. Both elements affect the rolling resistance of the wheel. The recent car tires, which do not require tubes, are called “tubeless tires”. A tire has three parts: (1) the bead area, which is in contact with the rim of the wheel; (2) the crown, which is in contact with the road via the tread; and (3) the sidewall that links the bead area to the crown. Due to tire symmetry, all tires have two bead areas and two sidewalls, but only one crown. The two principal tire families are radial-ply and cross-ply, which refer to the type of carcass used in the tire. This choice of carcass has a significant influence on the tire’s rolling resistance.

The rolling resistance force of tires on hard surfaces comes mainly from the deformation of the tire as it rolls and the behavior of the tire material itself. Such deformation induces energy dissipation, which accounts for about 90% of the rolling resistance force [7]. Two other mechanisms account for the last 10%: microslippage and aerodynamic drag of the rotating tire (fan effect). Microslippage occurs mainly between the tread blocs and the road surface as the tire rotates. When the vehicle is driven in a straight line without braking or accelerating, microslippage accounts for less than the 10% of rolling resistance previously

mentioned. When dealing with FEV, the fan effect may be neglected, because of the low speeds of FEVs compared to cars.

3.1.1. Definitions

Rolling resistance force

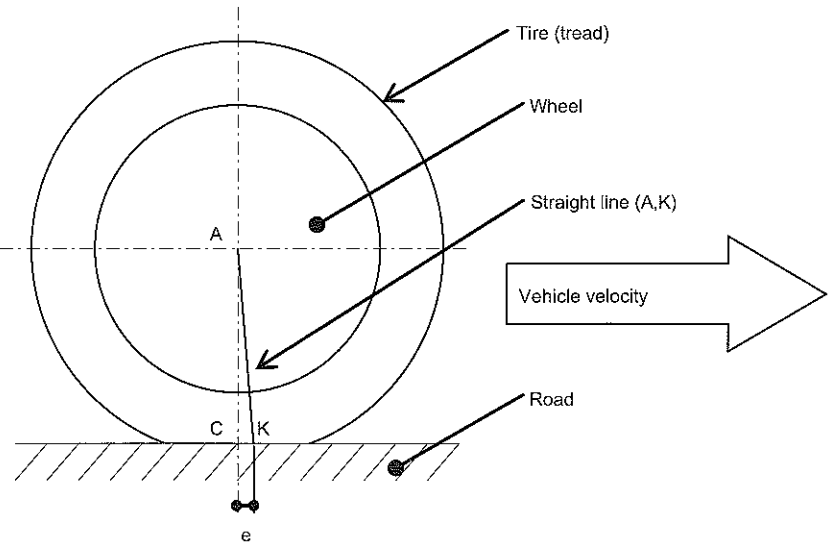


Figure 3-1: Wheel and tire in contact on a flat, horizontal road. Wheel center A; Centroid of the normal pressure distribution K; Theoretical road-tire contact point C.

Consider a tire mounted on wheel that is in contact on a flat horizontal road (Figure 3-1). A vertical load, due to the vehicle weight, is applied to the wheel center A, but with zero brake or drive applied torque. The vehicle is driven in a straight line at a constant speed. Because of tire deformation and the visco-elastic behavior of the tire material, the normal road-tire pressure distribution is higher in the forward portion of the contact zone where tread blocs are forced radially inwards, and lower in the rear portion of the contact zone where tread blocs are forced radially outwards. This forcing leads to a forward shift of the centroid K of the normal road-tire pressure distribution, at a distance e from the theoretical road-tire contact point C (i.e., the point where the non-deformable tire and the road make contact). Consequently, at the centroid of the normal pressure distribution, the sum of moments of the road-to-tire forces (normal and tangential to the road plane) is null.

Consequently, the wheel-tire assembly is subjected to two forces and zero torque, one force applied at the wheel center A, and another force applied at the centroid K of the normal pressure distribution. To be in equilibrium, these forces must have the same intensity, must be on the same straight line (A,K), and must be exerted in opposite directions. Since (A,K) is not perpendicular to the road plane, the force applied in K is not perpendicular to the road plane either. Therefore, this force has a component in the road plane that is non-null; it is oriented in the opposite direction of the vehicle velocity. This horizontal force is generally known as the rolling resistance force F_R . When the entire vehicle is considered, the sum of each rolling resistance force that exists at each wheel is known as tire drag.

Rolling resistance coefficient

For a given tire and given use conditions (e.g., ground type, velocity, inflation pressure), the ratio of the rolling resistance force F_R to the normal tire load F_z is constant. This ratio is the rolling resistance coefficient f_r , which is dimensionless. Equation (3.1) expresses this fundamental relationship.

$$f_r = \frac{F_R}{F_z} \quad (3.1)$$

The following list gives an idea of the order of magnitude of the rolling resistance coefficients of several specific kinds of tires:

- 0.013 for a standard automobile tire rolling on asphalt [3];
- 0.006 for a bicycle tire [4];
- 0.0024 for a 44-406 cross-ply Michelin tire; and
- 0.00081 for a 45-75R16 radial ply tubeless Michelin tire.

For comparison, the rolling resistance coefficient of a train wheel [8] is 0.00073. Obviously, a train wheel has no tire, and the type of contact is steel-on-steel; nonetheless, its rolling resistance coefficient is interesting to keep in mind since it can be considered as the lower limit that can be reached nowadays.

3.1.2. Parameters affecting the rolling resistance coefficient

The rolling resistance coefficients listed above are associated with specific use conditions. A number of factors influence the rolling resistance force of a pneumatic tire, including the tire structure (i.e., type of construction and materials) and its operating conditions (e.g., surface conditions, inflation pressure, speed, and temperature). The most important parameters in terms of FEV are presented below.

Tire construction

Radial ply tires, whether for passenger or heavy-duty vehicles, usually have a lower rolling resistance coefficient than cross-ply tires due to the orientation of the carcass, which stresses tire materials differently. Likewise, tubeless tires usually have a lower rolling resistance coefficient than tires with a tube. The additional energy loss comes from the deformation of the tube and the microslippages that occur at the interface between the tube and the inside of the tire. Given this energy loss, removing the tube might be tempting, but remember that tires made to be used with a tube must be used with a tube, with the consequent risk of air-leakage.

Tire materials

Though we haven't investigated the materials question in detail, it seems appropriate at this point to offer a few observations about tire materials. The rubber compounds used in tires are reinforced, vulcanized elastomers. They are made up of polymers, which are combined with reinforcing fillers and sulfur. These polymers, which help the tires grip the road, can be synthetic or natural rubber. Natural rubber has a less hysteretic mechanical behavior than synthetic rubber and therefore provides a lower tire rolling resistance coefficient. The reinforcing fillers, which help the tires better resist wear and make them more rigid, can be either carbon black or silica, with silica leading to lower rolling resistance than carbon black. Sulfur gives the material cohesiveness and elasticity, but does not significantly affect the rolling resistance property of tires.

If manufacturer information is lacking, these general rules may help when selecting tires for FEV.

Tire diameter

Tire diameter should be considered at the very beginning of the design process. It has been shown that the effect of tire diameter is negligible on hard surfaces like concrete, but is considerable on soft (i.e., deformable) surfaces [9]. In the particular case of FEV running on a race track, the benefit of using large diameter wheels is not clear. If subsequent investigation demonstrates that large diameter wheels would really be better, choosing a vehicle design that puts them outside the body shell would be one possibility.

Tire pressure

Tire pressure, which has some effect on rolling resistance, can be easily and conveniently adjusted. Modest changes in the under/oversteering balance can be achieved by adjusting front to rear tire pressures. In general, except on very soft

ground, such as sand, the higher the pressure, the lower the rolling resistance [9]. At high pressures, the energy lost to tire deformation is lower. In addition, in terms of lateral force, the slip angle is lower, and consequently the tire drag resulting from cornering is also lower.

Unfortunately, the drawbacks of increasing tire pressure are fairly numerous:

- a higher risk of tire punctures. A tire puncture results in the canceling of the run. Given the effect of a flat tire on performance, continuing a run with a flat tire would not make sense. Since the number of runs is limited to four per race, this risk has to be considered seriously.
- a higher risk of a bursting tire or even rim. This can occur either during inflation or during the race, with possible projections of materials that could damage surrounding equipment or injure the pilot. A burst tire during the race usually leads to losing control of the vehicle and running off the track.
- a higher risk of bouncing tires. Fuel economy vehicles don't usually have a suspension system. Therefore, the risk of tires bouncing rather than rolling across the ground is higher, negatively affecting lateral guidance and drive, especially when cornering. In fact, additional drive energy is also lost in the road-tire contact zone, due to the vast number of microslippages generated by the bounces.

Tire temperature

Three kinds of tire temperatures can affect rolling resistance: surface temperature, internal tread and carcass temperature, and the temperature of the air in the tube. The ambient temperature, on the other hand, does not seem to have an effect on the tire rolling resistance coefficient. Unfortunately, no official information seems to be available on this subject for FEV tires, although many things are heard in the paddocks during the race. For some, the higher the temperature, the lower the rolling resistance coefficient. For others, there is an optimal temperature, which is higher than the ambient temperature. Who is right?

Essentially, tire temperature affects the rolling resistance in two ways: by changing the temperature of the air in the tire cavity, thereby changing the functional inflation pressure; or by changing the rigidity and hysteresis of the tire materials. In order to avoid the drawbacks mentioned in the previous sub-section about tire pressure, changes in the air temperature inside the tire must be taken into account. Modifying the characteristics of the rubber compound can have a positive or a negative effect on the rolling resistance. In radial-ply passenger car tires, for example, higher internal temperatures appear to lower the rolling resistance coefficient [10, 11]. In contrast, modern race car tires have an optimum

temperature for maximum grip: too cold, and the tires will be slippery; too hot, and the rubber will melt, consequently increasing the rolling resistance coefficient (although at that point, the increased coefficient is hardly the most important problem).

Tire wear

Tire wear occurs when rubber is removed from the tire during its use. To determine whether or not the state of wear had an effect on performance, the team "Fancy Carol" tested the difference in rolling resistance for new and abraded tires [12], by conducting what they call a "simple rolling resistance test". They compared the performance of the same vehicle equipped with new and abraded bicycle race tires, using a belt grinder to abrade the tires. Their results led them to conclude that the rolling resistance of an abraded tire is less than that of a new tire, but they provided no figures or orders of magnitude that would allow their results to be verified.

Vibration

Since the rolling resistance of tires is primarily caused by material hysteresis, it stands to reason that everything that could be a source of vibration should be avoided. Vibrations are mainly due to the road surface, but other sources of vibration can include incorrect wheel balance, poor tire or wheel geometry (e.g., run out, lateral run out, off-center distance), poor tire-rim fit, to name but a few.

Track surface conditions

Though it is often ignored because it cannot be changed during the race, the surface condition of the track is quite important. If the road is soft, additional rolling resistance comes from the deformation of the road itself and the behavior of the soil material as the tire rolls on it. If the surface condition of the road is rough, the rolling resistance coefficient increases, as a result of higher energy lost coming from microslippage. On smooth, hard surfaces, the rolling resistance is considerably lower than on a soft rough road. For instance, the rolling resistance of passenger car tires on seal-coated asphalt is 33% higher than on new concrete, while it is 12% lower on polished concrete [13].

The following anecdote demonstrates the importance of the track surface in performance. In March 2005, we had planned to carry out some rolling tests with PAC-Car II. However, because of poor weather conditions in Zurich, we were not able to use our usual test track, a taxiway at the Dübendorf military airport. After nearly a month of waiting, we decided to look for an indoor backup solution. In the absence of a cycle stadium, we fell back on a multi-purpose sports hall. The initial results were very bad, with the rolling resistance about ten times higher than

expected. After a final verification of the vehicle, we realized that the ground surface was very soft!

Other parameters

The list of parameters that influence the tire rolling resistance is even longer, but the most influential and most easily modified parameters for fuel economy challenges have been discussed above.

3.1.3. Measuring tire drag

As usual in such a project, experimental testing is more valuable than theoretical calculations for saving a few tenths of a Newton in tire drag. Measuring the rolling resistance of a tire itself, while varying the parameters described above, can help to determine the tire's best use conditions. However, it is measuring the tire drag of the entire vehicle that will actually help you to break a record! The following two sections offer some advice for designing your own experiments.

Measuring the rolling resistance of a tire

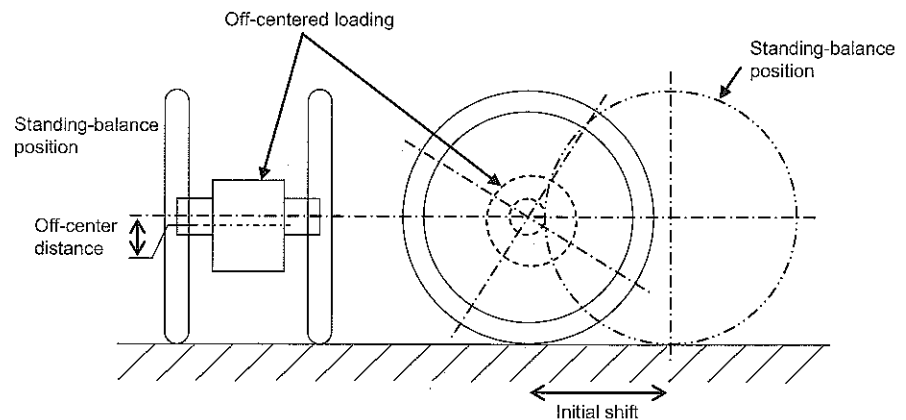


Figure 3-2: Tire rolling resistance test apparatus (front and side views).

To insure the greatest possible accuracy when measuring the rolling resistance of a tire, as many external physical influences as possible must be excluded from the experiment. These external physical influences can include, for example, the flatness of the ground on which the tire is rolling, the drag torque from wheel ball bearings, or the aerodynamic drag. This sounds very obvious, but is really difficult to achieve.

The experimental apparatus shown in Figure 3-2 provides good results. It consists of two wheels connected together by a stiff shaft, without any wheel bearings. The vertical load is obtained from a load connected to the center of the shaft. The center of gravity of the load is shifted a few millimeters from the shaft's axis. Together, these parts form an oscillator. By pushing the wheels back twenty or so centimeters from its standing-balance position, the entire apparatus will oscillate for several minutes: the longer the period of oscillation, the less the rolling resistance.

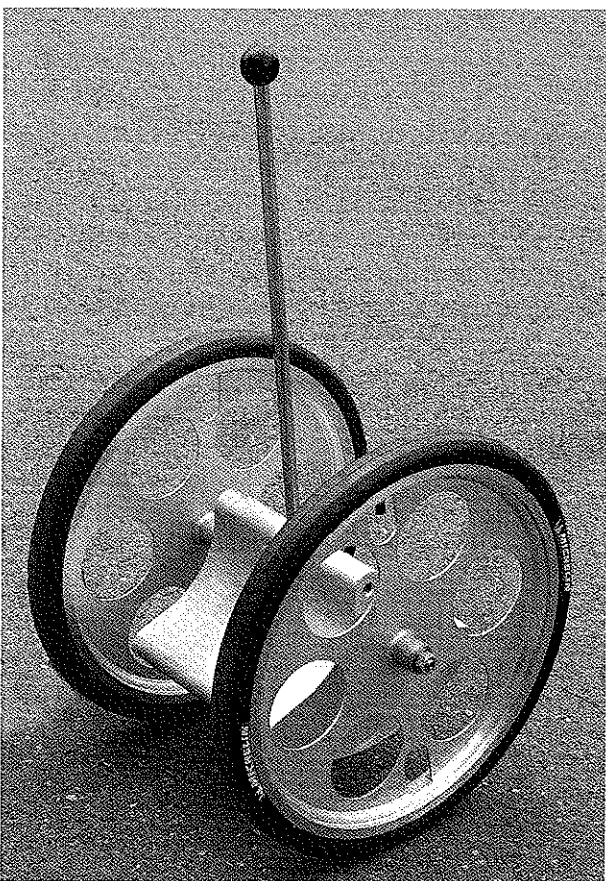


Figure 3-3: Sample of realization of the tire rolling resistance test apparatus.

Using this apparatus, it is possible to vary parameters (e.g., weight load, tire pressure, tire temperature, ground surface) to ascertain the best conditions for optimal tire performance. The differential equation characterizing the mechanical behavior of this apparatus can be easily written for preliminary investigations, or to obtain a correlation between the experimental and the theoretical results.

Measuring the tire drag of a vehicle

The Bosch Automotive Handbook [3] suggests determining the coefficients for aerodynamic drag and tire drag empirically. Consider a vehicle (mass m [kg], frontal area A [m^2]) coasting in neutral under windless conditions on a flat level road surface; the times t_1 and t_2 [s] that elapse while the vehicle coasts at a specific speed increment Δv [kmh^{-1}] (e.g., 5 km/h) are measured from the two initial velocities v_{a1} and v_{a2} [kmh^{-1}], where $v_{a1} > v_{a2}$. One is high (e.g., $v_{a1} = 60 \text{ km/h}$); the other is low (e.g., $v_{a2} = 15 \text{ km/h}$). This information is used to calculate the mean deceleration rates a_1 and a_2 [$\text{kmh}^{-1}\text{s}^{-1}$], as well as the mean velocities v_1 and v_2 [kmh^{-1}].

$$v_1 = v_{a1} - \frac{\Delta v}{2} \quad [\text{kmh}^{-1}] \quad (3.2)$$

$$v_2 = v_{a2} - \frac{\Delta v}{2} \quad [\text{kmh}^{-1}] \quad (3.3)$$

$$a_1 = \frac{\Delta v}{t_1} \quad [\text{kmh}^{-1}\text{s}^{-1}] \quad (3.4)$$

$$a_2 = \frac{\Delta v}{t_2} \quad [\text{kmh}^{-1}\text{s}^{-1}] \quad (3.5)$$

Given the results of these calculations, and assuming a constant deceleration rate, with the aerodynamic drag and the tire drag expressed respectively as Equations (2.3) and (2.1), Newton's second law yields:

$$c_x = \frac{6m(a_1 - a_2)}{A(v_2^2 - v_1^2)} \quad (3.6)$$

$$f_r = \frac{28.2(a_2 v_1^2 - a_1 v_2^2)}{10^2(v_1^2 - v_2^2)} \quad (3.7)$$

The team "Fancy Carol" [12] has proposed what they call a "simple rolling resistance test", in which the vehicle is launched at a low speed (e.g., 10 km/h) to minimize the influence of the aerodynamic drag, under windless conditions, on a flat level road surface. The distance covered by the vehicle is a function of the tire drag: the further the vehicle rolls, the lower the tire drag. Thus, it is possible to proceed qualitatively, comparing one test to another, after each parameter is adjusted. The difficulty is that launching the vehicle at exactly the same initial speed (i.e., kinetic energy) from one test to another is almost impossible. Therefore, they suggest placing the vehicle at the top of a ramp and allowing it to roll down the slope with no initial speed.

Of course, during this experiment, the engine is never used. Therefore, a simplified vehicle can be used, for instance one without engine, steering mechanism or pilot. If this test is carried out with a real vehicle but without a pilot, the steering mechanism should be clamped into position and a load should be added to simulate the weight distribution on each wheel as if the driver were lying down inside. Many variants of this experiment are possible. The only real requirement is an indoor area, whose the floor is perfectly flat because the result is actually quite sensitive to the slightest slope. Gymnasiums are usually not suitable because their surface is too soft. Cycle stadiums are perfect, despite the fact that the track does not run straight for long distances.

3.2. Ultra-low rolling-resistance tires on the market

Passenger car tires are the result of a trade-off between the specifications related to dynamic behavior (e.g., rolling resistance, mechanical performance when turning, braking or accelerating in various road conditions), comfort (e.g., shock absorption, noise filtering), service life (e.g., 50,000 km), and commercial aspects (e.g., cost, appearance), to name but a few.

The tires that have been developed for fuel economy races were designed to minimize the rolling resistance, to the detriment of the other characteristics, except for the price, which is still reasonable. Thus, FEV tires can be considered to be "non-trade-off" tires.

3.2.1. Michelin tires for Shell Eco-marathon vehicles

As far as we know, Michelin is the only tire manufacturer that designs and manufactures ultra-low rolling-resistant tires for FEVs. In 2005, three types of tires were available: 44-406, 45-75R16, and 35-406. Due to divergencies in the manufacturing process, the geometrical and mechanical properties can vary slightly from one year to another. The following three sections provide the general characteristics of each type of tire.

The 44-406

Historically, the cross-ply 44-406 tire was the first tire produced for Shell Eco-marathon race contest. According to Michelin [14], its specified characteristics are:

- type: flexible wire-bead tire;
- tube reference: 44-406 (20-9), tubeless mounting possible;

- seat diameter: 405.6 mm;
- overall diameter: from 496 to 498 mm, depending on the pressure and rim dimensions;
- section width: 44 mm;
- suitable crochet-type rim reference: 20x1.5 or 20x1.75;
- suitable pressure: 5 bar;
- rolling resistance coefficient: 0.0024 at 5 bar and 40 km/h; and
- weight: about 150 g.

The 45-75R16

The 45-75R16 tire was the second one to be made available. It was developed in 1997 for, and in conjunction with, the famous team from "Lycée La Joliverie" in Nantes (France). It is a tubeless radial-ply tire, designed to be mounted on a standard motorcycle rim with a "drop-center rim with cylindrical bead seats", and a width code of 1.35 (1 unit = 25.4 mm). (The complete list of rim dimensions can be found in the "Standards Manual" of the "European Tire and Rim Technical Organization" and are reproduced in Section 7.2.2.)

The 45-75R16 specifications include:

- type: tubeless radial ply tire;
- tube reference: N.A.
- rim diameter: 16 inches (= 406.4 mm);
- overall diameter:

$$40.64 + 2 \times 0.75 \times 4.5 = 46.64 \text{ cm} \quad (3.8)$$

This diameter can be calculated using the aspect ratio, which is 75%. The aspect ratio is the ratio of the tire's height (distance from the bead seat to the outer edge of the tread) to its width (maximum width across the shoulder).

- section width: 45 mm;
- suitable rim reference: standard motorcycle rim with a "drop-center rim with cylindrical bead seats", width code of 1.35;

- suitable pressure: 5 bar;
- rolling resistance coefficient: 0.001 at 4 bar, 0.00084 at 5 bar and 0.00081 at 6 bar; and
- weight: 400g.

The 35-406

The cross-ply 35-406 tire was designed for the 2005 Shell Eco-marathon in Nogaro (France). Its characteristics are similar to the cross-ply 44-406 tire [15]:

- type: flexible wire-bead tire;
- tube reference: 35-406;
- seat diameter: 405.6 mm;
- overall diameter: 478 mm, depending on the pressure and rim dimensions;
- section width: 34 mm, depending on rim dimensions;
- suitable crochet-type rim reference: 406-19C, 406-21C or 406-23C.
- suitable pressure: 5 bar;
- rolling resistance coefficient: 0.0024 at 5 bar and 40 km/h; and
- weight: about 150 g.

3.2.2. Other brands

The list of light vehicle tire manufacturers is huge. Some of the biggest are: Cheng Shin, Continental, Granfondo, Hutchinson, Innova, Intense, IRC, Kenda, Michelin, Nokian, Schwalbe, Tufo, Veloflex, Vredestein, and WTB.

The rolling resistance coefficient of tires is almost never included in these companies' technical specifications, so some of the criteria that can be used to identify a potentially good tire for high-mileage vehicles are: application category (e.g., bicycle, wheelchair), weight (lightweight means less materials and lower rolling resistance), maximum inflation pressure (higher pressure is synonymous with lower rolling resistance), and materials (latex is better than butyl for rolling resistance).

Though the market supply for 20-inch low rolling resistance tires is fairly small, the following tires are a good bet:

- Continental 5/285 28-406 Grand Prix;
- Kenda 28-451 Kwest Sportchair Racing; and
- Schwalbe Stelvio 28-451 handbike racing tire (wheelchair).

3.2.3. Synthesis

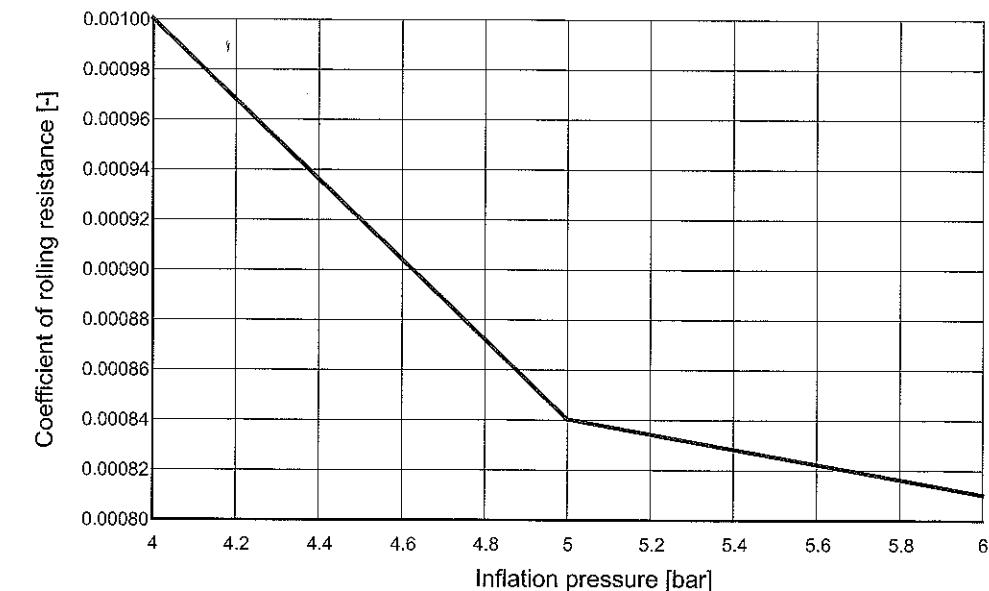


Figure 3-4: Rolling resistance coefficient of the 45-75R16 (500 N, 35 km/h), according to the figures provided by Michelin.

For the time being, the 45-75R16 Michelin tire appears to be the best tire available for FEVs. Its rolling resistance coefficient versus inflation pressure is quite good, as the numbers given in Section 3.2.1 show. These numbers, provided by Michelin and depicted graphically in Figure 3-4, were collected at a vertical force of 50 daN and a velocity of 35 km/h using an 8.5 m perimeter test drum.

3.3. Relevant tire mechanics basics

Tire mechanics is an incredibly complex subject, and the following pages summarize just a very tiny part of the information available. Given that tire manufacturers themselves make very little data available, in this summary, we strove to present the information that would best serve the ultimate goal of the project.

Some mechanical tire models can be considered as a black box with certain input and output quantities. The input includes the large variety of parameters that characterize the tire and specify its use (e.g., revolution speed, slip angle). The output consists of mechanical quantities (e.g., forces and moments).

The following example is used throughout the rest of Section 3.3 as a basis for explaining the notions of “input” and “output”:

Consider an upright wheel rolling freely (i.e., without applying drive torque) on a flat level road surface along a straight line at zero side slip (i.e., the wheel’s central plane and its plane of motion are permanently merged). This can be defined as a starting situation, from which a relatively small pulling force is needed to overcome the tire rolling resistance. When the wheel motion deviates from this initial situation, complex phenomena (e.g., tire deformation or partial sliding in the contact patch) result in horizontal forces and torques being generated between the ground and the tire.

The sub-Section 3.3.2 describes the use inputs (i.e., the main angles that position the wheel) and 3.3.3 describes the outputs (i.e., tire forces and moments). But, before that information can be useful, it is necessary to define an axis system (3.3.1). In these explanations, we assume steady state conditions, which means that all the variables – be they mechanical, kinematic or geometric – are fixed in time. The formulas used are very simplified versions of the widely used Pecejka’s semi-empirical tire model, the so-called Magic Formula [16]. The term “semi-empirical” means that the model is based on measured data, but uses structures from the field of physics.

3.3.1. Road contact axis system

The Road Contact Axis System (RCAS) is a right-hand orthonormal axis system which originates at the theoretical road-tire contact point C (Figure 3-5). C is defined as the point of intersection of three planes: the road plane, the wheel-center plane and the plane containing the wheel spin axis, which is normal to the road plane.

The axes **x**, **y**, and **z** of the RCAS are defined as follows:

- **x** is on the line of intersection of two planes, the wheel-center plane and the road plane, and is oriented in the direction of wheel heading;
- **y** is contained in the road plane, so chosen to make the axis system orthogonal and right-hand; and
- **z** is normal to the road plane and oriented downward.

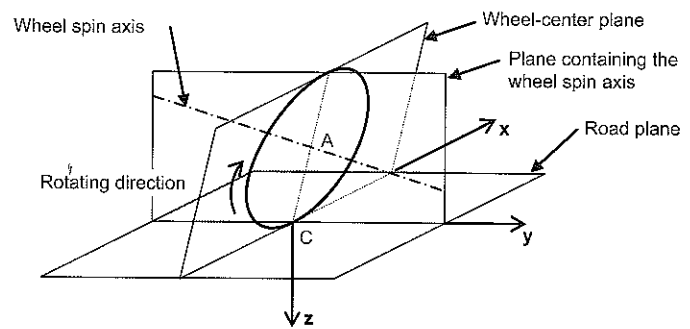


Figure 3-5: The Road Contact Axis System (RCAS).

3.3.2. Tire positioning-angles

As soon as the theoretical road-tire contact point C is known, the position of the wheel, relative to its direction of travel, may be defined with 2 angles: the inclination angle and the slip angle. The angular position of the wheel along its spin axis is not considered here.

As an introduction to the inclination angle, the camber angle is first defined.

Camber angle

The camber angle Φ is the angle between a tilted wheel’s center plane and its vertical plane. It is positive if the top of the wheel leans away from the vehicle, and it is negative if the top of the wheel leans towards the vehicle. This angle is used to show how the wheels are tilted on a vehicle (Figure 3-6).

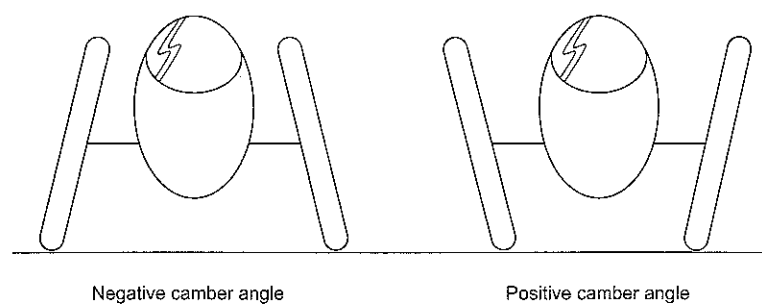


Figure 3-6: Example of a front view of FEVs with a non-zero camber angle.

Inclination angle

Unfortunately, the camber angle Φ is inappropriate for analyzing the mechanical behavior of car tires since the camber angle has the same sign (positive or negative) for both right-hand and left-hand wheels, whereas it induces a lateral force and an aligning torque in opposite directions depending on which side it is on. Therefore, the inclination angle is needed.

The inclination angle γ is the angle between the center plane of a tilted wheel and its vertical plane (Figure 3-7). In a vehicle moving forward, it is positive if the wheel is tilted to the right (as seen from behind).

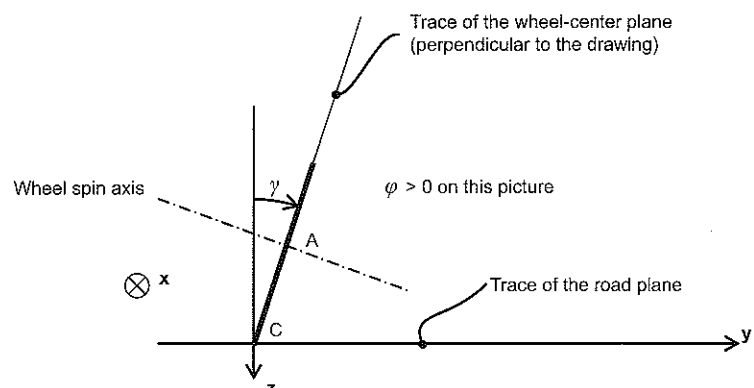


Figure 3-7: Inclination angle γ .

Slip angle

The slip angle α is the oriented angle from the direction of travel \mathbf{V} to the x-axis \mathbf{x} of the RCAS (Figure 3-8).

The direction of travel is defined by the direction of the velocity vector of the theoretical road-tire contact point C, considered as fixed in the vehicle axis system, relative to a ground axis system.

\mathbf{V} is calculated using the turn rate and the distance between the theoretical road-tire contact point C and the center of rotation of the vehicle I. These two quantities must therefore be known in order to calculate the slip angle and, consequently, the tire cornering force and aligning torque needed to analyze the global equilibrium of the cornering vehicle. (This subject is dealt with in Chapter 4.)

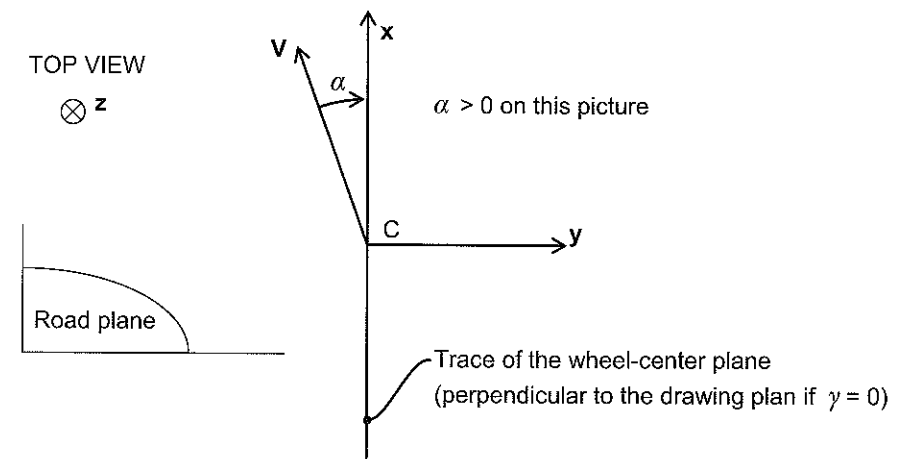


Figure 3-8: Slip angle α .

3.3.3. Tire forces and moments

Like all the contacts between two parts, the mechanical quantities that characterize the action (i.e., force and moment) exerted by the road on the tire can be summarized, at any given point, by a pair of vectors comprising one force and one moment. These vectors are usually expressed in a coordinate system, and thus are broken down into six components for analysis.

The definitions of the components depicted in Figure 3-9 are given below for the tire mechanics context:

The three components of the force vector acting on the tire from the ground, as expressed in the RCAS, are named:

- in the x direction: the longitudinal force F_x ;
- in the y direction: the lateral (or cornering) force F_y ;
- in the z direction: the normal load F_z .

The three components of the moment vector in C acting on the tire from the ground, as expressed in the RCAS, are named:

- in the x direction: the overturning moment M_x ;
- in the y direction: the rolling resistance moment M_y ;
- in the z direction: the aligning (or self-aligning) moment M_z .

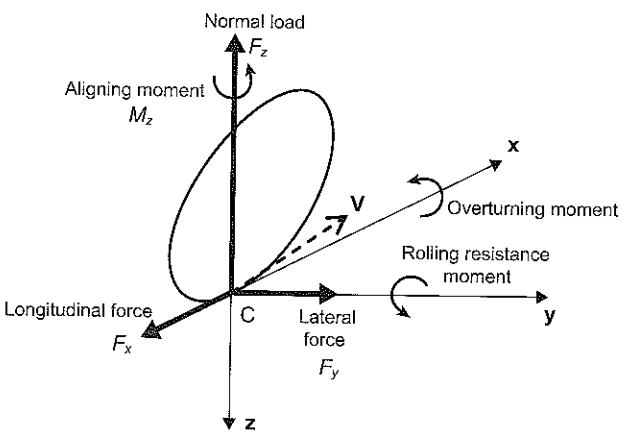


Figure 3-9: Tire forces and moments.

The components used later in this chapter are explained in more detail in the following sub-sections.

Normal load

All the tire forces and moments are a function of the normal load, plus other operating variables.

The normal load F_z counteracts the instantaneous weight of the vehicle (wheel weight included) transmitted through the wheel's revolute joint. This load is calculated using a part of the vehicle weight plus the vertical dynamic effects (i.e., longitudinal and lateral load transfer distribution).

The normal load vector is oriented upward, in the opposite direction of the z -axis in RCAS. As it is always the same sign, F_z is now considered as a positive value ($F_z > 0$).

Longitudinal force

The longitudinal force comes from the driving or braking torques, as well as rolling resistance force, F_R . If the driving and braking forces are nonexistent, the longitudinal force becomes:

$$F_x = -F_R = -f_r F_z \quad (3.9)$$

The minus sign shows that, in this specific case, the longitudinal force is in the opposite direction of the x -axis in RCAS. By convention, F_z is considered to be positive.

Lateral force

Under cornering conditions, a centrifugal force is applied at the vehicle's center of gravity at high speeds. To counteract this force, the tires must develop a lateral force F_y .

At low slip angles (5 degrees or less) the relationship is linear:

$$F_y = C_\alpha \alpha \quad (3.10)$$

where C_α represents the cornering stiffness of the tire (expressed in N. $^\circ$ $^{-1}$) and α , the slip angle (expressed in degrees).

For a given tire, the normal load F_z and the inflation pressure P are the main factors affecting its cornering stiffness C_α . A simplified version of Pacejka's "magic formula" model yields the following relationship for the cornering stiffness of non-cambered wheels:

$$C_\alpha = (\alpha_{30} + \alpha_{31}P) \sin\left(2 \tan^{-1}\left(\frac{F_z}{\alpha_{40} + \alpha_{41}P}\right)\right) \quad (3.11)$$

where P is the tire pressure expressed in bar, F_z is the normal load expressed in kN, and a_{ij} are 4 coefficients of Pacejka's "magic formula". According to Michelin, the coefficients of the radial-ply 45-75R16 tire are:

Table 3-1: Coefficients to calculate the cornering stiffness of the Michelin radial-ply 45-75R16 tire.

a_{30}	a_{31}	a_{40}	a_{41}
57.806	15.101	-0.082	0.186

These coefficients are only valid if the inflation pressure and the normal load, respectively, are within the following limits: $4 < P < 6$ bar and $0.3 < F_z < 0.6$ kN. The function is plotted Figure 3-10.

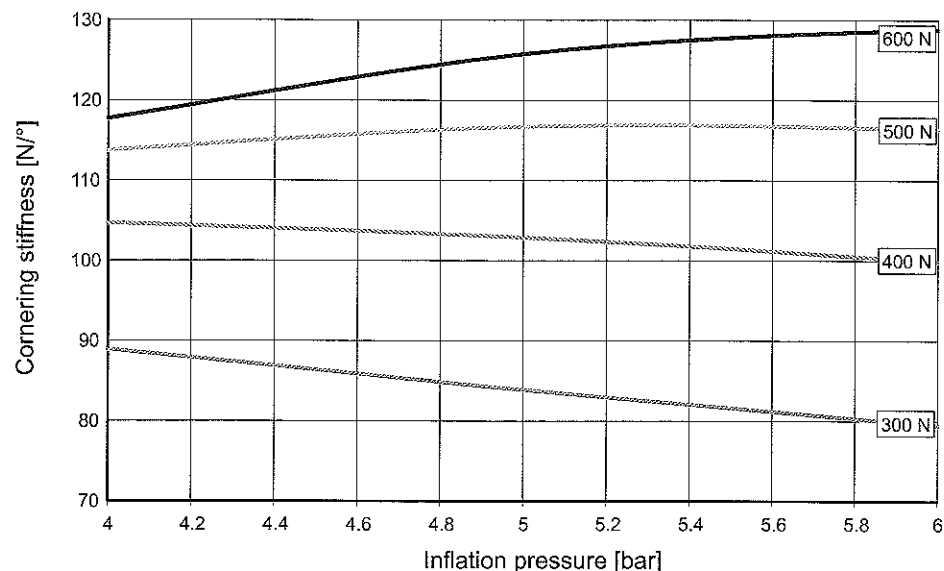


Figure 3-10: Cornering stiffness of the 45-75R16 versus the inflation pressure for various vertical loads.

Aligning moment

The aligning moment M_z of the vehicle's tires expresses the resistance to the attempted turn. The aligning moment has a more significant influence on the steering system than on vehicle dynamics.

At low slip angles (5 degrees or less), the relationship is linear:

$$M_z = G_z \alpha \quad (3.12)$$

where G_z represents the aligning stiffness of the tire (expressed in $\text{N.m.}^{\circ-1}$) and α , the slip angle (expressed in degrees).

For a given tire, the load and the inflation pressure are the main factors that affect aligning stiffness. A simplified version of Pacejka's "magic formula" model yields the following relationship for the aligning stiffness of non-cambered wheels:

$$G_z = \frac{(c_{30} + c_{31}P)F_z^2 + (c_{40} + c_{41}P)F_z}{e^{(c_{50} + c_{51}P)F_z}} \quad (3.13)$$

where P is the tire pressure expressed in bar, F_z is the normal load expressed in kN, and c_{ij} are 6 coefficients of Pacejka's "magic formula". According to Michelin, the coefficients of the radial-ply 45-75R16 tire are:

Table 3-2: Coefficients to calculate the aligning stiffness of the Michelin radial-ply 45-75R16 tire.

c_{30}	c_{31}	c_{40}	c_{41}	c_{50}	c_{51}
1.802	-0.201	-1.804	0.197	-2.927	-0.047

These coefficients are only valid if the inflation pressure and the normal load, respectively, are within the following limits: $4 < P < 6$ bar and $0.3 < F_z < 0.6$ kN. The function is plotted Figure 3-11.

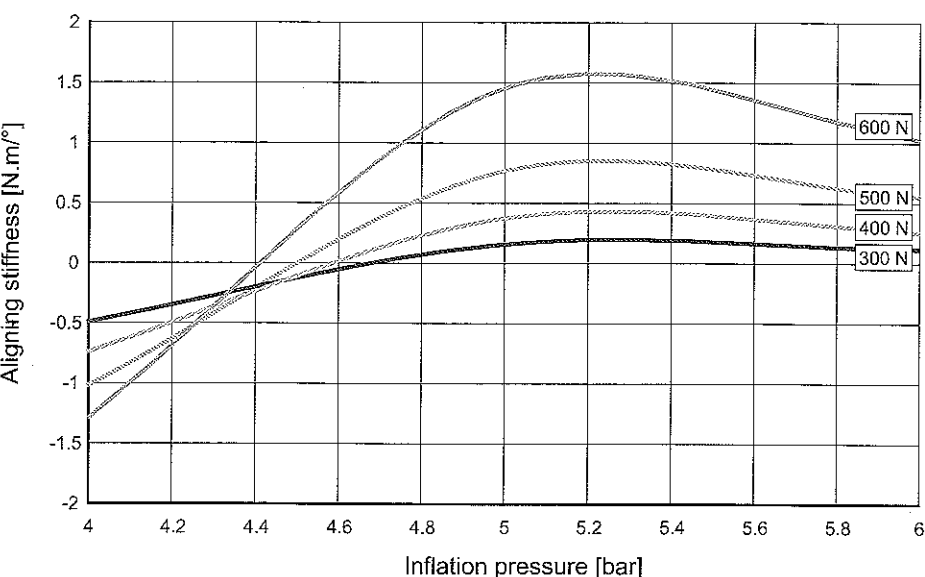


Figure 3-11: Aligning stiffness of the 45-75R16 against inflation pressure for various vertical loads.

3.3.4. Total rolling resistance

Under cornering conditions, the total rolling resistance force F_r can be calculated by adding the rolling resistance F_R and the cornering force F_y , both projected in the direction of travel \mathbf{x} , as expressed in the following equation:

$$F_r = F_R \cos \alpha + F_y \sin \alpha \quad (3.14)$$

where F_r is the total rolling resistance force [N], F_R is the wheel rolling resistance force [N], F_y is the cornering force [N], and α is the slip angle [$^\circ$].

3.3.5. Coefficients of friction

The static friction coefficient and the sliding friction coefficient are used in Chapter 4 to determine whether a tire slips when cornering. These coefficients are defined as the ratio of the lateral force to the normal load for two different conditions:

- the tire sticks to the road laterally: the static friction coefficient is calculated using the maximal lateral force.

- the tire slips laterally: the sliding friction coefficient is calculated using the lateral force that is independent from the slip velocity.

For passenger car tires, traveling at a vehicle speed of 50 km/h on a dry concrete or asphalt road surface, the static coefficient of friction between the tire and the road surface is between 0.85 and 1 (dimensionless), depending on the tire condition (new or worn) [3]. A figure for FEV tires is not currently available, but it has been assumed to be 0.8, given the non-trade-off specificity of such tires. The sliding friction coefficient (for a locked wheel) is, in general, lower than the static friction coefficient.

3.4. The mechanical effects of cambered wheels

3.4.1. Lateral force

In general, a cambered wheel with a pneumatic tire produces a lateral force in the direction of the tilt. At a zero slip angle, this lateral force is called camber thrust.

As far as we know, the relationship between the inclination angle and the lateral force hasn't been investigated specifically for FEV tires. Nevertheless, the following rules are usually accepted for passenger-car tires:

- the curve of the lateral force plotted as a function of the slip angle moves along the y-axis with the inclination angle;
- the inclination angle has the same effect on the lateral force as the slip angle, just to a less degree: on a radial tire, about 10 to 15 degrees of camber are required to produce the same lateral force as 1 degree of a slip angle [17];
- a higher lateral force occurs at a nonzero camber angle, with a negative camber angle of about 5° producing the largest increase in lateral force;
- the camber effect is less significant with radial-ply tires than cross-ply tires.

3.4.2. Aligning moment

The previous observations about lateral force are also valid for the aligning moment, but the effect is a bit smaller.

3.4.3. Rolling resistance force

The lack of information available about the influence of the camber angle on the rolling resistance force pushed us to conduct our own experimental investigations.

Our primary question was: how much is tire drag increased by using cambered wheels? Our ultimate goal was to identify the camber angle that would provide the best balance between decreased aerodynamic drag – due to lowering the frontal area – and increased tire drag.

Experimental apparatus

The experimental apparatus consisted of three devices: a truck, a speed controlled treadmill, and a drag force measuring device (Figure 3-12).

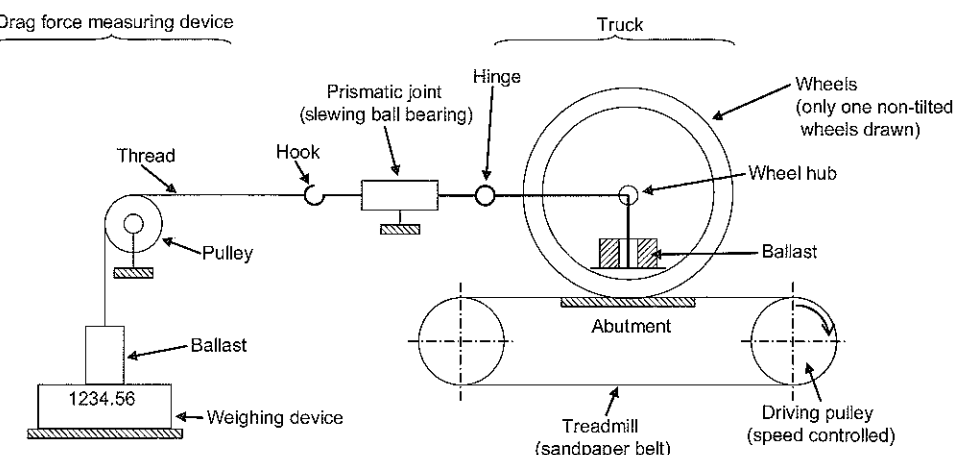


Figure 3-12: Experimental apparatus (side view).

The truck structure was mainly two wheels equipped with hubs that could be cambered with the help of two clampable hinges (Figure 3-13). A scale supporting ballast allowed the same normal load to be exerted on the two tires. A prismatic joint, equipped with a slewing ball bearing to limit friction, allowed movement in only one direction, and a horizontal hinge allowed the wheels to roll on the treadmill.

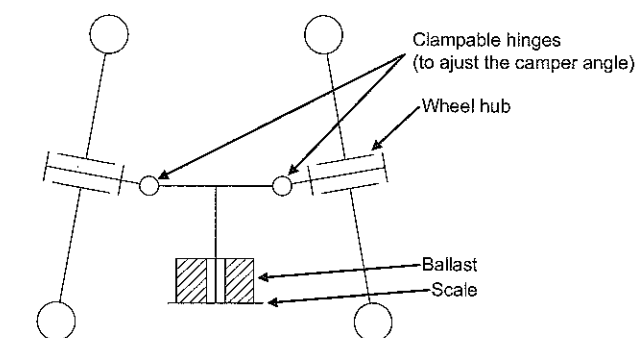


Figure 3-13: Experimental apparatus (front view).

The treadmill was made of two parallel cylinders connected by a sandpaper belt. A steel plate, called an abutment, was placed under the belt, vertical to the theoretical contact point of the wheel and the belt, in order to support the vertical force and avoid belt movement. An antifriction coating limited the intensity of the slip forces between the abutment and the belt, thus limiting the possibility of overheating. A driving cylinder, whose velocity was electronically controlled, maintained the upper part of the belt stretched.

A high-precision mechanical weighing device was used to measure tire drag. This device was equipped with a kind of integrated damper that filtered the vibrations from the truck that could distort the measurement accuracy.

Experimental Protocol

For a given camber angle, tire pressure and velocity, weights were added one by one on the truck's scale to increase the vertical load. Each time, the weight displayed by weighing device was noted. When the full load was reached, the process was reversed, with the weights being removed one by one and the weight noted at each removal. Loading and unloading phases highlighted the hysteresis produced by the prismatic joint and the pulley. This cycle was performed several times, each time changing one parameter, for instance, the camber angle.

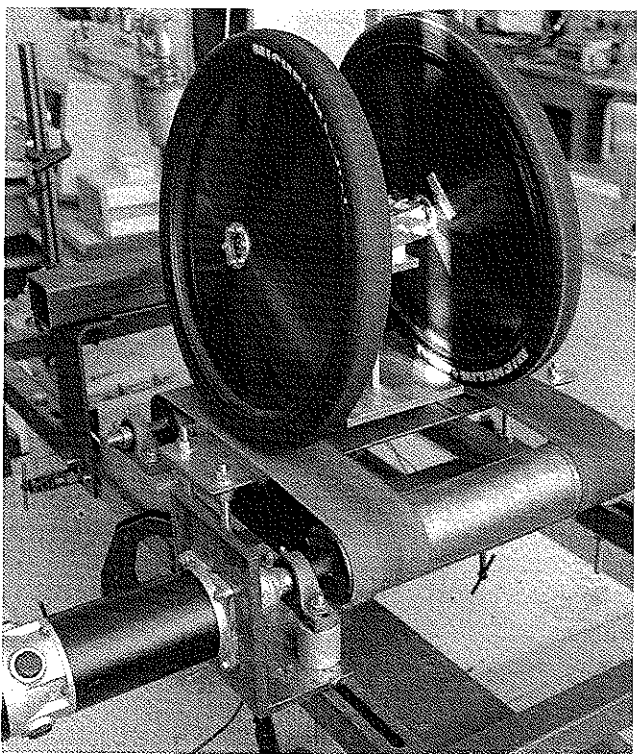


Figure 3-14: Survey of the experimental apparatus.

Experimental results

Figure 3-15 represents a curve showing the influence of camber angle on the rolling resistance coefficient of one tire, under the following conditions:

- radial-ply tubeless tire: Michelin 45-75R16;
- vertical load: 350 N on two wheels;
- tire inflation pressure: 7 bar; and
- temperature: unknown.

The maximum and the minimum values measured are represented by y-error bars.

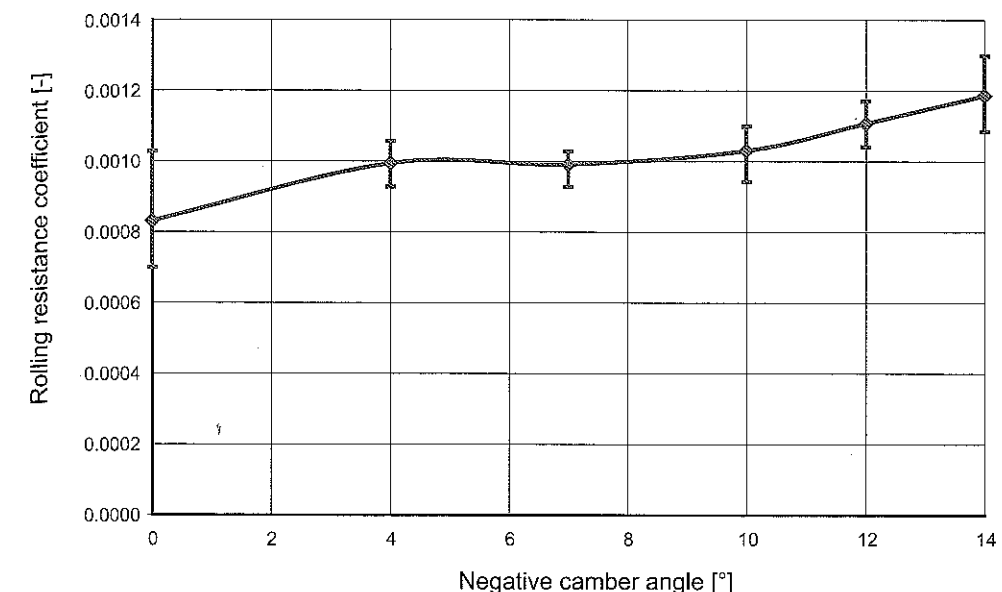


Figure 3-15: Coefficient of rolling resistance versus negative camber angle (experimental measurements).

Analysis and conclusion

The experiment shows that the rolling resistance coefficient of the 45-75R16 tire increases when the camber angle decreases from 0 to -4° . Then, the rolling resistance coefficient remains stable as the camber angle decreases from -4 to -9° . For lower values of the camber angle, the rolling resistance coefficient increases again.

At a nil camber angle, the rolling resistance coefficient is 0.000832, which is very close to the manufacturer's figure of 0.00081, despite a higher tire pressure and the additional friction induced by the wheel hub.

At the same nil camber angle, the scatter plot is more widespread than anywhere else, meaning that the measurement dispersion is higher when the camber angle is zero. In fact, the truck suffered from a lack of lateral guidance, and thus the oscillations that occurred that made the experiment less reproducible. A camber angle over or under zero creates camber thrust, which improves the lateral guidance of the truck. In order to avoid this phenomenon in the real vehicle, we suggest either tilting the wheels by applying a negative camber angle of about 0.5° or adjusting the toe-in angle of the wheels. The latter possibility is discussed in the next section.

3.5. Mechanical effect of toe-in angle

According to the Bosch Automotive Handbook [3], “the toe-in is the angle between the vehicle’s longitudinal axis and a plane through the center of the steer wheel’s tire”. The toe-in angle is positive when the distance between the front of the wheel rims is smaller than the rear.

As mentioned in the last section, improving lateral guidance of the tires mounted on the double-wheeled axle has a slightly positive effect on the rolling resistance when the vehicle is moving forward in a straight line. This effect can be induced either by tilting the wheels or adjusting the wheel alignment with a non-nil toe-in angle. The other benefit is that adjusting the toe-in angle preloads the steering mechanism and therefore compensates for backlash in the links. A positive toe-in angle is generally used on the front steer wheels of a rear-wheel-drive vehicle.

Nevertheless, if the toe-in angle is not nil, the tires roll with a slip angle equal to the toe-in angle. Thus, tire drag increases with increasing toe-in angles. The tire drag increase, which can be calculated with Equation (3.14), was calculated for a vehicle whose 75 kg weight was equally distributed over each wheel and plotted in Figure 3-16. The results shown in the figure suggest that the rolling resistance of a vehicle is quite sensitive to the toe-in angle.

Based on the above investigations, the main technical advice that we can offer is as follows:

- Adjust the toe-in angle to about 0.05° to reduce the tire drag. The losses due to the slip angles are counterbalanced by better lateral guidance, which reduces lateral oscillations and their negative effects. This advice can be applied to the front axle of any rear-wheel-drive vehicle, regardless of whether it is steered by a front or a rear wheel.
- Adjust the toe-in angle in real conditions. This means on the race track, with a ready-to-race vehicle, with a pilot sitting in it. The adjustment procedure should follow one of the protocols presented. This kind of experimental approach gives much better results than attempting to adjust the toe-in angle to a target value using measurement tools.
- Make the structure of the vehicle as rigid as possible. A change in the wheel alignment while the vehicle is cornering can dramatically increase tire drag. Therefore, the structural rigidity of the vehicle should be carefully analyzed during the design phase.

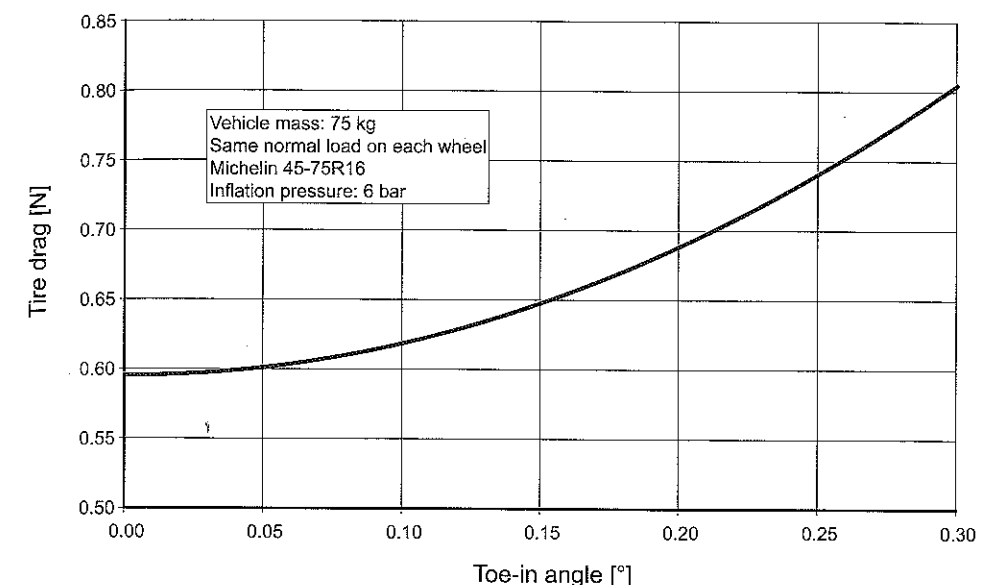


Figure 3-16: Increased tire drag versus toe-in angle (simulation).

Chapter 4: Tire drag when cornering

By Jean-Jacques Santin.

The previous chapter introduced the notion of rolling resistance in tires. One of the principle underlying hypotheses of that discussion was that the vehicle was moving in a straight line, which, depending on the race circuit, may actually represent less than two-thirds of the total run. During the other third of the race, the vehicle is cornering. This change in the vehicle's direction of travel has an energy cost since, as a consequence of the principle of inertia (Newton's first law of motion), the natural tendency of the vehicle is to move in a straight line. Thus, it seems logical to ask what the consequences of cornering on vehicle drag might be. Different approaches, including theoretical modeling and hands-on experiments, can be used to answer this question. In general, a model is most useful at the beginning of the design process since models allow the sensitivity of vehicle parameters to be analyzed and the right choices to be made in less time and using less money. Experiments, on the other hand, are more useful once the initial decisions have been made, since though they provide more accurate results, they are also less flexible, more time consuming and more expensive. This chapter focuses on the models that were developed during the PAC-Car II project to examine the effect on cornering on vehicle parameters, particularly tire drag. Some of the questions we sought to answer are listed below:

- What are the main geometrical parameters that influence a vehicle's tire drag when cornering?
- What is the best vehicle architecture (e.g., wheel configuration, position of the center of gravity)?
- What forces are transmitted from the road to the wheel, via the vehicle structure, when cornering?
- What degree of rigidity is needed in the vehicle structure or in the steering mechanism?
- What axle parameters must be adjustable?

Three different steady-state vehicle cornering models are presented in Section 4.2., along with a comparison of their results. In Section 4.3, the different kinematic laws governing the steering mechanism are analyzed, with special attention paid to

the tire drag when cornering. Section 4.4 focuses on the road-tire forces and moments generated by the three-wheel vehicle model, which can be used as input data when dimensioning the vehicle structure (e.g., using FEM software). Section 4.5 presents an application of the three-cycle vehicle model, with the objective of optimizing the three vehicle-architecture parameters that most influence tire drag when cornering, namely the wheelbase, the track width and the distance from the ground to the vehicle's center of gravity.

4.1. Vehicle Fixed Coordinate System

It is a good idea to define the Vehicle Fixed Coordinate System (VFCS) at the very beginning of a project because it can be used not only for analytical studies of vehicle dynamics, but also to express the results of wind tunnel tests, CFD simulations and FEM calculations, and to position vehicle parts in CAD drawings, for example.

Consider a vehicle in its natural use position, ready to be used on a perfectly flat and horizontal road, but with no pilot onboard.

The VFCS is a right-hand orthonormal coordinate system originating in O at the intersection of the vehicle's rear axle and its longitudinal symmetry plane. The VFCS coordinates are:

- x_v : forward along the longitudinal plane of symmetry;
- y_v : lateral along the right side of the vehicle;
- z_v : vertical in the downward direction.

The vehicle motion variables are called:

- longitudinal (or forward) velocity: translation motion in the x_v direction;
- lateral (or transversal or side) velocity: translation motion in the y_v direction;
- vertical (or normal) velocity: translation motion in the z_v direction;
- roll velocity: rotational motion in the x_v direction;
- pitch velocity: rotational motion in the y_v direction; and
- yaw velocity: rotational motion in the z_v direction.

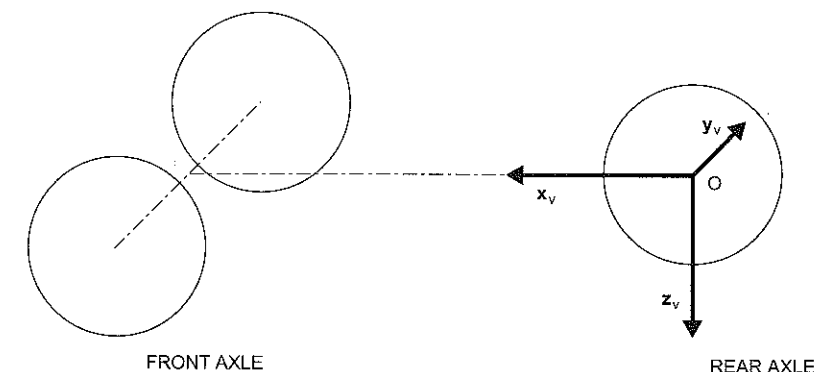


Figure 4-1: Vehicle Fixed Coordinate System of a vehicle equipped with two front wheels and a single rear wheel.

4.2. Steady-state cornering models

A mechanical model is called “steady state” when all the variables (i.e., mechanical, kinematic and geometric) are fixed in time. This kind of model makes it possible to consider the equilibrium of a cornering vehicle in the VFCS.

Three steady-state models are described below: a uni-cycle vehicle model, a bi-cycle vehicle model and a tri-cycle vehicle model.

In these models, the vehicle is moving forward at a constant velocity V_G , cornering to the right with a constant turn radius R . The center of the turn is I, and the center of gravity of the vehicle is G. The vehicle is subjected to centrifugal force F_c , applied at the vehicle's center of gravity, in the direction of IG. Its intensity can be calculated as follows:

$$F_c = \frac{MV_G^2}{R} \quad (4.1)$$

where M is the mass of the vehicle (driver included); V_G , the speed of the vehicle's center of gravity G; and R , the radius of turn (i.e., the distance between G and I).

The wheels are not tilted. The cornering force, the normal load and the longitudinal force, described in detail in Section 3.3.3, are all taken into account, though the aligning moment is not, since it has no significant influence on vehicle dynamics.

A tractive force T – representing either the force that the powertrain must deliver to keep the vehicle's velocity constant or the tire drag that acts to decrease the vehicle velocity – is applied to the vehicle's center of gravity in the direction of travel V_G . This force is the most relevant result provided by the FEV models in terms of the fuel economy.

4.2.1. The uni-cycle vehicle model

The single wheel, or uni-cycle, vehicle model is the simplest model for estimating the tire drag generated by cornering. This model represents a single wheel that supports the entire vehicle's weight. The vehicle's center of gravity G is assumed to be at the center of the wheel A, which is also the theoretical tire-road contact point C. Under such conditions, one single point, located on the road plane, represents the entire vehicle.

Analysis

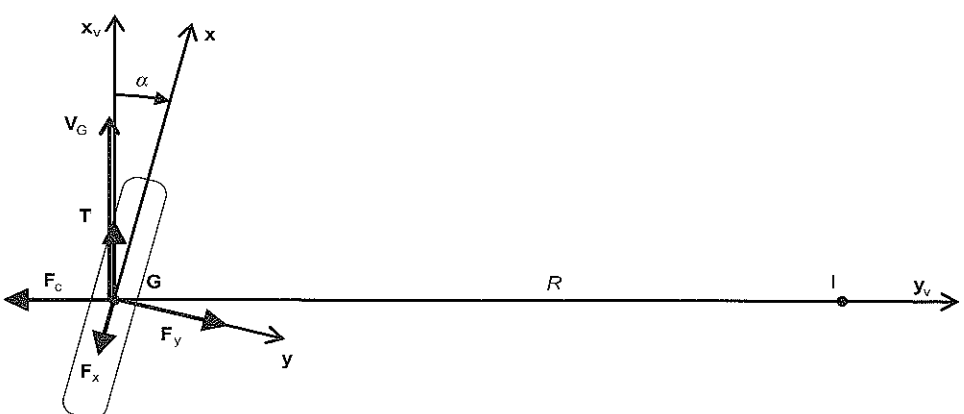


Figure 4-2: The uni-cycle vehicle model (free-body diagram, top view).

Let the “wheel” be a free-body. The mechanical forces exerted on it include:

- the road-tire contact forces F_x and F_y (see Section 3.3.3);
- the centrifugal force F_c ; and
- the tractive force T .

Figure 4-2 depicts a free-body diagram of the problem.

The vehicle's equilibrium conditions, expressed in the VFCS, are as follows:

$$F_y \cos \alpha - M \frac{V_G^2}{R} - F_x \sin \alpha = 0 \quad (4.2)$$

$$T - F_y \sin \alpha - F_x \cos \alpha = 0 \quad (4.3)$$

Equation (4.3), indicating that the tractive force must compensate for the tire drag, has already been introduced (Equation (3.14)).

Based on equations (3.9) and (3.10), (4.2) and (4.3) yield:

$$C_a \alpha \cos \alpha - M \frac{V_G^2}{R} - f_r Mg \sin \alpha = 0 \quad (4.4)$$

$$T = C_a \alpha \sin \alpha + f_r Mg \cos \alpha \quad (4.5)$$

As the slip angle α is 5° or less:

$$\cos \alpha \approx 1 \quad (4.6)$$

$$\sin \alpha \approx \alpha \times \frac{\pi}{180} \quad (4.7)$$

The Equations (4.6) and (4.7), substituted back into (4.4) and (4.5), yield:

$$\alpha(C_a - f_r Mg \frac{\pi}{180}) = M \frac{V_G^2}{R} \quad (4.8)$$

$$T = C_a \alpha^2 \frac{\pi}{180} + f_r Mg \quad (4.9)$$

where the slip angle α is expressed in degrees.

For a given vehicle whose C_a , f_r and M values are known, under known cornering conditions (i.e., the values for V_G and R are known), the slip angle α can be calculated from Equation (4.8). Substituted back into Equation (4.9), these figures, coupled with α , provide the tractive force T that the tire drag must counterbalance.

Numerical mapping

Figure 4-3 shows the tire drag of a 75 kg vehicle, equipped with Michelin 45-75R16 tires, for various vehicle velocities and turn radii. The aerodynamic drag curve is also plotted for a frontal area of 0.25 m² and an aerodynamic drag coefficient of 0.1.

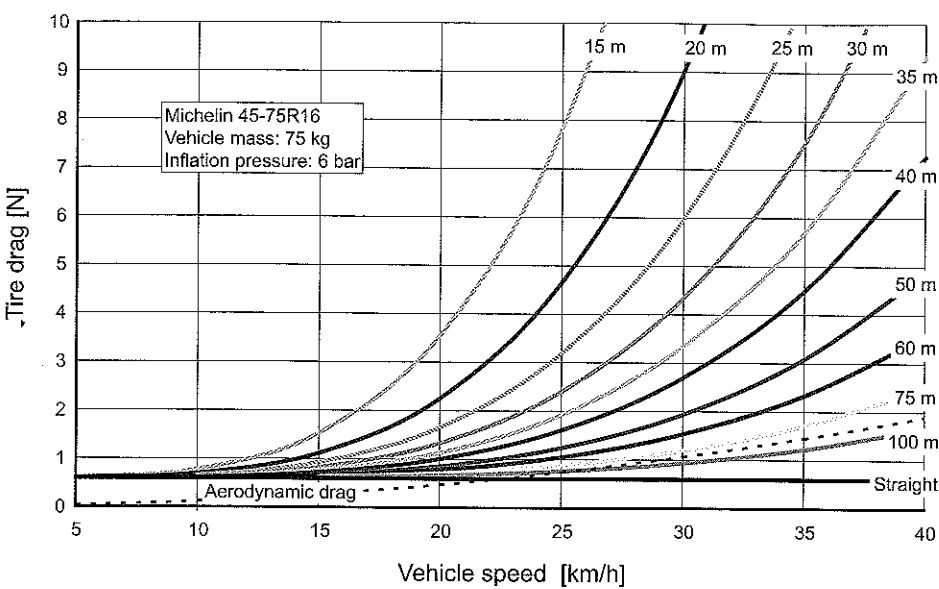


Figure 4-3: Tire drag provided by the uni-cycle vehicle model for different speeds and turn radii.

The above results clearly indicate that the tire drag is much higher when cornering than when moving straight ahead. At a velocity of 35 km/h, for instance, the tire drag when cornering increases twofold for a turn radius of only 100 m, although it does remain under the value for aerodynamic drag. This means that it is essential to evaluate vehicle dynamics accurately so that the cornering tire drag can be reduced as much as possible, leading to reduce the vehicle fuel consumption. In the next two sections, two more accurate models are presented and discussed.

4.2.2. The bi-cycle vehicle model

The two-wheel, or bi-cycle, vehicle model is appropriate for estimating the tire drag generated by cornering. This model consists of two wheels connected by a solid, absolutely rigid chassis, situated at a distance L corresponding to the vehicle's wheelbase. Given a vehicle with two front wheels and a single rear wheel, two front steer wheels can be treated as a single front steer wheel. Thus, the steer angle δ can be considered as equal to the average steer angle of the inner and the outer wheels. The vehicle's center of gravity G is assumed to be located in the vehicle's longitudinal plane of symmetry.

Analysis

Figure 4-4 shows a free-body diagram of the bi-cycle problem. The symbols used to analyze the mechanical problem are the same as the one used in the uni-cycle vehicle model. (Direction of Travel (D.T.) is defined in Section 3.3.2.)

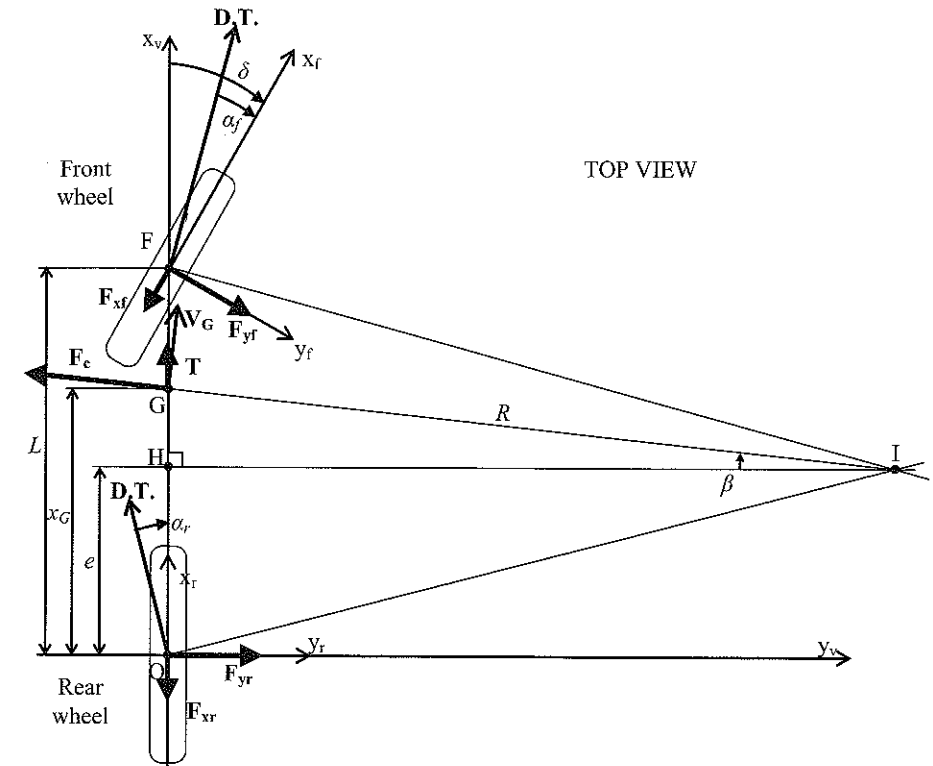


Figure 4-4: Bi-cycle vehicle model (free-body diagram, top view).

The known data for the problem are:

- vehicle characteristics: mass M , wheelbase L , and the X-axis coordinate for the vehicle's center of gravity in the VFCS x_G ;
- tire characteristics: cornering stiffness C , and the rolling resistance coefficient f_r , which both depend on tire pressure and the normal load; and
- cornering conditions: turn radius R , and vehicle velocity V_G .

The unknowns are:

- the steer angle δ ;
- the angle β that positions the turn center I in the VFCS, given a known turn radius R ;
- the front slip angle α_f , and the rear slip angle α_r ;
- the tire forces: normal loads F_{zf} and F_{zr} , cornering forces F_{yf} and F_{yr} , and longitudinal forces F_{xf} and F_{xr} ; and
- the tractive force T.

The problem can be solved using the steps and equations below:

- (1) Calculate the normal load F_z on each wheel by writing the equilibrium equation for the vehicle in its vertical plane of symmetry:

$$F_{zf} + F_{zr} = Mg \quad (4.10)$$

$$x_G F_{zr} = F_{zf} (L - x_G) \quad (4.11)$$

- (2) Calculate the cornering stiffness and the rolling resistance coefficient of each wheel using Equation (3.11) and the curve of Section 3.2.3, where P is the inflation pressure of the tires:

$$c_{\alpha_j} = f(P_j, F_{zj}) \quad j = \{f, r\} \quad (4.12)$$

$$f_\eta = f(P_j) \quad j = \{f, r\} \quad (4.13)$$

- (3) Calculate the longitudinal force on each wheel using the equation (3.9):

$$F_{xj} = f(f_\eta, F_{zj}) \quad j = \{f, r\} \quad (4.14)$$

At this stage, there are still 7 unknowns: α_f , α_r , F_{zf} , F_{yf} , F_{xr} , F_{yr} and T.

- (4) Solve the following 7 equations [(4.15) (4.16) (4.18) (4.19) (4.20) (4.21) (4.22)] numerically using Matlab³:

³ Matlab/Simulink is a registered trademark of TheMathWorks, Inc. (Natick, MA, USA); www.mathworks.com

For the geometric relationships:

$$\tan(\delta - \alpha_f) = \frac{L - e}{R \cos \beta} \quad (4.15)$$

$$\tan \alpha_r = \frac{e}{R \cos \beta} \quad (4.16)$$

where the intermediate unknown e is given by the geometric relationship:

$$\sin \beta = \frac{x_G - e}{R} \quad (4.17)$$

For the mechanical behavior of the tires (equation (3.10)):

$$F_{yf} = C_{\alpha f} \alpha_f \quad (4.18)$$

$$F_{yr} = C_{\alpha r} \alpha_r \quad (4.19)$$

For the vehicle equilibrium equations in the road plane:

$$T - F_{xr} - F_{xf} \cos \delta + F_c \sin \beta - F_{yf} \sin \delta = 0 \quad (4.20)$$

$$F_{yr} - F_{xf} \sin \delta - F_c \cos \beta + F_{yf} \cos \delta = 0 \quad (4.21)$$

$$-x_G F_{yr} + (L - x_G)(F_{yf} \cos \delta - F_{xf} \sin \delta) = 0 \quad (4.22)$$

Numerical mapping

Due to space considerations, we have not provided a numerical mapping for the bicycle model. Because the tri-cycle vehicle model is more accurate, we chose to give the detailed results from this model instead.

Nonetheless, the tire drags delivered by these three models are compared in section 4.2.4.

4.2.3. The tri-cycle vehicle model

The three-wheel, or tri-cycle, vehicle model offers greater analysis possibilities than the previous two models because, as a 3D model, it is able to take the real vehicle architecture into account by adding more parameters, such as track width, wheel diameter, or the position of the vehicle's center of gravity. For instance, this model allows the comparison of 3 steering systems (e.g., front steer wheels versus

rear steer wheels versus three steer wheels); of different kinematic laws governing the steer wheels (e.g., Ackerman versus parallel geometries); and/or of the influence of different default values (e.g., unbalanced tire inflation pressure or wheel misalignment). It can also be used to detect wheel slip or the beginning of a rollover.

Analysis

The data for the problem differs from the bi-cycle model. For that model, the vehicle velocity and the turn radius were given, and the steer angle and the tire drag were calculated. In tri-cycle model, the vehicle velocity and the three steer angles are given and then the turn radius and the tire drag are calculated.

The known data for the problem are given below:

- vehicle characteristics: mass M , wheelbase L , track width a and the coordinates of the vehicle's center of gravity in the VFCS x_G and z_G ;
- tire characteristics: cornering stiffness C_a and the rolling resistance coefficient f_r , which both depend on the tire pressure and the normal load.
- cornering conditions: steer angles δ_r , δ_i , δ_o (respectively, the rear, inner and outer steer angles) and vehicle velocity V_G .

The unknowns are:

- the position of the turn center I in the VFCS, as defined by the angle β and the turn radius R ;
- the three slip angles α_f , α_i , and α_o ;
- the tire forces for each wheel: the normal loads F_{zr} , F_{zi} and F_{zo} ; the cornering forces F_{yr} , F_{yi} and F_{yo} ; and the longitudinal forces F_{xr} , F_{xi} and F_{xo} ; and
- the tractive force T.

Figure 4-4 represents the free-body diagram of the problem, in which the absolute rigidity of the vehicle chassis is assumed.

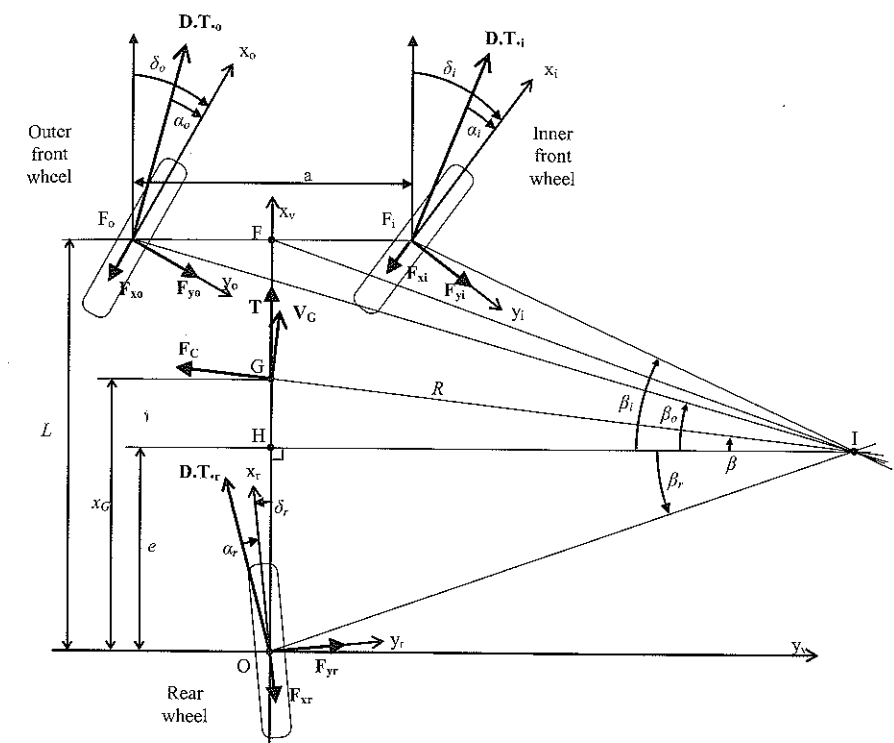


Figure 4-5: The tri-cycle vehicle model (free-body diagram, top view).

The principles applied in the bi-cycle model are again used to formulate the tri-cycle problem. As the load transfer, and thus the rolling resistance of the front wheels, depends on an unknown turn radius, the problem cannot be solved sequentially. Almost the entire set of equations has to be solved using a Matlab iterative solving function, using the following relationships:

- The cornering stiffness and rolling resistance coefficient of each wheel, where P is the inflation pressure of the tires:

$$c_{aj} = f(P_j, F_{aj}) \quad j = \{f, i, o\} \quad (4.23)$$

$$f_{rj} = f(P_j) \quad j = \{f, i, o\} \quad (4.24)$$

- The longitudinal force on each wheel:

$$F_{xj} = f(f_{rj}, F_{aj}) \quad j = \{f, i, o\} \quad (4.25)$$

- The geometric relationships:

$$\tan(\delta_i - \alpha_i) = \frac{L - e}{R \cos \beta - \frac{a}{2}} \quad (4.26)$$

$$\tan(\delta_o - \alpha_o) = \frac{L - e}{R \cos \beta + \frac{a}{2}} \quad (4.27)$$

$$\tan(\delta_r - \alpha_r) = \frac{-e}{R \cos \beta} \quad (4.28)$$

where the intermediate unknown e is given by the geometric relationship:

$$\sin \beta = \frac{x_G - e}{R} \quad (4.29)$$

- The mechanical behavior of the tires:

$$F_{yj} = C_{\alpha_j} \alpha_j \quad j = \{f, i, o\} \quad (4.30)$$

- The vehicle equilibrium:

$$\begin{aligned} & T + F_c \sin \beta \\ & -F_{xr} \cos \delta_r - F_{xi} \cos \delta_i - F_{xo} \cos \delta_o \\ & -F_{yr} \sin \delta_r - F_{yi} \sin \delta_i - F_{yo} \sin \delta_o = 0 \end{aligned} \quad (4.31)$$

$$\begin{aligned} & -F_c \cos \beta \\ & -F_{xr} \sin \delta_r + F_{xi} \sin \delta_i + F_{xo} \sin \delta_o \\ & +F_{yr} \cos \delta_r + F_{yi} \cos \delta_i + F_{yo} \cos \delta_o = 0 \end{aligned} \quad (4.32)$$

$$F_{xr} + F_{xi} + F_{xo} = Mg \quad (4.33)$$

$$\frac{a}{2}(F_{zo} - F_{zi}) - F_c(r - z_G) \cos \beta = 0 \quad (4.34)$$

$$x_G F_{xr} = (F_{zi} + F_{zo})(L - x_G) \quad (4.35)$$

$$\begin{aligned} & \frac{a}{2}\{(-F_{xo} \cos \delta_o - F_{yo} \sin \delta_o) - (-F_{xi} \cos \delta_i - F_{yi} \sin \delta_i)\} \\ & -x_G(-F_{xr} \sin \delta_r + F_{yr} \cos \delta_r) \\ & +(L - x_G)\{(+F_{xo} \sin \delta_o + F_{yo} \cos \delta_o) + (+F_{xi} \sin \delta_i + F_{yi} \cos \delta_i)\} = 0 \end{aligned} \quad (4.36)$$

where r_r is the rolling radius of the wheels.

Numerical mapping

Figure 4-6 shows a graph of the total rolling force provided by the tri-cycle vehicle model, plotted as a function of the turn radius for several vehicle velocities. The vehicle characteristics are noted on the graph. The kinematic law governing the two front steer wheels is called “parallel steering”, meaning that they turn at the same steer angle ($\delta_i = \delta_o$). The influence of steering laws is discussed in more detail in Section 4.3.

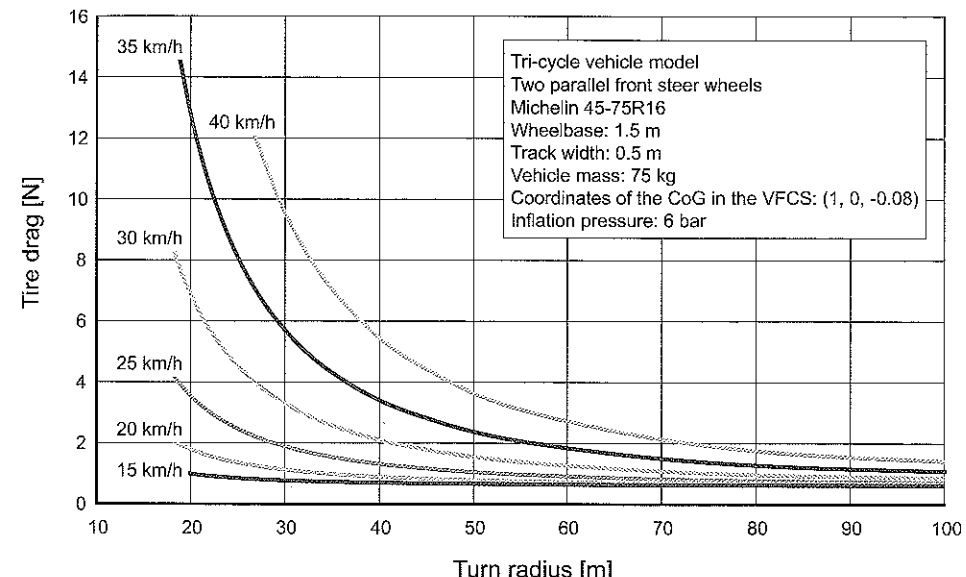


Figure 4-6: Tire drag versus turn radius for several vehicle velocities.

4.2.4. Comparison of the tire drag generated with the three models

The three models above were used to generate values for the total rolling force when cornering. Based on the same input data, the results from the three models

are compared in this section. Figure 4-7 shows the curves plotted for tire drag versus turn radius.

The following vehicle characteristics were used to compare the model results:

- wheelbase: 1.5 m;
- track width: 0.5 m;
- vehicle mass: 75 kg;
- coordinates of the vehicle's center of gravity in the VFCS: $x_G = 1 \text{ m}$, $y_G = 0$, $z_G = -0.08 \text{ m}$;
- tire inflation pressure: 6 bar; and
- vehicle velocity: 30 km/h.

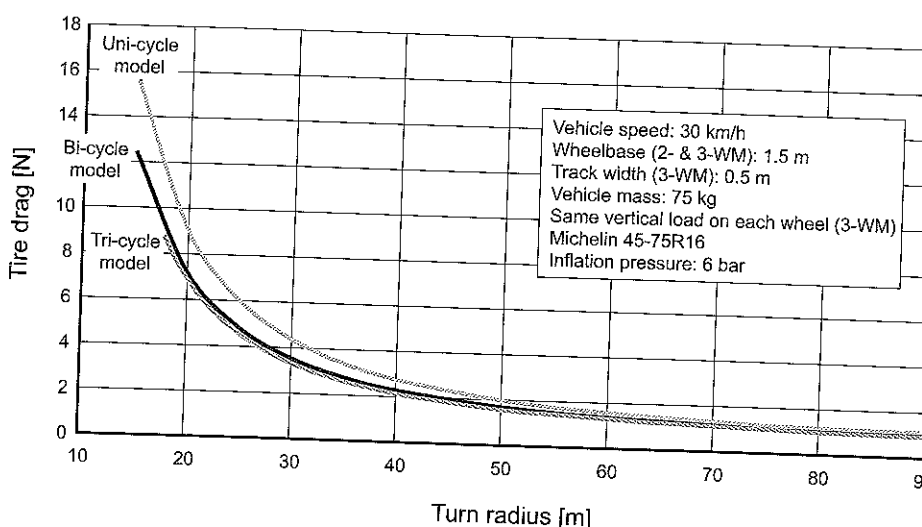


Figure 4-7: Cornering tire drag provided by the three models.

The different results are coherent, and the tendencies of the curves are identical. Overall, the uni-cycle model produces a 20% higher tire drag than the tri-cycle vehicle model, whereas the results for the bi-cycle and the tri-cycle vehicle models are fairly close.

4.3. Comparison of three steering system types

The goal of our analysis remains unchanged: identifying the best vehicle architecture and the optimal kinematic steering law in order to minimize the tire drag. Since the tri-cycle vehicle model allows different steering systems to be simulated, we did so and compared the results.

4.3.1. Analysis

Three vehicles were compared:

- a vehicle with two parallel front steer wheels;
- a vehicle with two parallel front steer wheels, whose steering mechanism respects Ackerman's geometric relationships; and
- a vehicle with a single rear steer wheel and two parallel front wheels.

Ackerman's geometric relationships provide the steer angles, according to the turn radius R , the wheelbase L and the track width a . These relationships are expressed in the following equation:

$$\tan \delta_i = \frac{L}{R - \frac{a}{2}} \quad \text{and} \quad \tan \delta_o = \frac{L}{R + \frac{a}{2}} \quad (4.37)$$

These relationships are easily calculated by assuming that the three wheel spin axes converge at the turn center I. This configuration is actually the best at very low velocities of only a few kilometers per hour. Because the centrifugal force in this configuration is almost non-existent, the tires do not have to develop a lateral force to compensate for it.

An example of the steer angles obtained by applying Ackerman's geometric relationships is given Figure 4-8. The steer angles are very close together, except for the short turn radius, which never really occurs with FEVs. However, since the tire drag has been shown to be quite sensitive to wheel alignment when moving straight ahead, a significant influence was expected from the kinematic law when cornering.

We didn't simulate the three-wheel steering vehicle for a practical reason: the steer angle of the rear wheel provides one additional degree of freedom. Implementing three steer wheels would make the vehicle architecture heavier and more complex, with the attendant risk of decreasing reliability (see Section 8.2).

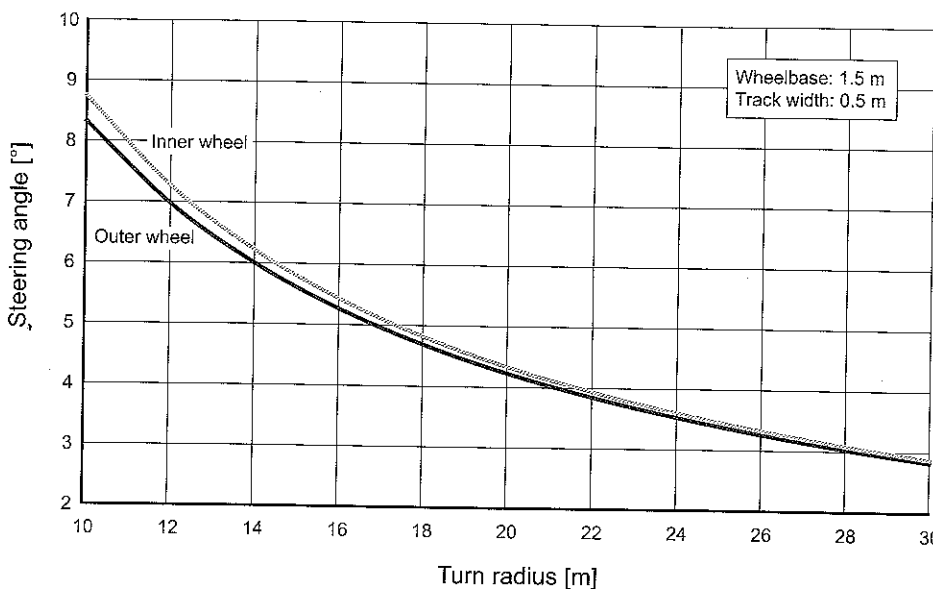


Figure 4-8: Ackerman's geometry.

4.3.2. Results

The tire drag provided by the 3 types of vehicles is shown in Figure 4-9 for the vehicle characteristics listed in Section 4.2.4. Only the steering mechanism was changed.

As shown clearly in figure 1-9, the curves are superimposed, which means that the type of steering system has no significant effect on the tire drag when cornering. Consequently, this criterion can be ignored when selecting the vehicle architecture. Because vehicles steered from the rear appear to be the most interesting configuration, the next section considers only this kind of vehicle (see Section 8.2).

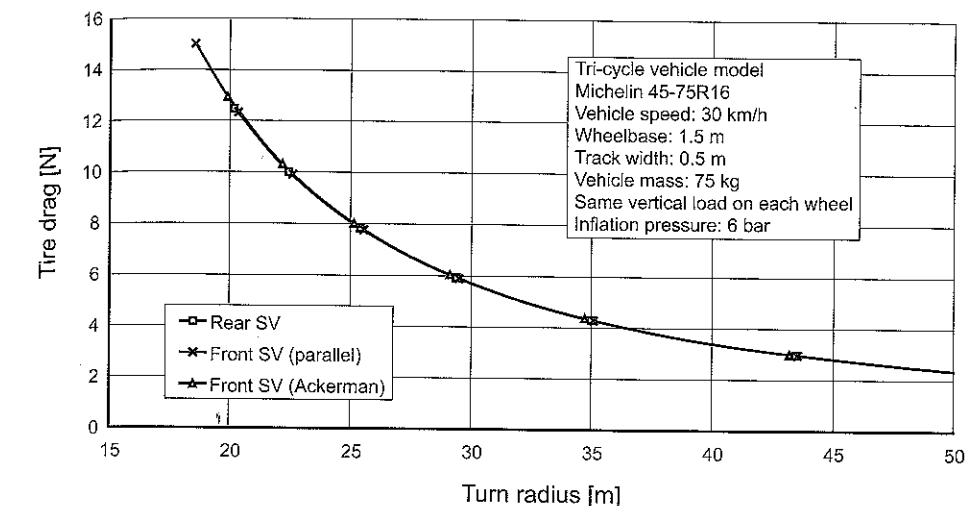


Figure 4-9: Cornering tire drag versus turn radius for three kinds of steering mechanisms: a single rear steer wheel, two front steer wheels governed by Ackerman's kinematic laws, and two front steer wheels governed by parallel kinematic law.

4.4. Tire forces and moments when cornering

It is very important to know the intensity of the forces and moments of the road-tire contact since they provide the information needed to design the vehicle parts and to choose the mechanical components. We used these values during the PAC-Car II project to design the wheel structure (Chapter 7) and the body-shell (Chapter 6), as well as to choose the wheel bearings (Section 7.1).

In the simulation reported below, the vehicle characteristics were:

- symmetrical vehicle;
- single rear steering wheel;
- two parallel front wheels;
- non-tilted wheels (camber angle nil);
- vehicle mass: 75 kg;
- wheelbase: 1.5 m;

- track width: 0.5 m;
- x-axis coordinate of the vehicle's center of gravity, in the VFCS: 1 m;
- z-axis coordinate of the vehicle's center of gravity, in the VFCS: -0.08 m (i.e., 8 cm above the wheel spin axis);
- wheel diameter (loaded): 0.48 m;
- tires: Michelin 45-75R16 radial-ply;
- inflation pressure: 6 bar; and
- tire adhesion coefficient: 0.8 (used only to detect slipping).

The results plotted in the next three figures were obtained with the tri-cycle vehicle model under cornering conditions.

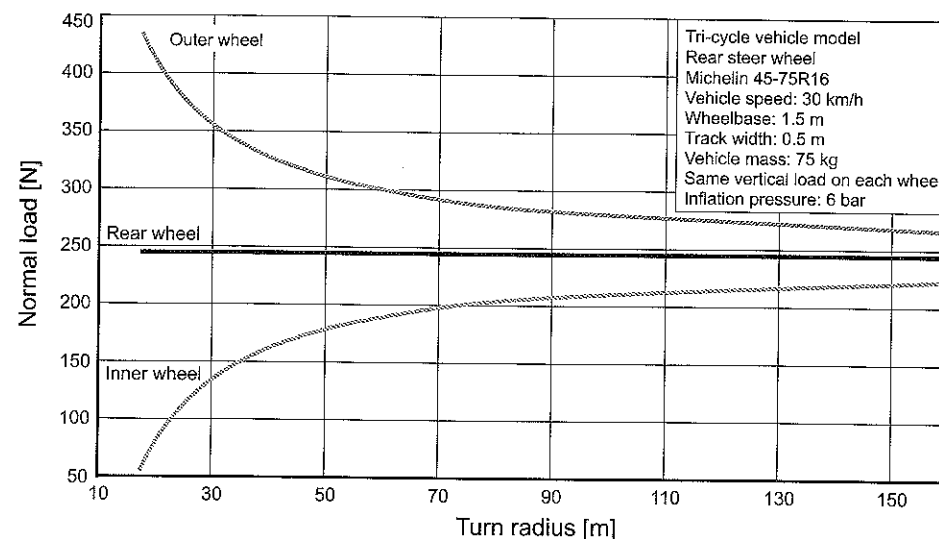


Figure 4-10: Normal load versus turn radius.

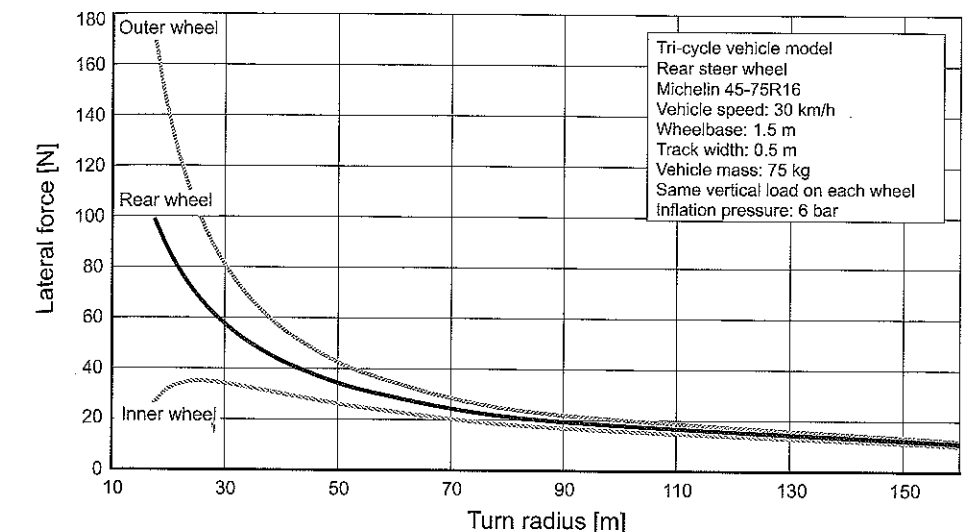


Figure 4-11: Cornering force versus turn radius.

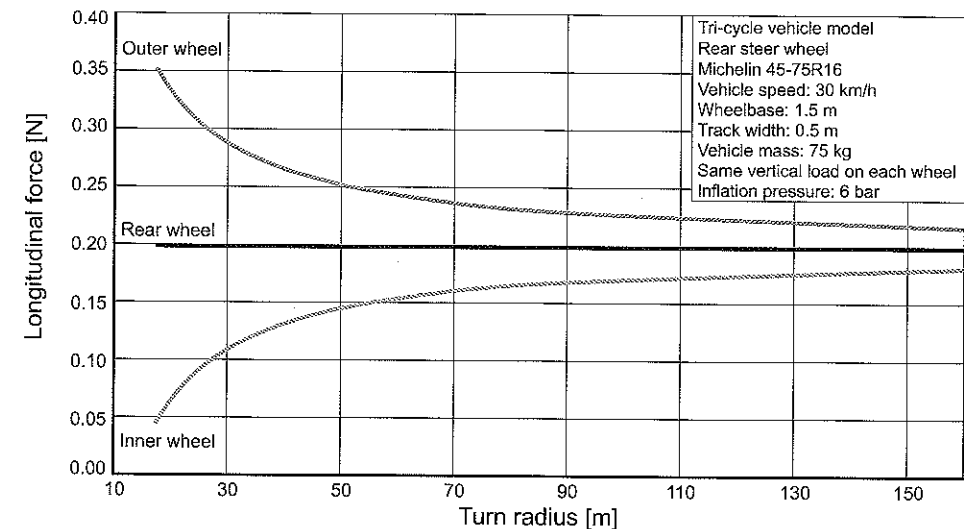


Figure 4-12: Longitudinal force versus turn radius. The graph represents the rolling resistance on each wheel.

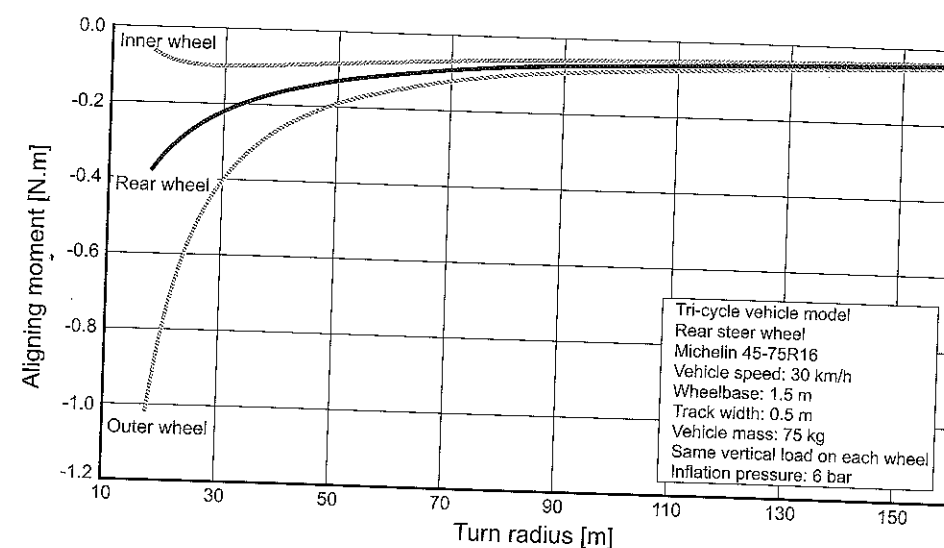


Figure 4-13: Aligning moments versus turn radius

4.5. The optimization of the vehicle architecture parameters

The parameters of the vehicle architecture considered here include the wheelbase, the track width and the ground-CG distance. Obviously, other parameters could have been included, but we felt it would be better to limit our discussion to these three main parameters in order to provide an example for your own further investigations.

We decided that the cornering tire drag value calculated with the tri-cycle vehicle model (Section 4.2.3) was the objective function that should be minimized. Any values in the following parameter constraint ranges can be used:

- wheelbase: from 1 to 2 m;
- track width: from 0.5 to 1.1 m; and
- z coordinate of the CG, expressed in the VFCS: from -0.15 to 0 m, with the ground-CG distance being calculated by adding this figure to the wheel radius (i.e., 0.25 m).

All the other parameters, including the drive parameters, such as vehicle velocity or turn radius, remain unchanged and equal to the values listed in Section 4.4.

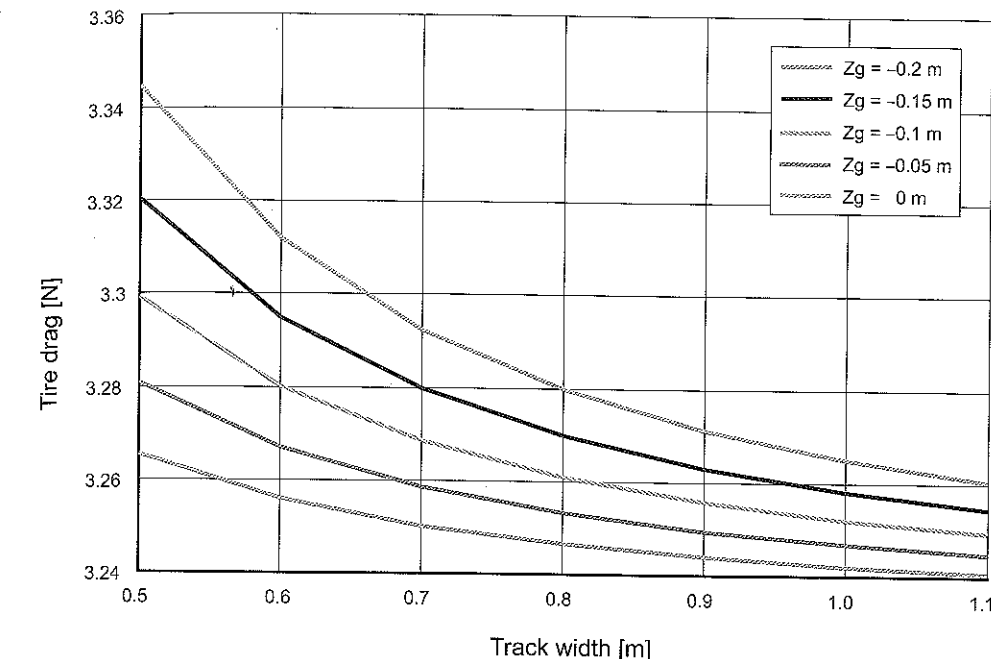


Figure 4-14: Tire drag of a vehicle, according to track width and the z coordinate of the CG (in the VFCS). Other parameters remain constant.

As it only takes a few seconds for Matlab to calculate the tire drag from a given set of parameters, we built a map from ordered triples and a sampling that provides 210 values for the objective function.

The results are as follows:

- the wheelbase has no influence on the tire drag when cornering;
- the track width has a slight influence on the tire drag when cornering, with a wider track leading to lower tire drag values; and
- the ground-CG distance influences the tire drag when cornering, with a larger ground-CG distance leading to lower tire drag values. However, the gain between the two bound values is only 2.5%.

The Figure 4-14 illustrates the results obtained with a wheelbase of 1.5 m (i.e., the wheelbase of PAC-Car II).

The results presented here were not sufficient to yield a general conclusion, but they did help us to fine-tune the project. Other investigations, such as testing modifications of vehicle velocity, turn radius, or vehicle weight, were also essential to our final conclusions.

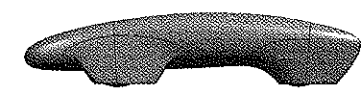
Chapter 5: Aerodynamics

By Nicolas Weidmann.

The PAC-Car II's aerodynamic design won the ECARA AWARD from the European Car Aerodynamics Research Association in 2007.



The CAD file of the shape of PAC-Car II is available for educational purposes. Please visit www.paccar.ch for further information about the transfer of the CAD-data.



In Chapter 2, aerodynamic drag was cited as being responsible for approximately half of the power demand of a fuel economy vehicle cruising on a flat, level road. In light of this reality, high-quality aerodynamics are clearly essential to such a vehicle's success. This chapter describes the tremendous effort expended to improve the PAC-Car II's aerodynamics. The CAD modeling and body manufacturing processes employed once the most aerodynamic shape had been determined are discussed in the next chapter, since these two processes also play an important role in the success of the final product.

Section 5.1. of this chapter introduces the aerodynamics fundamentals relevant to the body design of a fuel economy vehicle, and Section 5.2 explains the PAC-Car II body design process in terms of these fundamentals. The vehicle's aerodynamic performance and the possibilities for improvement are presented in Section 5.3., while the experimental methods and simulation processes used to optimize the body's aerodynamics are described in Section 5.4. The chapter concludes with a short discussion of the aerodynamic study conducted for this project (Section 5.5).

5.1. Fundamental principles of aerodynamics for low-drag vehicles

When designing the shape of a competitive low-drag vehicle, the designer must keep in mind the fundamentals of aerodynamic drag and its causes. This section provides an introduction to the field of aerodynamics.

5.1.1. Aerodynamic drag force

The aerodynamic drag of a vehicle's body in a streaming fluid is obtained using the Equation (2.3).

Between the factors that appear in this equation, only c_x and A depend on the shape of the vehicle body, with c_x being a function of the yaw angle β and the pitch angle α , as shown in Equation (5.1) (see Section 4.1 for the definition of these angles).

$$c_x = c_x(\alpha, \beta) \quad (5.1)$$

To minimize a vehicle's aerodynamic drag, the drag area (i.e., the product of c_x and A) needs to be minimized.

5.1.2. The sources of aerodynamic drag

There are basically two different kinds of aerodynamic drag: friction drag and pressure drag. A vehicle body streaming in a fluid generates both friction drag and pressure drag. Their ratio depends on the shape of the body, as shown in the following formula:

$$F_{\text{Aerodynamic drag}} = F_{\text{friction}} + F_{\text{pressure}} \quad (5.2)$$

Friction drag

When air flows over a vehicle body, friction is generated between the air and the body surface. Due to the "no slip condition" of air on this surface, the airflow is slowed by the bodywork, which provokes shear stress τ on the body surface (Figure 5-1), which in turn causes friction drag.

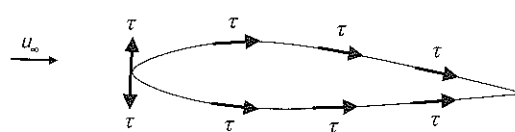


Figure 5-1: Shear stress τ tangential to the vehicle body surface.

Directly above the body surface, there is a thin zone, called the boundary layer, in which the flow velocity depends on the flow's distance from the surface. At a distance δ , the flow velocity is equal to 0.99 of u_∞ , the velocity of the undisturbed flow. This distance, called the boundary layer thickness, increases along the

streamline according to its location x relative to the starting edge of the flat plate: $\delta = f(x)$.

The quantity of shear stress and the resulting friction drag depend on the nature of the airflow within the boundary layer. Laminar flows generally cause lower shear stress than turbulent flows. The velocity distribution of these two flow types within the boundary layer is also quite different (Figure 5-2).

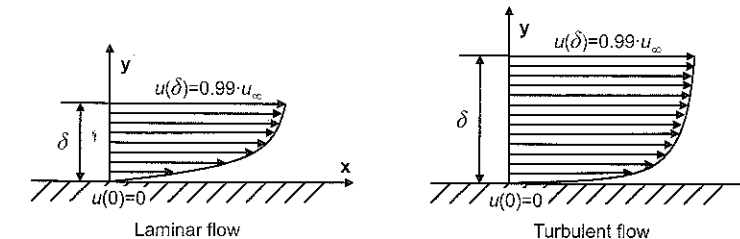


Figure 5-2: Laminar and turbulent velocity profiles for a flat surface.

The condition of the airflow (i.e., laminar or turbulent) depends on the local Reynolds number at location x :

$$Re_x = \frac{ux}{v} \quad (5.3)$$

where u is the air velocity; v is the kinematic viscosity; and x is the distance from the edge, where the boundary layer starts to develop, to the location where the airflow is analyzed (Figure 5-3).

There is a critical Reynolds number, below which the flow in the boundary layer is laminar, and above which the flow is turbulent. The critical Reynolds number Re_{crit} for a flat plate with a smooth surface is as follows:

$$3 \times 10^5 \leq Re_{crit} \leq 3 \times 10^6 \quad (5.4)$$

Between these two flow states (i.e., laminar and turbulent), there is a transition zone in which the flow starts to be perturbed (Figure 5-3).

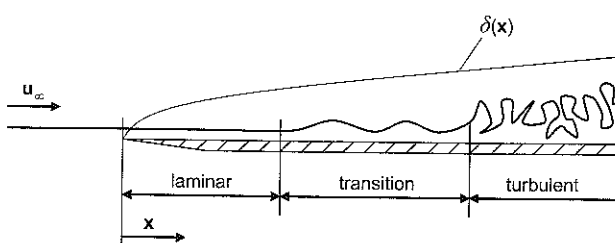


Figure 5-3: Boundary layer on a flat plate.

Assuming that pressure drag has been reduced to a minimum, friction drag is dominant in streamlined vehicles. Friction drag is proportional to the vehicle surface overflowed by the air, called the wetted area. Thus to minimize this source of drag, the surface of a vehicle must be minimized.

Pressure drag

The integrated pressure distribution over the entire body surface produces a force, and the x-component of this force is pressure drag. The other components are lift (z-axis) and lateral force (y-axis). As shown in Figure 5-4, the pressure acts perpendicularly to the surface.

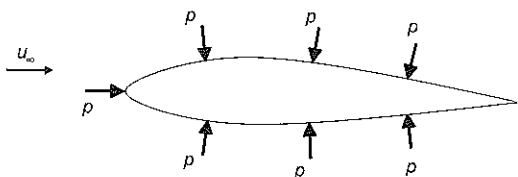


Figure 5-4: Pressure p acting normal to the vehicle body surface.

Four different types of pressure drag sources can be distinguished: flow separation, induced drag, interference drag, and boundary layer pressure loss. These different types are explained in further detail below.

Flow separation

When the pressure gradient along a streamline becomes too high, the airflow is no longer able to follow the surface and thus separates from the vehicle body. Figure 5-5 shows the back streaming that occurs in the case of flow separation.

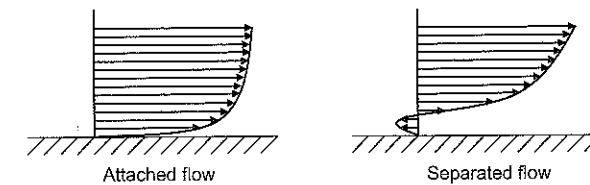


Figure 5-5: Attached and separated flows with back streaming.

In these zones of separation, the pressure is more or less equal to the ambient pressure. The overpressure on the frontal part of the body creates a drag force on the vehicle. Blunt body shapes, such as passenger cars and airfoils with high angles of attack, tend to cause flow separation (Figure 5-6).

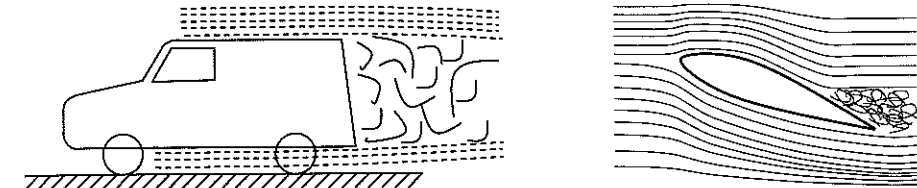


Figure 5-6: Flow separation behind a car and behind an airfoil with a high angle of attack.

Pressure drag due to separation influences the aerodynamic drag significantly. Consequently, rough surfaces and steep trailing-edge angles should be avoided under any circumstances when designing a low-drag vehicle.

Induced drag

Vehicle bodies in streaming air can generate lift or downforce, depending on the shape of the body and its angle of attack. Lift and downforce both cause induced drag and should basically be avoided for vehicles running at low speeds, especially FEV. Unlike fast cars, such vehicles do not have to generate downforce for reasons of road adherence, and according to Tamai [18], increasing a vehicle's lift in order to reduce rolling resistance drag provides no improvement.

Interference drag

When two vehicle bodies are close to each other in the airflow, their surrounding pressure fields are superposed. This superposition changes the properties of the

airflow and can increase the total aerodynamic drag force of the assembled single bodies. To reduce the interference drag to a minimum, critical areas, such as the seams and joints of the wheel fairings and the vehicle body, should be designed carefully.

Boundary layer pressure loss

Consider the case of a streamlined vehicle body without flow separations, thus creating a boundary layer over the entire surface. This boundary layer stops the potential flow from closing again at the rear edge of the vehicle, thus preventing the pressure at the rear stagnation point from attaining the same value as the pressure at the front stagnation point. Integrating the pressure difference over the entire body creates an additional drag force in the direction of the airflow. The boundary layer pressure loss is the direct consequence of the friction between the air and the body. Even when this pressure drag component is relatively small compared to the friction drag of the entire streamlined vehicle, it is still not negligible.

5.1.3. Vehicle body shape

A fuel economy vehicle can have many forms. However, certain aerodynamic factors related to aerodynamic drag must be taken into consideration before deciding on the final shape of a low-drag vehicle. These factors are explained below.

Cambering

A vehicle body at ground level behaves differently from the same body in free-streaming air, as can be seen in Figure 5-7. A symmetrical vehicle body in free air generates neither lift nor downforce. However, the same body at ground level generates downforce. In fact, the area between the underside of the vehicle and the ground behaves like a Venturi tube. According to Bernoulli, the velocity increases in the narrow section of the tube (i.e., the area between the ground and the vehicle), consequently decreasing the pressure and generating downforce. Since, as mentioned in Section 5.1.2, lift and downforce should be avoided, this behavior poses a problem for FEV designers.

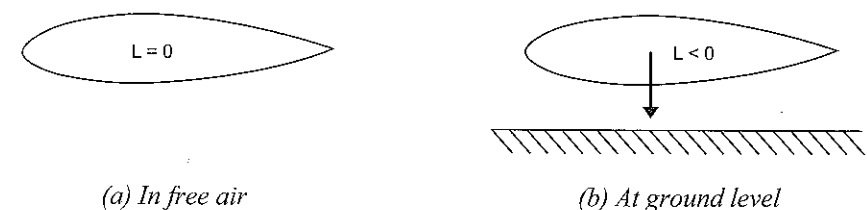


Figure 5-7: Behavior of the same symmetric vehicle body in two configurations. (L = Lift force)

One solution to the above problem is to use camber. Though a cambered body in free air does generate lift, the same body at ground level can have zero lift (Figure 5-8). Since FEV are, in actual fact, bodies moving at ground level, they can be slightly cambered to avoid downforce.

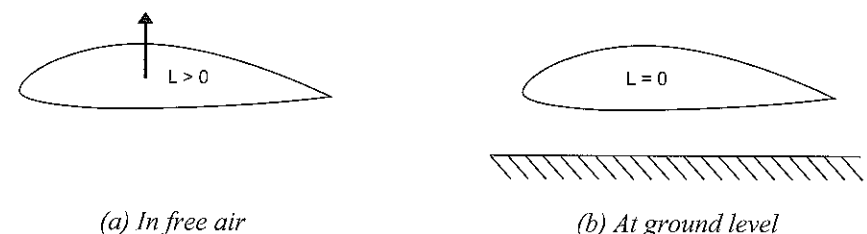


Figure 5-8: Behavior of the same cambered vehicle body in two situations. (L = Lift force)

Still, it is difficult to estimate how much camber should be applied to generate zero lift. A vehicle body can have very different lift or downforce properties for different yaw angles. Nothing is gained if, for example, the vehicle has zero lift at 0° yaw, but high lift or, even worse, downforce, at slightly higher yaw angles. Given the diverse conditions at the various competitions, the designer must make the best compromise possible, trading off between the different factors to achieve low-drag throughout the competition.

Ground clearance

The optimal ground clearance was not easy to determine, and time was too short to research the topic exhaustively. According to Tamai [18], the aerodynamic drag of a moving vehicle body at ground level behaves as shown in Figure 5-9. A ground clearance under a certain minimum produces very high levels of drag, while above this minimum, the curve is quite flat. Therefore, we recommend following Tamai's

suggestion for solar cars with torpedo-shaped bodies, and setting the minimal ground clearance between 0.15 m and 0.25 m.

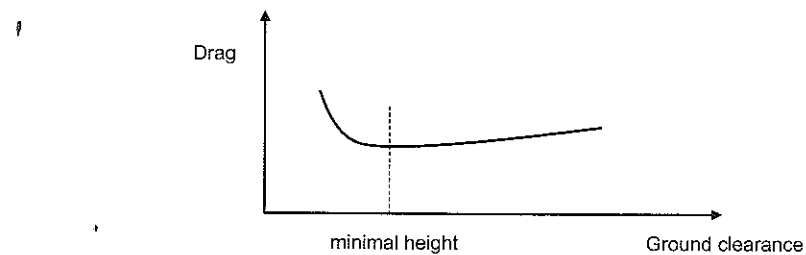


Figure 5-9: Minimal ground clearance.

Side winds

As shown in Figure 5-10, side winds change the air velocity and the angle of attack of the air stream.

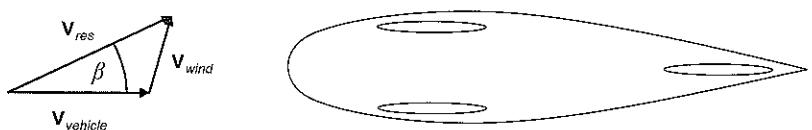


Figure 5-10: Side winds
 V_{wind} : the velocity vector of the wind, $V_{vehicle}$: the velocity vector of the vehicle,
 V_{res} : the sum of V_{wind} and $V_{vehicle}$ and β the angle of attack.

Since the average speed of fuel economy vehicles is low, the wind can have a relatively strong influence. In 2004, the direction of the wind and the driving speed were measured during a fuel economy race run by PAC-Car I. Based on the results of those measurements, a graph was drawn of the percentage of time in one run that PAC-Car I advanced at a certain velocity and at a certain angle (Figure 5-11). Based on this graph, the PAC-Car team decided to design the PAC-Car II with yaw angles from -15° to $+15^\circ$. (A detailed description of the experimental apparatus used to measure wind speed and angle of attack is given in Section 5.4.1.)

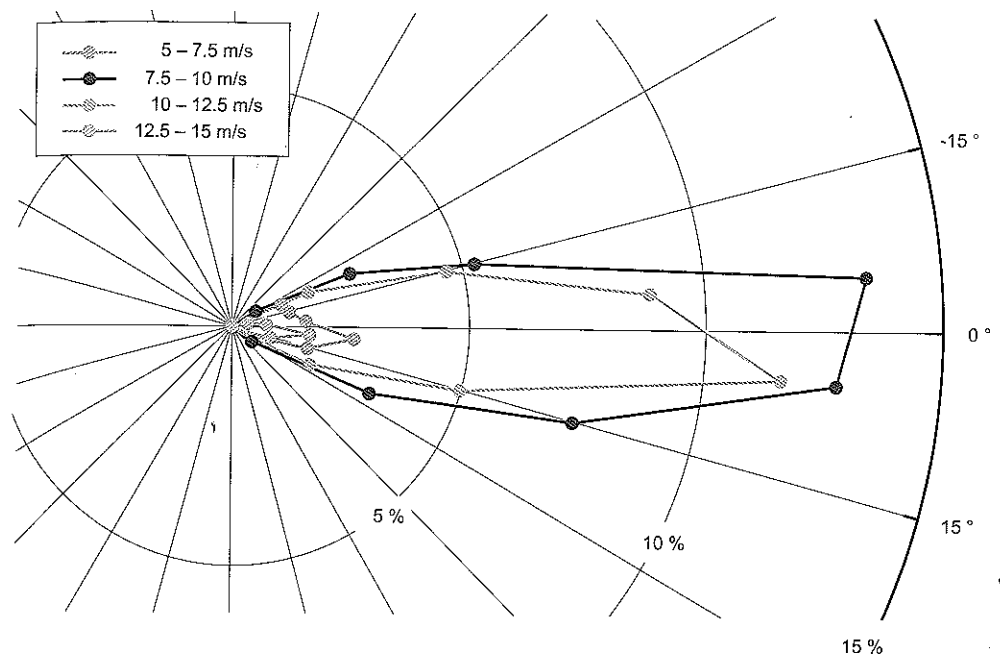


Figure 5-11: Angle of attack for various wind speed ranges. (top view of the vehicle)

Internal flow

Holes in the outer vehicle shell generate additional aerodynamic drag due to internal airflow, and thus should be avoided if possible. Wind tunnel tests with PAC-Car I confirmed this fact. Unfortunately, internal air flow is needed, both to remove the vapor that builds up on the inside of the windshield when it rains and to provide the pilot with fresh air, especially when the sun makes the cockpit too warm. During a 50-minute run at the Nogaro competition, the cockpit temperature reached 50°C , which is really the limit. Obviously, for a variety of health and safety reasons, sufficient fresh air for the pilot is necessary. In the PAC-Car II design, the gaps between the wheel fairing openings and the wheels were considered adequate, and no additional air inlets were needed.

5.2. Design process for the PAC-Car II body shape

A FEV body shape design is limited by certain qualitative and quantitative parameters summed up under the term, "design constraints." These constraints come from a variety of sources, including race regulations, ergonomics and

aerodynamics. At the end of the preliminary design phase, which mainly consists of making choices about vehicle architecture and listing the design constraints, these constraints constitute the vehicle's "topological model." With this model as the starting point, a series of modifications are carried out during the aerodynamic design phase in order to improve the vehicle body's aerodynamic properties, using two complementary tools: Computational Fluid Dynamics (CFD) and wind tunnel experiments.

This section provides a brief summary of the design constraints for the PAC-Car II project, followed by a more detailed description of the model iterations that occurred during the project's aerodynamic design phase. Figure 5-12 shows a top-down view of the design process of the body shape of PAC-Car II.

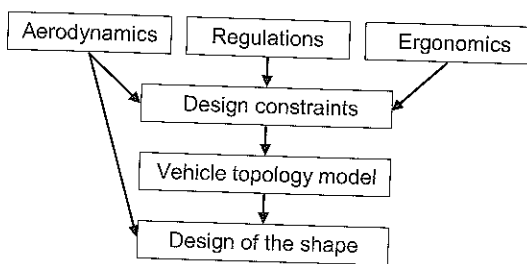


Figure 5-12: Overview of the PAC-Car II body shape design process.

5.2.1. Sources of the design constraints

Three design constraint sources were taken into account when designing PAC-Car II: race regulations, ergonomics and aerodynamics. Other constraints could also have been considered, such as the rigidity, strength or manufacturability of the vehicle body. However, we decided that, if our goal was to obtain the best aerodynamic shape inside which a pilot would be able to lie down, these other constraints were secondary compared to the three already mentioned. Once the shape had been decided upon, we could determine how to make it more rigid and how to build it.

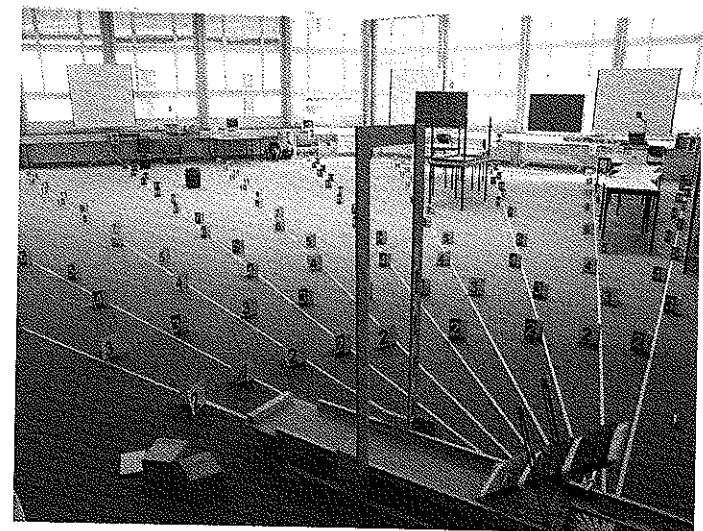


Figure 5-13: Driving position and visibility tests. Overview of the experimental apparatus, with the mock-up chassis model in the foreground and the labels used to quantify the pilot's field of vision in the background.

Race regulations

The race regulations are designed to insure the fairness, safety and spirit of the competition. All participating vehicles have to abide by these rules in order to be admitted to the competition. For example, the maximum height measured at the top of the cockpit must be less than the dimension imposed by the regulations. Section 1.3 discusses these rules in more detail.

Ergonomics

When designing the vehicle, it was very important to pay special attention to ergonomics and such natural boundary conditions as the pilot's physical dimensions. The pilot needs to feel safe in the vehicle as well as comfortable enough to drive the vehicle without needing to maintain excessive concentration throughout the run. Intensive experiments about the ergonomics of the vehicle design were conducted, and the result contributed decisively to PAC-Car II's success. Figure 5-13 and Figure 5-14 depict the driving position and visibility tests. Numerous wheel positions (Figure 5-15) were tested and evaluated according to a variety of ergonomic and technical criteria, such as the pilot's field of vision, in order to define the best driving position.



Figure 5-14: Driving position and visibility tests. Measurement of the minimal height of the vehicle body.

Vehicle topological model

Once the design constraints had been evaluated, a vehicle topological model, including the pilot, was created using computer-aided design (CAD) software (Figure 5-16). This CAD model was fully parametric so that changes could be made as required. The final PAC-Car II shape design was based on this model.

Aerodynamics – the preliminary design

Since the body shape design and its resulting aerodynamics are based on the vehicle topology, aerodynamic principles had to be considered early in the design process. As mentioned in Section 5.1, a vehicle's aerodynamic qualities depend on its drag coefficient c_x and its frontal area A , with the drag area of a vehicle (i.e., $A c_x$) being minimized to achieve the least possible amount of air drag.

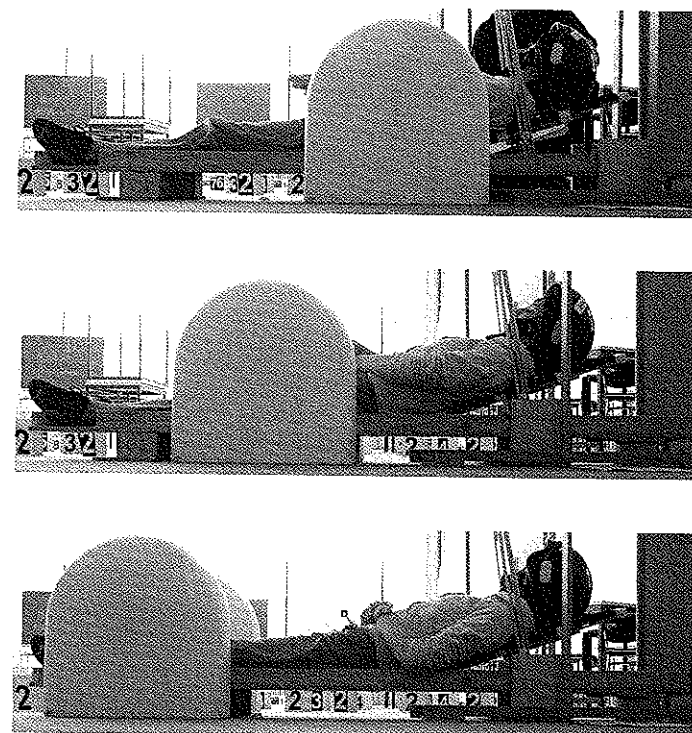


Figure 5-15: Driving position and visibility tests. The three front wheel positions.

Based on the vehicle's topological model, sketches and drawings of the vehicle's hard points were done by hand (Figure 5-17). In the preliminary design, streamlined airfoils (e.g., Natural Laminar Flow (NLF) profiles) were used for the top and side views. NLF profiles are specially designed for estimating laminar airflow over the length of the airfoil, allowing the qualities of a 3D wing at a certain aspect ratio to be estimated from the 2D airfoil data. However, since the PAC-Car II is shaped like a "torpedo" rather than a wing, it was difficult to judge the benefit of accurately converting the NLF profiles from 2D to 3D. Therefore, in the PAC-Car II design phase, these profiles were used qualitatively to help us deal with the dimensional constraints.

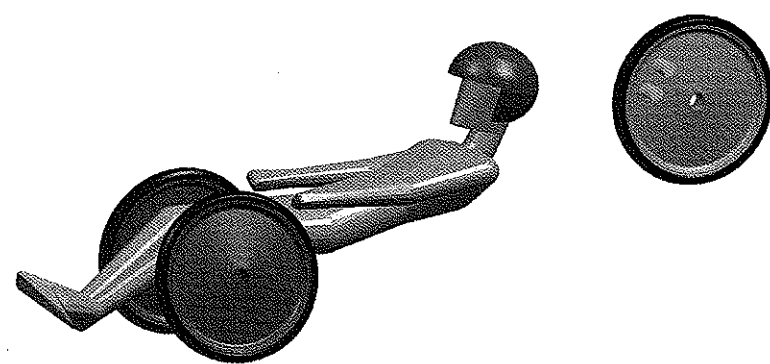
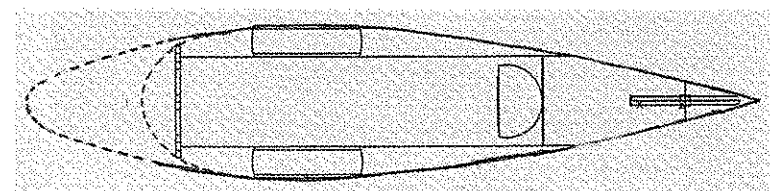
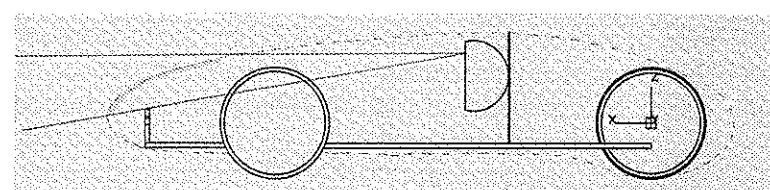


Figure 5-16: Vehicle topological model in CAD.



(a) Top view



(b) Side view

Figure 5-17: Application of NLF profiles on a simplified topological model.

Consider, for example, the design of the vehicle's nose. As shown in Figure 5-17, the vehicle would have been much longer if the original NLF airfoil had been used, which would have led to additional friction drag and additional weight. Since it was also not clear if applying the NLF airfoils in 3D would produce the same good quality laminar airflow as in the 2D version, the PAC-Car team decided to modify the shape of the profile a little.

An important element considered during the preliminary design phase was the windshield. According to the theory of optics, the more perpendicular the windscreens is to the pilot's line of sight, the better the pilot's vision will be, as the effects of reflections and surface defects will be minimized. This theory had to be kept in mind when we were designing the windshield.

5.2.2. The body shape design

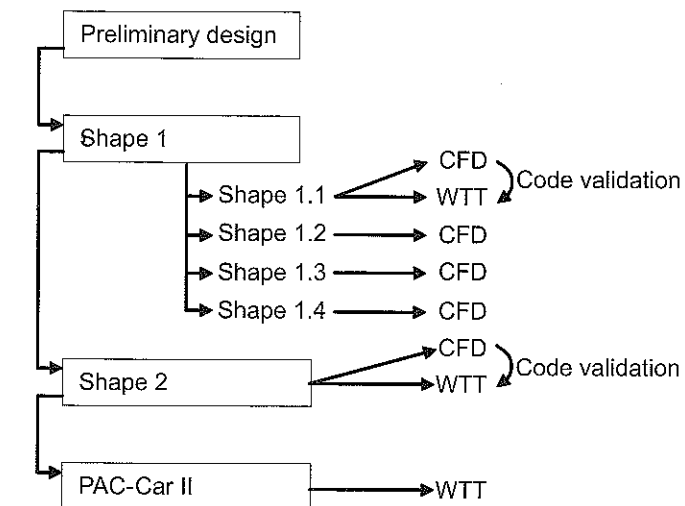


Figure 5-18: Steps of the PAC-Car II aerodynamic design process.
(CFD: Computational Fluid Dynamics, WTT: Wind Tunnel Test)

The body shape design was the result of several progressive steps (Figure 5-18). Once the preliminary design described above had been established, several model iterations based on that design were developed and tested using wind tunnel trials and CFD analysis. The results of these tests were taken into account in subsequent iterations of the body shape design. After numerous model iterations, the final shape of PAC-Car II was defined.

Model iterations

Five model iterations were created during the PAC-Car II design process. These iterations can be divided into two types: Type 1 had non-tilted front wheels (Shape 1.x), and Type 2 had tilted front wheels (Shape 2). Because the various aspects of the vehicle were researched and developed in parallel, the results of the rolling

resistance tests with tilted front wheels were not available at the beginning of the design process for Shape 1.x; thus, these results were only applied to Shape 2.

Shape 1.1

The results of the preliminary design phase (Section 5.2.1) were imported into a CAD application in order to draw a first shape: Shape 1.1 (Figure 5-19). Streamlined profiles were used for the wheel fairings (i.e., wheel covers). The frontal area of Shape 1.1, which measures 0.3 m^2 , bulges slightly more than necessary on the sides, in order to guarantee enough space for the front wheels. Though this bulge clearly increases the frontal area, it also makes for a more rounded, smoother shape at the intersection of the vehicle's roof and side wall. Such a smooth shape can be expected to perform better aerodynamically in cross winds, since the risk of flow separation is lower. The challenge is to find the best trade-off between a small frontal area and a smooth shape with sufficiently good cross wind aerodynamics.

In this shape, the junctions between the wheel fairings and the main vehicle body are smooth in order to reduce interference drag to a minimum. Though the frontal area increases with the radius of these junctions, the interference drag is decreased. Thus, in order to obtain the lowest over-all aerodynamic drag, a trade-off is also necessary here.

Our wind tunnel trials and CFD analysis showed that the wheel fairing design has a great impact on the aerodynamic quality of the overall shape of the vehicle. The wheel fairings in Shape 1.1 have certain flaws, such as concavities on the outer sides of the body surface, mostly due to CAD design errors. In the wind tunnel, large separation bubbles – visible at an angle of attack between 10° and 15° – occurred near these concavities on the lee side of the vehicle. Since CFD simulations confirmed these observations, the wheel fairings had to be improved in subsequent model iterations.

Shape 1.2

Since the wheel fairings of Shape 1.1 were not optimal, the team decided to perform two additional model iterations, modifying only the fairings. The first of these iterations, Shape 1.2 (Figure 5-19), has the same basic body form as Shape 1.1, but the wheel fairings have no concavities and are thicker and more symmetrical than in Shape 1.1. The effect of these modifications was calculated in CFD; as expected, the critical zones of separation were smaller than for Shape 1.1. Though these modifications did increase the frontal area (by less than 1%) the drag coefficient c_x was reduced, which compensated for the increased size.

Shape 1.3

The second of the wheel fairing model iterations, Shape 1.3 (Figure 5-19), again has the same body form as Shape 1.1, but this time the wheel fairings are thinner than in the previous shapes. As a result of this modification, the size of the frontal area is reduced. Compared to the flow separation produced by Shape 1.2 in the critical areas on the lee side of the wheel fairings, the separation bubbles produced by Shape 1.3 are significantly smaller. This difference can be explained by the smaller trailing-edge angle at the rear edge of the wheel fairings, leading to lower pressure gradients along the streamlines.

Shape 1.4

Shape 1.4 examined the effect of modifications to the vehicle's pitch angle. As has been mentioned previously, Shape 1.1 generates lift even at 0° Yaw. However, according to the literature, there is no advantage in creating lift or downforce in FEV. Thus, the PAC-Car II team decided to investigate how changing the pitch angle would influence lift or downforce. Shape 1.4 has exactly the same body form and wheel fairings as Shape 1.1, but the vehicle is turned around its y-axis by a pitch angle of -1° . The results of the CFD analysis showed that this pitch angle modification could decrease the lift by 50 % for 0° Yaw.

Shape 2

Based on the results of the wind tunnel trials and the CFD analysis, as well as the results of our rolling resistance experiments, we completely redesigned the vehicle. The front wheels of Shape 2 (Figure 5-19) were tilted 8° , which changed the shape of the body significantly. The frontal area was reduced to 0.254 m^2 , and the cross flow qualities were improved considerably. The wetted area was also reduced by 7.1%, which had a direct impact on the level of friction drag and on the drag coefficient c_x . Table 5-1 provides a comparison of the basic numbers for Shape 1.1 and Shape 2.

Table 5-1: Comparison of Shape 1.1 and Shape 2 (Scale 1:1).

	Shape 1.1	Shape 2
$c_x [-]$	0.08	0.07
Frontal area [m^2]	0.292	0.254
Drag area [m^2]	0.02336	0.01778
Wetted area [m^2]	4.2	3.9

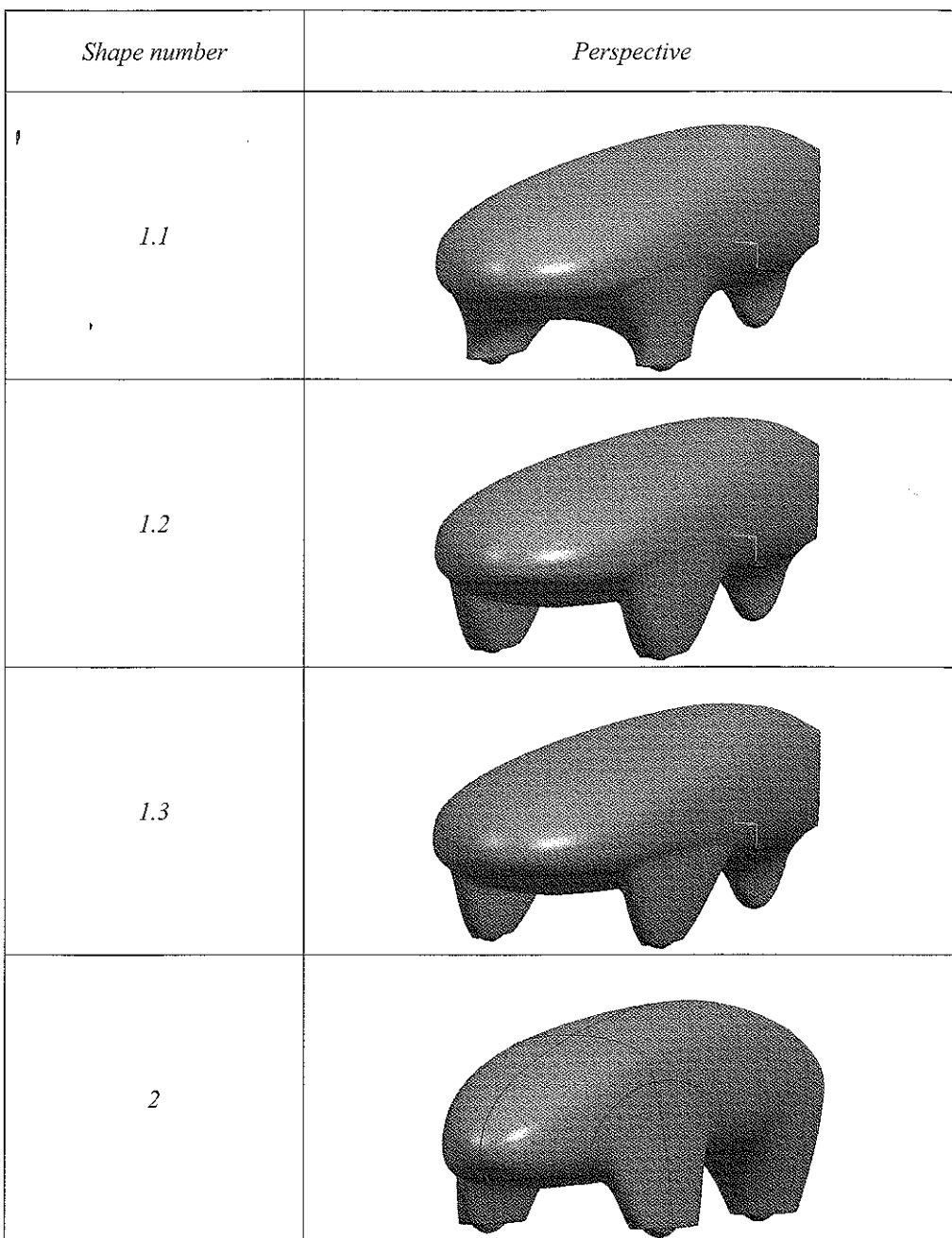


Figure 5-19: Comparison of the body shapes at various stages of the design process.

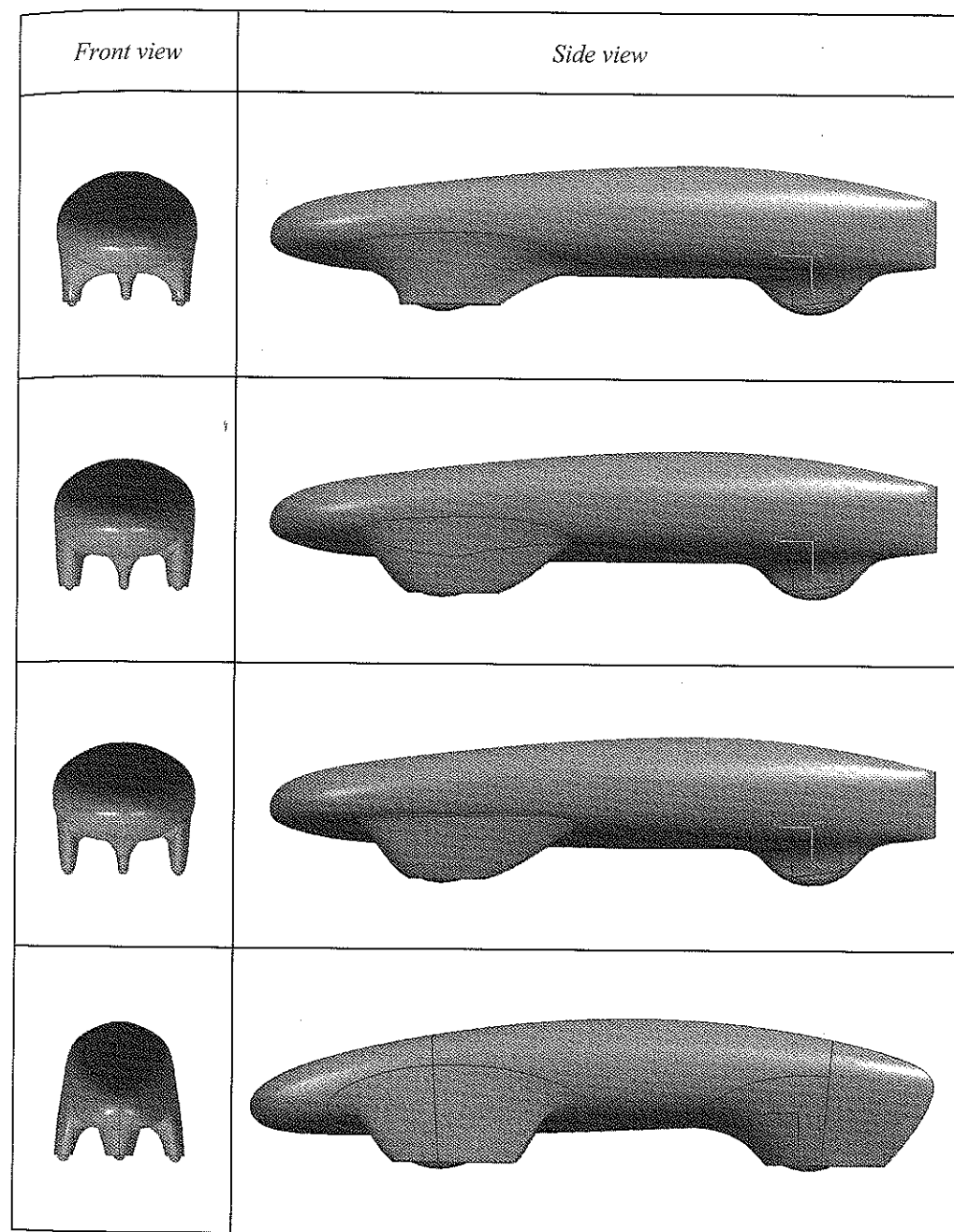


Figure 5-19 (continued).

From Shape 2 to PAC-Car II

Given the satisfactory aerodynamic qualities of Shape 2, the team decided to use this shape for PAC-Car II. Only small millimetric changes (e.g., slight modifications of the surface curvature to influence the lines of reflection) were made. These changes had no significant effect on the aerodynamic quality of PAC-Car II.

5.3. Aerodynamics of the PAC-Car II

This section provides a general overview of PAC-Car II's aerodynamic characteristics (Sections 5.3.1). Specific design elements are explained in detail in Sections 5.3.2, 5.3.3 and 5.3.4, and some wind tunnel trial [19] results are reported and compared with those produced with the wind tunnel model. The additional PAC-Car II aerodynamic improvements, and their benefits as shown by the wind tunnel trials, are discussed in Section 5.3.5.

5.3.1. Overview

As mentioned in Section 5.2.1, PAC-Car II is streamlined in order to achieve the best aerodynamic properties. Seen from above (Figure 5-20), the vehicle looks like a tear drop.

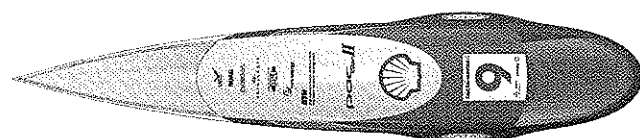


Figure 5-20: Top view of PAC-Car II.
(Courtesy of Tribecraft AG, Zurich)

As recommended in Section 5.1.3, the sides of PAC-Car II are slightly cambered to achieve zero-lift properties (Figure 5-21).

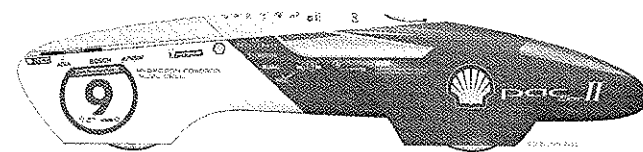


Figure 5-21: Side view of PAC-Car II.
(Courtesy of Tribecraft AG, Zurich)

In keeping with aerodynamic principles, the overall surface of PAC-Car II is very smooth to reduce the effect of side winds.

The overall aerodynamic characteristics of PAC-Car II are given in the table below:

Table 5-2: The aerodynamic characteristics of the PAC-Car II.

Frontal area (from Shape 2, scale 1:1) [m^2]	0.254
c_x (from PAC-Car II wind tunnel trials) [-]	0.075
Cruising speed [km/h]	30
Vehicle length [m]	2.8
Re_L [-]	1.6×10^6

5.3.2. Wheel fairings

As explained in Chapter 7.2.1, wheels have considerable influence on a vehicle's overall aerodynamic quality, making it worthwhile to pay special attention to this element. As recommended by Tamai [18] and Carroll [20], the wheels of PAC-Car II are covered by wheel fairings, the light-weight drag-reducing pieces covering the gaps and spaces created by the wheels. The wheel fairings used in PAC-Car II can, from an aerodynamics point of view, be compared to airplane wings. These wheel fairings are described more in detail below.

Junctions

Figure 5-22 shows the junctions between the wheel fairing and main vehicle body. These junctions are smooth, in order to reduce the interference drag caused by the gap between the two parts. In addition, the radii of the rounded junctions are fairly small, in order to avoid increasing the frontal area too much.

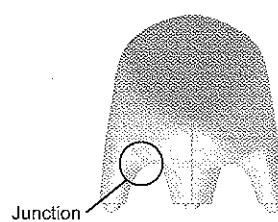


Figure 5-22: Junction between wheel fairing and main vehicle body.

Cross-sections

The cross-sections of the wheel fairings, perpendicular to the wheel's plane of symmetry, are streamlined for the same reasons as the main vehicle body. There is a round nose and a sharp closing edge where the air streaming around the profile meets again. The angle Φ between the direction of the incident airflow and the tangent of the profile's rear end should not be too large; otherwise, the pressure gradients become too high, especially in the event of side winds, and the risk of flow separation increases. Figure 5-23 shows the angle Φ for an airfoil.

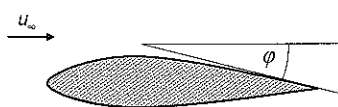


Figure 5-23: Trailing-edge angle.

For PAC-Car II, these wheel fairing profiles are symmetric because the wind direction distribution during the race is symmetric. According to the CFD results, making the wheel fairings symmetric was probably not the best choice for two reasons:

- A small separation area occurs behind the rear edges of the front wheel fairings, even at a 0° yaw angle. Figure 5-24 shows the velocity distribution in the x-direction at 0° Yaw. The blue fields signify zones with higher velocities, and the red ones, zones with lower velocities. Black fields depict the zones where the flow streams backwards, indicating flow separations that increase aerodynamic drag. It is, however, difficult to quantify the influence of this additional drag.

- A Venturi effect exists between the two front wheel fairings, the main vehicle body and the ground. This narrowing cross-section causes a higher velocity and lower pressure in this area, which generates a downforce and additional rolling resistance.

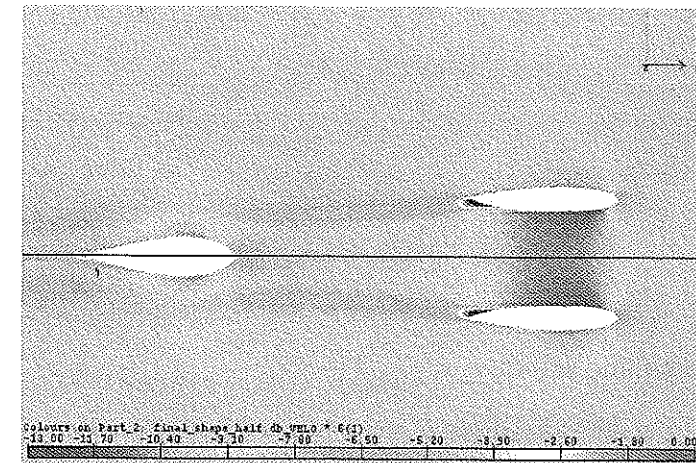


Figure 5-24: Velocity distribution around the wheel fairings of Shape 2.
(Courtesy of RUAG)

As mentioned above, it is difficult to quantify the additional drag resulting from the wheel fairing asymmetry. In any case, the design for the wheel fairings could be improved, possibly by cambering the fairings slightly, as shown in Figure 5-25. Another possibility would be to extend the wheel fairings in the x-direction to reduce the trailing-edge angle, thus decreasing the risk of flow separation. Of course, doing so would most likely increase friction drag because of a larger wetted area. CFD analysis can help to evaluate these kinds of relative improvements. In addition, since CFD analysis is less costly and time-consuming than wind tunnel tests, it would also make it possible to perform a larger number of model iterations.

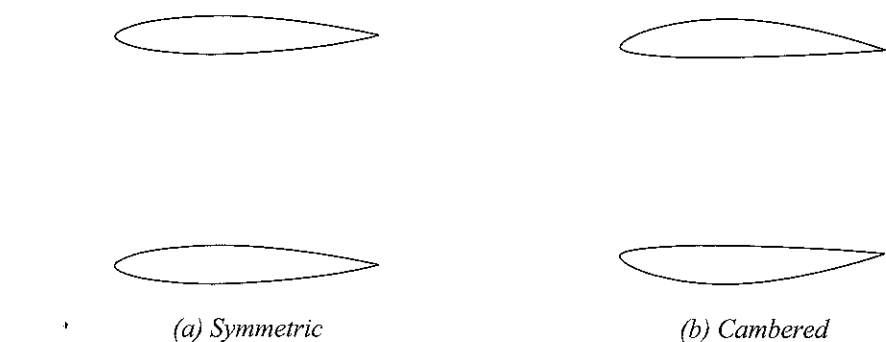


Figure 5-25: Front wheel fairings.

5.3.3. The sailing effect

In the event of a side wind from a given yaw angle β , the shape of PAC-Car II behaves like an airfoil placed at an angle of attack. If the flow over the body is attached, it generates lift normal to the flow direction (Figure 5-26). As long as the x-component of the induced drag is small enough compared to the x-component of this lift, the resulting force has a positive component in the x-direction, called the sailing force. However, the y-component of the lift will make the vehicle drift. To drive straight ahead, this drift must be counteracted by the tires and the steer wheel, which causes additional rolling resistance. Since we did not investigate this drift factor further, we don't know if the sailing effect has a positive consequence that would help to drive the vehicle.

The sailing effect occurs only in a specific range of angles of attack. When the angles are too high, the flow separates, decreasing the lift and increasing the drag dramatically. Enlarging the sailing area in order to increase the sailing effect results in enlarging the wetted area, with the consequent increase in friction drag. Additional model iterations could help discover if the sailing effect can be optimized, and if so, how far. Subsequently, the lateral section of the PAC-Car II wheel fairings could be varied, and the effect of the variation could be measured or simulated at different angles.

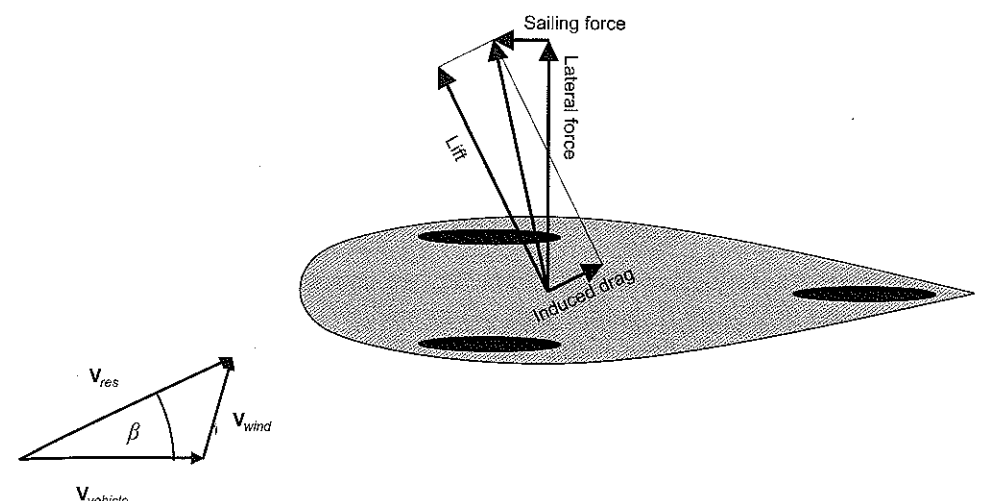


Figure 5-26: Sailing effect.

5.3.4. Rear-view mirrors

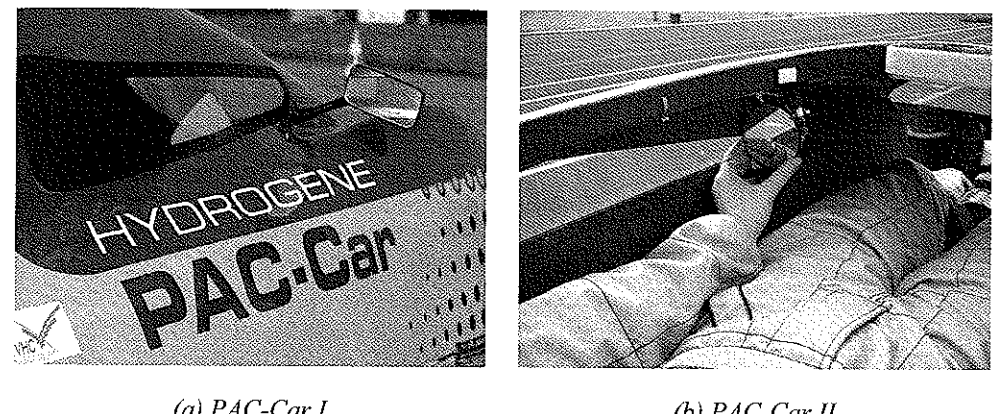


Figure 5-27: Rear-view mirrors.

The race regulations require two rear-view mirrors in order to insure an adequate view of behind the vehicle (Section 6.1). Ideally, these mirrors should be integrated into the body shape (Figure 5-27). Based on the results of wind tunnel tests carried out with PAC-Car I, we estimated that adding two external rear-view mirrors to PAC-Car II would have increased its aerodynamic drag by over 50%.

5.3.5. Final improvements

Surface quality

A smooth vehicle surface is very important because it facilitates laminar flow on a larger wetted area. Since the aerodynamic drag of laminar flow is lower than that of turbulent flow, the gain could be appreciable.

To investigate the influence of this parameter, we carried out several wind tunnel tests with the PAC-Car II before and after applying polish. We managed to improve the aerodynamic drag of the vehicle by 4% with successive applications of "High-Tech Fahrzeugpflege – Protect All" polish.

The gap between the canopy and the vehicle body



*Figure 5-28: Closing the gap between canopy and the body [19].
(Courtesy of Christian Hübner and Manuel Lengg)*

The PAC-Car II's canopy and its body were made of two different materials. To guarantee safe rearview visibility, the canopy was made from a large transparent pane of Plexiglas. The vehicle body, on the other hand, was made of carbon-fiber reinforced plastic (CFP). These two materials have different thermal expansion coefficients, leading to different materials deformations, and thus a gap of a few millimeters between body and canopy. As explained in Section 5.1.2, such gaps generate interference drag. To reduce this drag, the gaps were closed with tape as shown in Figure 5-28. The results of our wind tunnel tests show that closing this gap reduced the aerodynamic drag by another 4%. Since the race regulations insist that the pilot be able to open the canopy without any help (Section 1.3), several layers of tape were applied to make the edge more rigid and then the tape was cut along the gap with a sharp knife. This thin cut had a minimal effect on the drag.

The wheel openings

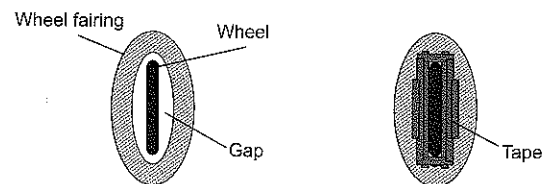


Figure 5-29: Closing the original wheel fairing with tape.

Since openings in the outer shell of a vehicle cause additional aerodynamic drag, we tried to avoid them where possible. The only openings in the PAC-Car II shell are caused by the three wheels. The gap between the wheels and the body was reduced to the minimum with tape as shown in Figure 5-29. Wind tunnel tests on PAC-Car II showed that the tape decreased the aerodynamic drag by 0.6%. Nonetheless, driving tests and races have shown that the pilot still has plenty of fresh air, which is important given the high temperatures that can result from sunshine.

5.3.6. Conclusion

The aerodynamic drag coefficients for PAC-Car II (Shape 2) are plotted in Figure 5-30 for a variety of yaw angles:

- wind tunnel model of Shape 2 (scale 1:2);
- PAC-Car II without final improvements; and
- PAC-Car II with the improvements mentioned above.

In the chosen coordinate system, negative c_x values indicate drag. The curve for the optimized PAC-Car II has the same shape as the one for the Shape 2 wind tunnel model, which suggests that the final improvements to the PAC-Car II vehicle had a greater effect than expected.

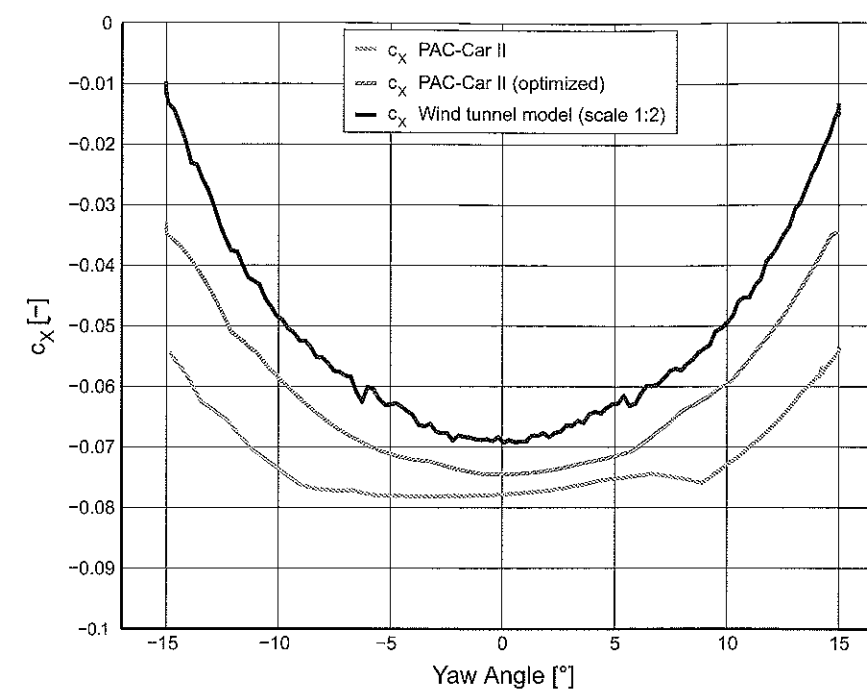


Figure 5-30: The Shape 2 drag coefficient c_x plotted for various yaw angles: the wind tunnel model, the initial PAC-Car II and the optimized PAC-Car II.

5.4. Experimental and numerical optimization methods



Figure 5-31: Visualization method: smoke (wind tunnel model 1).

During the aerodynamic development of PAC-Car II, wind tunnel tests and CFD simulations were performed in order to optimize the vehicle's shape. These experimental methods are presented below.

5.4.1. Experimental methods

Wind tunnel testing

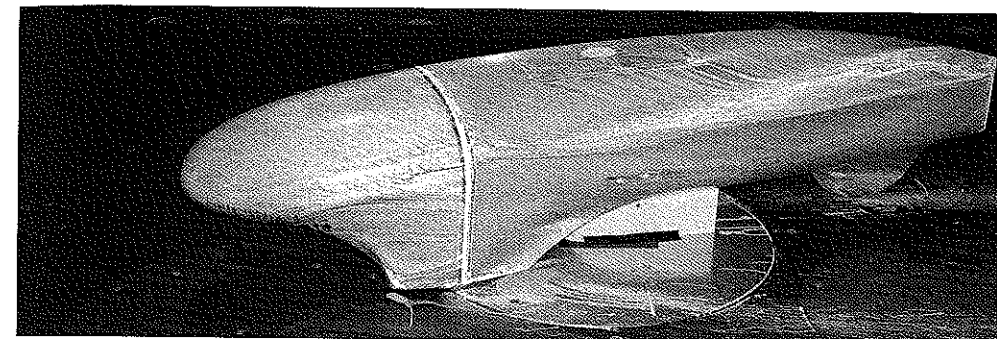


Figure 5-32: Visualization method: titanium white (wind tunnel model 1).

To obtain meaningful results from the wind tunnel tests, the wind tunnel model must be high quality so that the results for the model can be aptly compared to the original vehicle. This implies accurate and professional manufacturing, which is costly and time-consuming. In addition, conducting wind tunnel tests and correctly interpreting the results requires experience. Wind tunnel models for Shape 1.1 and Shape 2 were manufactured on a scale of 1:2. To move from the models to the real thing, the wind tunnel tests had to be conducted under comparable conditions. According to Reynolds similarity law, the Reynolds numbers of the model and the real car must be equal:

$$Re_{model} = Re_{original} \quad (5.5)$$

Assuming equivalent air properties for both the model and the original, given the scale, we obtain the following relation:

$$u_{model} = 2u_{original} \quad (5.6)$$

signifying that, when testing the 1:2 models, the air velocity in the wind tunnel must be double the air velocity for the original vehicle.

Different methods were used in order to visualize the airflow around the vehicle: smoke (Figure 5-31), titanium white (Figure 5-32), wool strings (Figure 5-33 & Figure 5-34) and a stethoscope (Figure 5-35).

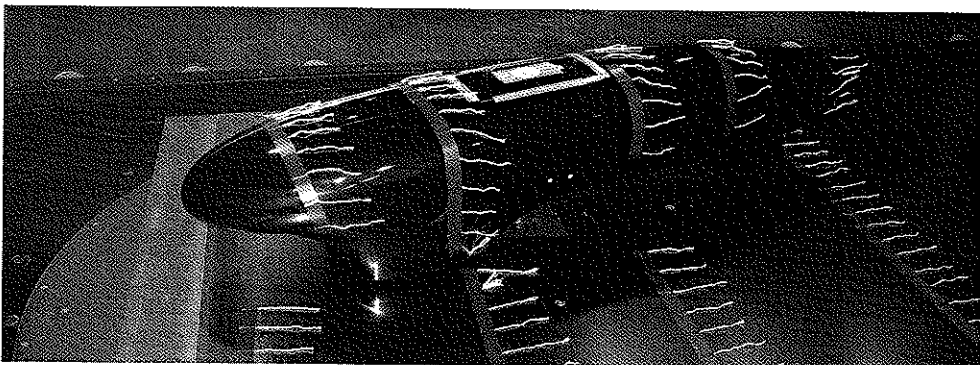


Figure 5-33: Visualization method: wool strings (wind tunnel model 1).

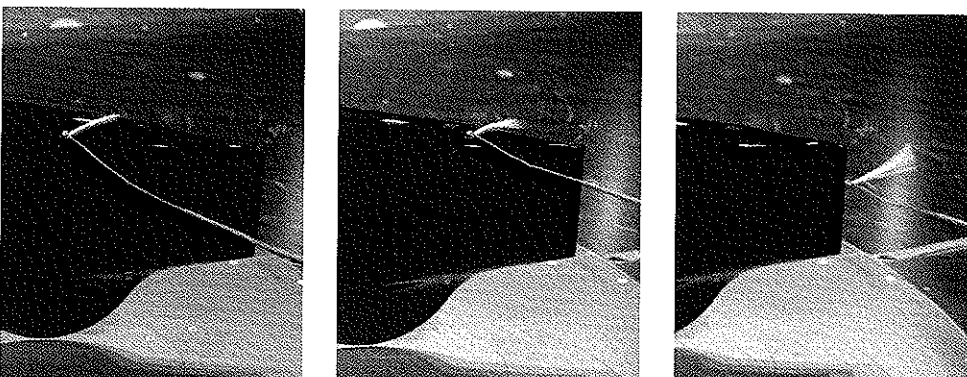


Figure 5-34: Visualization method: a wool string at the end of a pole (wind tunnel model 1).

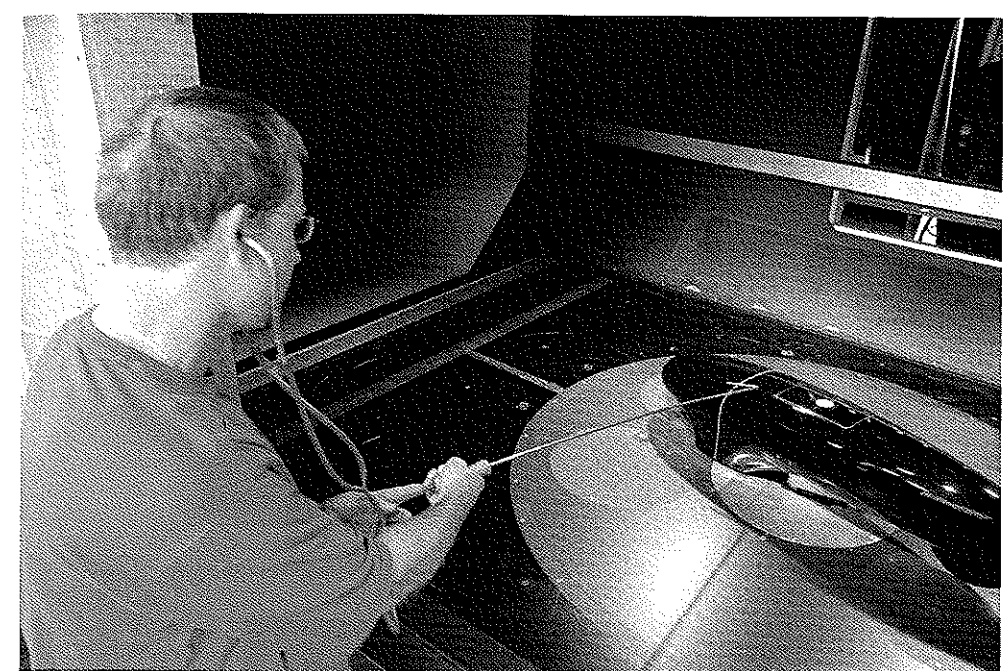
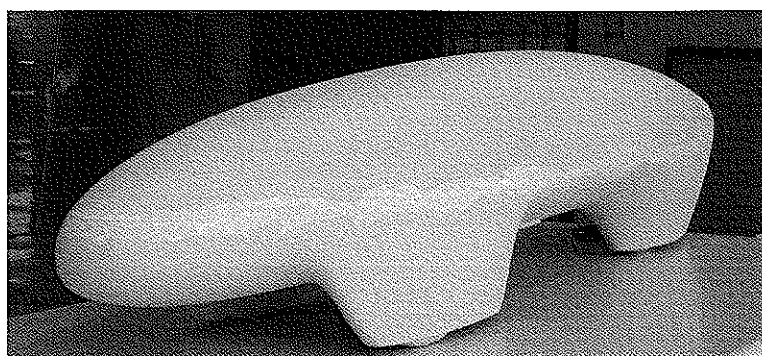


Figure 5-35: Visualization method: a stethoscope to detect local boundary layer types (wind tunnel model 1).

Manufacturing the wind tunnel models

The wind tunnel models for PAC-Car II were manufactured from polyurethane foam with a density of 400 kg/m^3 . This density offered a good trade-off between cost, weight, and milling capacity. The models were milled on a CNC milling machine based on a 3D CAD model. After milling (Figure 5-36), a finish was applied to the models (Figure 5-37), the pores were closed with a spatula, and the model edges were beveled. After that the models were painted black to facilitate the visualization of the air flow in the wind tunnel.



*Figure 5-36: Wind tunnel model 2 after milling.
(Courtesy of Esoro)*

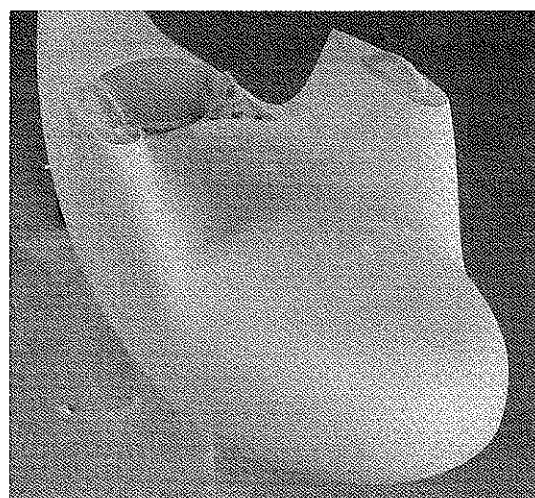
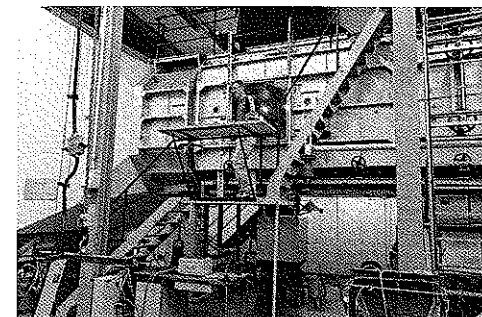


*Figure 5-37: Wind tunnel model 2 during the finishing procedure.
(Courtesy of Esoro)*

Wind tunnels

The wind tunnel tests for PAC-Car II were carried out in the Institute of Fluid Dynamics' wind tunnel at ETH Zurich (Figure 5-38) and in the automotive wind tunnel of RUAG Aerospace, a PAC-Car II partner (Emmen, Switzerland). The

wind tunnel at ETH Zurich is a closed-circulation wind tunnel. Different six-component balances allow the aerodynamic forces and torques acting on the model to be measured, while continuously varying the model's attitude (pitch, yaw). The wind tunnel at RUAG Aerospace, on the other hand, is an Open Jet wind tunnel with a rolling floor. It was specially designed for 50% race car models.



(a) Outside view



(b) Inside view

Figure 5-38: The Institute of Fluid Dynamics' wind tunnel, ETH Zurich.

Embedded wind direction and speed sensors

In 2004, PAC-Car I was equipped with an embedded data acquisition system wired to several sensors. The idea was to collect as much information as possible about the different parts of the vehicle, such as the fuel cell system (e.g., flow, pressure, temperature, voltage, current) and the power train (e.g., velocity, voltage, current), as well as the vehicle itself (e.g., velocity, acceleration, steering angle, track position).

Two aerodynamic sensors were included in this system: a wind direction sensor and a wind speed sensor.

The wind speed sensor, a Schiltknecht MiniAir6, measures the air flow using a freely-turning propeller. This sensor delivers a voltage proportional to relative air speed.

The wind direction sensor consists of a vane mounted on a low-drag torque (about 0.5 g.cm) contactless 360° continuous rotary potentiometer, Sicovend⁴ CP-2U-33.

⁴ www.sicovend.ch

The sensor delivers a voltage signal that looks like a sinusoidal function of its angular position.

An example of the graph resulting from the post-processing of the data provided by these two sensors is shown Figure 5-11.

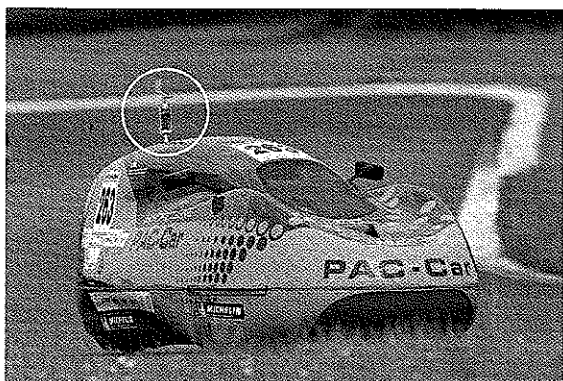
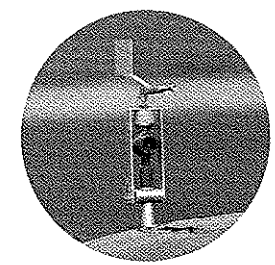


Figure 5-39: Wind direction and wind speed sensor mounted on PAC-Car I.



5.4.2. Numerical methods

CAD software

The CAD program used to design the shape of PAC-Car II and the preliminary wind tunnel models was Unigraphics NX 2. This CAD system, which allows fully parametric modeling, has very good free-form modeling capabilities.

CFD software

The CFD software used during the aerodynamic design process was a Navier Stokes Multi-Block Solver, developed by CFS Engineering, (Lausanne, Switzerland). This software uses structured grids for calculations. The grids for PAC-Car II were produced with ICEM⁵ mesh generation software at RUAG Aerospace. (Further information on the use of CFD during the PAC-Car II aerodynamic design process can be found in [21].)

⁵ www.ansys.com/products/icemcfds.asp

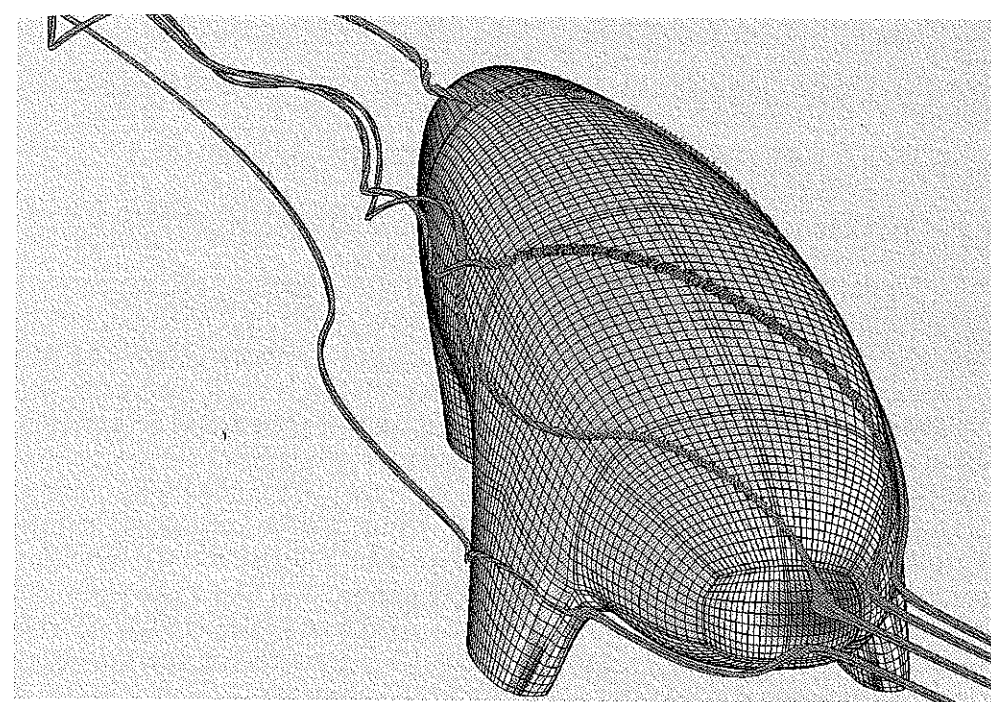


*Figure 5-40: Shape 2 in CFD.
(Courtesy of RUAG)*

5.5. Conclusion

Our team was quite satisfied with the aerodynamic results of the PAC-Car II. However, there is clearly still room for improvement. Additional CFD model iterations, validated in the wind tunnel, could improve the shape of PAC-Car II. As mentioned above, a lot of effort was expended to keep the outer dimensions as small as possible, without decreasing the aerodynamic quality of the vehicle. A next-generation PAC-Car could be even a little smaller than the current version. In retrospect, our detailed investigations of the vehicle topology were very important. The use of 1:1 mock-up models (Section 5.2.1) was also very helpful for identifying the correct boundary conditions. The use of CFD analysis permitted additional model iterations, though it must be mentioned that the absolute results must be handled with care, especially when the friction forces dominate the pressure forces. Still, the relative changes suggested by the CFD simulations were all confirmed in the wind tunnel, proving the value of the tool.

Chapter 6: Vehicle body structure

By Pius Kobler and Nicolas Weidmann.

As the design of PAC-Car II progressed, the range of technical solutions that could still be adopted became narrower and narrower. The shape of the vehicle's body had been fully defined based on aerodynamics (see Chapter 5) and a number of pertinent technical solutions had been implemented: (1) the wheel configuration, defined by such parameters as wheelbase, track width, position of the center of gravity (see Section 4.5), provides sufficient ground clearance and an optimal weight distribution on each wheel, while allowing rollovers to be avoided under normal driving situations, including cornering, passing or obstacle avoidance; (2) the single rear wheel is the unique steer wheel, whereas the two wheels on the front axle are fixed in place and slightly tilted to insure the best trade-off between rolling resistance and aerodynamic drag; and (3) the pilot can be settled in comfortable position, with a good forward field of vision. Nevertheless, a lot of work still had to be done on the vehicle body design: the dimensions of the windshields and windows had to be defined precisely, and the industrial design (i.e., graphic design) of the vehicle exterior had to be determined definitively. At this stage, the body was just a sort of skin that had to be made sufficiently solid and rigid, while meeting two additional design constraints related to weight and manufacturability.

Section 1.1 of this chapter presents our design considerations for two elements related to the pilot's field of vision: the shape of the windshields/windows and the choice and positioning of the rear-view mirrors. Section 6.2 deals with the bodywork design process, involving CAD surface modeling and CAD graphics. Section 6.3 focuses on the finite-element model (FEM) calculations that help to identify the places where the vehicle body must be reinforced in order to carry the required mechanical loads, while at the same time working to limit the vehicle's weight. The last section (6.4) presents the body manufacturing process.

6.1. The pilot's field of vision

The pilot's field of vision was a very important consideration in PAC-Car II project for at least three reasons:

- (1) given that the vehicle body itself is used to carry the loads, without any additional chassis or frame, any holes that are cut in this shell for a windshield,

windows or other openings will make the structure less rigid. Thus, the windshield/window dimensions need to be reduced to a minimum, while still allowing the pilot to see clearly.

(2) clear visibility allows the pilot to better control the vehicle trajectory, which can have a great influence on fuel consumption. Obviously, even the best vehicle is worthless if the pilot is not able to drive it properly.

(3) since the pilot's field of vision is verified for safety reasons during the technical inspection prior to the race, the success of the whole project depends on successfully passing this inspection.

The following sections explain how this factor was dealt with in the PAC-Car II project.

6.1.1. CAD modeling

A first attempt to determine the size of the front windshield was done using CAD (Figure 6-1). The vehicle body, including the front wheels and the pilot in driving position, was modeled. The shortest curve of the track was also modeled, with the vehicle positioned on the inside of the curve. A cone-shaped visibility zone was then drawn, starting at the pilot's eyes and extending to the track. The curve resulting from the intersection between the track and the visibility cone shows the boundaries of the track area that is visible. Likewise, the curve resulting from the intersection between the vehicle body and the visibility cone suggests the boundaries of the windshield. A tradeoff between the two curves then had to be made in order to determine the minimum windshield size that would still provide satisfactory track visibility. Actually, it is the front wheels (here assumed to be opaque disks) that limit the pilot's forward field of vision the most and the shape of the visibility cone helped to take them into account.

The same basic procedure was used for the rear visibility. This time, two cones were modeled, based on the reflected image of both sides of the vehicle as seen in a mirror attached to the canopy in front of the pilot. The size, position, and bending radius of the mirror could be changed by varying the CAD parameters. The two cones revealed the ideal position of the rear window, as well as the part of the bulkhead (i.e., the fire-wall between the pilot and the powertrain) that would need to be cut away to allow it to be set in place.

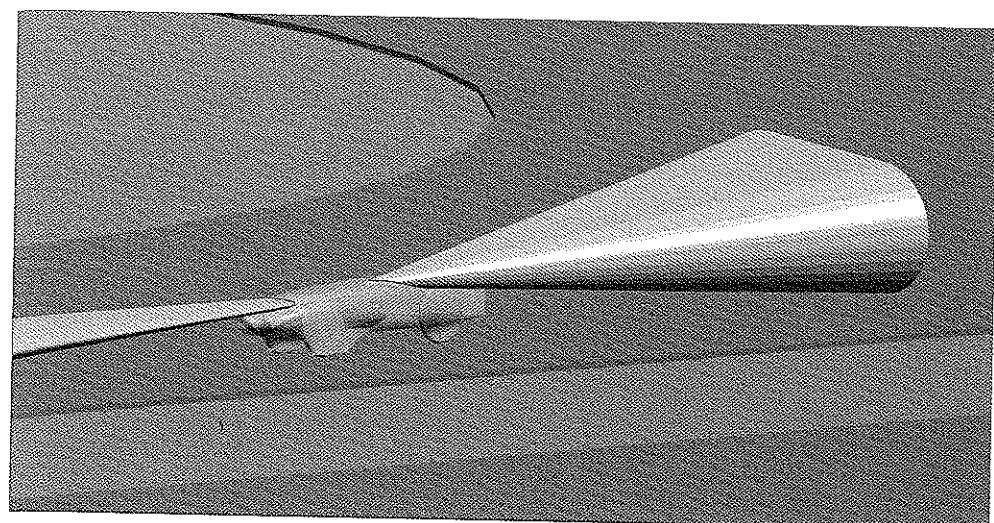


Figure 6-1: CAD model of the pilot's front and rear field of vision.

6.1.2. The vehicle mock-up

The CAD method used to determine the shape of the windshield and rear window could not be used for the side windows since the movement of the pilot's head greatly influences the visibility zone. Thus, the only way to determine the minimum size for the side windows was to build a mock-up (Figure 6-2). In this mock-up, the pilot's seat was made of wooden boards, and the front wheels were made from cardboard. The section of the body surrounding the pilot's helmet was formed of wooden planks with small strips of wood connecting them, so that the pilot's head could move as it would be able to in the real vehicle.

Marks were made on the floor in front of the vehicle to indicate the area visible through the windshield, given pilot head movement, which helped determine how long the side windows would need to be to compensate for the lack of visibility through the front windshield. In addition, it was necessary to comply with the race regulations governing rear visibility, which state that the side windows must be long enough for the pilot to see at right angles to the direction of movement.



Figure 6-2: Mock-up used to define the side windows.

6.1.3. Improvements

For safety reasons, the windshield and rear window were made slightly larger than the minimum. The right and left sections of the rear window were merged to creating one large windshield that would allow the rear powertrain to be viewed from outside of the vehicle.

The visibility through the rear window was greatly reduced by the light reflected off the powertrain. Several attempts at applying an anti-reflective coating were made, but these coatings just decreased the visibility even more, given that all such products are slightly opaque. Finally, a piece of non-glossy black fabric was stretched over the engine compartment, which reduced the reflections so that they no longer affected visibility. This dark fabric had the added benefit of helping to keep the fuel cell system warm when exposed to sunlight.

To increase the field of vision through the rear window, the two small internal windows implanted in the bulkhead were replaced by Fresnel lenses, which expanded the rear field of vision but did not distort the view in a way that would make the pilot dizzy. Concave mirrors, instead of simple flat mirrors, were used to magnify the view seen through the Fresnel lenses.



Figure 6-3: Rear view of PAC-Car II, canopy removed.

Unfortunately, once the pilot began driving the vehicle, we discovered that the rear view was unsatisfactory. A passing vehicle could only be seen when it was right behind the vehicle or driving alongside. To get rid of this blind spot, wide-angle convex mirrors were attached inside the vehicle body in the front of the side windows (see Figure 5-27). These mirrors give the pilot a 360° field of vision (Figure 6-4). These improvements led to the PAC-Car II being judged one the vehicles with the best visibility during the technical inspection, despite the relatively small size of its windshields/windows.

6.2. Vehicle body design process

6.2.1. The perfect vehicle body design

The regulatory, ergonomic, and aerodynamic design constraints helped us define the overall shape of the PAC-Car II. However, creating the “perfect vehicle body” – one that was aerodynamically advanced and met the ergonomic requirements – demanded a great effort in terms of CAD modeling.

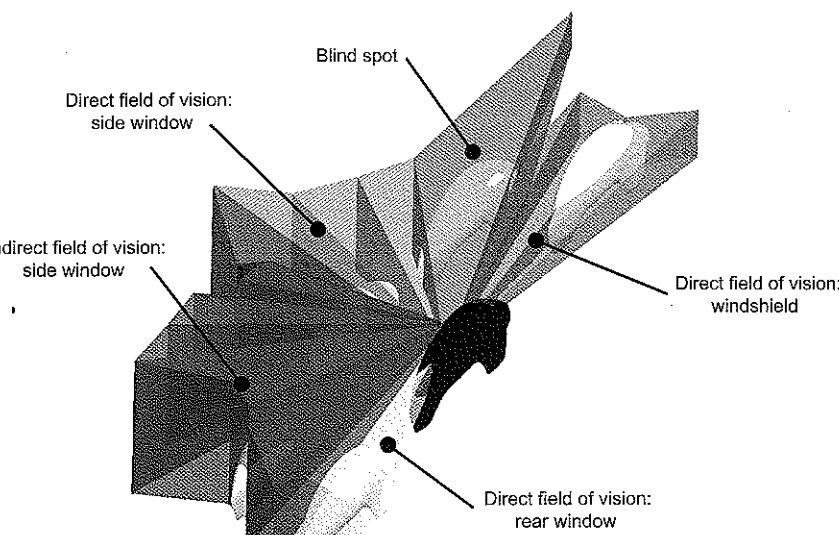


Figure 6-4: PAC-Car II is represented in black. The geometric shapes around it (in colors) correspond to the pilot's fields of vision. The white ovals, representing other vehicles, were used to verify that there would be sufficient visibility.

Class A surfacing

After making the initial conceptual decisions (e.g., about rear-wheel steering and tilted front wheels) and performing the preliminary aerodynamic model iterations (Section 5.3), we remodeled the vehicle body to meet Class A surfacing standards. “Class A surfacing” is a term used in transportation design to describe surfaces with a high esthetic quality, requiring that the surfaces be modeled very precisely with controlled surface modifications. Although esthetic quality was not our main concern, the methods used during Class A surfacing to accurately model and control a freeform surface would allow us to reach our primary goal: a “perfect” vehicle body.

Since the aim was to meet all the design constraints (e.g., available interior space, aerodynamics, industrial design criteria) while maintaining G2 and G3 surface continuity for the outside of the shell, we needed to work on a fully parametric model.

In CAD modeling, the term “continuity” is used to describe the transition gradient between two adjacent curves or surfaces. This continuity is ranked from G0 to G3. G0 refers to two non-continuous curves with matching endpoint positions. G1

curves are “tangentially continuous”, meaning their endpoint positions and angles match, while G2 curves are “curvature continuous”, meaning their endpoints match in position and curvature. G3 curves have “acceleration continuity”, in that the position and acceleration of their endpoints match. Establishing G2 and G3 surface continuity insures that the surface changes over the length of the vehicle body are always as smooth as possible. It’s the best way to control freeform surfaces in CAD-Modeling and is state of the art in automobile engineering.

We chose a modeling strategy that would allow us to control the curves and surfaces of all the important vehicle body parts, working from the trunk to the nose and from the trunk to the tail. These curves were finetuned using a curvature analysis tool, called a curvature comb, to insure the derived surfaces were correct. The outer body shell was then optimized several times using the parametric model and controlled using different surface analysis tools.

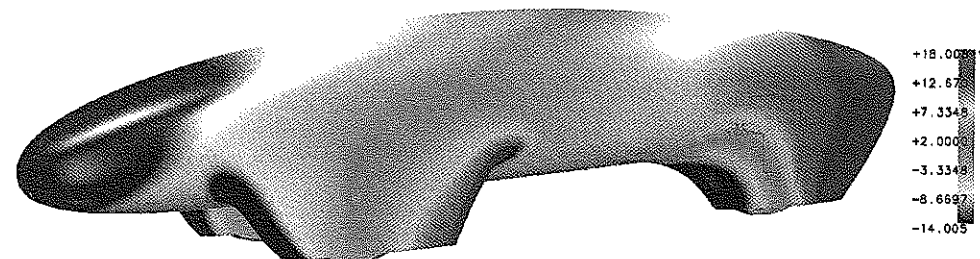


*Figure 6-5: Surface analysis: slope distribution.
(Courtesy of Tribecraft AG, Zurich)*

Cutlines

The positions and approximate sizes of the windshields/windows and the canopy were chosen (Section 1.1) based on the regulations and the ergonomic constraints. The key concern was then integrating them into a consistent design theme. As the body shape can be described as sleek and tense, we decided to define all physical and graphic cutlines using straight planes that penetrate the body to produce pure, dynamic curves – which would best suit the image we wanted the vehicle to have. This also meant that there we would not have to deal separately with graphics later on, as they would be an integral part of the vehicle body’s look.

6.2.2. Vehicle perception

Right at the start of the project, we began thinking about the character of PAC-Car II and the way it should be perceived.

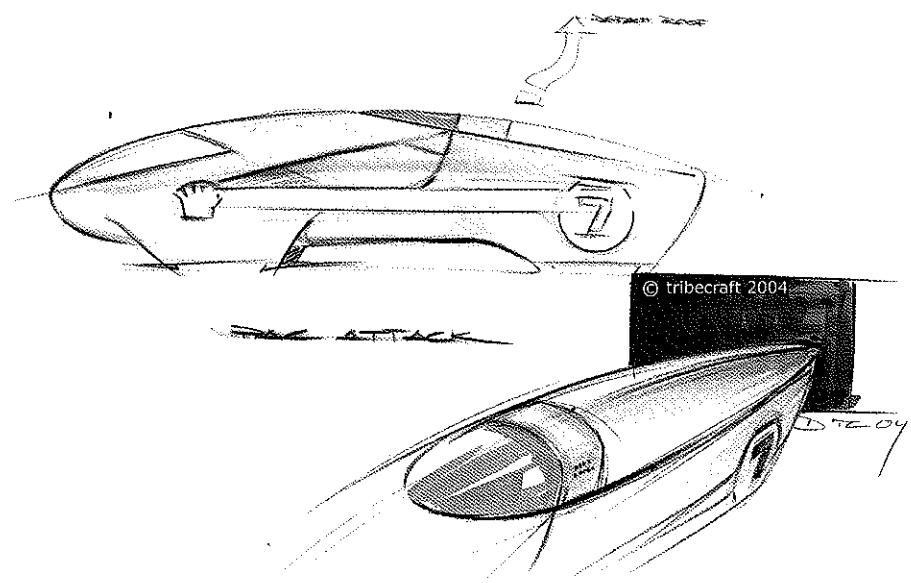


*Figure 6-6: Proportions and accent study.
(Courtesy of Tribecraft AG, Zurich)*

Character

The goal was to reproduce the sporty character of a long distance runner. Since it was hydrogen propelled, we wanted PAC-Car II to look cool and clean, technologically advanced, intelligent but yet likeable. The colors – a warm grey and a cold blue – support this aim. The vehicle's friendly proportions are reinforced by strict, straight graphic lines separating the colors and creating tension.

Graphics

The Shell Eco-marathon regulations define exactly how and where the various logos need to be placed. Our main objective was to avoid scattering patches of

color and graphics all over the vehicle. This was accomplished by integrating all the graphic elements into the overall design theme, distinguishing the pre-defined colored stickers of the official race sponsors from the monochromatic partners and sponsors of the PAC-Car II project.

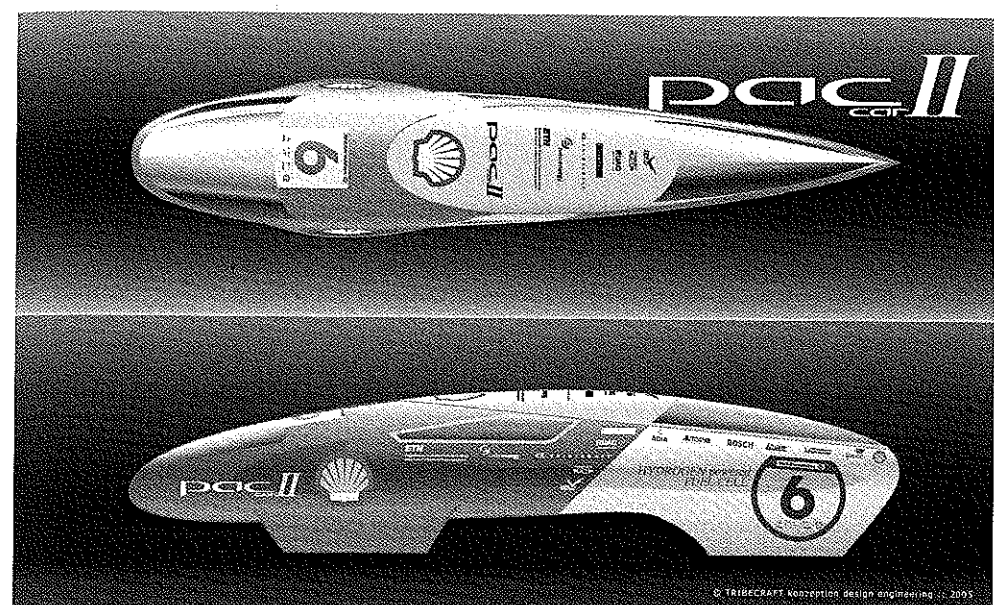


*Figure 6-7: Graphic layout and surface subdivision.
(Courtesy of Tribecraft AG, Zurich)*

The vehicle's graphics concept integrates the pre-defined official stickers both in terms of color and layout: the scallop shell logo of the Shell Group draws attention to the wheel area and the colorful sponsor stickers run along the top standing out clearly on the white background. The monochromatic partner logos work together to calm down the visual complexity.

Special attention was given to details like window outlines, as they help the vehicle to be seen as one object, despite the graphic separations.

Corporate design

The Shell Eco-marathon is not a typical race; it is an event. To embody the spirit of the team, the vehicle, its logo and the shirts all had the same basic corporate design. We believe that this strong attention to esthetics underlined the team's commitment to setting the world record and made it easier to obtain media attention, which in turn helped the team and the partners to communicate their dedication to that goal.

6.3. Structural optimization of the body

The vehicle body of PAC-Car II is like an insect exoskeleton: it carries the loads without any additional chassis or frame. This solution was chosen in an effort to reduce the vehicle's weight. Since it is the outermost part of the vehicle, the body shell has the highest potential for increasing vehicle strength by increasing its rigidity. The main drawbacks to this solution are: (1) restricted potential for modifications, due to the high level of component integration; (2) poor accessibility of internal parts; and (3) a narrow opening for the pilot to enter the vehicle.

This section describes the method used to analyze the body's load flows and to determine the correct quantities, global and local, of composite materials.

6.3.1. The optimization method and tools

We originally planned to perform a parametric optimization based on evolutionary algorithms to optimize diverse parameters (e.g., material properties, wall thickness and laminate lay-up angles) prior to using FEM for a structural optimization. Regrettably, lack of time made using this powerful method impossible.

Instead, we used a pragmatic method to optimize the body structure. A FEM model was set up, in which such parameters as wall thickness or material properties were varied manually between succeeding calculations. Given our industrial partners' experience and knowledge in choosing material and analyzing FEM model behavior, the minimum structure for the vehicle body was quickly estimated.

All FEM calculations were done using the software, Ansys 8. The CAD data were transferred from Unigraphics NX II⁶ to Ansys using Parasolid files.

6.3.2. Load cases

Of the many situations PAC-Car II would be in, the following are the most critical for the body structure: (1) during transport and work on the vehicle; (2) during the pilot's ingress; (3) during the technical inspection; and (4) during cornering.

(1) The loads born by the vehicle during transport or maintenance situations (e.g., when the vehicle is being lifted or people are leaning on it) should not be underestimated. Some areas of the vehicle body will need to be reinforced to

⁶ Unigraphics NX II is a registered trademark of UGS Corp. (Plano, TX, USA); www.ugs.com

withstand the load, even though this reinforcement is not necessary to the vehicle's race performance.

(2) During ingress into the vehicle, the pilot's weight is concentrated in a small area in the center vehicle body floor. In fact, the pilot is by far the heaviest load that the PAC-Car II has to deal with (i.e., one and half time the vehicle's weight), making this load case the most critical in terms of the body strength.

(3) During the technical inspection, the vehicle needs to brake on a ramp with a 15° slope, which causes the forces on the brake and the point of fixation of the rear wheel to reach their maximum value.

(4) When the vehicle is cornering, centrifugal force twists the entire vehicle body due to the use of a single rear wheel. Though this load case is not critical in terms of body strength, the vehicle displacement nonetheless must be kept low enough to avoid tilting the rear wheel, which would increase the rolling resistance force (see Chapter 4).

6.3.3. Boundary conditions

Loads

As mentioned above, some of the most critical loads occur when the vehicle is lifted (e.g., hands could break the thin laminate in the front of the vehicle) and when someone is leaning on the rim while working on the inside of the vehicle. We discovered the solution to these risks without using FEM calculations. In fact, the basic laminate used to manufacture the vehicle body is strong enough to withstand the forces caused by people leaning on the vehicle or hands lifting it up. Reinforcing the rim to make the body more rigid (Section 6.3.5) makes it strong enough to withstand both these loads and the one caused by the pilot's hand grip while stepping into the vehicle.

The most critical load during the pilot's ingress into the vehicle occurs at the moment when all the pilot's weight is concentrated on one foot on the floor of the vehicle. At this moment, the laminate on the bottom of the vehicle is stressed locally around the foot and the entire vehicle body bends due to this heavy load in the middle. The load of the pilot during ingress was simulated for one foot in the vehicle (i.e., attached to the nodes of the FEM model in the area where the foot would touch the vehicle body) and for both hands on the rim (i.e., pilot weight evenly distributed over both hands). The force vectors of these loads are illustrated in Figure 6-8. The force vectors behind the bulkhead are the forces of the fuel cell system acting on the vehicle body.

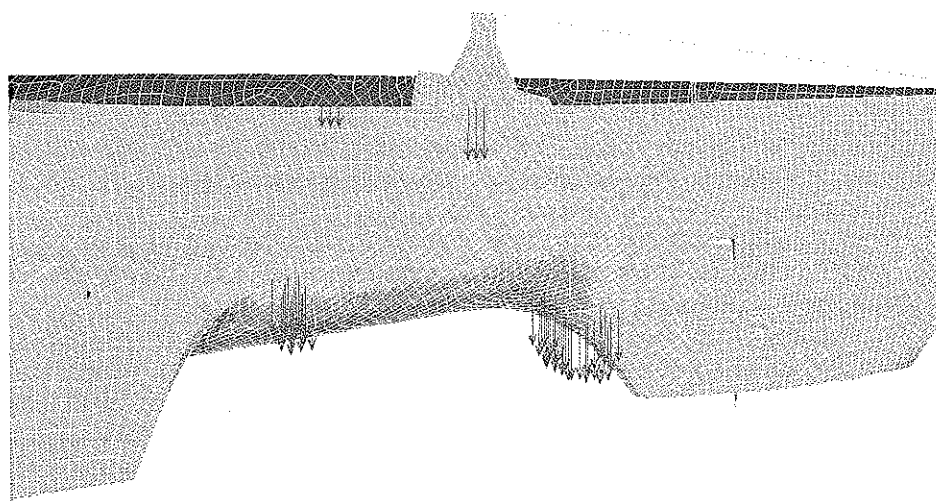


Figure 6-8: Loads applied during pilot ingress into the vehicle. (Force intensities do not correspond to arrow length.)

The force of the brakes during the technical inspection was modeled to act on the nodes of the strengthening strut to which the brakes were later attached. The force transmission between the brakes and the vehicle body did not need to be modeled in detail, as the global reaction of the body to the brake forces is the essential point of these calculations. The weight of the pilot in the supine position is spread over the nodes corresponding to the entire contact surface between the pilot's back and the vehicle body.

The main forces acting on the vehicle body when it is being driven in a curve are displayed in Figure 6-9. The forces from the pilot and the fuel cell system are now acting in y (centrifugal forces) and in z (gravitational force) direction.

Degrees of freedom

The reduction in degrees of freedom applies to the points where the wheels touch the ground. The front wheels and the front axle were considered as one very rigid unit in the FEM model, using only the wheel and axle surface measurements to avoid volume calculations. Consequently, the forces are transmitted from the tire-road contact point to the points where the axle attached to the vehicle body. The rear wheel was not modeled; it was replaced by a construction of beam elements, with the same static properties (see Figure 6-10).

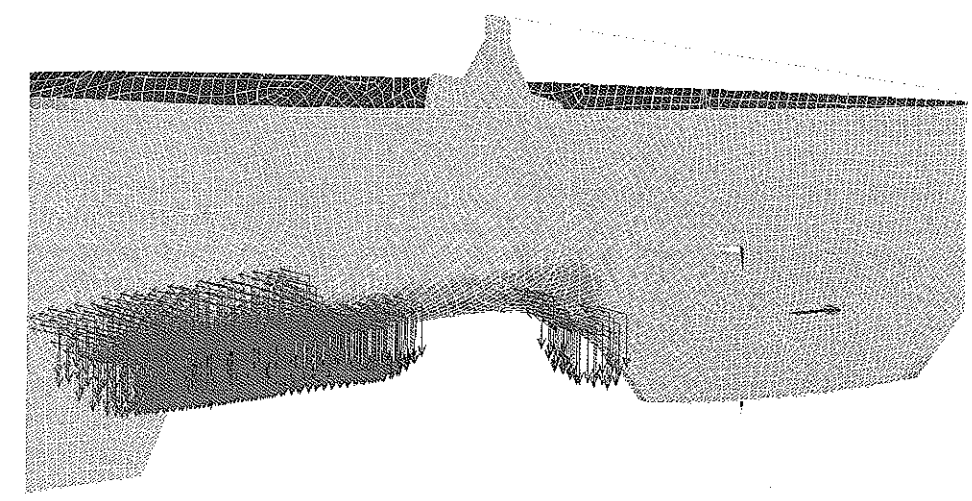


Figure 6-9: Main forces applied on the vehicle body while the vehicle is cornering.

The degrees of freedom are similar in all the load cases. The front wheels are locked in the z and y direction at the point of tire-road contact. The degree of freedom in the direction of movement (x) remains free to simulate the rolling of the wheels, though it could also be locked at the rear wheel by assuming locked brakes. To simulate this condition with the beam construction presented in Figure 6-10, the nodes on top of the construction (i.e., where three beams meet and where the construction is attached to the horizontal strut) need to be locked in the x direction.

6.3.4. Materials

Sandwich construction

A first FEM model calculation, with the vehicle body consisting of a thin base laminate only, showed buckling at the rear, where the struts to which the rear wheel will be attached are located, and movement of the side walls around the side windows, with a maximum displacement at the front of the side windows. To avoid the buckling and reduce the side wall movement, the vehicle body was partially reinforced with a sandwich laminate, as shown in purple in Figure 6-11.

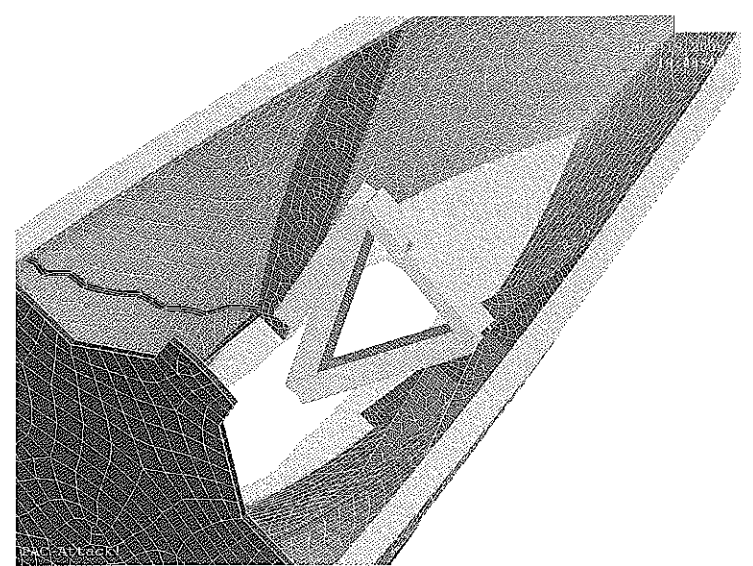


Figure 6-10: Beam construction used to simulate the rear wheel.

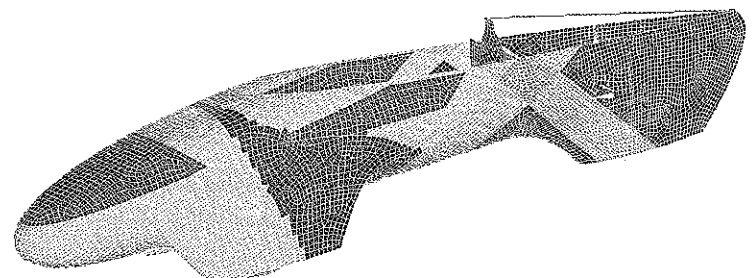


Figure 6-11: Materials distribution.

UD-straps

The lateral forces in the load case of a cornering vehicle caused the vehicle body to twist, as the rear part was pushed outwards by centrifugal force. To increase the body's torsional rigidity, two straps of unidirectional (UD) fiber material were laid around the body (one towards the front, one towards the back), starting at the top of

the vehicle near the place where the bulkhead is attached and reaching to the bottom of the vehicle (see Figure 6-11).

The improvements provided by the sandwich laminate and the UD-straps improved the performance of the vehicle body satisfactorily, but the manufacturing process to implement these solutions was too complicated to justify the procedures, given the relatively small increase in rigidity obtained. Since it is not flexible enough, the foam material in the core of the sandwich laminate would have needed to be broken into many small pieces to conform to the twice cambered surfaces. The gaps between these foam parts would have then needed to be filled with resin, which would have made the sandwich laminate much heavier than a carbon-reinforced laminate. In the end, the decision was made to reinforce the entire vehicle body with carbon-reinforced laminate only. Esoro AG, one of the PAC-Car II partners, has been designing bodies similar to the PAC-Car II body for years, and their experience indicated that a body of carbon-reinforced laminate would be light enough for a FEV, while still providing the necessary rigidity. The result was a vehicle body that was sufficiently strong and rigid, but a little bit heavier than the lightest possible version that would have been possible with further FEM calculations. Thus, potentially, the weight of the PAC-Car II could be reduced even further in the future.

Body sections

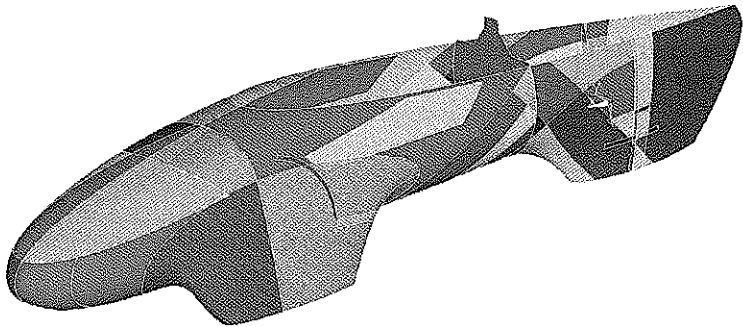


Figure 6-12: Sections of the vehicle body model.

The vehicle body had to be divided into sections with different material properties. For example, the area where the two UD-straps cross each other has more layers than the areas where only one strap lies, or the area surrounding the straps. The surface area of the body was already divided into these sections in the CAD model. After cutting all the surfaces for sectioning and avoiding the T-problem (see

Section 6.3.5), the model of the vehicle body looked like a big patchwork quilt (Figure 6-12).

6.3.5. Meshing

Surface method

To minimize computation time, all FEM calculations were based on the surfaces in the CAD model, meshed with body shell elements. Only these surfaces were imported into Ansys from the CAD model for the bulkhead, the struts for attaching the rear wheel, the skin of the vehicle body, and even for the front wheels on the front axle.

T-problem

Since Ansys 8 does not support automatic mesh recognition, the T-problem can occur. For example, a strut attached in the middle of a surface does not share nodes with this surface in the FEM model. In this case, the T-problem occurs if the surface does not have an edge where the strut is connected, and therefore no forces can be transmitted from the strut to the base surface.

To avoid this problem, the surface needs to be cut apart where the strut is connected. At the two ends of the strut, the surface must then be cut again to obtain the strut length with the new edge. This strut is now surrounded by four surfaces instead of one, and the edge of the strut and the new edge of the surface then need to undergo the same fragmentation with a predefined element size. After remeshing both the strut and the surrounding surfaces, the elements of the strut fit together with the elements of the base surfaces.

Element types

Most of the model is set up using the surface method. The mesh of these surfaces consists of Shell181 elements. A laminate lay-up can be defined for these elements, including thickness and orientation angle for every laminate layer, which allows the carbon-based laminate, the steel (e.g., front wheel axle), and the sandwich laminate to be modeled using only one element type.

Only the rim along the junction with the canopy, the rim around the windows (which must be thicker due to manufacturing constraints), and the beam construction simulating the rear wheel are modeled with Beam188 elements. A cross section can manually be defined for these elements, using a U-shape for the main rim and a rectangular shape for the window rims and the beam construction.

6.3.6. Results

Maximum stress and strain

Due to the vehicle's low speeds and light weight, the loads on the vehicle body are small compared to the loads on a passenger car or a racing car. These small forces do not deform the vehicle body critically. The strain does not exceed 0.3 % on any part, which guarantees that the materials used are not stressed up to their limits.

Deformations

The deformation of the side walls and the twisting of the vehicle body while cornering (Section 6.3.4) are the critical points for the body design. For this reason, a greater rigidity than strictly needed for material safety was required. For the cornering load case, a maximum displacement of 30 mm was set for the nodes located at the point where the rear wheel is attached, and the body structure was then optimized to stay within this limit.

6.4. Manufacturing Process

ESORO AG⁷, one of the industrial partners involved in the project, manufactured the body of PAC-Car II.

6.4.1. Manufacturing steps

The manufacturing procedure consisted of four main steps:

- milling of a one-to-one foam model;
- laminating a four-part negative form, called a mold;
- laminating the vehicle body sections; and
- assembling the body sections.

Each of these four steps is described in more detail below.

⁷ www.esoro.ch

6.4.2. Milling the one-to-one model

The shape of PAC-Car II was first milled out of polyurethane foam (400 kg/m^3) on a CNC tool machine by applying 3D CAD data directly. The model was then coated with a product to eliminate the porosity of the material and ground to achieve a smooth surface. A final coat of high-quality lacquer was then applied.

6.4.3. Laminating the mold

The vehicle body consists of 2 separate parts: the body itself and a canopy that can be removed to allow the pilot to get into and out of the vehicle. There was one mold for the body and another for the canopy. Both were made of composite glass fiber and epoxy materials.

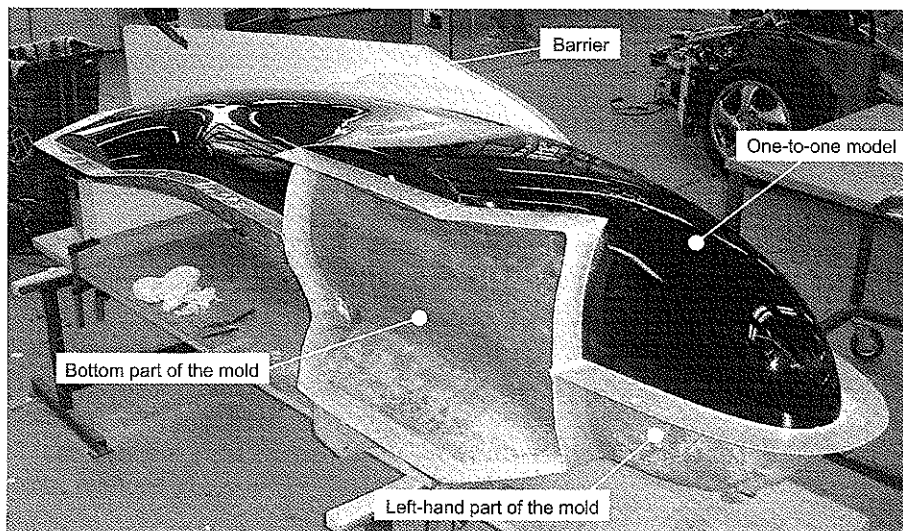


Figure 6-13: The one-to-one model (in black) laid on its side, fitted with two sections of the mold and a flat barrier (in white), is ready for the right side section of the mold to be laminated. (Courtesy of Esoro)

The body mold had 3 sections: two side sections (left and right); and one connecting section at the bottom of the body, between the wheels.

The parts of the body mold were laminated one after the other in the following order: the connecting part, the left side section, the right side section and the canopy. This was done directly on the model, and simply separated with a form release agent.

The join between the sections was comprised of flat laminated surfaces, either on an additional barrier or on the already hardened adjacent part. Figure 6-13 shows the configuration before the right side section of the mold was laminated.

6.4.4. Laminating the body sections

Each section that forms the PAC-Car II vehicle body was laminated separately in the mold (Figure 6-14).



Figure 6-14: Laminating of the right side part of the body mold. (Courtesy of Esoro)

The edges of the carbon laminate sections were laminated stepwise to allow a better join between sections that would later be glued together (Section 6.4.5). The first layers, applied directly on the negative mold, were laminated up to the rim, so as to create a smooth connection between the two sections. A gap was left between the two parts for the connecting strips.

The laminate was compressed with a vacuum bag and hardened at a temperature of 50°C (Figure 6-15). An absorbent fabric was placed under the vacuum bag to remove any excess epoxy resin, which would have increased the weight of the body sections.

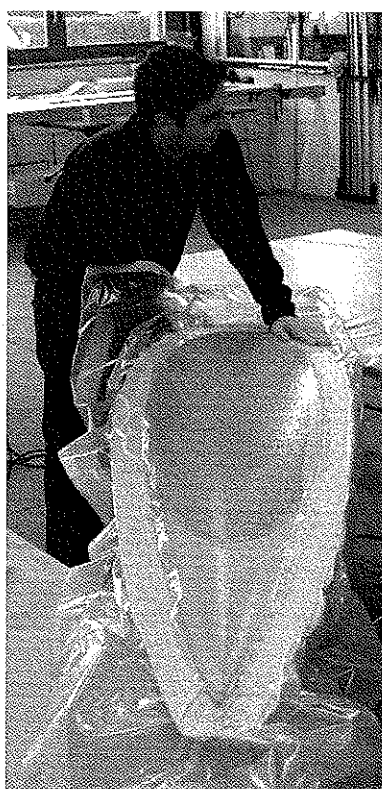


Figure 6-15: The canopy in its mold, fitted with the absorbent fabric and the vacuum bag.
(Courtesy of Esoro)

6.4.5. Assembling the vehicle body sections

The carbon laminated body sections were assembled without removing them from their mold (Figure 6-16). The three body section molds were first screwed together, and then several layers of carbon laminate strips of various widths were applied to fill in the gap at the edges (Figure 6-17), which had been deliberately left empty for this purpose (Section 6.4.4).

The joins between the sections then had to be coated with the anti-porosity product and ground to achieve a smooth and napless bond. Then, the entire surface of the PAC-Car II body had to be coated with a very thin layer of high-quality lacquer and smoothed to achieve a high-quality finish before painting.

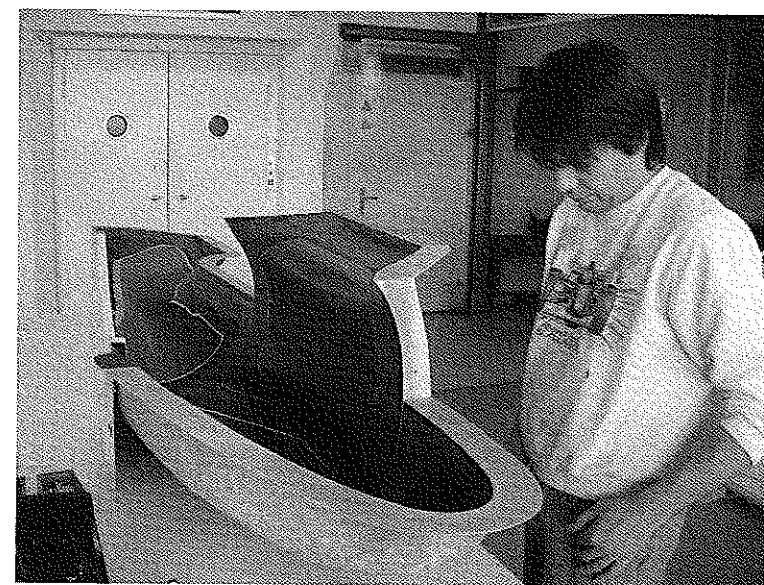


Figure 6-16: Two body sections, still in their mold, in position to be assembled. The gap left for the connecting straps can be seen.
(Courtesy of Esoro)

6.4.6. Construction details

Materials

Two types of carbon reinforcements were used to laminate the PAC-Car II body: a thin reinforcement of 145 g/m^2 and a thicker one of 245 g/m^2 . Epoxy resin was used for all laminates.

Laminate lay-up

First of all, one layer of the thin reinforcement was applied to the outside of the vehicle body to achieve a good quality surface. On top of this laminate base, several layers of the thick laminate were added. The distribution of the different laminate strips is shown in Figure 6-18.

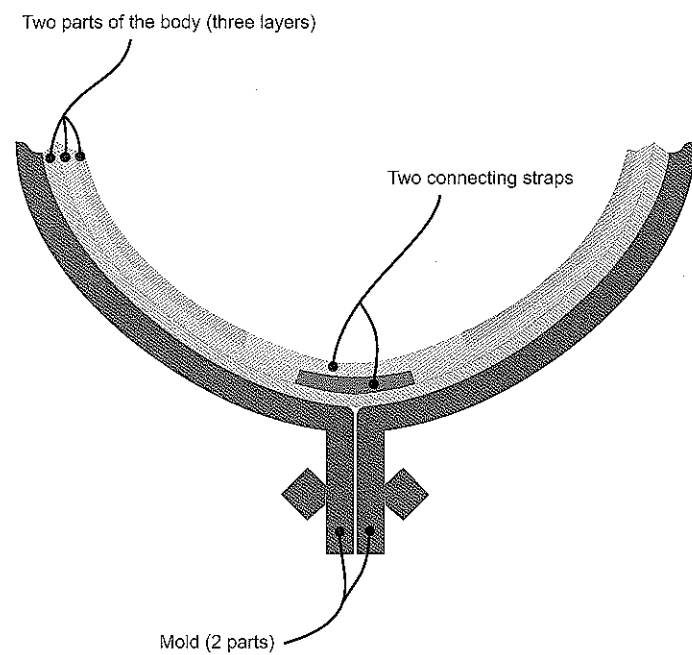


Figure 6-17: Close-up of the join between two body sections.

Inserts

To prevent deformations of the laminate while the resin was hardening, the inserts, the bulkhead and the struts for attaching the rear wheel were added to the body before it was removed from the mold. The inserts for the front axle were held precisely in position by a specially built tool until hardening was completed.

Struts

The struts added in the rear of the body to carry and distribute the load from the rear wheel were made of carbon laminate plates glued and laminated inside the vehicle body.

Rim and canopy connection

The U-shape of the rim that constitutes the interface with the canopy was laminated simultaneously on each side of the vehicle body. The additional wooden part, added to the mold for that purpose, can be seen in Figure 6-14.

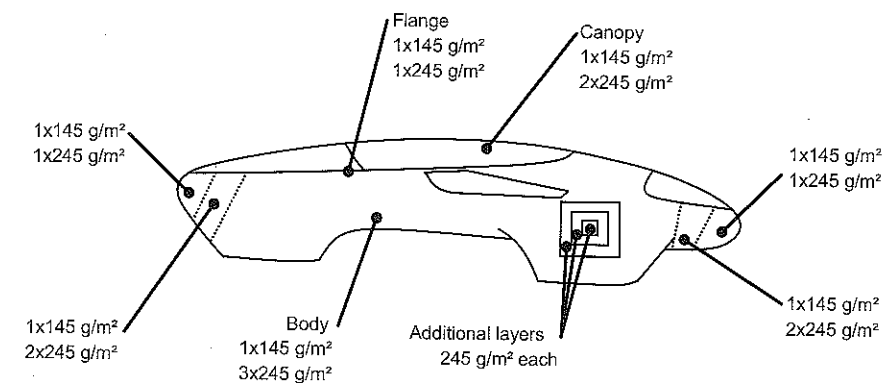


Figure 6-18: The distribution of the different laminate strips.

Integration of the windshields/windows

The next figures depict the manufacturing process of the PAC-Car II's windshield in chronological order. The windshield (F), rear window and two side windows were made from polycarbonate. They were manufactured using vacuum snap-back thermoforming of heated plates on positive molds (E). These molds were glass fiber laminated in the negative molds (B) used previously to laminate the vehicle body (C). To extend the window and windshield molds several centimeters larger than the final form of the window (which is necessary for the manufacturing process), the vehicle body molds (B) were extended locally using modeling wax (D).

Finally, the polycarbonate windshield and windows were cut into the right shape and then glued into the rabbets previously obtained from the shape of the molds. The join was coated and smoothed, and the paint on the vehicle body was extended around the windows to hide the rabbets, which would otherwise have been visible.

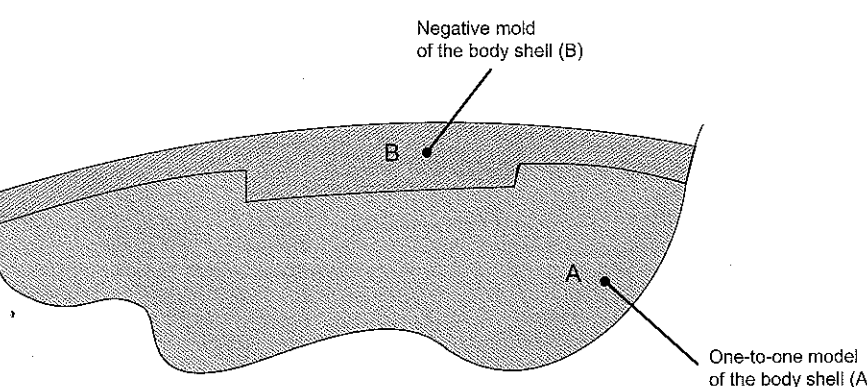


Figure 6-19: Cross-section of the one-to-one model and the body mold, where the windshield will be placed, during the body mold manufacturing.

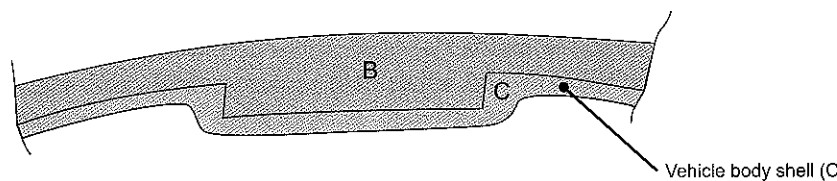


Figure 6-20: Cross-section of the vehicle body shell during its working.

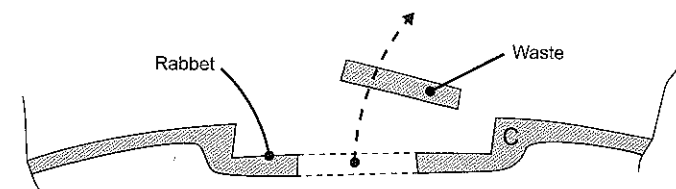


Figure 6-21: Cross-section of the vehicle body shell.

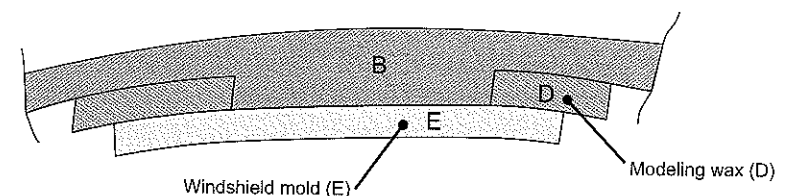


Figure 6-22: Cross-section of the windshield mold during its manufacturing.

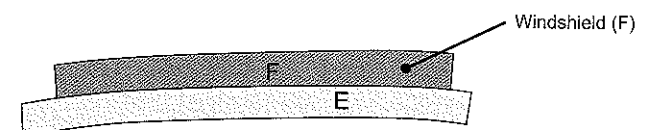


Figure 6-23: Cross-section of the windshield during its forming.

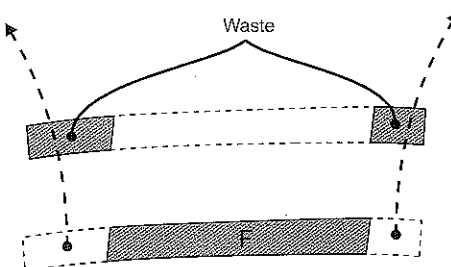


Figure 6-24: Cross-section of the windshield.

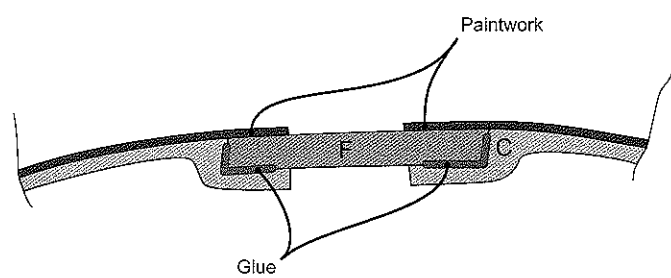


Figure 6-25: Cross-section of the vehicle body fitted with its windshield.

Chapter 7: Wheels

By Jean-Jacques Santin.

Though the wheel may very well be humanity's most ancient and important invention, neither characteristic makes wheels easy to design and manufacture. This is important for the teams who plan to embark on this FEV adventure to know.

The performance¹ of a fuel economy vehicle is greatly affected by its wheels. For proof of this statement, it is only necessary to compare the fuel consumption of the same vehicle, first equipped with spoke wheels, then with disk wheels! Manufacturing a disk wheel seems to be easy, just a question of gluing a rim and a hub onto a honeycomb plate. But, in fact, producing lightweight, rigid and geometrically perfect wheels is very expensive and time-consuming. The difficulty of the task convinced us of the importance of including a chapter about wheels in this book. We hope our experience, acquired when crafting the wheels for PAC-Car II, can help other teams avoid the pitfalls that we confronted when manufacturing our own wheels.

This chapter is divided in two parts: Section 7.1 focuses on the wheel hub and bearings, and Section 7.2 deals with the design and manufacture of the wheel itself.

7.1. Wheel bearings

This section is based on the Mechanical Engineering Master's thesis of Thomas-Pierre Delannoye [22]. The SNFA⁸, a company in the SKF Group, provided technical support for this part of the PAC-Car II project, and this support is gratefully acknowledged.

The drag produced by wheel bearings is almost one hundred times smaller than the drag produced by tires (Section 2.2.1). Nevertheless, this drag can increase dramatically if the right bearings are not chosen, or if they are poorly assembled or incorrectly lubricated. Without a close partnership with a ball bearing manufacturer,

⁸ www.snfa.com

the task can be daunting. In lieu of such a partnership, we offer the following advice for reducing the wheel hub frictional moment.

7.1.1. Choosing the wheel bearings

Bearing type

In this FEV application, in which the speeds and loads are both low, ball bearings usually have a smaller frictional moment than those fitted with other rolling elements, such as tapered rollers. As the frictional moment is partially the result of ball and raceway deformations, it is important to manage the load distribution on each ball correctly. The only way to do this is to apply a preload force. In our opinion, this force can be best optimized by using angular contact ball bearings instead of deep groove ball bearings.

Bearing geometry

When designing a ball bearing, three parameters can usually be adjusted: ball size, the number of balls and the contact angle. Reducing the ball diameter reduces the contact area between the balls and raceways (where sliding occurs), while increasing the number of balls reduces the load on each ball. Since these two geometric modifications also lower the frictional moment, the tendency is to use a large number of small balls. However, it is important to remember that the lower limit is given by the static load-carrying capacity, which also decreases with size, making the bearing more sensitive to shocks that could produce permanent deformations in the rolling elements and the raceways, with the result of increasing the frictional moment.

Angular contact ball bearings are most often available with angles of 15° or 25°. In terms of the frictional moment, a 15° contact angle is preferable when cruising straight, while in a curve, a 25° contact angle is better. Since the vehicle runs straight more often than it corners, both at Rockingham and Nogaro, we chose to use 15° contact angle ball bearings.

Ball and cage materials

Using ceramic balls instead of steel balls halves the frictional moment and also reduces the wheel weight since ceramics are lighter than steel. In this FEV application, a cage made of plastic laminate offers a good trade-off between weight and friction.

Bearing arrangement and preloading

A back-to-back arrangement with two 15° angular contact ball bearings is more suitable than a face-to-face arrangement. The bearings arranged back-to-back can accommodate larger tilting moments, particularly when cornering, and also reduce the risk of deterioration resulting from exceptional rolling conditions. As an added bonus, this arrangement is usually simpler and requires fewer parts.

Preloading the bearings allows for a better load distribution on all the rolling elements, which reduces the contact deformation and, consequently, the frictional moment. This is particularly significant when the bearings operate under external forces that have radial and axial components (i.e., when the vehicle is cornering). The preload force value must be carefully chosen and special attention given to the design and manufacture of the sleeves (e.g., materials, shape, tolerances and thermal expansion). One good option is to use spring washers.

Lubrication and sealing

Rolling bearings can be lubricated with grease or oil.

With grease-lubricated bearings, the frictional moment can be 3 or 4 times higher than the value obtained with oil-lubricated bearings, mostly due to grease viscosity but also to the poor grease distribution inside the bearing that may occur, especially just after the bearings have been refilled. In addition, excessive amounts of grease can also generate higher friction values.

Even the simplest method of oil lubrication (i.e., the oil bath) complicates the possible solutions from the technical point of view. Lubricating the bearings with a few drops of oil when mounting them is also risky because the oil can flow out of the bearings (due to gravity or a centrifugal effect), making them run dry.

In fact, it is probably best to mount the bearings using the recommended amount of grease (or a bit less) and then let the wheel turn for a few hours. This offers a double benefit: the grease is redistributed within the free space around the bearings as it churns around, and the components become suitably broken in. Using new bearings for an important run definitely is no more recommended than using new hiking boots to climb Mount Everest!

To maintain a low level of friction, it is also quite important to protect the bearings from dust. The use of contact seals or bearings with integral seals must be rejected since the frictional moment they generate is several times higher than the frictional moment of the bearings themselves. Therefore, the best solution is to use the grease mentioned above as the first line of defense in which the grease acts as a dust magnet. Two non-contact shields may also be used, one on each side of the bearing

arrangement, to narrow the openings, giving dust less space to enter the bearing arrangement, thus inducing the dust to stick to the grease outside the bearings.

7.1.2. The wheel bearings of the PAC-Car II

Ball bearings

The ball bearings used in the PAC-Car II wheels are produced by the SNFA, an international company in the SKF group that specializes in high-speed, high-precision bearings for the aircraft, aerospace and machine tool industries. Sold under the reference VEX20 /NS 7 CE1 DD M, they are single-row angular-contact ball bearings, with a 15° contact angle and ABEC 7 precision. The balls are made of ceramic (Si_3N_4) and the cage of cotton-fiber-reinforced phenol resin. These bearings are sold by the pair, to be arranged back-to-back. Inserting two sleeves of the same length, one between the two outer rings and another between the two inner rings, provides a light axial preload of 12 daN.

Compared to the PAC-Car I, this ball bearing solution reduced the ball bearing drag torque in the PAC-Car II by half. Table 7-1 provides the main numbers for the two ball bearing solutions.

Table 7-1: Main numbers for the ball bearings used in PAC-Car I and PAC-Car II.

Vehicle	PAC-Car II	PAC-Car I
Manufacturer	SNFA	SNFA
Reference	VEX20 /NS 7 CE1 DD M	E212 /NS 7 CE1 DD M
Bore diameter [mm]	20	12
Outside diameter [mm]	42	32
Width [mm]	12	10
Number of balls	12	9
Ball diameter [mm]	6.350	5.556
Dynamic bearing load [daN]	760	720
Static load-carrying capacity [daN]	410	440
Calculated relative frictional moment	0.5	1
Weight [g]	65	35

Bearing arrangement

The sectional drawing of the bearing arrangement is shown in Figure 7-1.

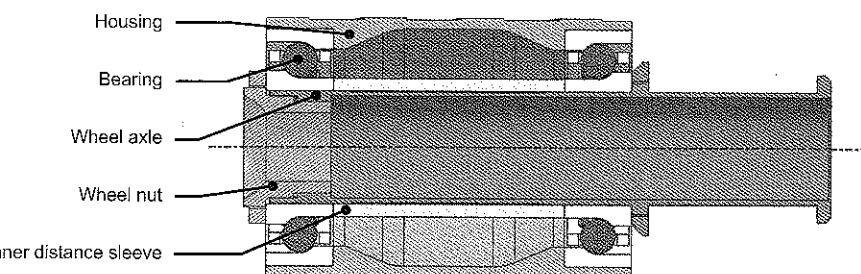


Figure 7-1: Sectional drawing of the bearing arrangement (front wheel).

To achieve the expected preload, the inner and outer spacer sleeves must be the same length. The ball bearing manufacturer recommends using steel sleeves and grinding them together on a surface grinder, so that the difference in length is less than 1 μm . Unfortunately, the weight of steel sleeves was not acceptable for PAC-Car II, and we chose to use a two-shoulder housing and a removable inner spacer sleeve, both made of aluminum. We managed to manufacture the inner spacer sleeve to be the same length as the shoulders, and to design these parts to give them equal rigidity.

7.2. The wheel criteria

This section is based on Stefano Righetti's *Diplomarbeit* (Diploma Thesis) in the field of mechanical engineering [23].

The challenge is to manufacture wheels that are:

- aerodynamic enough to minimize energy loss due to their rotation;
- compatible with tubeless tires;
- lightweight;
- rigid enough to keep the tires in the right position to minimize vehicle tire drag; and
- geometrically precise enough to obtain low runouts and avoid vibrations.

The factors taken into consideration to produce good results for the above criteria are described in order in the following sub-sections.

7.2.1. Aerodynamics

Wheel aerodynamics were investigated by constituting a bibliography of works dealing with such things as time-trial bicycles, solar- and human-powered vehicles and fuel economy vehicles [18, 24-30]. The explanations given below are based on those works.

First of all, a decision had to be made as to whether or not the wheels should be enclosed in a wheel fairing (i.e., a wheel cover). When using a fairing, the wheel can be considered to exist in calm ambient air. The relative wind velocity distribution is bi-dimensional and depends only on the wheel's rotational speed and the distance between the considered point and the wheel spin axis, whatever the vehicle velocity and the weather-wind speed (Figure 7-2a). On the other hand, without a wheel fairing, the relative wind velocity distribution is different at each point on the wheel, combining as it does two movements, one due to vehicle velocity and the other due to the wheel's rotational speed (Figure 7-2b). In addition, if the weather-wind speed is not in the direction of movement (i.e., there are crosswinds), an aerodynamic axial force appears that will deflect the vehicle from its lane.

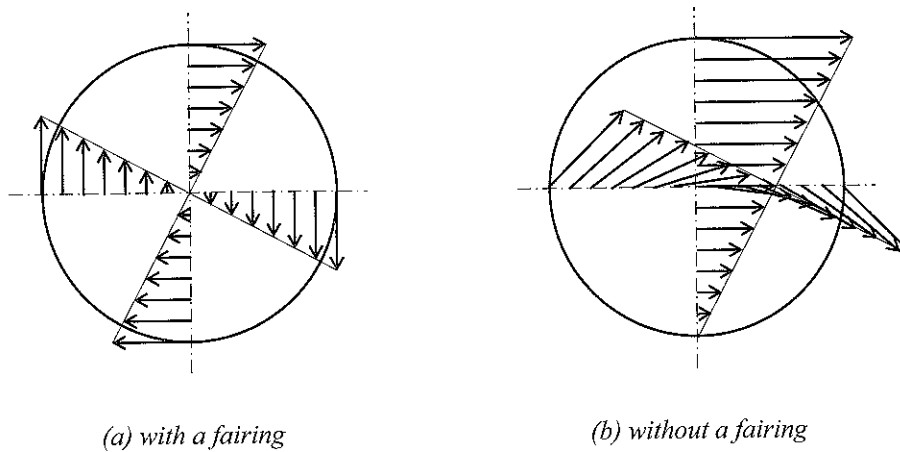


Figure 7-2: Wind velocity distribution on a wheel.

Second, the type of wheel (i.e., spoke or disk wheel) had to be chosen. It has been proved that, for wheels enclosed in fairings, the lower the number of spokes, the better the drag torque. However, the optimal solution in terms of aerodynamics is clearly a disc wheel. Given the various shapes of disk wheels available, the rim may or may not be flush with the side walls. But this doesn't matter; in fact, a perfectly smooth surface between the side walls and the rim will not significantly

improve the wheel's aerodynamics since the tire already protrudes slightly from the rim. Disc wheels can also be expected to be more rigid than spoke wheels, which is especially important for countering the axial forces generated when cornering.

The only major disadvantage of disc wheels compared to spoke wheels is their greater weight. Thus, the aim of our wheel design phase was to find the best compromise between rigidity, weight and manufacturability for disc wheels.

7.2.2. Tubeless tire compatibility: the wheel rim profile

Since earlier in the vehicle design process we had already decided to use the Michelin tubeless radial-ply tire 45-75R16, we needed to design a wheel that would be compatible with this tire. The 45-75R16 is made to be mounted on a standard motorcycle drop-center rim with cylindrical bead seat. Thus, the rim and hub dimensions are two of the design constraints for the wheels, with the rim dimensions being determined from the tire and the hub dimensions, from the wheel bearings. According to the "European Tire and Rim Technical Dimensions", the chosen rim has the contour dimensions shown in Figure 7-3 and Table 7-2.

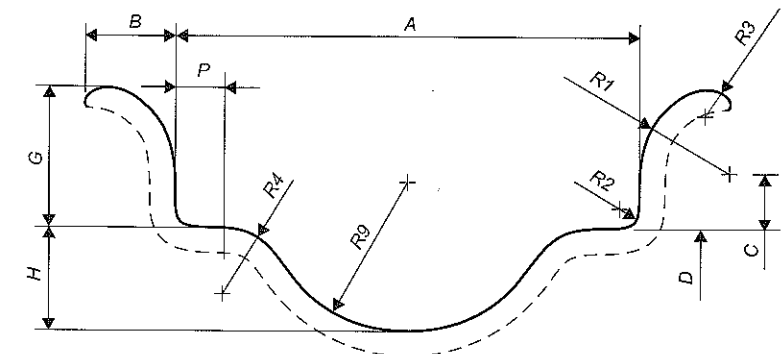


Figure 7-3: Rim profile for the 45-75R16 Michelin tire, according to the "European Tire and Rim Technical Dimensions".

These technical specifications thus had to be taken into consideration when designing the wheels of the PAC-Car II.

Table 7-2: Rim contour dimensions and tolerances according to the "European Tire and Rim Technical Dimensions".

Parameter	Value [mm]	Tolerance	Parameter	Value [mm]	Tolerance
A	34	-0.5/+1	D	405.6	Ref.
B	6.5	-0/+2	R1	6.5	Ref.
G	10	± 0.5	R2	1.5	Max.
P	3.5	-0/+2	R3	2	Min.
H	7.5	-0.5/+1	R4	5	Min.
C	4	Ref.	R9	7	Min.

7.2.3. Sandwich construction versus a free-core disc

The wheels needed to respect certain weight and rigidity constraints so that they would not add too much to the overall weight of the vehicle and would be sufficiently rigid to both maintain the correct tire position, thus minimizing tire drag, and reinforce the wheels' load-carrying capacity.

A sandwich-type construction was first analyzed, and then dismissed, because using a foam core would have significantly increased the weight of the wheel. A flat disc wheel has a width of about 40 mm and a diameter of about 400 mm, for a total volume of about 0.005 m^3 . Filling this volume with standard foam (e.g., Airex R63) with a density of 60 kg/m^3 would increase the wheel weight by 300 g. Even if the foam thickness were reduced to half the volume, the additional weight would still be significant.

The same is true of honeycomb cores, be they made of aluminum or of aramid. Both materials have a minimal density of 30 kg/m^3 , resulting in a wheel weight increase of 150 g for a 40 mm thick wheel.

Thus, we decided that, if possible, we would eliminate the core. A discussion with our resident composite material experts confirmed that a core-free wheel would indeed be possible and would pose no particular difficulties. Consequently, we worked to optimize a core-free wheel design, thus eliminating the extra weight.

7.3. Design process

The optimal design of the wheel was generated in four stages, as detailed below (Sections 7.3.2, 7.3.3, 7.3.4, 7.3.5). However, before these stages can be explained, the load cases and boundary conditions used in the FEM computations performed during the four stages must be presented (Section 7.3.1).

7.3.1. Load cases and boundary conditions

This section presents the load cases and the boundary conditions used in the FEM computations.

Load cases

Many situations must be taken into account when calculating wheel dimensions. Three possible load cases are described below.

(1) Given the position of the wheels on the vehicle – two wheels in front and one at the rear – the load distribution on each wheel is about 1/3 of the total weight when the vehicle is running straight or at a stop. The critical situation occurs when running the vehicle on a curve. During this cornering situation, as much as the entire load (normal and lateral forces) of the two-wheel axle can be transferred to the external wheel, increasing its load from the initial 1/3 to a maximum of 2/3 of the weight, while the single-wheel rear axle continues to carry 1/3 of the total weight.

(2) During acceleration and braking maneuvers, torque is only applied to the traction wheel. The critical situation arises during the brake test before the race, throughout which the vehicle must be positioned on a 20° slope with full brakes applied (static test). Since the objective is to prevent the vehicle from moving, the entire vehicle's weight must be supported by the braking wheel. Assuming there is no slipping between the tire and the slope surface, this means it must support a force of about 420 N (mass of vehicle 125 kg), equivalent to a moment of 100 Nm.

(3) The high air pressure between rim and tire is another important load that must be taken into account. The air acts on the rim in two ways: directly, with a constant pressure perpendicular to the rim surface, and indirectly via the tire, with a contact pressure between the rim and the tire bead. To lower the tire's rolling resistance, the inflation pressure is relatively high, with 6 bar being the maximum pressure recommended by Michelin (Section 3.2.1). For safety reasons, we decided to apply a security factor to the inflation pressure in the FEM calculations. Therefore, a 15-bar inflation pressure was taken into consideration.

The relevant loads are listed in Table 7-3.

Table 7-3: Load cases.

Description	Rear wheel (drive & brake)	Front wheel (free)
Maximum torque during acceleration [Nm]	12	0
Maximum torque during braking [Nm]	100	0
Radial force [N]	420	840
Peak radial force [N]	1000	1000
Lateral force [N]	400	800
Tire pressure [bar]	15	15

Boundary conditions

Using a cylindrical coordinate system, the nodes located in the bearing position were constrained in such a way that the rotation of the wheel axle was still possible. The rotation of the wheel was limited by eliminating the degree of freedom on the nodes located on the contact surface between the brake disc carrier and the brake disc.

Loads

The load on the wheel must be defined as close as possible to real load values.

Even though the forces and moments transmitted from the road to the tire can be known for various driving conditions – for instance, by using the tri-cycle vehicle model presented in Section 4.2.3 –, transferring them to the tire-rim contact surface is still difficult, especially when the tire behavior is unknown. Despite this lack of information, we were able to resolve this issue with quite good results. Our method is described below.

The axial, radial and tangential forces that are transferred from the road to the tire were distributed on a 20°-sector of the rim, using the cosine function (7.1):

$$f(\alpha) = F \frac{\pi}{4x} \cos\left(\alpha \frac{\pi}{2x}\right) ; -x \leq \alpha \leq x \quad (7.1)$$

Where f is the force applied to the rim at the point of the rim that has the polar coordinate α ; F is the tire-road contact force that has to be transferred to the rim; and x defines the sector width.

In this equation, we used $x = \pi/18 (= 10^\circ)$ with success. Figure 7-4 illustrates the resulting Sinus distributed force model.

In addition, to incorporate the security factor mentioned above, we applied forces corresponding to the 15-bar inflation pressure and the contact with the tire bead.

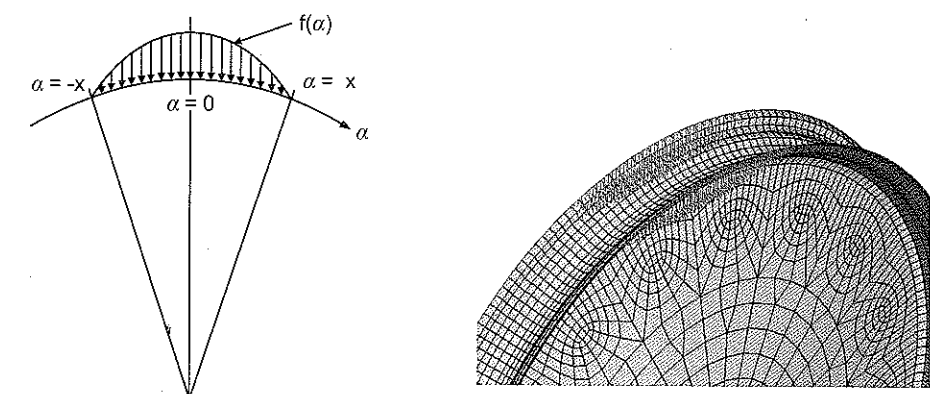


Figure 7-4: Sinus distributed force model.

7.3.2. Stage one: finding the best profile

Three different cross-section profiles of the disc wheel were compared: an open L profile, a closed U profile, and a closed V profile. The comparison was made using the shape optimizer of the CAD software, CATIA⁹. These profiles are illustrated in Figure 7-5.

Three parametric models were used, all working with an isotropic material (aluminum). The main parameters were the side-wall thicknesses near the hub and near the rim. We maximized the rigidity of each profile, while maintaining a fixed wheel weight of 2 kg.

The axial displacement value of the rim borders for the different profiles are listed in Table 7-4.

⁹ CATIA is a registered trademark of Dassault Systèmes S.A. (France); www.dassault.com

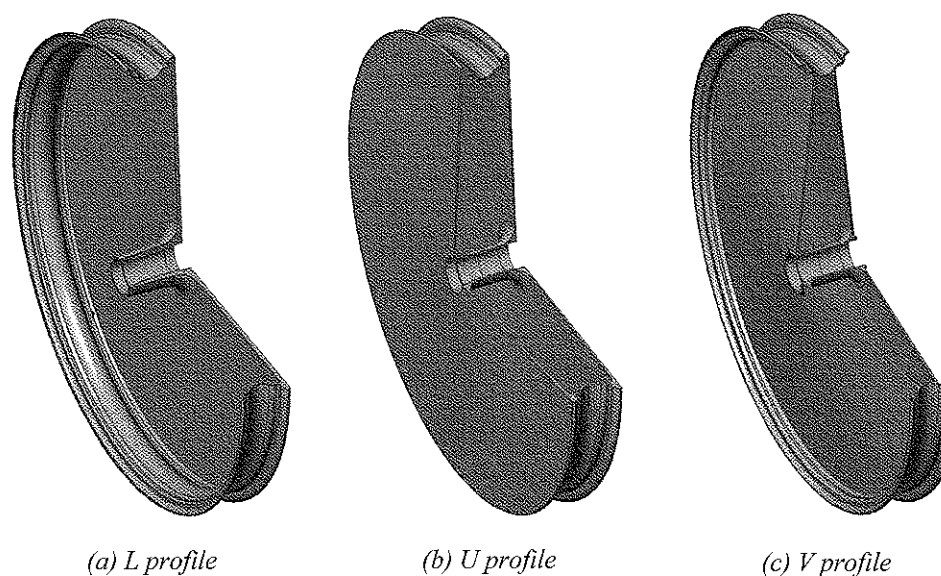


Figure 7-5: Wheel profile types.

Table 7-4: Displacement of the rim border of several profiles.

Wheel profile	Wall thickness [mm]		Displacement [mm]	Mass [g]
	Near hub	Near rim		
L profile	5.3	2.8	6.8	1741
	6.6	2.0	6.0	1743
	5.0	3.0	7.0	1743
U profile	1.0	1.2	0.44	1734
	1.3	1.0	0.44	1726
V profile	2.0	1.6	0.16	1724
	1.3	2.0	0.17	1725

The results clearly show that the V profile is the most rigid. The others were therefore excluded from any further investigations.

7.3.3. Stage two: optimizing the V profile

The next step was to optimize the selected V profile. To this end, a parametric model was created using the finite element software, ANSYS¹⁰. Starting with the wheel section profile (Figure 7-6(a)), a solid model (Figure 7-6(b)) was created by rotating the profile around the wheel axis. Given the symmetry of the wheel, only half a wheel was created and any perpendicular surface displacement in the plane of symmetry was prevented.

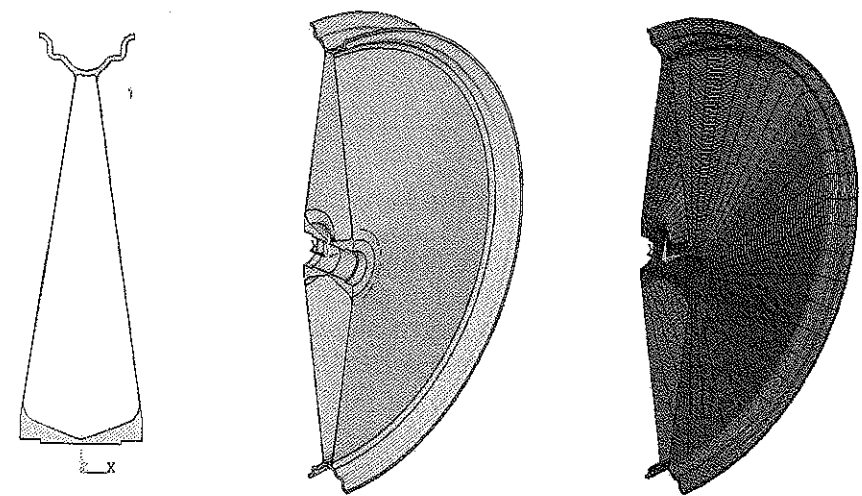


Figure 7-6: ANSYS solid model.

The ANSYS model was then optimized using DynOPS¹¹, which connects the simulation software ANSYS to an evolutionary algorithm. Ten parameters were introduced; the resulting optimization parameters are listed in Table 7-5.

¹⁰ ANSYS is a registered trademark of Ansys, Inc. (Canonsburg, PA, USA); www.ansys.com

¹¹ DynOPS – Dynamic Optimization Parameter Substitution – is a registered trademark of EVEN – Evolutionary Engineering AG (Zurich, Switzerland); www.even-ag.ch

Table 7-5: Parameters of the V-profile wheel after optimization.

Description	Value [mm]
external width of the rim	2.11
rim border thickness	2.32
hub thickness at center	1.78
hub thickness at side	11.3
wall thickness near axle	0.33
wall thickness near rim	0.27
radius between side wall and rim border (external)	-
radius between side wall and rim border (internal)	-
radius between side wall and hub	-
hub center radius	-

7.3.4. Stage three: optimizing the laminate

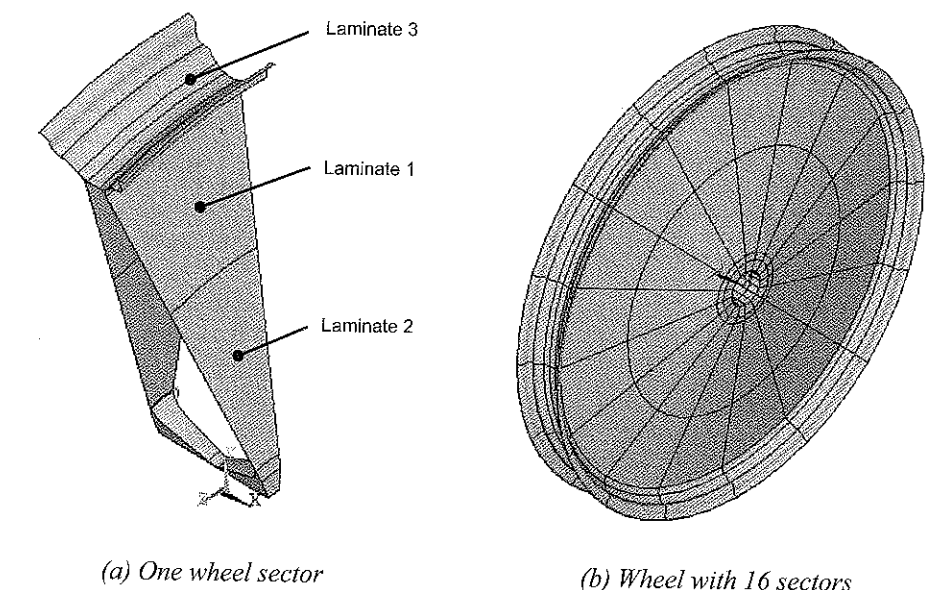
To optimize the laminate, a new model had to be created using composite materials, which have orthotropic properties. The previously optimized parameters were used to shape the profile. Additional parameters were added to model the orthotropic materials. For instance, the wheel was divided into a parameterized number of sectors, each one with the same angle.

As shown in Figure 7-7, each of these sectors was divided into two different laminates (Laminate 1 and Laminate 2). Another laminate (Laminate 3) was defined for the rim border. Initially, the further partitioning of Laminate 3 into different layers (external, middle and internal layers) was analyzed using an optimization technique. Because the changes offered by these three layers were so small, and because it would have taken a lot of time to position the thin fiber strips during manufacturing, we decided not to further partition Laminate 3.

The wheel is made of three different laminates, each with many parameters. The DynOPS optimization of the orthotropic model parameters yielded the optimal lay-up to be used when constructing the wheel. The resulting values are listed in Table 7-6.

The rim border consists of a 3.44 mm thick laminate (20 plies). It has $\pm 45^\circ$ and $0/90^\circ$ oriented fibers and a core made of unidirectional fibers aligned to 90° . The main force acting on the rim is the high tire pressure of 15 bar.

The internal sector of the side walls is made of a symmetrical 4-ply laminate (0° , 20° , 20° , 0°). The 0° oriented fibers account for most of the axial force, and the 20° fibers account for the braking moment. The external sector of the side walls has one 20° ply less than the internal one.

*(a) One wheel sector (b) Wheel with 16 sectors**Figure 7-7: Location of the laminates on one wheel sector.*

The wheel has 13 sectors measuring about 28° each. Table 7-7 lists the lay-up for the different laminates shown in Figure 7-7.

Table 7-6: Optimized laminate parameters. See Figure 7-7 for an illustration of the different laminate numbers.

Laminate	Description	Value
Laminate 1	thickness of the first ply [mm]	0.14
	thickness of the second ply [mm]	0.14
	orientation of the first ply [$^\circ$]	0
	orientation of the second ply [$^\circ$]	20
Laminate 2	thickness of the first ply [mm]	0.14
	thickness of the second ply [mm]	0.28
	orientation of the first ply [$^\circ$]	0
	orientation of the second ply [$^\circ$]	20
Laminate 3	thickness of the first ply ($\pm 45^\circ$) [mm]	0.72
	thickness of the second ply ($0^\circ/90^\circ$) [mm]	0.72
	thickness of the third ply (90°) [mm]	0.56

Table 7-7: Optimized laminate lay-up. See Figure 7-7 for an illustration of the different laminate numbers.

Laminate	Ply	Material	Thickness [mm/ply]	Orientation [°]
Laminate 1	1	UD	0.14	0 (radial direction)
	2	UD	0.14	20
	3	UD	0.14	0
Laminate 2	1	UD	0.14	0
	2-3	UD	0.14	20
	4	UD	0.14	0
Laminate 3	1-4	0°/90°	0.18	45
	5-8	0°/90°	0.18	0
	9-12	UD	0.14	90 (axial direction)
	13-16	0°/90°	0.18	0
	17-20	0°/90°	0.18	45

7.3.5. Stage four: verifying the results

Following the FEM computations, the results were analyzed. In order to compare the ANSYS data with the material properties, the strength of the three laminates along the X and Y axis was calculated using the program ESAComp¹². The critical load results showed that the maximum stress was below the limits of the laminates. The strains on the wheel were also shown to be well below the limits. The analysis of the displacement on each wheel element showed that the side walls buckled about 1.3 mm (Figure 7-8), which was confirmed by the test results for the first wheel manufactured.

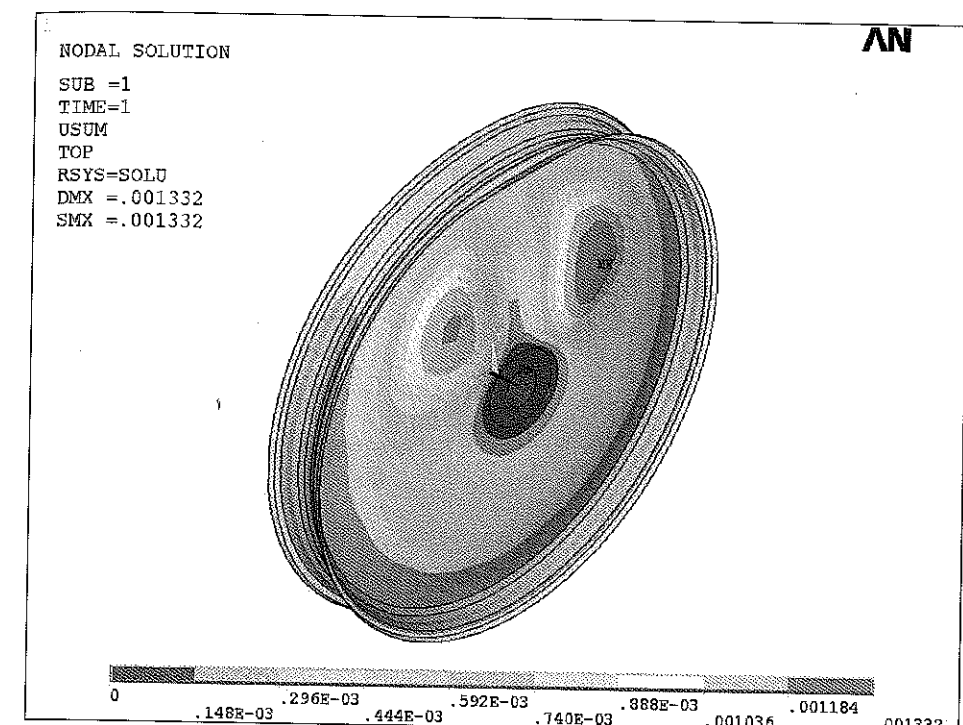


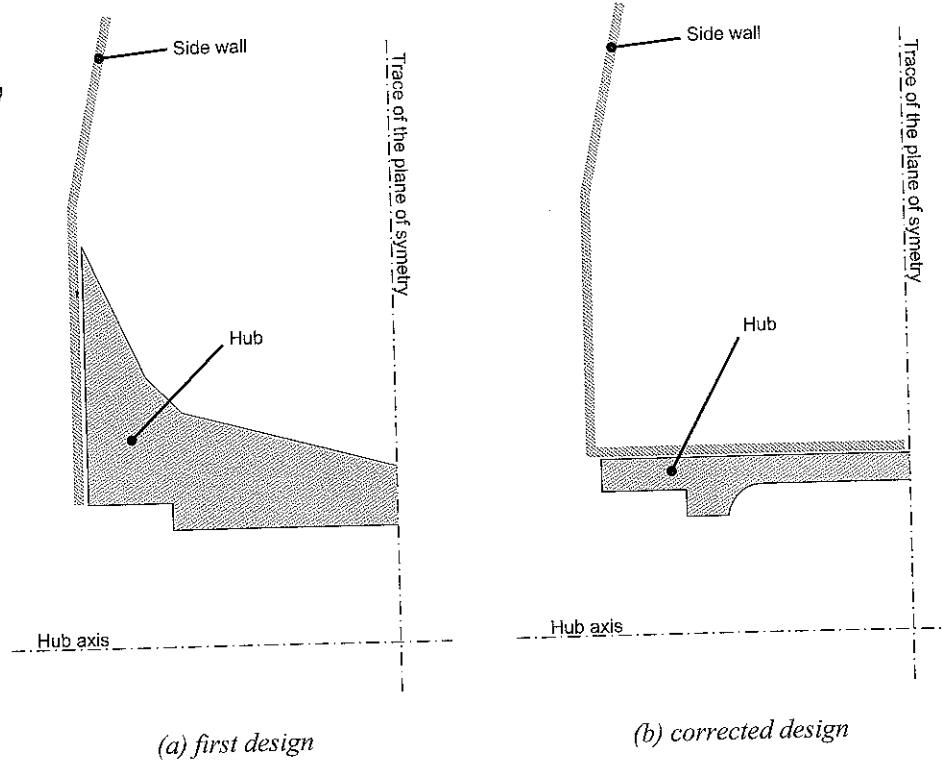
Figure 7-8: Displacement on one side of the wheel under a critical load. The buckling of this side wall can be clearly seen.

Problems arising from the optimized solution

The tests carried out on the first manufactured optimized wheel showed two major problems.

First, the glued join between the side walls and the hub did not hold when the tire was inflated to 10 bar for the first time. In fact, the rim diameter decreased under the high inflation pressure. Due to the V profile, the walls had a tendency to open near the hub, causing these two parts to come apart. This problem was solved by not gluing the walls to the side surfaces of the hub, but rather to its external cylindrical surface (Figure 7-9).

¹² ESAComp is a registered trademark of Componeering Inc. (Helsinki, Finland); www.componeering.com/esacomp

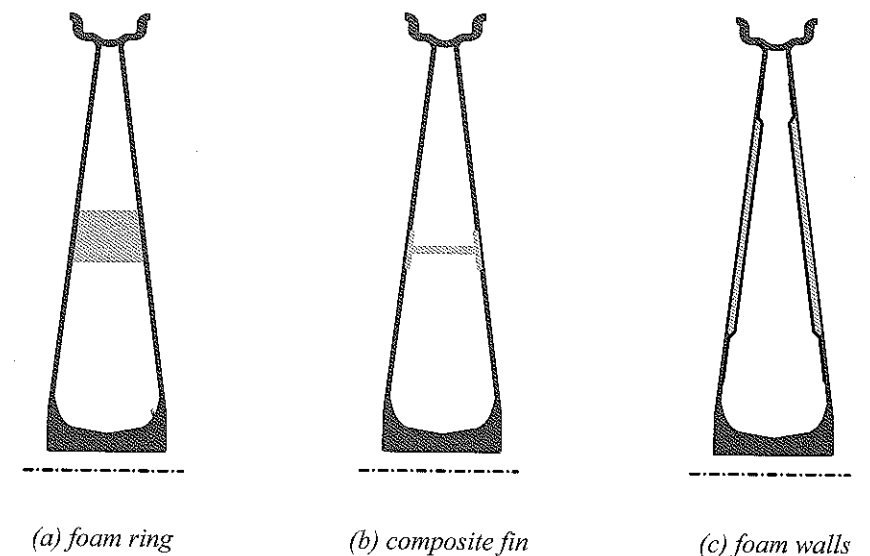


(a) first design

(b) corrected design

Figure 7-9: Modified glue join between the walls and the hub.

Second, the previously calculated side wall buckling occurred when cornering. Everybody who saw PAC-Car I racing in Nogaro in 2004 should have noticed that, at each turn, the vehicle produced a strange noise that sounded like a drum roll. This noise was caused by the movement of the buckled area when the wheel rotated. This problem had to be fixed for at least two good reasons: such a noise can be energy consuming and is also incompatible with the noiseless and environmentally friendly image that a fuel cell vehicle is supposed to convey! As shown in Figure 7-10, several possible solutions to the problem were available. Solution (c) was finally chosen, as it appeared to be the simplest to produce.



(a) foam ring

(b) composite fin

(c) foam walls

Figure 7-10: Three possible solutions to the wall buckling problem.

Final wheel design

The final wheel design is shown in Figure 7-11. This wheel weighs 700 g, without the valve, tire and bearings.

7.4. Manufacturing process

The wheels were manufactured in the composite materials workshop at the Institute for Mechanical Systems, a part of ETH Zurich.

The manufacturing process presented below is the one that was used for the first wheel. The two major problems encountered with this first prototype necessitated a few modifications in the design. (See Section 7.3.5 for details about these problems and their solutions.)

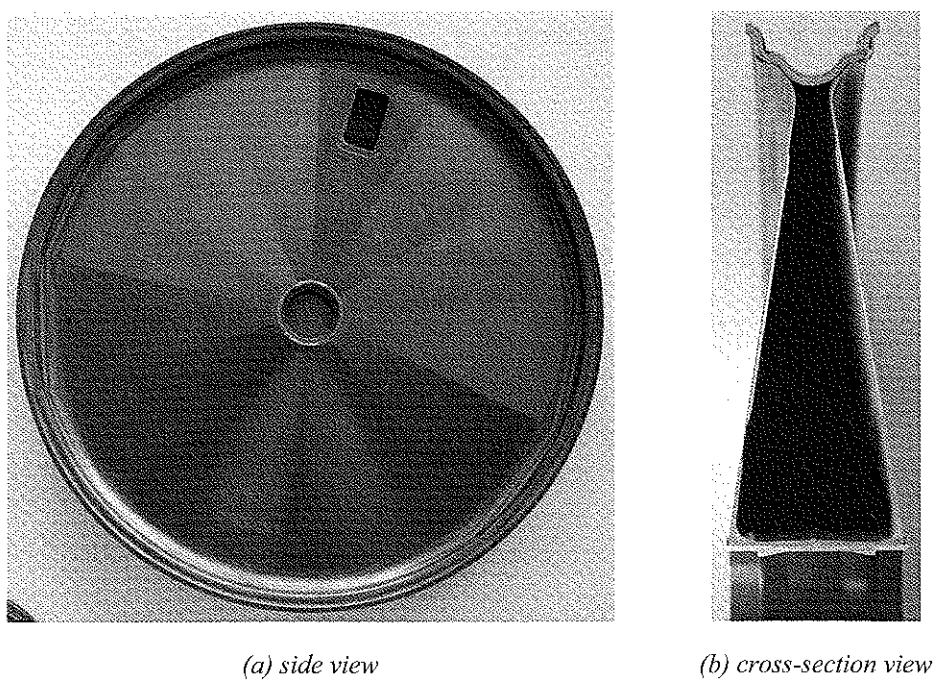


Figure 7-11: Pictures of the final wheel.

7.4.1. Preliminary considerations

To manufacture the wheel, several alternatives were considered. In an attempt to reduce production costs, steel forms (molds) were initially chosen. However, steel has many disadvantages compared to composites. Steel forms are heavier, more difficult to machine, and have a rather large expansion coefficient, which cannot be ignored if an autoclave process is used. Due to the high temperatures (120–150 °C) during the curing phase, expansions of up to 0.5 mm are to be expected. In addition, in order to minimize the expansion differences during the heating phase (internal stress), the metal has to be thermally treated before, and probably after, the rough machining.

It was therefore decided to use carbon composite forms, using a prepreg-system consisting of a particular carbon fiber lay-up, specially made to be used with epoxy forms. The laminate was first cured at a low temperature (55 °C), and then tempered at 180 °C without further dimensional variations.

An integral construction of the wheel was also considered, but was judged to be too difficult to realize because of the closed shape. With a closed shape, the only way

to compress the walls is to insert a bag between them and raise the pressure inside the bag. The small hub diameter (32 mm) only added to the difficulties. Thus, the decision was made to build the wheel by gluing the different parts together. A hub, two side walls, and the rim border were laminated separately, and these parts were then glued together, using a specially developed gluing tool (Figure 7-18).

7.4.2. Method of manufacturing

The four-step method is listed below:

- manufacturing the positive epoxy molds;
 - laminating the negative composite molds using the positive molds;
 - laminating the parts of the wheel using the negative molds;
 - gluing the parts together; and
 - finishing and finetuning the final wheel.

These steps are described below, for the rim, the walls and the hub.

Manufacturing the epoxy positive molds

The positive molds for the rims and the walls were made of epoxy. Blanks with a diameter of about 420 mm were cut on a manual lathe with tools that had the exact negative shape of the print required in the negative molds. This solution was preferable to using a CNC milling machine, which requires a lot of finishing and is not as accurate as a turning machine. Obviously, the best solution would have been to use a CNC lathe, but such a machine was not available at the ETH Zurich.

The tools used to cut the blanks were manufactured on a wire electrical discharge machine. The principle is illustrated in Figure 7-12 for the rim, and in Figure 7-13 for the side wall.

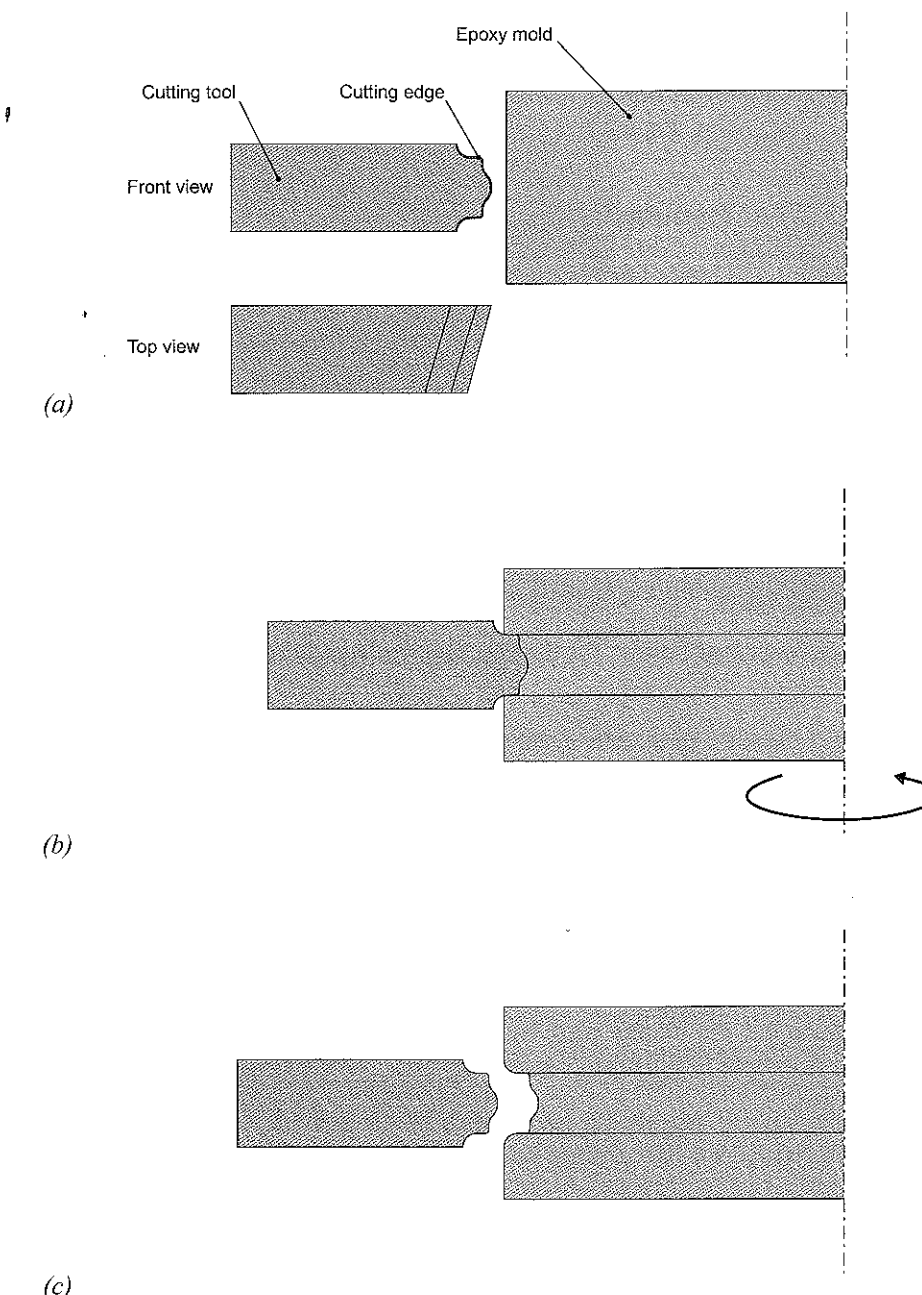


Figure 7-12: Manufacturing principle for the positive mold of the rim.
(a) tool and blank; (b) cutting phase; (c) finished pattern cavity

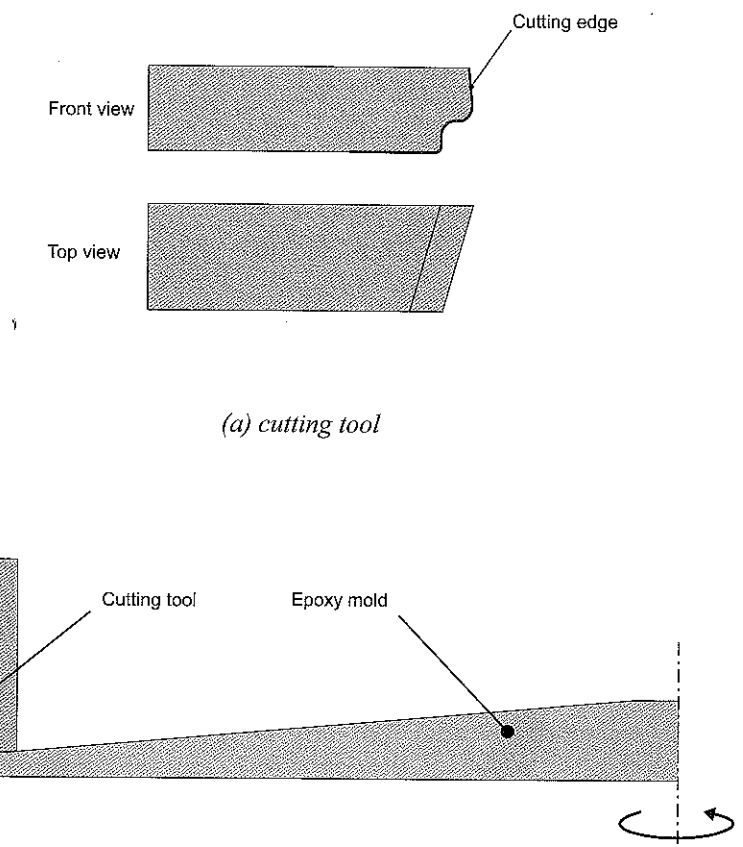


Figure 7-13: Manufacturing principle for the positive mold of the side wall.

Laminating the negative molds

When the positive molds were ready, it was possible to laminate the negative molds over them with prepreg material. Negative molds made of silicon were manufactured as well, to compress the laminate during the lamination process.

The negative mold for the external side of the rim (the side where the tire would be mounted) was divided into three parts (120° each), to allow for the unmolding operations. This was done as follows:

- a 120° section on the external rim mold had to be fashioned using two separation walls, as shown in Figure 7-14, to which nuts could be fastened (centering pins were also used for positioning);
- after curing, the two separation walls were removed, and the resulting surfaces were then used as a wall for the next 120° section; and
- these two steps were repeated until the three sections were completed.

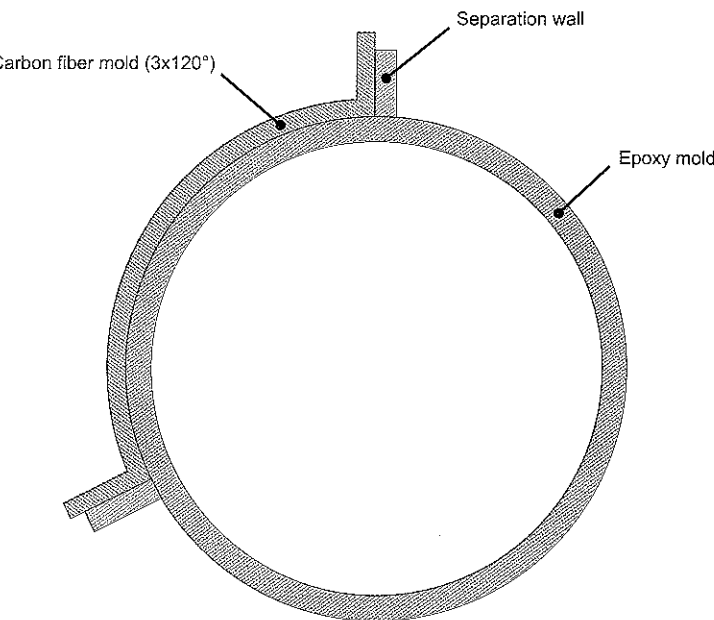


Figure 7-14: Manufacture of the external rim molds.

The next step was to produce a silicon mold for the internal side of the rim, which provided a satisfactory surface when the rim was laminated. The manufacturing process was similar to the one used for the external rim mold.

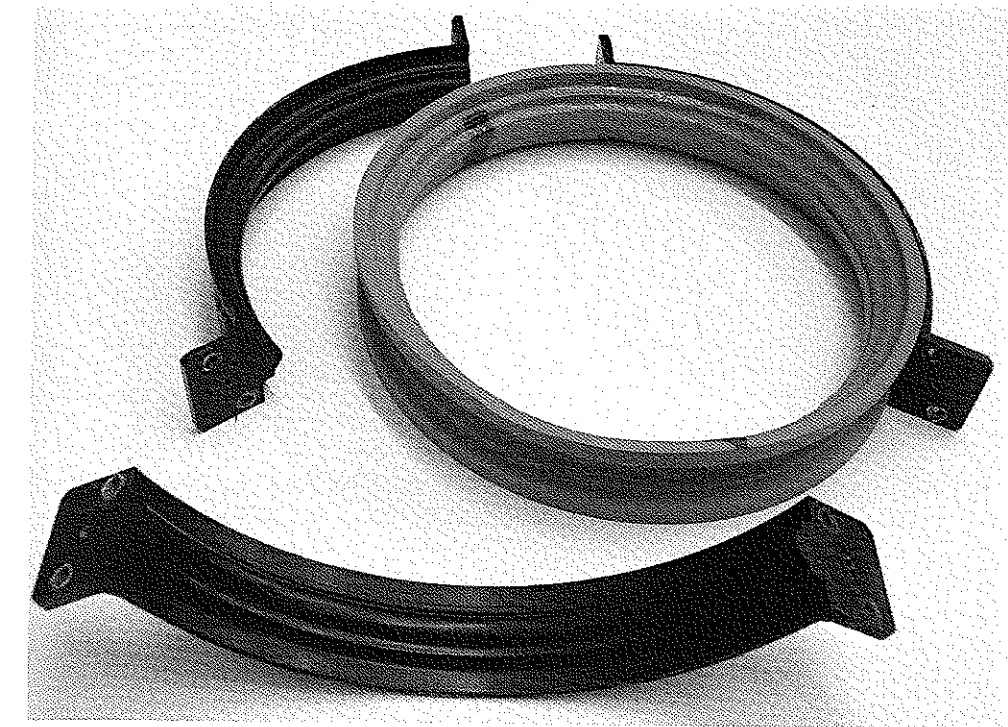


Figure 7-15: The three-part carbon fiber mold used for the external side of the rim (in contact with the tire) and the silicon mold for the internal side.

Manufacturing the negative molds for the side walls involved a similar process. Figure 7-16 shows what these side wall molds look like.

Laminating the wheel parts: rim and walls

All the parts needed to laminate the different parts of the wheel were now ready. Two side walls and a rim were laminated on the prepared molds as shown in Figure 7-17.

Direct vacuum-bagging frequently causes folds to form on a 3D surface. This can be avoided by using the silicon mold to compress the fibers during the lamination and curing processes, which accelerates the production time and significantly simplifies the manufacturing phase.

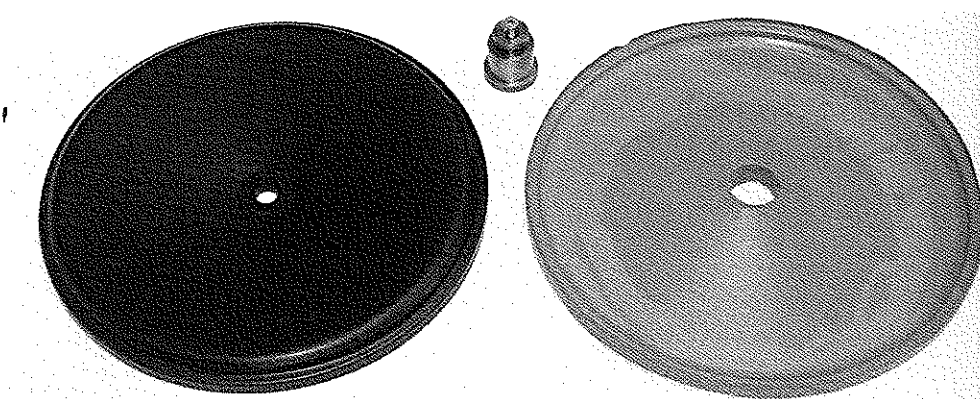


Figure 7-16: The carbon-fiber mold used for the outer side of the wheel wall and the silicon mold for the inner side.

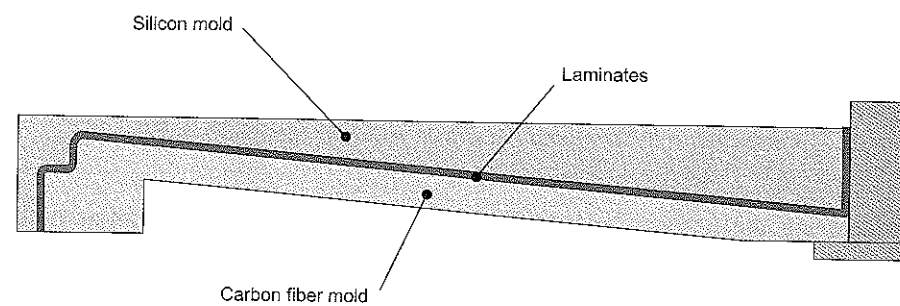


Figure 7-17: Lamination process on composite molds (wheel side wall).

Gluing the laminated wheel parts together

The three parts (two side walls and one rim) were now ready to be glued. The parts were first positioned precisely on a special gluing tool (Figure 7-18). The rim border was fixed with the external supports and the wall was positioned on the center shaft. When the glue hardened, the other side wall was glued in place using the same procedure. Please note that, near the hub, the walls were glued to the rim, but not to one another. The aluminum hub (glued in place later) was used to connect the two walls.

Before gluing the second wall, a small piece of foam was inserted in one of the side walls in the spot where the valve access hatch was later drilled. This foam core was intended to prevent damage to the thin side walls during the drilling operation and later protect the interior of the wheel from dirt and water.

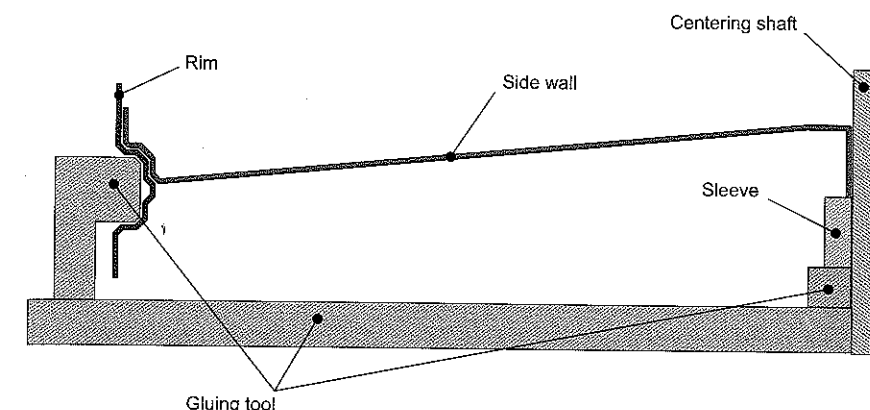


Figure 7-18: Gluing the wheel parts together.

7.4.3. Finishing

The wheel was now ready for the finishing phase. The gluing tool was specially made to fit in a lathe to allow the hub to be machined while the wheel was positioned on the reference surface of the rim. The bearing supports inside the hub were then machined, and the rim's external border cut to the final dimension. Finally, two holes were drilled, one on the rim and one on the side wall. The first one was for the valve. The second one, intended to allow access to the valve within, was covered with adhesive tape to prevent any air turbulence, which would increase drag.

Chapter 8: Front axle & steering system

By Dominik Isler and Jean-Jacques Santin.

This chapter describes and explains the work done to design the front axle and the steering system of the PAC-Car II. The front axle is important because it links the vehicle's two front wheels to its body shell. In Section 8.1, rather than talking about front axles in general, we present the specific characteristics of the PAC-Car II's front axle and explain how it was designed. The PAC-Car II's steering system is composed of two subsystems: the steering mechanism, which connects the steer wheel to the vehicle structure, allows the wheels to be maneuvered, and the steering transmission link, which converts driver input to change the steering angle of the steer wheel. Section 8.2 begins with a list of the specifications for fuel economic vehicle steering systems (Section 8.2.1). Section 8.2.2 presents our analysis of the steering mechanism of a rear steered vehicles, paying special attention to the origins and effects of wheel wobbling, and discusses the choices made for the PAC-Car II's steering mechanism. The last section (8.2.3) focuses on the steering transmission link, presenting and comparing the main technologies and detailing the choices made for PAC-Car II.

8.1. The front axle

Since PAC-Car II is steered from the rear, the rotational axes of the two front wheels remain immobile with respect to the body shell. As mentioned in Section 3.4, these front wheels are tilted, with an 8° inclination angle. As there is also no suspension in PAC-Car II, the front axle is fixed inside the body shell and is thus considered a part of the vehicle structure.

8.1.1. List of front axle specifications

The front axle has to fulfill two main requirements: (1) it must maintain the wheels in the proper position, whatever the forces transmitted from the road to the wheels, and (2) it must be adjustable to allow the wheel alignment to be finetuned.

(1) Wheel position. It is important to maintain the wheels in the proper position in relation to each other, whatever the forces transmitted from the road to the wheels,

because if the angles positioning the wheels change, this has consequences on tire forces and moments and might increase the tire drag (Section 3.4).

(2) Adjustability. The front axle must allow the wheel alignment (toe-in angle) to be adjusted in order to minimize the rolling resistance of the vehicle when it is moving in a straight line (Section 3.5).

8.1.2. Design concept

The axle design concept of PAC-Car II is illustrated in Figure 8-1. As shown in this schematic, the front axle consists of a curved shaft (1) attached to the body's side walls (2) in A and B.

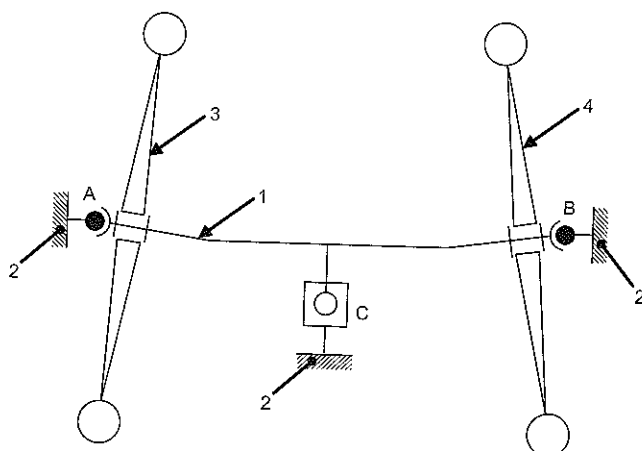
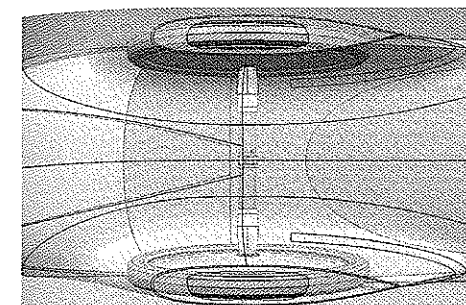
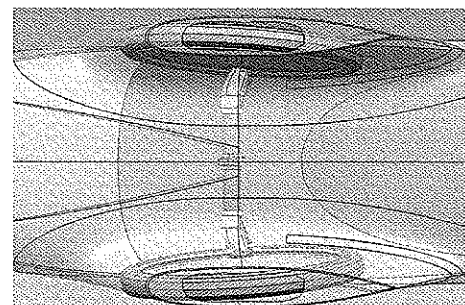


Figure 8-1: Schematic of the PAC-Car II's front axle.

The wheels (3 and 4, see Figure 8-1) are mounted with wheel bearings on the slanted parts of the curved shaft, which determines the inclination angle. With this design, the forces between the two wheels are transmitted through the curved shaft and not through the body shell, which means that the body needs less reinforcement and thus is lighter (see Figure 8-3 (a)).



(a)



(b)

Figure 8-2: Bottom view of PAC-Car II. The front wheels are shown in two different angular positions (a) and (b) in relation to the curved shaft. The variation in the toe-in angle is clearly visible.

The joint in A and B is ball pivot type, which allows the curved shaft to turn around the axle (A, B). This rotation is used to finetune the toe-in angle, as shown in Figure 8-2. The body shell and the curved shaft are connected at the middle of the shaft in C (Figure 8-1) with an adjusting screw. This screw is used to adjust and lock the rotation and thus the wheel alignment. The set of parts in C is called the "mid-body shell interface". The methodology used to adjust the wheel alignment is explained in Section 3.1.3.

The side walls of the body shell, where the ball pivots A and B are attached, behave like membranes; they have very little rigidity perpendicular to the plane (the y direction in the VFCS), and therefore don't hold any lateral forces, although they do hold vertical forces very well (the z direction in the VFCS). Actually, the mid-body shell interface was designed to hold lateral forces, as well as to allow the wheel alignment to be adjusted. The various force flows between the front axle and the body are shown in Figure 8-3.

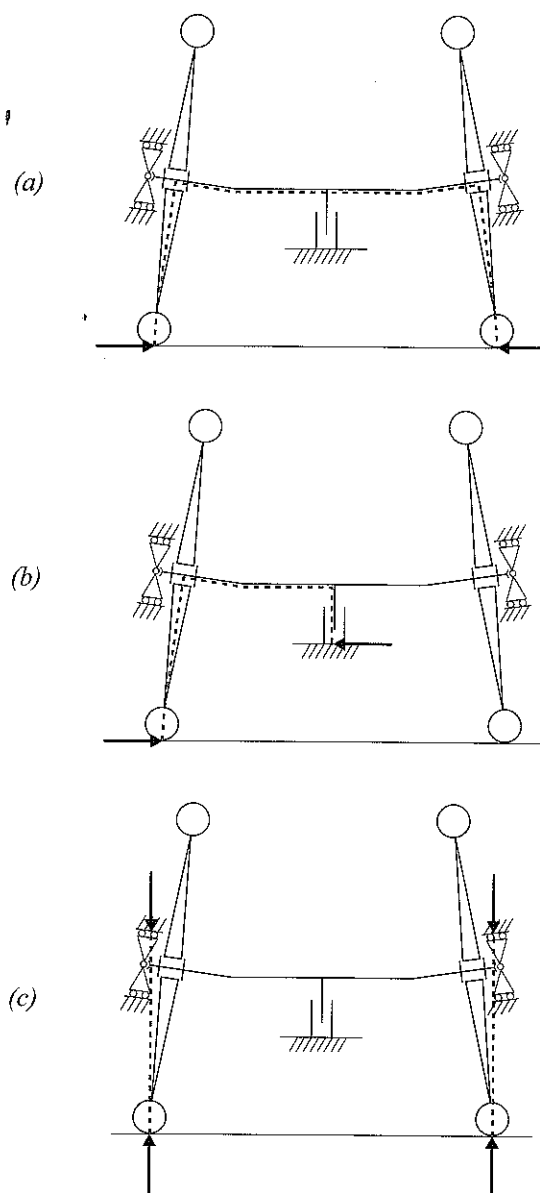


Figure 8-3: Schematic of the possible force flow patterns in the front axle of the PAC-Car II (considered as a free-body).

8.1.3. Construction details

The following figures show some of the details about the construction of the PAC-Car II's front axle.

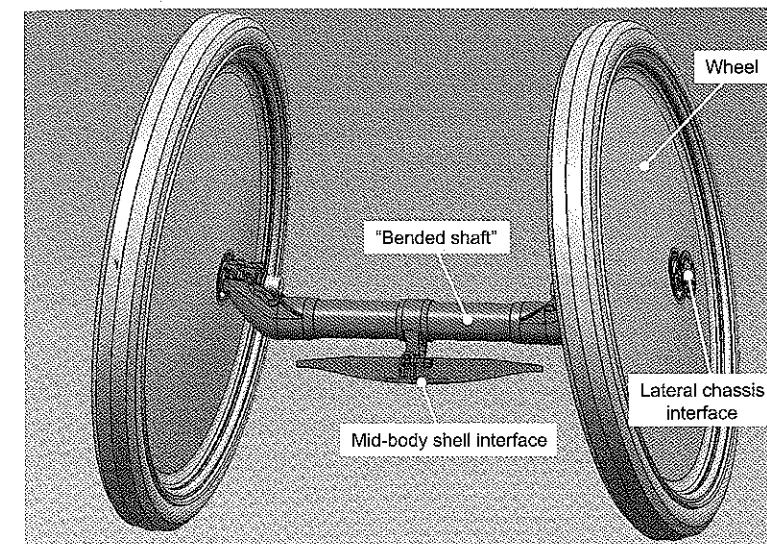


Figure 8-4: Overview of the front axle of PAC-Car II. The body of the vehicle is not represented.

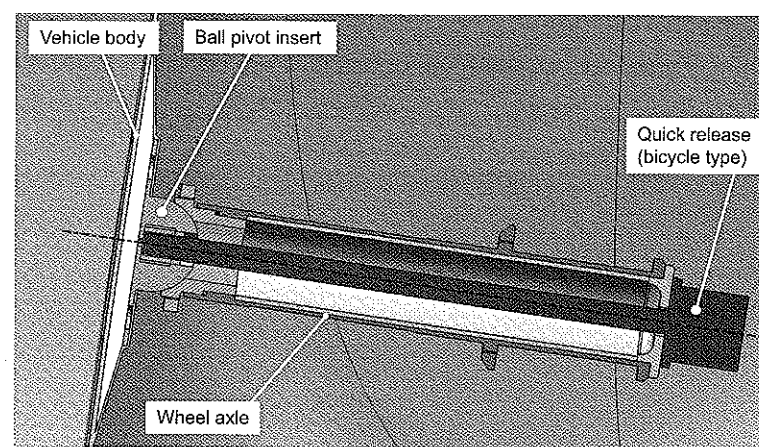


Figure 8-5: Close-up of the lateral body shell interface.

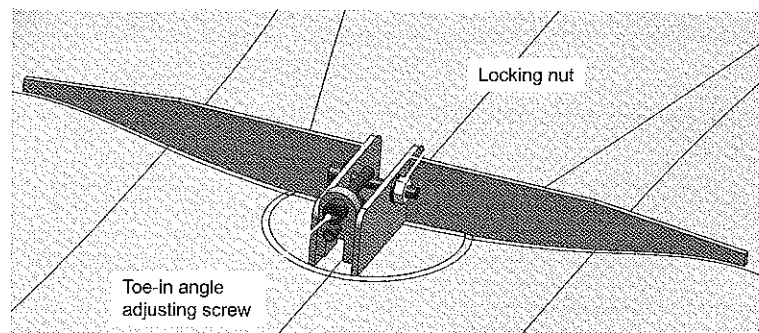


Figure 8-6: Close-up of the mid-body shell interface.

8.2. The steering system

The steering system of a fuel economy vehicle is of primary importance for at least three reasons: (1) it positions the steer wheels properly in order to minimize the total rolling resistance force (see Section 3.5); (2) it is the most crucial component of the driver interface, allowing the pilot to steer precisely and providing feedback about the tire-road contact conditions (sticking or slipping); and (3) it insures the safety of the pilot by providing 100% reliable steering.

PAC-Car II is a rear steered vehicle. This type of steering system was actually an innovation when the University of Applied Sciences Western Switzerland (HES SO) entered their “Consomini” vehicle in the 2003 competition. The year after, the “Consomini” was joined by “Ecomobile 4” from the IUT Nancy-Brabois (Villers-lès-Nancy, France). Even in 2005, the year that PAC-Car II won the competition, such vehicles were still scarce, numbering 5 out of 200 competitors. Choosing the rear-steer-wheel vehicle architecture was one of the most difficult decisions we had to make when designing the PAC-Car II. At the time, this architecture was said to be prone to instability and wheel shimmy. Our responses to these potential problems are discussed in detail in Section 8.2.2.

8.2.1. List of steering system specifications

The main specifications of the steering system for a fuel economy vehicle are listed below:

- S1: in case of two steer wheels, the steering mechanism must change the steering angle of the inner and the outer wheels, while respecting a specific steering kinematics rule (e.g., Ackerman’s);
- S2: the steering interface must have no play, especially in the straight-ahead position;
- S3: when the driver’s steering interface is released, the wheels must automatically return to the straight-ahead position and remain stable in this position;
- S4: the driver must receive feedback on how well or poorly the wheels adhere to the road surface; and
- S5: the steering cannot be subjected to any torques from the drive or brake forces or from irregularities in the road surface.

8.2.2. The steering mechanism

Distances and angles that position the steering axis

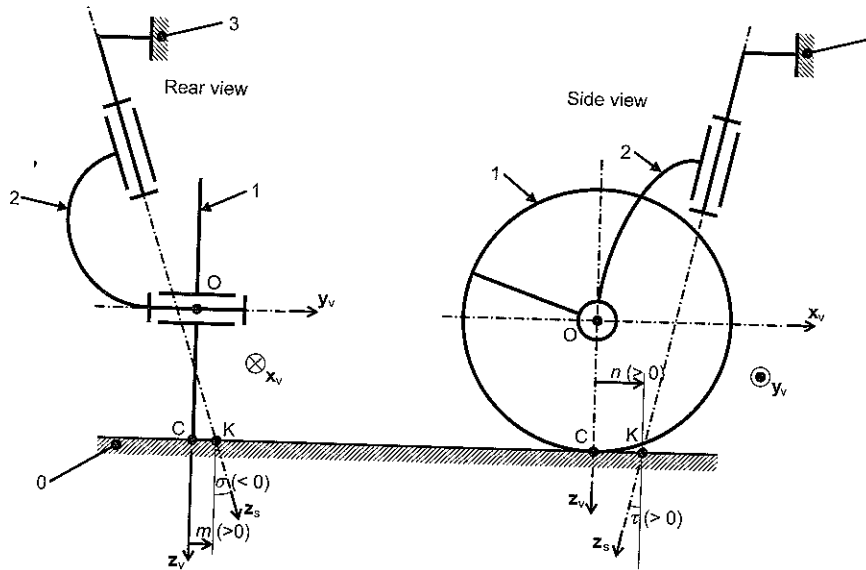


Figure 8-7: Distances and angles that position the steering axis.
0: ground; 1: wheel; 2: hub carrier; 3: vehicle structure.

The parameters that position the steering pivot axis are summarized in Figure 8-7. These parameters are defined below:

- Caster length or mechanical trail n : viewed from the side, this is the distance between the wheel's contact point C and the point K at which the swivel axis intersects the road plane. The parameter is positive if oriented in the direction of the x-axis in the RCAS when the vehicle moves forward.
- Caster angle τ : viewed from the side, this is the angle between the swivel axis and the vertical plane.
- Kingpin offset m : viewed from the front, this is the distance between the point C and the point K. The parameter is positive if oriented towards inside the vehicle and away from C.
- Kingpin angle σ : viewed from the front, this is the angle between the swivel axis and the vehicle's longitudinal plane. This parameter is always positive.

The other angles used in the following discussion are:

- the swivel angle ψ is defined as the rotational angle along the swivel axis z_s , set to zero when the vehicle runs straight. This angle is controlled by the pilot through the steering mechanism;
- the steering angle δ is defined as the angle between the trace of the wheel-center-plane in the road plane and the vehicle's longitudinal plane;
- the inclination angle γ is defined in Section 3.3.2; and
- the slip angle α , is defined in Section 3.3.2.

Instability and wheel shimmy

According to Pacejka [31], "shimmy is a violent and possibly dangerous vibration that may occur in the front wheels of an automobile and in aircraft landing gears. The wobbling of the front wheel of a motorcycle is an unstable oscillatory mode similar to shimmy". This author analyzes both phenomena in detail in the work cited.

According to some fuel economy racers who drive rear-steered vehicles, a phenomenon similar to wheel shimmy is possible if the steering system design is poor. In fact, among the few rear steered vehicles competing, some have had accidents in which they ran off the track because the vehicle became impossible to steer in specific situations (e.g., freewheeling cornering at certain speeds). To avoid such accidents, we paid special attention to this phenomenon. Our analysis led to a number of ideas about what might influence the wheel stability, including:

- the tire-road contact forces and moments;
- the vehicle's centrifugal force;
- the vertical motion of the vehicle's center of gravity;
- the gyrostabilization of the wheel; and
- the rigidity of the steering system and chassis.

These possibilities are discussed in detail below.

Influence of the tire-road contact forces and moments

Consider a caster similar to the one depicted in Figure 8-7, but with the caster angle, kingpin offset and kingpin angle set to zero in order to simplify the analysis. As

explained in the chapter about tire mechanics (Section 3.3.4), if the wheel's direction of travel is not contained in the wheel center plane, a side force F_y and an aligning torque M_z are generated. Figure 8-8 shows a top view of the caster in question, drawn with a positive caster length n . As the wheel-center-plane is located along x_2 and as the direction of travel is x_v (i.e., the vehicle is moving straight), the steering angle δ , swivel angle ψ and slip angle α are all equal.

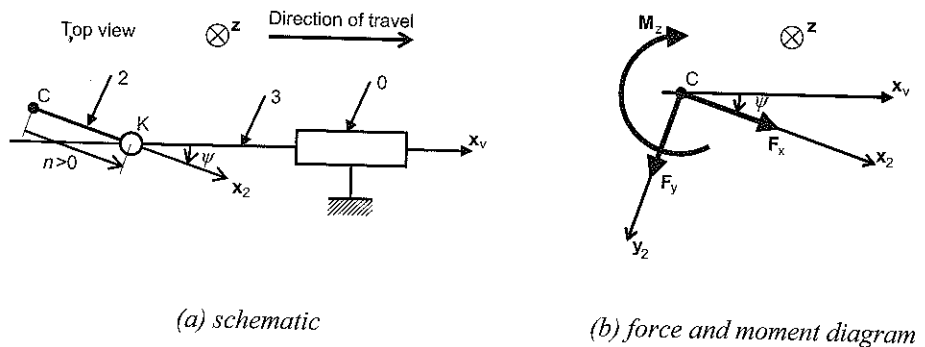


Figure 8-8: simple model of a caster.
0: ground; 2: hub carrier; 3: vehicle structure.

At the contact center C, with a slip angle under 5° , the forces acting on the tire from the ground are:

$$F_y = C_\alpha \alpha y_2 \quad (8.1)$$

$$M_z = -G_\alpha \alpha z \quad (8.2)$$

where F_x represents either the rolling resistance force, the driving force, or the braking force.

At point K, where the swivel axis intersects the road plane, the torque resulting from the previous forces is:

$$\begin{aligned} M_z(K) &= M_z(C) + CK \wedge F_y = -G_\alpha \alpha z + nx_2 \wedge C_\alpha \alpha y_2 \\ M_z(K) &= (-G_\alpha + nC_\alpha) \alpha z \end{aligned} \quad (8.3)$$

$M_z(K)$ tends to affect the steering, making it stable or unstable, depending on its sign compared to the sign of α . If $M_z(K)$ and α have the same sign, the tire-road contact forces tend to increase α , which makes the steering unstable when moving straight ahead. If $M_z(K)$ and α have opposite signs, the tire-road contact forces tend

to decrease α , which makes the steering stable when moving straight ahead. $M_z(K)$ can also remain nil, whatever the value of α , which makes all the steering positions stable. Actually, the problem may be compared to a pendulum problem, in which the following configurations are possible:

- unstable position: a small change in the steering angle from the straight position produces forces that tend to increase the steering angle;
- stable position: a small change in the steering angle from the straight position produces reverse forces (side force and aligning torque) that tend to decrease the steering angle; and
- neutral position: a small change in the steering angle from the straight position has no effect, and the new position is stable.

In the configuration that leads to a stable position, the system can be seen as a mechanical oscillator, which means that (1) after moving away from a stable position, the system moves back to stability after several oscillations; and (2) the system has its own eigen frequency (or natural frequency) that can be excited by an external source of vibration. Thus, these oscillations can be considered as a kind of wheel shimmy.

In the neutral configuration, $M_z(K)$ remains nil if $(-G_\alpha + nC_\alpha)$ is nil, which corresponds to a particular caster length, called the neutral caster length, generated with:

$$n_n = \frac{G_\alpha}{C_\alpha} \quad (8.4)$$

Given the characteristics of the 46-75R16 tire used in the PAC-Car II (see Figure 3-10 and Figure 3-11), at a 6 bar inflation pressure, and depending on the vertical load (respectively 300 and 600 N), the caster length varies from 1.5 to 8.1 mm in front of the contact center. Thus, the torque transmitted to the pilot through the steering mechanism is less related to the tire-road contact conditions (specification S4 in Section 8.2.1).

Now, consider what occurs when caster angle is not nil. If the caster angle τ remains small, the inclination angle γ_ψ that is induced by the steering system may be ignored. However, for larger caster angles, this induced inclination angle causes a side force that, added to the side force produced by the slip angle, can either increase or decrease the overall side force, thus potentially affecting the stability of the caster.

The rotational angle ψ along the swivel axis develops both a steering angle δ and an induced inclination angle γ_ψ , respectively, as expressed in equations (8.5) and (8.6).

$$\delta = \cos^{-1} \left(\frac{-\cos \psi}{\cos^2 \theta + \sin^2 \theta \sin^2 \tau} \right) \quad (8.5)$$

$$\gamma_\psi = 90 - \cos^{-1}(-\sin \psi \sin \tau) \quad (8.6)$$

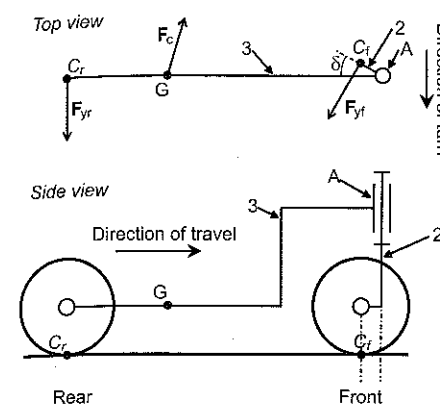
These relations show that:

- the steering angle δ is reduced compared to the swivel angle ψ in conjunction with caster angle τ , whatever its sign;
- when the vehicle is cornering to the right (δ and ψ are positive), a positive caster angle τ generates a positive induced inclination angle γ_ψ , which develops a side force towards the right, which in turn slightly raises the side force towards the right that results from the slip angle. Of course, this side force is also increased when cornering to the left if the caster angle is positive. On the other hand, a negative caster angle decreases rather than increases the side force when cornering either to the right or to the left.

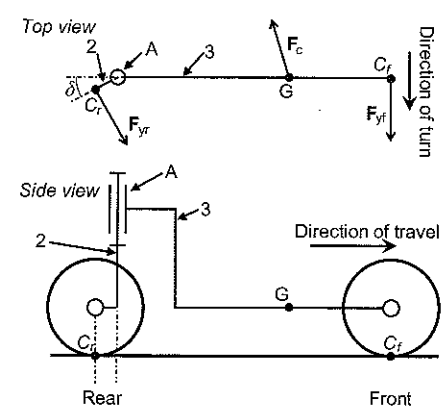
Influence of the vehicle's centrifugal force

When the vehicle is cornering, its center of gravity is subjected to a centrifugal force as explained in Section 4.2 (Equation (4.1)). In the bi-cycle vehicle model described in Section 4.2.2 of that chapter, each tire-road contact center can be considered as a turning point between the road and the vehicle, while the steering pivot is a third point of a deformable triangle.

As shown in Figure 8-9, centrifugal force may not have the same effect on the steering system of a front-steered vehicle as it has on a rear-steered vehicle, despite the fact that these two vehicle types have the same steering geometry (i.e., the same caster, caster angle, kingpin offset and kingpin angle). In Figure 8-9(a), centrifugal force F_c tends to reduce the steering angle δ , meaning that it increases the steering torque the driver needs to apply to the steer wheel when cornering. On the other hand, in Figure 8-9(b), F_c tends to reduce δ , therefore decreasing the steering torque that needs to be applied by the driver, even inverting this torque, which could make the vehicle impossible to drive safely.



(a) front-steered vehicle



(b) rear-steered vehicle

Figure 8-9: Example of the influence of a centrifugal force on the steering mechanism of a vehicle which is turning to the right.

2: hub carrier; 3: body shell; A: steering pivot.

Influence of vertical motion of the vehicle's center of gravity

According to Lejeune-Dirichlet's theorem [32], the positions that have a local potential energy minimum are stable states of equilibrium. This means that if a small change in the steering angle from the straight position tends to increase the height of the vehicle's center of gravity, this position is stable. Conversely, it also means that if a small change in the steering angle from the straight position tends to decrease the height of the vehicle's center of gravity, this position is unstable.

As shown in Figure 8-10, a non-nil caster or kingpin angle may lift the vehicle up or down when the steering angle is changed from the straight position, depending on the geometry.

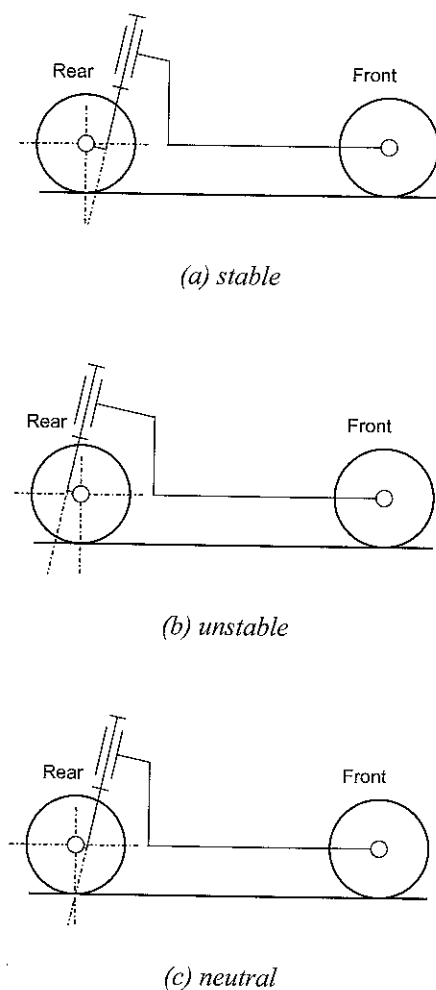


Figure 8-10: Example of a stable, unstable and neutral gravity configuration given a straight steering position in a rear-steered vehicle.

The effect of gravity is of primary importance when the slip angle is very low (e.g., at low speeds or at high turn radii), because the cornering force and the aligning moment are insignificant and therefore have no effect on the steering torque. Of course, the effect of gravity could be counterbalanced by the other effects mentioned in Section 8.2.2.

Influence of the wheel's gyroscopic stabilization

Gyroscopic stabilization is a physical phenomenon that can stabilize an equilibrium that is initially unstable. To do so, a part, generally a disc, is rotated at high speeds around its axis, and then when the disk is pushed out of its initial position, the rotating disk creates forces that counter the initial disturbance. A top is a well-known toy based on gyroscopic stabilization. This phenomenon is also used to stabilize motorcycles.

Due to lack of time, we didn't investigate the influence of gyroscopic stabilization on the rear steer wheel of a fuel economy vehicle. Given the low weight of the wheel (about 700 g for the wheel and 300 g for the tire), its low rotational speed (about 300 rpm), we judged that this factor could be ignored in our preliminary analyses, despite the wheel's large diameter (about 0.5 m).

Influence of the steering and chassis rigidity

The basic model previously considered has a chassis moving in a straight line, without any possibility of even slight lateral or rotational movement. The reality is quite different from this model. Depending on the moment of inertia of the rear steer wheel assembly, the moment of inertia of the overall vehicle, the lateral rigidity of the chassis, the rigidity of the steering mechanism, the driver's behavior, to name but a few factors, energy transfers may occur, possibly engendering oscillations that could induce wheel shimmy.

The vehicle during braking or acceleration

According to tire mechanics, the behavior of a passenger car's steering system is slightly different when braking than when accelerating. We did not analyze the differences between the effects of braking and acceleration for two reasons. First, we assumed that the brakes would never be used, and second, we judged that the acceleration provided by the electric drive motor would be very smooth (see Section 9.2.1), which would allow the driver to master any strange vehicle behavior before it could have any negative consequences.

Steering geometries comparison and conclusion

The above discussion provides an overview of the phenomena that might influence steer wheel stability. With this knowledge, we needed to determine what the best compromises would be for the geometry of a rear wheel steering system.

The influence of the two most important parameters (i.e., caster length and caster angle) are summarized below:

- caster length influences wheel stability via the mechanics of the tire-road contact and via centrifugal force; and
- caster angle influences the induced inclination angle; when combined with caster length, it also influences the vertical motion of the vehicle's center of gravity.

The caster length n can be higher, lower or equal to the neutral caster length n_n . The caster angle τ can be positive, negative or nil. The two parameters make 9 (i.e., 3×3) configurations possible. In order to compare the rear-wheel steering system with the front-wheel steering system, which is a well known system that can be used as a reference value, a front wheel steering system was added to the analysis. Given the parameter choices, 18 configurations were possible. These possibilities are summarized in Table 8-1, in which the columns contain the caster length and the kind of wheel steering system, and the rows contain the caster angle and the criteria. These criteria are numbered from C1 to C4 and ranked in decreasing order of importance:

- C1: tire-road contact mechanics;
- C2: centrifugal force;
- C3: induced inclination angle; and
- C4: vertical motion of the vehicle's center of gravity.

In Table 8-1, the positive, negative or neutral influence of each criterion is shown in white, black and gray, respectively. The "least bad" solution for rear-wheel steering systems and front-wheel steering systems are outlined in blue. Unlike the front-wheel steering systems, there are no rear-wheel steering solutions in which the two first criteria are positive.

The "least bad" solution for a rear-wheel steering system is obtained when:

- caster length is equal to the neutral caster length n_n (or set to nil in the case of lack of information); or
- caster angle is close to zero. (It can be either positive or negative, because due to the low steering angle needed to reach the minimum turn radius, criterion C3 is not very important.)

Table 8-1: Comparison of the possible steering system geometries.

RWS: Rear Wheel Steering; FWS: Front Wheel Steering.

C_i: criterion number (see the text). Influence on stability: White- positive; Black- negative; Gray- neutral.

		Caster length n					
		> n_n		$= n_n$		< n_n	
		RWS	FWS	RWS	FWS	RWS	FWS
Caster angle τ	> 0	C1					
	> 0	C2					
	> 0	C3					
	> 0	C4					
	= 0	C1					
	= 0	C2					
	= 0	C3					
	= 0	C4					
	< 0	C1					
	< 0	C2					
	< 0	C3					
	< 0	C4					

The PAC-Car II steering system geometry

The steering mechanism of PAC-Car II was based on a completely different design concept than the one described above. The reason is that we were worried about the risk of instability that remains with the "least bad" rear-wheel steering solution previously discussed and we looked for something new. We started from scratch and designed a steering geometry, called "triangular steering". Unlike the hypothesis mentioned in Section 8.2.2, in this new geometry, the caster length and caster angle are nil, but kingpin offset and kingpin angle are not nil. The triangular steering system has two main parts: (1) a horizontal wheel axle, with one rod end attached to the body shell; and (2) a nearly vertical rod fitted with two rod ends, the lower one attached to the body shell and the other connected to the free end of the wheel axle. The axle, rod and body shell form the triangle that gives the steering mechanism its name. The system pivots along an axis that passes through the centers of the 2 rod ends attached to the body shell. The vehicle is steered by pushing or pulling the free end of the wheel axle. Figure 8-14 illustrates the steering principle; Figure 8-15 shows two CAD drawings in which some of the construction details can be seen.

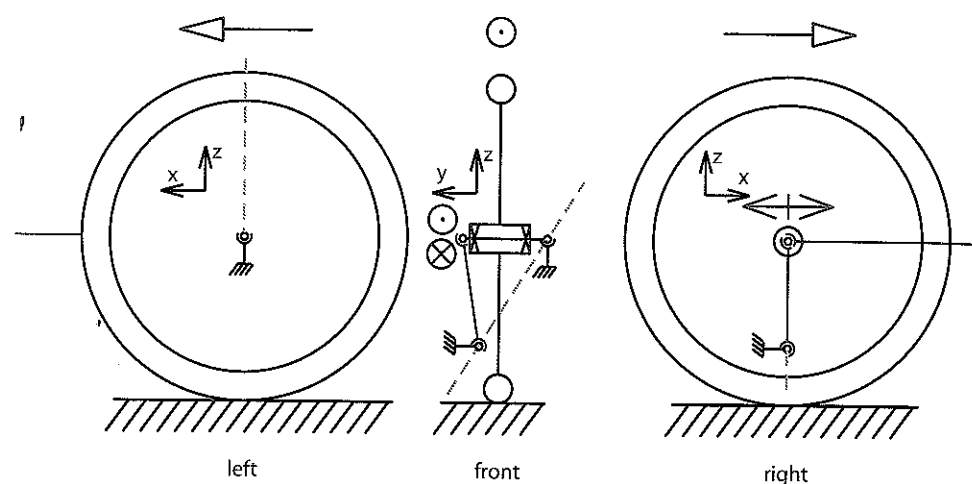


Figure 8-11: Schematic of the “triangle steering” of PAC-Car II.

There are multiple advantages to this triangular steering system:

- it requires less space than the fork system used in the “Consomini” (see Figure 2-3(b)) or the parallelogram system used in the “Ecomobile 4”;
- the body shell interface is very simple and only requires two threaded holes;
- the straight position is very stable since the vehicle is lifted when steered;
- under steering conditions, the wheel’s small induced inclination angle compensates for the torsion of the body shell; and
- simple balance equations suffice to determine the magnitude of the load carried by the two rod ends connected to the body shell. The resulting force flow can be calculated easily, which allows the structure to be designed with the minimum dimensions.

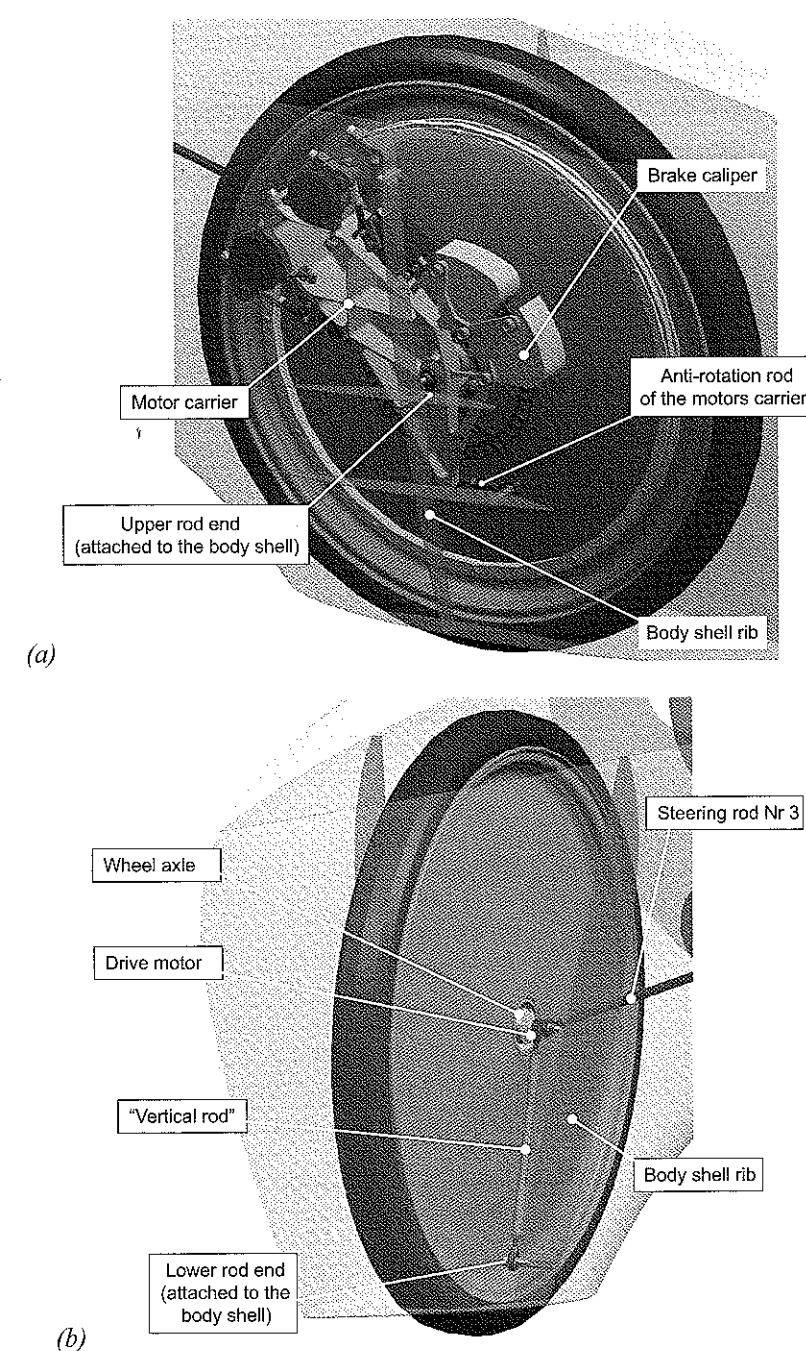


Figure 8-12: Construction detail of the steering mechanism of PAC-Car II.
(a) CAD view of the left side (rear); (b) CAD view of the right side (rear)

In this triangular configuration, the position of the 2 rod ends attached to the body shell and the position of the anti-rotation rod of the motor carrier (i.e., the part that carries the drive motors and brake calipers) must be carefully studied using balance equations to make the steering insensitive to braking or accelerating phases.

8.2.3. Steering-transmission link

Several types of steering-transmission links (e.g., cables or rods) can be used to transmit the steering wheel position to the steer wheels. Some of these links are discussed below.

Cable

What we call a cable is a flexible steel rope like those used in bicycle brakes or derailleurs. This connecting solution is lightweight and makes the steering mechanism design flexible, but also has some drawbacks due to friction between the cable and its sheath and a lack of rigidity that can increase the risk of wheel shimmy and decrease the precision of the steering.

In addition, the cable works under tension (i.e., it can only give something a pull), whereas the cable sheath operates under compressive loads. This makes the cable unsuitable for steering mechanism applications, unless a second cable is used to provide the opposite movement. This dual configuration, called the desmodromic control cable system, is sometimes used for motorbike throttle cables, but is mainly used in lightweight aeronautics for flap control. The rear-steer-wheel FEV, "Consomini" (see Figure 2-3(b)), uses this type of steering mechanism.

Push-pull cable

A push-pull cable is a special type of cable, which, combined with its sheath, provides either a push or a pull. We briefly looked at this solution for the PAC-Car II steering mechanism, but the products we found on the market were too heavy and had too much play when changing from push to pull and vice versa.

Steering-by-wire

The term "steering by-wire" refers to a system in which the steering mechanism is replaced by electric controls. This option sounded great for a fuel economy vehicle since removing the mechanical components of the steering mechanism would reduce the vehicle's weight. We investigated this solution for PAC-Car II and tested it on PAC-Car I after the 2004 competitions. The system is composed of a strong model building servo, linked to the rear steer wheel by a rod. We used an electronic device sold for servo testing to control the position of the servo. As

shown in Figure 8-13, the system looks very simple. The potentiometer that provides the position set point for the electronics could have been replaced by a small and lightweight joystick in the PAC-Car II.

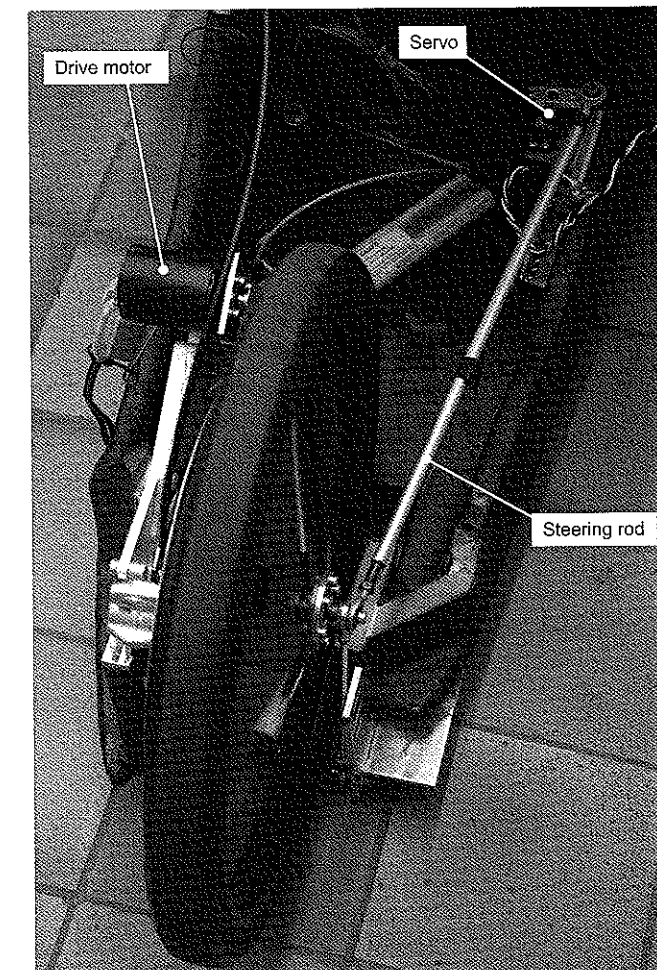


Figure 8-13: Steering-by-wire implemented of the rear wheel of PAC-Car I.

Unfortunately, the tests carried out were disappointing for several reasons:

- the response time of the system was too slow, which made the vehicle difficult to handle, when turning quickly to avoid an obstacle, for instance;
- the electrical consumption of the system was fairly high, even when running in a straight line, and consequently a big additional battery was needed. The

weight of that battery made the solution less appealing, and the battery itself would have been confusing on an electric vehicle like PAC-Car II;

- the system was not sufficiently reliable and it malfunctioned several times; and
- the components used were made for models and not for real vehicles designed to transport a passenger.

In the end, we made what we think was a wise decision and abandoned this idea.

Linkage

The linkage solution consists of one or several rods running from the steer wheel to the driver's steering interface (e.g., steering wheel, handlebar or joystick). These rods can be either pushed or pulled. The solution is lightweight and doesn't have too much play, but allows less flexibility in the design than the push-pull cable since the rods are usually straight and limited in length to avoid the buckling that could occur when the rod is pushed. Though small elbows in the rods are possible, they tend to make the rods less rigid and heavier. Though a single straight rod is too encumbering, two rods can be linked using a lever that can freely turn along an axle attached to the body shell.

The PAC-Car II steering mechanism

The last solution, linkage, was used in the PAC-Car II. Figure 8-14 shows an overview of the system. It has two levers and three rods, running from the steering joystick to the rear wheel. Each rod is made of a carbon tube (7 mm outer diameter, 0.5 mm thick) and two M3 male threaded rod ends.

The driver's steering interface is shown in Figure 8-15. It is a kind of joystick mounted on the right-hand side of the vehicle and always held in the driver's right hand. The only possible motion is a rotation along the axis of the joystick fixation tube, allowing a side-to-side movement that turns the wheels. The first steering rod and lever are also shown on this figure.

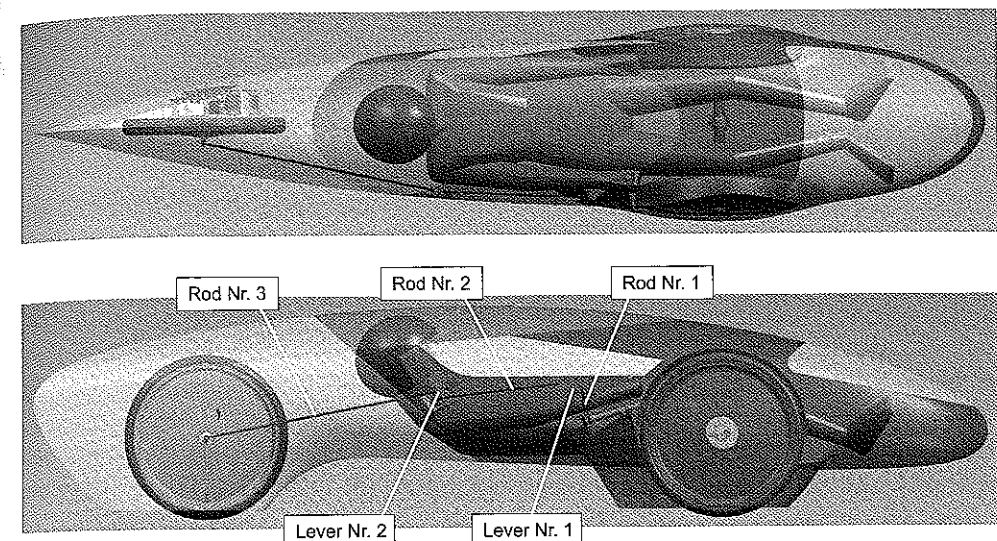


Figure 8-14: Overview of the steering linkage of PAC-Car II.

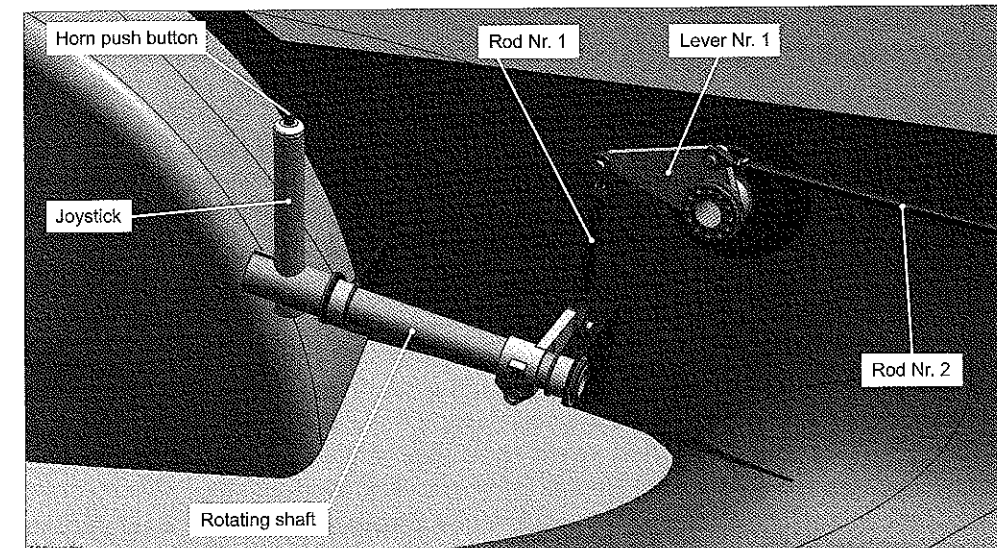


Figure 8-15: Close-up of the steering joystick of PAC-Car II.

Chapter 9: Powertrain

By Dominik Isler & Jean-Jacques Santin.

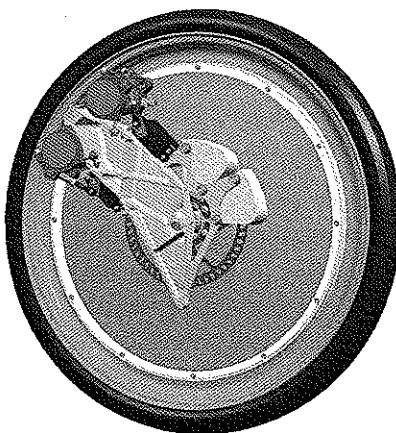
What is usually called the “powertrain” of an electric vehicle is the set of components included in the power path. Basically, the electric powertrain of a fuel economic vehicle can include the following components, listed in order based on the direction of the power flow when driving: the electric generator, the power electronics, the drive motor, the drive train (also called the transmission), the clutch and the wheel. This order, from the motor and wheel, may vary a little from one vehicle to another.

The various sections of this chapter deal with the possible choices and designs for some of these components. Each section is structured in the same basic pattern: specifications, the choices or design possibilities (depending on whether it is an off-the-shelf component or one that is designed specifically for FEV use), and a conclusion providing measurements and possible improvements, for example. Since a discussion of the general FEV case risked being too vague to be valuable, we chose instead to explain and justify our choices for the PAC-Car II. Thus, this chapter reflects our experience, with all of the imperfections of such a real-life project.

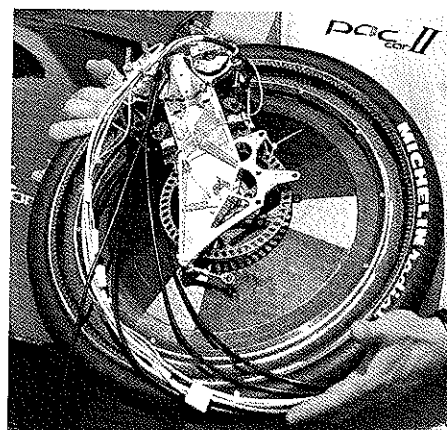
Section 9.1 presents an overview of the PAC-Car II powertrain, describing its general architecture and introducing the technical vocabulary. The first two items on the above list of powertrain components – the electric generator (i.e., the fuel cell system) and the power electronics – are dealt with in a separate chapter (10). This structural choice was dictated primarily by the space needed to examine the subject completely, but was also influenced by the fact that the power electronics used in the drive motor is the same type used in the fuel cell system actuators. Thus, section 9.2 skips to the third item on the list – the drive motor – and presents a range of information, from preliminary specifications to performance efficiency data. Section 9.3 focuses on the drive train, first presenting several possible solutions (e.g., chains, belts and gear pairs) and then describing the gear pair design used in the PAC-Car II. Section 9.4 introduces the clutch system, which allows the wheel to be connected to the rest of the powertrain when power is required and disconnected when it is not. The last section (9.5) concentrates on the braking system used in PAC-Car II because, though they are not part of the power path when driving, from a mechanical point of view, the brakes are a highly integrated part of the PAC-Car II powertrain.

9.1. An overview of the PAC-Car II powertrain

A wall, called the “bulkhead”, divides the interior of the vehicle into two compartments: to the front is the cockpit where the pilot lies and to the rear is the engine compartment that contains the powertrain components. The electric generator and the power electronics are located in the engine compartment. The drive motor, the drive train and the clutch work together to turn with the rear steer wheel. A kind of aluminum beam, called the “carrier,” holds the drive motor, the drive train, the clutch, the brake calipers and the rear wheel together (Figure 9-1).



(a) 3D CAD drawing



(b) The powertrain mounted in the
PAC-Car II, just prior to the attempt to
break the world record
(Courtesy of Dieter Wanke)

Figure 9-1: Overview of the powertrain of PAC-Car II.

With its bearings, the rear wheel is mounted on this carrier in order to prevent any relative displacement, except wheel rotation. The bearing arrangement is nearly identical to the one used for the front wheels (Figure 7-1). Two brake calipers are attached to the carrier and act on the brake disk that is linked to the wheel.

Two slightly different drive motors are used. An internal gear pair is used to transmit power to the wheel. The driven internal gear is attached to the wheel, and the driving pinions are attached to the motor shafts. The motor housings are connected to the carrier via hinges that allow the pinion of each motor to mesh (or not) with the internal gear. These hinges are controlled by two electric actuators, called “servos,” which are themselves controlled by an electronic supervisor on the “main board” (Section 10.3). Three speed sensors measure the speed of each gear

(i.e., the two pinions and the internal gear), providing the information used to mesh each gear pair. The motor speed is controlled until the relative slippage between the pinion and the gear is nil, and then the servo moves the drive motor to perform the meshing without any risk of breaking a gear tooth. The clutch function mentioned in the introduction is used to engage and disengage the pinions and the internal gear.

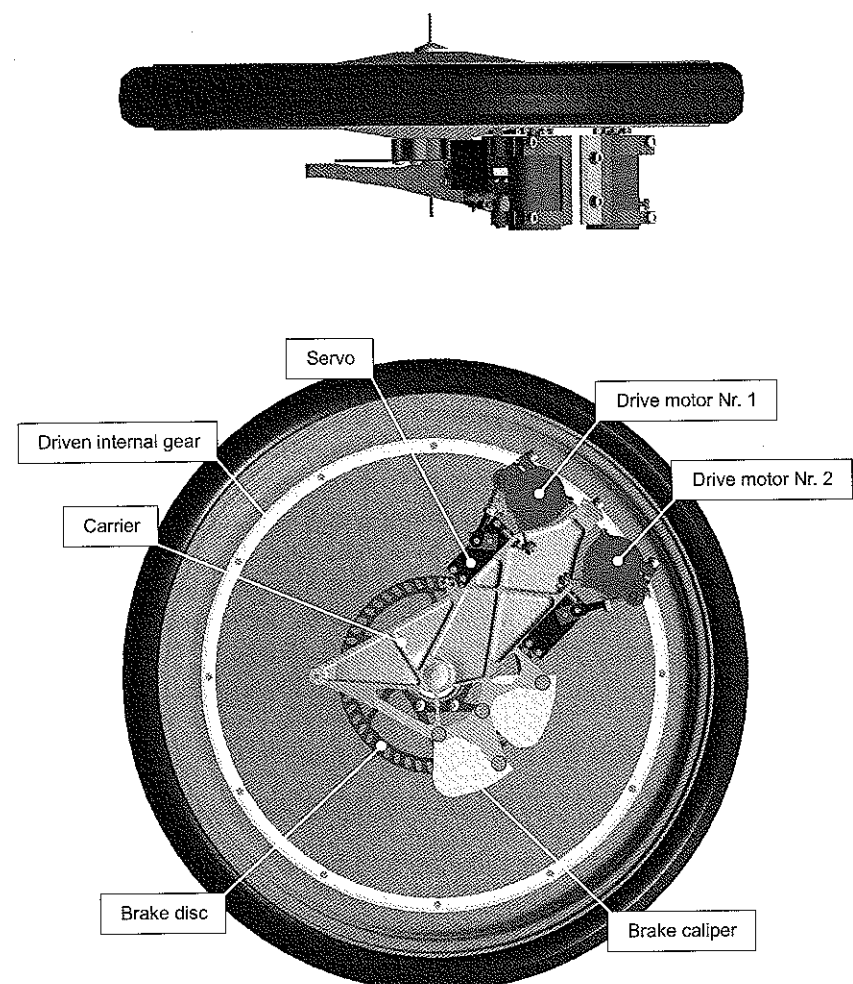


Figure 9-2: Overview of the PAC-Car II powertrain assembly

9.2. The drive motor

As noted in the introduction, the fuel cell system and the power electronics are discussed in Chapter 10. Thus, this section skips directly to the decisions involved in choosing the drive motor. The choice of the drive motor and the choice of the drive train speed ratio are closely connected. Both are iterative processes that require making the right assumptions about the characteristics of a vehicle that has not yet been designed (e.g., aerodynamic drag, rolling resistance force) and about the characteristics of the track (e.g., slopes). In addition, assumptions about the driving strategy (i.e., speed profile) may also be relevant to the choice of the drive motor.

This section presents our discovery process leading to the choice of the drive motor. We felt that such a summary would be more valuable for the reader than a more objective but artificial discussion of the possibilities. Our real experience can later be adapted by interested readers to new projects.

9.2.1. The drive motor specifications

The drive motor specifications defined at the beginning of our research are described in this section. Please note that in 2003, the year in which we wrote these specifications, our intention was to participate in two Shell Eco-marathon races in 2005: Nogaro and Rockingham. A few weeks before the Nogaro event, we had to change the second event and so we went to Ladoux, which explains why we speak about the Rockingham race but not the Ladoux race. Also, at this point, we didn't know as much about the power demand as we did after the research presented in Chapter 11. Finally, though it was already clear that a "stop-and-go" strategy would most probably be adopted, we were unable to define the duty cycle of the drive motor precisely when we wrote these specifications.

Duty cycle

The speed profile of the vehicle during the race was projected as follows:

- launch speed: one start from a full stop to a velocity of 30 km/h (350 rpm on the wheel) for Nogaro; 24.6 km/h (280 rpm on the wheel) for Rockingham
- cruising speed: fifty minutes at a more or less steady speed of 30 km/h for Nogaro; 24.6 km/h for Rockingham
- stopping speed: one stop to 0 km/h at the end of the attempt

Power requirement at the wheel during launching

- Constant wheel torque: 7–10 Nm
- Maximal power: 300 W
- Maximal wheel speed: 350 rpm for Nogaro; 280 rpm for Rockingham

Power requirement at the wheel during cruising

- Speed: 350 rpm for Nogaro, 280 rpm for Rockingham
- Average torque: 2.15 Nm Nogaro, 2.08 Nm for Rockingham

Efficiency

Since the vehicle is operated most of the time at a constant 30 km/h (Nogaro) or 24.6 km/h (Rockingham), the powertrain efficiency must be optimized for those operating speeds. The target average fuel cell-to-wheel efficiency is 90%, which includes the power electronics, motor(s) and drive train efficiencies.

Constraints

- Two different drive trains are possible for Nogaro and Rockingham; alternatively, there can be two different motors or powertrains.
- Voltage available from the fuel cell is 14–18 V DC (Direct Current).
- When no drive power is needed (i.e., on a down slope), the wheel must experience the least possible resistance from the non-powered drive train.
- Maximum feasible drive train ratio (assuming a one-stage drive train) is 25:1
- Total drive train weight (i.e., drive motor + drive train) is less than 1 kg

Possible options

- One or several motors can be used.
- If more than one motor is used, they can be identical or different, or permanently or non-permanently coupled.
- A wheel motor or motor + drive train can be used.

- Either a constant drive train ratio or gearbox is possible.
- Water cooling is possible.

9.2.2. Choosing the drive motor technology

This section presents the motor choices, starting with a discussion of the principle electric motor families and ending with our final choice of two different brush DC motors.

Wheel motor versus motor and drive train

A wheel motor is a slow-speed electric motor, whose nominal speed of rotation tallies with the wheel speed. This technology allows the motor shaft to be directly coupled to the wheel hub, without any speed reducers. The mechanical drive is shorter, which could lessen mechanical energy loss.

Unfortunately, we were unable to find a suitable product in the power range required. The wheel motors we found were large, heavy, and inefficient, whatever their technology.

DC motor versus other motor types

After rejecting the idea of manufacturing our own motor, we conducted a wide investigation of all the available electric motors. According to the Internet and the main manufacturers' catalogues, DC technology appeared to be the most efficient in the power range required (300 W). But there were two types of DC motors available – brush or brushless – and thus we needed to choose between them.

Brush versus brushless motors

At first, the brushless motors appeared to be very interesting: we thought the absence of brushes would reduce friction and the electronic commutation would be more efficient than the mechanical one. Lightweight (about 500 g), efficient (up to 90%) and sold with their own power electronics making the system almost plug-and-play, they were available on the market in the right power range (around 300 W) for model applications, such as radio controlled helicopters. In addition, a few switches allowed the behavior of the electronics to be adapted for a specific application: helicopter, plane or car model. Based on this initial good impression, we decided to test one of these motors on a modified version of PAC-Car I, called PAC-Car I+. Figure 9-3 shows the motor placement in the vehicle.

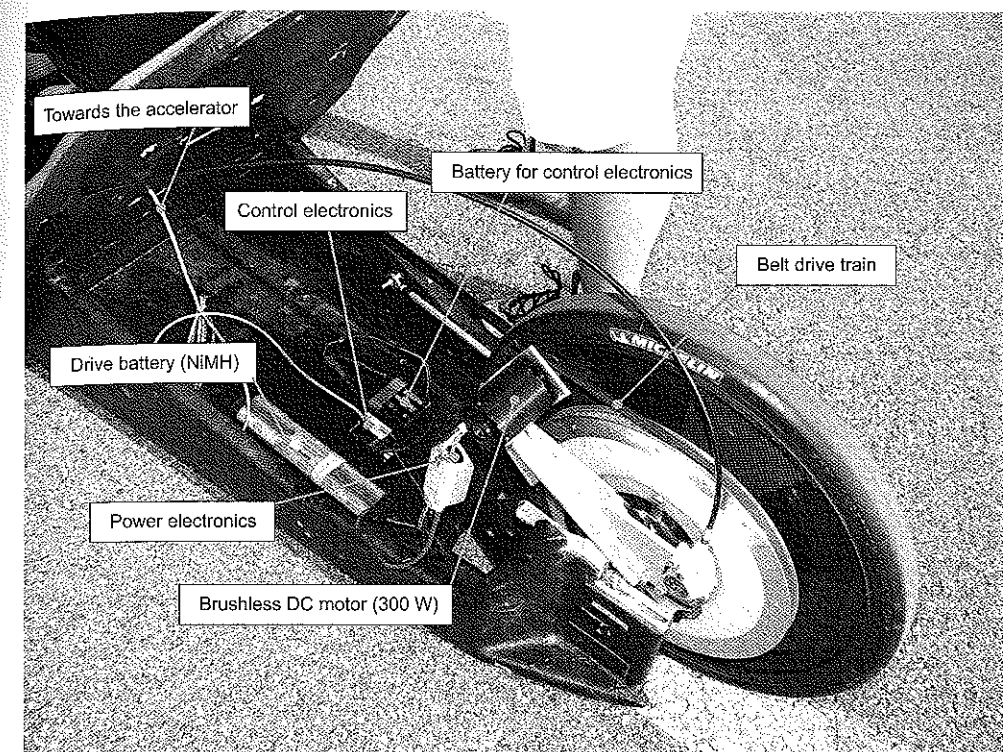


Figure 9-3: Brushless drive motor mounted in PAC-Car I+.

Unfortunately, the results of this test were very disappointing: the motor was unable to launch the vehicle from its full stop position. If the vehicle was moving slowly, or if the pilot was not seated in the vehicle (which made the vehicle lighter), the brushless motor performed satisfactorily. In fact, the inertia of the vehicle was too high for the motor to compensate, and tuning the power electronics (using the switches mentioned above) didn't have any influence on the results. As nobody on the team had any experience with power electronics for brushless motors, we rejected this type of motor definitively.

Choosing the right brush DC motor

A quick review of the brush DC motor manufacturers around the world showed that the motors from Maxon Motor¹³ were the most efficient. The fact that Maxon Motor was a Swiss company helped, because communication would be easier.

A first selection was made from the Maxon Motor catalogue. The power converter was taken into account when choosing the voltage. After a general investigation, it was clear that only the step-down technology would offer the best all-round efficiency. The nominal voltage was set at around 16 V, reflecting the expected voltage of the fuel cell. The motors that did not satisfy the torque requirement, spun too fast or weighed too much were eliminated. The database CD was used to plot the efficiency of the remaining candidates against the torque. According to this graph, the most efficient solution was a pair of 148867-24V Maxon Motor DC motors. For the 16 V application, the efficiency was over 89% (for standard version motors, power converter efficiency excluded) when delivering a power of 40–50 W at a speed of 5500 rpm. These motors are made to turn in only one direction, imposed by the manufacturer, which has a big influence on the powertrain design.

We tested these motors on a test bench to verify their efficiency and to build the maps that would be used later to devise the driving strategy (Chapter 11).

Improving the chosen motors

In order to make them even more efficient, the Maxon motors were specially adapted to include a silver collector, optimized brush spring loading and ball bearings lubricated with low viscosity oil. One motor had increased copper content in the brushes, while the other had brushes of precious metals that were expected to increase efficiency significantly. However, with precious metal brushes, the current in the motor is limited to some 2 A, which is enough to achieve the “cruising” torque but not enough for launching. For this reason, the other motor had graphite-based brushes that would allow the high current needed for launching. Figure 9-4 shows the efficiency curves of these two motors, plotted from our own measurements.

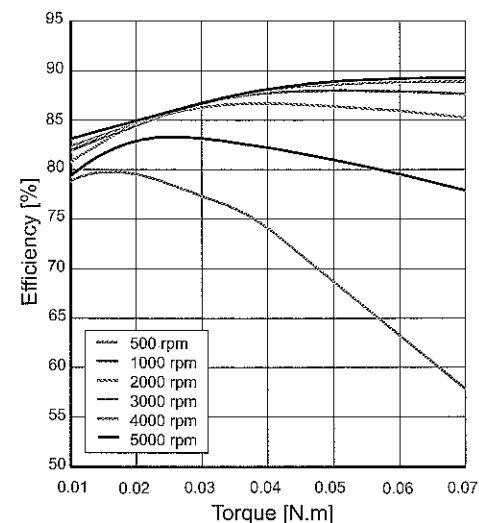
¹³ Maxon Motor AG; www.maxonmotor.com

Two drive motors: the power split strategy

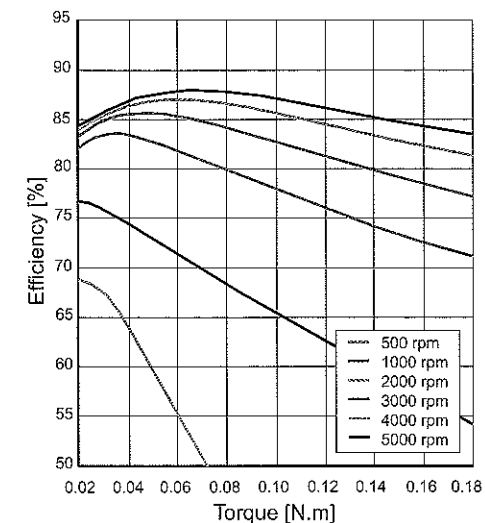
Depending on the power demand, our power split strategy consisted of using the right motor, or both motors, to maximize the efficiency of the entire powertrain (i.e., including the fuel cell system) and keep the motors from overheating.

The first strategy considered called for:

- using the precious metal brush motor (called the “precious motor”) primarily, but with a current limitation of 2 A, which produces a torque of 60 mNm; and
- using the graphite brush motor (called the “improved motor”) to provide an additional boost when the other motor could not satisfy the power demand.



(a) “Precious motor”



(b) “Improved motor”

Figure 9-4: Measured efficiency of the two motors.

The final power split strategy is presented in detail in Chapter 11.

9.3. The drive train

Once the wheel motor solution had been rejected for efficiency reasons, a drive train had to be designed that would provide a suitable speed ratio, allowing the motor to be used at its most efficient operating point as much as possible. The launching capabilities of the powertrain (i.e., the acceleration that it is able to

provide to take the vehicle from full stop position to cruising speed) also had to be considered when determining the speed ratio, although this criterion is secondary as long as the launching time is not too long.

Several types of drive trains are possible, including those driven by gear pairs, chains or belts. The final speed ratio can be obtained in one stage, or several stages, the latter meaning that several types of drive trains can be used in the different stages. In this section, we present the way we solved the drive train design problem, given the options available.

9.3.1. Determining the speed ratio

The idea was to use the motors at their most efficient operating point, employing a start-and-stop strategy in which the motors were used on several occasions for a short time during an ascent, for instance. Given the chosen motors, the problem was the speed, which determines motor efficiency, rather than the torque, which is sufficient in all conditions. In an effort to resolve this problem, we simulated the vehicle's behavior on the track for the expected PAC-Car II characteristics to identify the smallest speed ratio that, combined with a start-and-stop strategy, would allow the necessary average speed to be attained.

Our input was:

- track elevation profiles (data provided by the race organizers of Nogaro and Rockingham);
- vehicle weight: 80 kg;
- drag area: 0.02 m²;
- rolling resistance coefficient: 0.0008;
- motor current limitation: 6 A, with an acceptable overload current factor of 2 that could last up to 30 s.

From that input, we obtained the following results:

- for Nogaro: a speed ratio of 15, start-and-stop speeds of 25 and 29 km/h, an average speed of 30.4 km/h, and a maximum speed of 41 km/h;
- for Rockingham: a speed ratio of 22, start-and-stop speeds of 13 and 16 km/h, an average speed of 25.3 km/h, and a maximum speed of 48 km/h.

Given the significant differences between the results for the 2 races, we decided to manufacture a drive train for each race, with 4 different speed ratios so that we

would be able to adjust the ratio on the spot based on the real behavior of the vehicle and the definitive driving strategy. The four speed ratios for the two drive trains were:

- for Nogaro: 13.5, 14.25, 15, 16.5;
- for Rockingham: 19.8, 20.9, 22, 23.1.

9.3.2. One-stage or a multi-stage?

Whatever the type of the drive train, the higher the speed ratio, the lower the efficiency. The best efficiency is always obtained for a speed ratio of one (i.e., without speed decreases or increases). Based on this logic, theoretically, a two-stage speed reducer could have a better efficiency than a one-stage speed reducer, especially when the speed ratio is high. For instance, a speed ratio of 22 could be obtained with a two-stage speed reducer with twice a 4.7 speed ratio ($4.7 \times 4.7 \approx 22$), but due to the low power range of such an application, the advantage would be offset by the energy losses in the bearings of the intermediate shafts (or idlers) needed for each additional stage. In addition, a multi-stage reducer would be more complicated and heavier, just because it requires additional parts.

Given this analysis, we rejected the idea of a two-stage reducer, with a first stage integrated in the motor (e.g., a gearhead module). In any case, the efficiency of such a gearhead module is close to 90%, regardless of its technology or brand, which is already out of our specifications.

9.3.3. The choice of the drive train technology

The three possible drive train technologies were: belts, gears and chains. The primary decision criterion is drive train efficiency. Comparing the efficiency of several drive train technologies for the general case is almost impossible because efficiency measurements are quite sensitive to operating conditions. Even when these conditions are well known, theoretical efficiency calculations are usually not precise enough to allow the best solution to be chosen, and thus experimental investigations remain the only means of evaluation that can be trusted. Unfortunately, in the case of a newly designed vehicle, time for such experiments is always short, and the art of the engineer is to intuit the solution with the most potential.

By comparing the figures provided in the catalogues of the major drive train manufacturers, we estimated that the best efficiency ratings for the different possible solutions – assuming the best operating conditions, including a speed ratio of one – are as follows:

- belts: 99% for a Powergrip HTP synchronous belt [33];
- gears: 99.9% [34] (see Section 9.3.5);
- ¹ chains: 98.5% for a precision roller chain, 99.7% for an HV inverted tooth chain [35].

For PAC-Car I, the belt was the best solution. Belt systems are lightweight, low cost, offer more design flexibility, and require no lubrication. As the goal of PAC-Car I was to investigate the potential of fuel cell technology in a FEV, the efficiency of the drive train was of secondary importance.

However, for PAC-Car II, the situation was slightly different. The main parameters for choosing the drive train were efficiency and weight. From this perspective, a gear system appeared to be the solution with the most potential. The fact that all system parameters (e.g., geometry, materials and coatings) could be chosen to respond to our precise needs was an added bonus.

Since the gear solution met our needs, the chains used most often in FEV were not investigated at all.

The next two paragraphs provide detailed information about the way we managed the design of the two drive train technologies we investigated: belts and gears. The belt solution is described briefly (Section 9.3.4) since it was only used in PAC-Car I, whereas the description of gear pair solution used on PAC-Car II (Section 9.3.5) is very detailed.

9.3.4. Belts

As stated in the previous section, belt drives were used in PAC-Car I. Despite the absence of top efficiency ratings, this type of drive train is still a very attractive solution for use with an electric drive motor.

We studied belt drive systems for the two main versions of PAC-Car I. Remember that PAC-Car I raced a total of 3 times in 2003 and 2004. After its last race, PAC-Car I was equipped with a rear steer wheel and a brushless motor and renamed "PAC-Car I+". Both versions of the vehicle used a synchronous belt instead of other drive belts. Although synchronicity between the angular position of the drive wheel and the motor is obviously not required, we chose this type of belt rather than the flat belt or the V-type belt, for example, because it had the best efficiency rating in its class and required a lower initial tension.

Figure 9-5 shows the system used in the 2003 PAC-Car I. The belt was a 9 mm wide Powergrip HTD from Gates¹⁴, with a 3 mm pitch standard metric type (i.e., 3M). The small pulley had 18 teeth; the large one, 306. A rotary belt tensioner was used for 4 reasons: (1) it increases the number of teeth in the mesh up to the minimum needed to transmit the launching torque without risk of jumping a tooth; (2) it provides a consistent tensioning force; (3) it provides a large center distance tolerance and allows the belt to be mounted and dismounted without changing the center distance; and (4) its fully automatic take-up action provides nearly constant tensioning force and avoids radial overload on the motor shaft resulting from the unavoidable radial run-out of the large pulley.

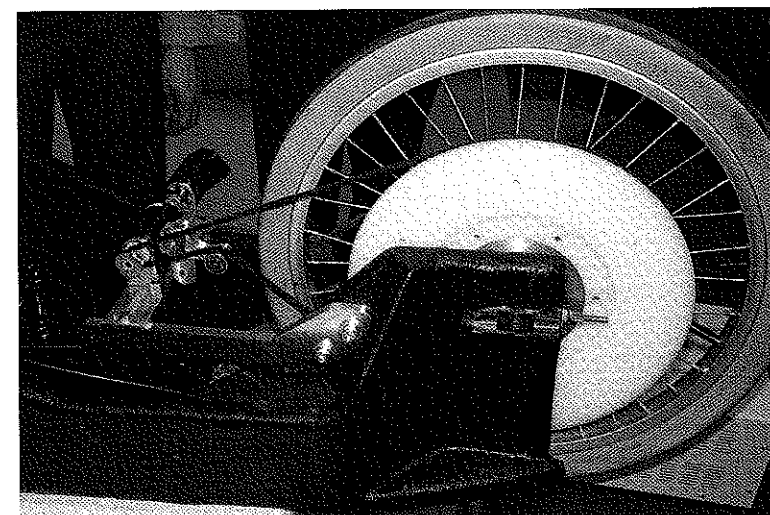


Figure 9-5: The PAC-Car I belt drive train.

Obviously, the tensioner is a major source of energy loss; we tried to eliminate this energy loss in the solution used in PAC-Car I+ (Figure 9-3). As we half expected, a few tooth jumps then occurred, which was not critical for vehicle that wasn't destined for competition racing.

Another problem with the belt drive is the large pulley. The number of teeth needed is too high (306) for it to be available on the market, which offers a 200-tooth maximum. Furthermore, the pulley is too large to fit in the machine tools used for cutting such a product and thus no manufacturer can produce it. The

¹⁴ www.gates.com

alternative is to manufacture it, tooth-by-tooth, on a CNC machine, which is a fairly long process given the smallness of the teeth. An alternative to the tooth-by-tooth solution is to cut one tooth every two or three teeth, or not to cut them at all (!), which is conceivable only if both the belt tension and the contact length between the belt and the pulley are sufficient to transmit the torque.

9.3.5. Gear pairs

The gear pair was the solution chosen for the PAC-Car II drive train. The details of our choice are explained below.

Specifications

The detailed drive train specifications are given in Section 9.2.1, but can summarize as follows:

- parallel shafts;
- peak torque on the driving gear: 360 mN.m, from null speed, produced by the stronger electric motor (Maxon Motor 148867) for 20 or so seconds;
- continuous maximum torque: 181 mN.m;
- service life: 500 km;
- maximum pinion speed: 5600 rpm;
- speed ratio: 1:15 for the Nogaro race, 1:22 for the Rockingham race.

The last element means that drive train is a speed-reduction gear set. The smaller gear, called the pinion, is the driving gear, and no torque reversal is expected. The larger gear, called simply the gear, is the driven gear. The solution presented here is the solution used for the race in Ladoux (Figure 9-1). It had an exact speed ratio of 11:210 (about 1:19.1).

Efficiency model

According to Henriot [34], the equation that describes the efficiency η of a parallel spur gear (involute shape) has the following form:

$$\eta = 1 - f_m \left(\frac{1}{r_1} \pm \frac{1}{r_2} \right) \frac{g_f^2 + g_a^2}{2(g_f + g_a) \cos \alpha} \quad (9.1)$$

where f_m is the friction coefficient, r_i is the pitch circle radius with $i = \{1;2\}$ representing the gear number, g_f is the length of approach path, g_a is the length of recess path, and α represents the pressure angle.

The symbol “±” means “+” for external gear pairs and “-” for internal gear pairs.

Equation (9.1) shows that the gear efficiency is higher if:

- an internal gear pair is used instead of an external gear pair;
- the friction coefficient is minimal;
- the gear diameters are maximal;
- the module is minimal (part of g_f and g_a); and
- the g_f and g_a are equal.

The following paragraphs examine, in reverse order, how the above conditions can be attained.

Equal values for g_f and g_a : This condition is easy to obtain by adjusting the tooth geometry using the addendum modification coefficient for each gear.

Minimal module: This parameter determines the tooth size. The lower limit is given by the mechanical durability, namely gear-tooth strength and gear-tooth surface durability. This limit is discussed in more detail below.

Maximal gear diameters: This condition is also easy to obtain, but works against size and weight reductions. As is explained later, the window for adjusting this parameter is fairly narrow for the FEV case, mainly because of the high speed ratio required.

Minimal friction coefficient f_m : This is the most sensitive parameter. As usual in mechanical engineering, the friction coefficient must be understood as an average value. It is not uniform during the gearing sequence and depends on several parameters, such as material pairs, surface roughness, lubricant viscosity, and sliding speed. According to Kelley [34], the friction coefficient f_m is usually between 0.02 and 0.07, with a typical value being 0.04.

Internal gear pair instead of external gear pair: Both types of gear pairs can be used in FEV, but internal gears are more expensive, and the energy savings achieved by using them can be ruined by the poor surface quality due to the cutting process, since internal gears cannot be ground and polished.

Design procedure

Once the gear solution had been chosen, we needed to choose between the different types of gears available. We rejected the helical gear pair in favor of a straight spur gear pair despite the higher efficiency and quiet movement of the former for three main reasons: (1) the efficiency of an helical gear appears to be only slightly better than a spur gear [34]; (2) quietness is not a priority for FEV competitions; and (3) helical gears cause additional mechanical design constraints, especially with respect to the motor, since the gear shafts are subjected to a thrust load when power is transmitted.

Figure 9-6 shows the procedure used to design the gear pair used in PAC-Car II.

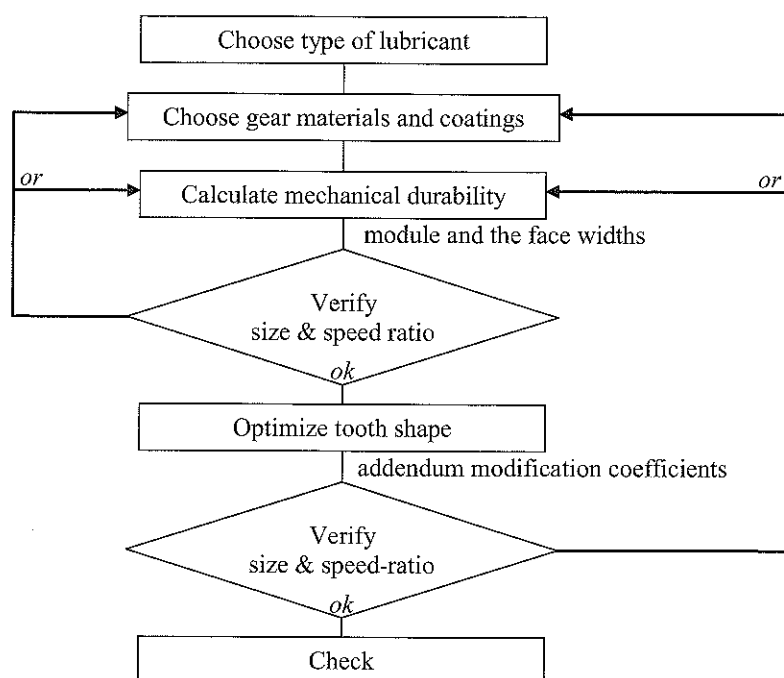


Figure 9-6: Procedure followed to design the PAC-Car II gear pair

The following sections examine each phase of the design procedure.

Lubricant type

The friction coefficients indicated by Kelley [34] suppose the use of a lubricant. Given the maximum rotational speed of the pinion (5600 rpm), oil or grease was

rejected as a lubricant: either one would have been expelled almost immediately due to the effect of centrifugal forces. A special device could have been added to lubricate the tooth surfaces during the gear mesh, but that would have required adding an oil-tight housing, which would have increased the weight and the complexity of the drive train system. Finally, we decided that a lubricated gear pair would be inappropriate for such a FEV.

Given this decision, we had two options. Either we could use materials that had a low friction coefficient, or we could use materials with a high degree of mechanical durability, in which case an antifriction coating would meet the friction specifications. In the end, we chose the second option, but not until we had eliminated several promising materials in the first.

Materials

As mentioned above, the materials themselves can have a low friction coefficient. Two in particular drew our attention: the plastics PTFE (PolyTetraFluoroEthylene) and POM (PolyOxyMethylene).

Given a contact pressure of 0.5 kg/cm^2 and a sliding velocity of 0.6 m/s , the friction coefficient of PTFE in contact with hardened ground steel has a very low coefficient of 0.09 [36]. Under the same conditions, POM, a material commonly used for plastic gears, has a dynamic friction coefficient of 0.34, which is too high [36]. Eventually, both materials were rejected primarily because their mechanical properties were unsuitable for transmitting the necessary torque using a tooth module that was compatible with the speed ratio. In every test, either the number pinion teeth was too low or the gear tip diameter was too large (actually larger than the wheel!). Using fillers [37] (e.g., fiber-glass) helped a bit by extending the load-carrying characteristics, while leaving the friction properties unaffected, but this was still insufficient. However, there was another reason for rejecting the plastics. In fact, the mechanical method used to design plastic gears is not described as often in the literature as the one for designing steel gears, and we felt that using anything other than steel would have been too risky.

Once this decision had been made, it seemed that the best choice would be to use materials with the specified mechanical durability, adding an antifriction coating to keep the friction coefficient under control.

In order to identify the best lightweight materials, we used the selection procedure suggested by Ashby [38]. Analyzing the FEV application led us to consider three performance indices that would minimize vehicle weight and take endurance (cyclic strength), elasticity (no irreversible strain) and hardness (contact pressure) into account. Inserting these indices into a global materials database, we found that laminated glass- or carbon-fiber materials ranked first, while the titanium alloys

and wrought stainless steels most commonly used in mechanics ranked second. Polymer materials took last place. After considering the parts manufacturing process, and consulting with the gear manufacturer, we pragmatically chose heat-treatable steel 42 CrMo 4 (AISI 4140), which was heat-treated before machining.

Anti-friction coatings

To determine which anti-friction coating would best serve, we investigated the properties of various antifriction coatings. The two that most drew our attention were Niflōr® and Cavidur®.

The Niflōr® coating is a few tenths of a millimeter thick, composed of a 25% volume of PTFE (PolyTetraFluoroEthylene) in an electroless nickel matrix. In contact with steel, it has a friction coefficient of at least 0.1 without any lubricant [39].

Cavidur® is a special type of amorphous carbon-based DLC (Diamond-Like Carbon) coating and is usually between 2 and 4 micro-meters thick. It is applied at temperatures below 200 °C using plasma-assisted chemical vapor deposition techniques. DLC coatings have a hardness coefficient comparable to and exceeding that of TiN coatings, a very low friction coefficient, and high wear resistance due to self-lubricating properties. In contact with steel and under dry conditions, the friction coefficient of DLC-type coatings is lower than 0.1 [40-42].

Given our materials choice, Cavidur® promised to provide the best friction coefficient for our FEV gears.

Mechanical durability calculations

We used the standardized method NF E 23-015 (Calculation of load capacity for cylindrical external gears for general use) [43] to calculate the mechanical durability of our chosen materials. This method takes gear-tooth strength and gear-tooth surface durability into account. The calculation indicated that a heat-treated steel gear with a 5 mm surface width could be used if its module was at least 0.5 mm. This very small module is mainly due to the smooth, low-level torque provided by the motors.

We chose a 0.8 mm module, trying to balance the following three conditions: (1) a reasonably small number of teeth on the pinion (18 is usually the minimum for a 20° pinion pressure angle); (2) a reasonably small module (the smaller the module, the higher its efficiency); and (3) a reasonably large module (the smaller the module, the more precise the shaft positioning must be).

Size and speed ratio verifications

The three size constraints that needed to be verified were: (1) the gear tip diameter had to be compatible with the powertrain design, and with the wheel diameter in particular; (2) the pinion tip diameter had to be compatible with the motor shaft diameter and its fixation device (expansive shaft coupling in our case); and (3) the surface widths of the gears and the pinions had to be compatible with the room available inside the engine compartment, since the PAC-Car II motors are quite long and are attached to one side of the rear wheel.

The desired speed ratio (determined by the preliminary fuel-efficiency simulations) cannot normally be obtained exactly because the final speed ratio is a fraction of the number of teeth, which are standardized to conform to machine tool manufacturing limitations, meaning that not all numbers can be used. For instance, we would have liked to use a gear with 421 teeth (prime number), but we had to be content with a 420-tooth gear.

Tooth shape optimization

When the number of teeth, the module, the helix angle and the surface widths had been chosen, there were still two parameters that had to be adjusted: the addendum modification coefficients for the two gears. As the center distance can be freely adjusted in our application, the two addendum modification coefficients were independent, allowing them to be chosen in such a way that the approach path length and the recess path length were equal. This independence is accompanied by two constraints: (1) to avoid cutter interference, the addendum modification coefficients must remain in a standardized range that depends on the number of teeth; and (2) to avoid meshing interference, the gear parameters must fulfill certain inequalities. (These constraints are described in detail in the NF E 23-015 standard [43].)

In order to compensate for the non-parallelism between the two gear axles, crowning teeth were manufactured on the pinion. Since this kind of tooth shape can only be manufactured on a grinding machine, crowning teeth cannot be used on an internal gear. They would also have been incredibly expensive to manufacture on an external 420-tooth gear! The table below (Table 9-1) summarizes the final geometric characteristics of the gears used in Ladoux.

Gear manufacturing process

The following procedures were carried out to produce the gears, including the pinion.

- Twenty-two-tooth pinion: turning of the blank part (reaming of the diameter 10H7 included), machining of the teeth, grinding of the crowning teeth, polishing in a plunge finisher, with an expected surface roughness better than $0.1 \mu\text{m}$ (center line average height), addition of the Cavidur® B coating.
- Internal 420-tooth gear: cutting of the blank part, machining of the teeth with a specified surface roughness of $1.6 \mu\text{m}$ (center line average height), polishing in a plunge finisher with a specified surface roughness better than $0.1 \mu\text{m}$ (center line average height), addition of the Cavidur® B coating.

Table 9-1: Characteristics of the PAC-Car II gear pair drive train, as configured for the race at Ladoux.

	pinion	gear
type	external gear	internal gear
face width [mm]	7	5
normal module [mm]	0.8	
normal cutter pressure angle [$^\circ$]	20	
number of teeth	22	420
basic rack	NFE 23-011	
helix angle on the reference circle [$^\circ$]	0	
cutter diameter [mm]	17.60	336.07
addendum modification coefficient	+0.430	+0.472
precision	7 (NFE 23-006)	
pitch center distance [mm]	159.23	
additional information	crowning teeth	
material and coating	heat-treated 42 CrMo 4 (ANSI 4140) Cavidur® B	

Gear fixation

The driven gear was fastened with screws to a supporting ring made of aluminum, which was glued on one side wall of the rear wheel. The pinions were fastened on the motor shafts using a cone clamping device.

Gear positioning

Any angular error between the axles of the gear pairs leads to additional transmission loss. However, a small variation in the center distances has no influence on efficiency.

Poor positioning due to the part manufacturing process may be compensated during the assembly phase. The main problem comes from the deformation of the parts that are involved in positioning the gear axles, which are mainly the rear wheel – since the gear is fastened on it – and the carrier. Wheel rigidity has already been discussed in Chapter 7, and so we won't mention it again here. Since carrier rigidity is also important, the carrier was designed to minimize the displacements resulting from the motor torques. Figure 9-7 shows an example of a displacement map calculated for the latest version of the carrier using FEM software.

Conclusion

Thus, the PAC-Car II drive train in its configuration for the race in Ladoux, consisted of a self-lubricating internal gear pair with a calculated efficiency of about 99.5%, and a weight of 350 g without the fastening parts.

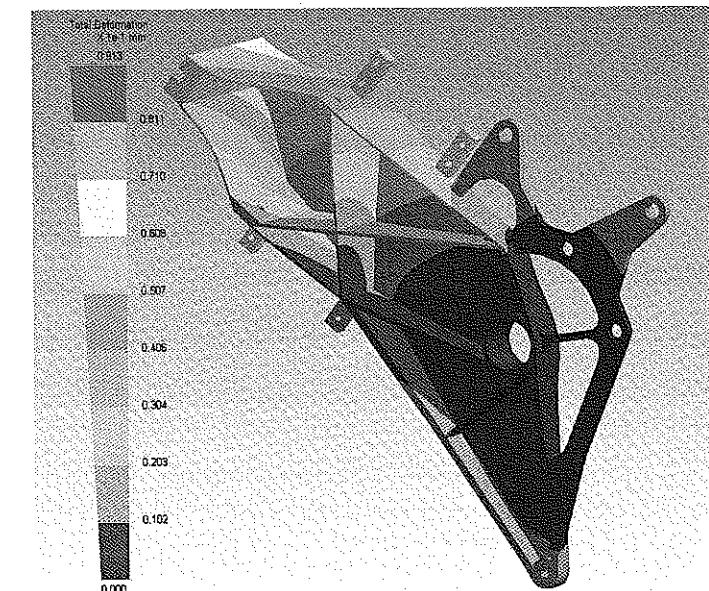


Figure 9-7: Displacement map of the carrier while the two drive motors deliver full torque (based on FEM simulations).

9.4. The clutch

The automotive clutch is a power transmission component located between the IC engine and the input shaft of the gearbox. It is required because of one of the drawbacks of the IC engine: it is unable to deliver drive torque under a speed of about 800 rpm. The clutch thus transmits the drive torque while compensating for the relative slippage that occurs during the vehicle launch phase, when the wheels are not yet in motion. The drives of electric motors are different since they provide full torque even at a full stop, making a slipping clutch useless in a vehicle like the PAC-Car II.

However, because of the chosen “stop-and-go” driving strategy, other clutch types can be used to reduce energy loss when the vehicle is gliding and thus no drive power is being delivered. The idea is to disconnect the powertrain from the wheel to avoid driving the wheel to no purpose.

9.4.1. One-way and jaw clutches

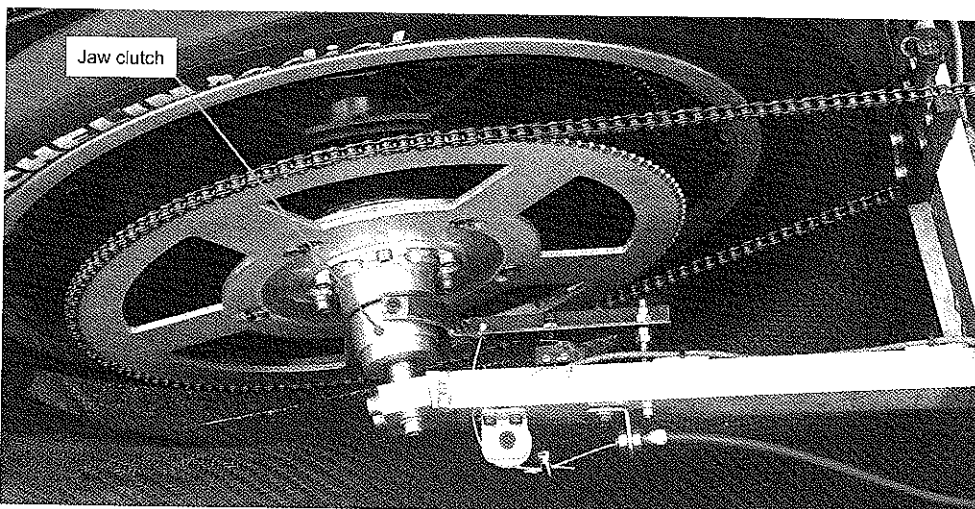
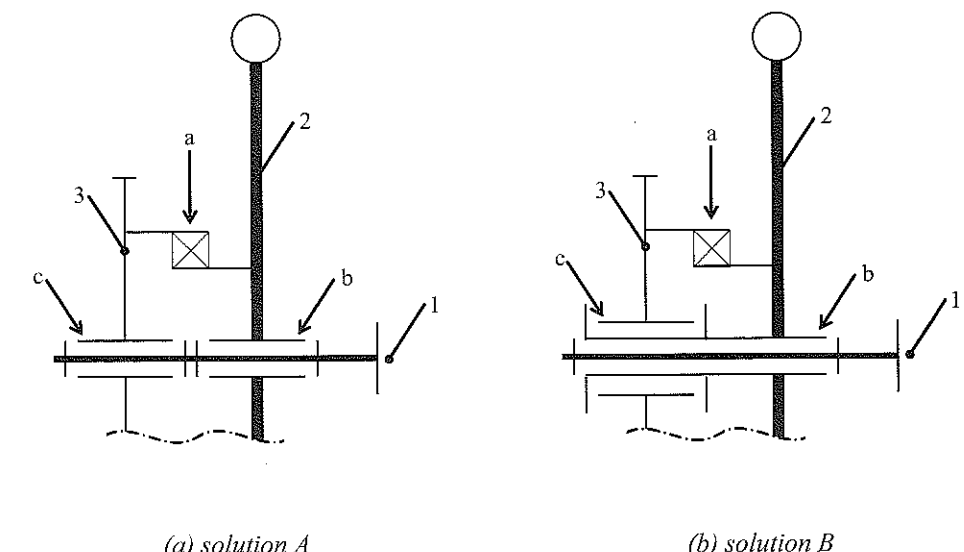


Figure 9-8: Cable-controlled jaw clutch.

The solutions usually used on fuel economic vehicles are one-way (or freewheel) clutches and jaw clutches (Figure 9-8). Such clutches are mounted in the wheel hub, like the overrunning clutch on a bicycle, thus lowering the number of drive train parts that are not driven when the clutch is open.

A freewheel is a power transmission element that mechanically disengages the driving shaft from the driven shaft automatically when the driven shaft rotates faster than the driving shaft. Depending on the shaft movement, the freewheel is called an overrunning, backstop or indexing clutch. Several types of freewheels are available on the market; they mainly differ in terms of the clamping elements they use: ratchets, sprags and rollers.

Depending on the technology, a low drag torque may exist when the freewheel is disengaged and the shafts turn freely. In a FEV, that drag torque reduces the gliding capabilities of the vehicle, and thus must be as low as possible. A freewheel with low drag torque is fairly difficult to find: the offer is huge, the drag torque is not always mentioned in the catalogues and measuring such a low torque is a long and demanding process. A few freewheels have clamping elements that are centrifugally disengaged, which cancels out the drag torque, but they cannot usually be used effectively in such an application since the rotation speed of the fastest shaft – linked to wheel – is not high enough to achieve the centrifugal effect.



(a) solution A

(b) solution B

Figure 9-9: Two freewheel arrangements

1: chassis, 2: wheel, 3: driven pulley, sprocket or gear.
a: overrunning clutch, b: wheel hub, c: hub of the pulley.

Another problem of the freewheel is that it is only designed to transmit torque between two shafts and not to guide the rotational movement of these shafts. A

freewheel must therefore be mounted in parallel with two bearings. Though a freewheel often looks like a rolling bearing, the former cannot replace the latter!

The consequence of the problems mentioned above is that using a freewheel always induces a drag torque coming both from the freewheel itself and from the guiding bearings.

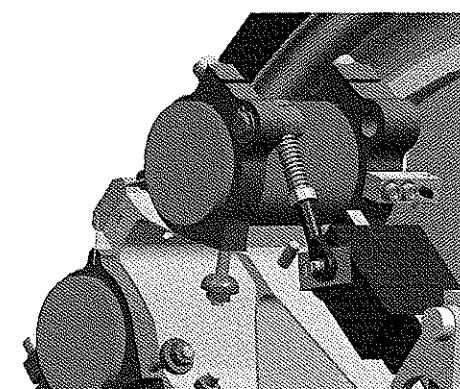
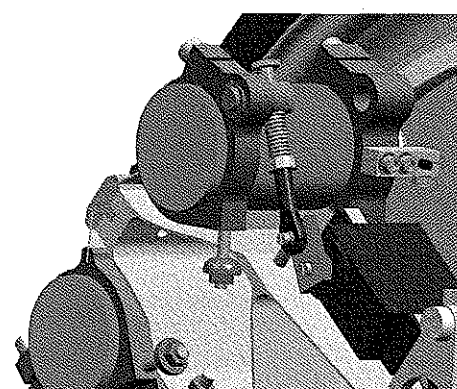
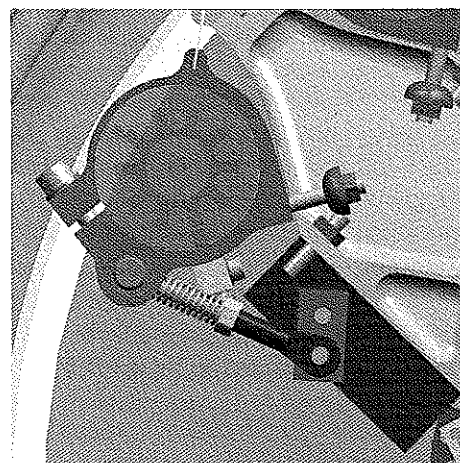
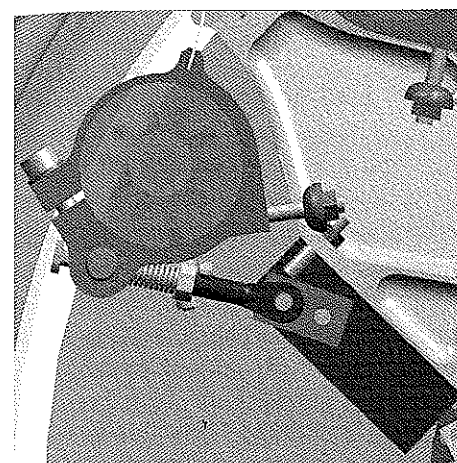
The two possible freewheel arrangements are illustrated in Figure 9-9. Solution A: the hub (c) containing the bearings guides the driven drive train component (3) in relation to the chassis (1). Solution B: the hub (c) uses the wheel (2) to guide the driven drive train component (3). The choice between these two solutions depends on the driving strategy. If the vehicle covers more than 50% of the total distance with its freewheel – used as an overrunning clutch – in the locked position, it is better to choose solution B; if not, the solution A is best.

9.4.2. The openable gear pairs of PAC-Car II

As PAC-Car II is equipped with two motors that can be switched on and off independently, we looked for a solution that would allow their mechanical connection and disconnection to the wheel. Without such a mechanism, the vehicle would have had to drive the unpowered motor when gliding, which would have been an additional source of energy loss. One option would have been to use overrunning clutches mounted between the pinions and the motor shafts, but the drag torque of the gears and overrunning clutches would still remain.



Figure 9-10: Close-up of the hinge that attaches the two drive motors on the carrier.



(a) Connected

(b) Disconnected

Figure 9-11: The two stable positions of the motors. The gears are shown in yellow, but the teeth have not been drawn.

As mentioned in Section 9.1, we decided to open the two gear pairs independently, as soon as one motor is turned off. In order to do so, the motor housings were linked to the carrier via hinges. Because of the low angular displacement needed (i.e., about 10°), the hinges were a simple film joint made of a thin plate of glass-fiber composite. This design is lighter and has less play than a classic mechanical hinge. Figure 9-10 shows a 3D CAD drawing of the assembly: the green parts hold the motors; the blue parts are the flexible film joints; and the pink part is attached to the carrier. At the beginning of the manufacturing process, the green and pink elements were part of a single block of aluminum that was cut in two perpendicular directions using a spark erosion wire. Then the blue film joints were glued inside

the notches marked for that purpose. Finally, the green and pink elements were separated by grinding the two small bridges that held them together.

The servos that move the motors are usually used in model building. The mechanism is designed so that the servos need to be fed only to move from the connected position to the disconnected position and vice-versa, which lessens the energy consumption during a run. A spring is used to make the disconnected position stable. The connected position is made stable, whatever the intensity of the motor torque, by the presence of a toggle lever mechanism. In the connected position, the play of the gear pairs can be finetuned by adjusting the position of the stop that prevents the toggle lever mechanism from moving. The two stable motor positions are depicted in Figure 9-11.

As mentioned in Section 9.1, speed synchronization is required to mesh a gear pair without any risk of breaking a gear tooth. Three inductive sensors with an integrated preconditioning circuit were used to measure the wheel speed and the motor speed. The wheel speed sensor points toward the brake disk (Section 9.5). The motor speed sensors point toward a pin wheel mounted on the motor shaft, close to the gear. We tried using the gear instead of a pin wheel, but the measurements had a low level of reproducibility. In general, measuring the motor speed was problematic due to the wide spread of speeds that had to be measured, speeds ranging from a few rpm to 6,000 rpm. Given these difficulties, we strongly recommend using another sensor technology.

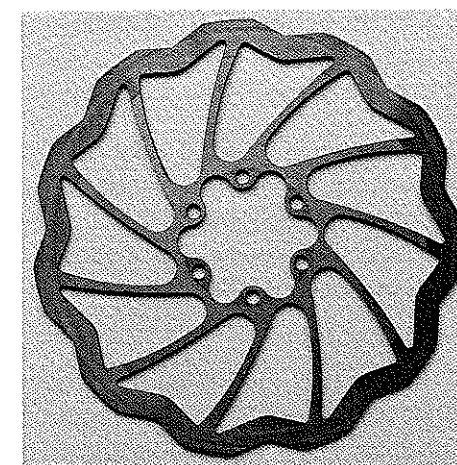
9.5. The brakes

Under normal circumstances, the brakes of a FEV are rarely used. In fact, they tend to be used only one or two times per run: first, at the beginning of the attempt, to remain at full stop on the starting line until the marshal singles the launch, and again at the end of the run to stop after crossing the finish line. In addition, the brakes are used during the technical inspection to maintain the FEV on a slope.

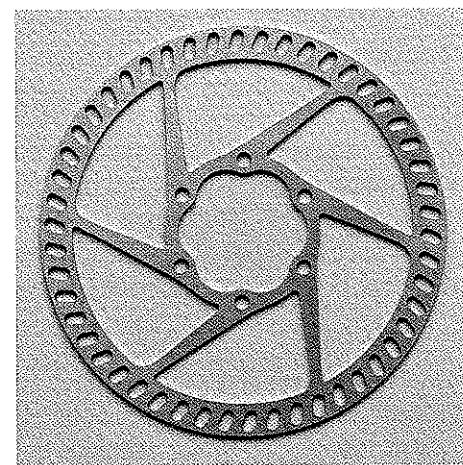
Because of this non-use, the brake specifications are mainly dictated by the race regulations (Section 1.3) and by the necessity of not producing any drag in their unused state. This last requirement is not so easy to achieve as might be believed. The hydraulically-controlled braking systems recommended by the regulations and available on the market are usually designed to maintain the brake pad close to the brake disk or the wheel rim in order to reduce response times and increase the effect of braking. The lack of play in the design makes these systems fairly sensitive to any deformations in the brake disks, wheels or mountings. We felt that this sensitivity constituted an unacceptable risk of energy loss.

Our choice for PAC-Car II was the Magura¹⁵ Marta SL braking system. Despite being a hydraulically-controlled disk brake, there is enough play in the system to avoid the energy loss risks described above. It is also one of the most lightweight systems available on the market, weighing 230 g without the brake disk. Its braking effect is more than we needed, making passing the brake tests during the technical inspection simplicity itself.

As the brake disk delivered with the braking system kit was not compatible with our wheel hub design, we designed and manufactured another one. Figure 9-12 shows the original brake disk and our design. The main changes we made included reducing the outside diameter from 160 mm to 150 mm and cutting 50 holes in the outer rim to reduce the weight and make vehicle velocity measurement easier (Section 9.4.2). This weight modification was made possible by a braking torque lower than the one required for a mountain bike.



(a) Standard Magura Marta SL disk



(b) Custom disk for PAC-Car II

Figure 9-12: Standard and custom brake disks (same scale).

Our brake disk is laser cut from a ground steel plate. The thermal stresses provoked by the laser cutting resulted in a disk that is not 100% flat. But, since the deformation is less than 0.2 mm, the maximal value acceptable by the caliper, the disk remains fully usable.

¹⁵ www.magura.com

The Marta SL features an integrated automatic pad-wear-adjusting mechanism, which theoretically means that the disk-pad distance is readjusted to 0.2 mm every braking cycle, whatever the wear on the brake pads. This mechanism actually had a drawback for our application, as is explained below.

The brake calipers in this brake system are equipped with two opposing pistons, both of which are pressurized with the same brake fluid line. The automatic pad-wear-adjusting mechanism adjusts only the delta volume of the brake fluid needed to move the pistons from the fully pressurized position to the non-pressurized position. It does not, however, guarantee that each piston will shift the same distance, which means that the total distance of 0.4 mm may only be distributed between one piston and the disk, while the other piston is still touching the disk.

We haven't really fixed this problem, but, if the brake disk turns without any large lateral run out and the distances between the pads and the disk are equal, the pads should never even touch the disk.

Chapter 10: Fuel cell system

By Chris Onder, Pius Kobler, Florian Kolb and Jean-Jacques Santin.

PAC-Car II is an electric-drive vehicle. This vehicle is powered by a sort of battery, called a fuel cell system, which runs on hydrogen. A discussion of the PAC-Car II's fuel cell system could have filled an entire book, and thus deciding what should be included in this volume was not easy! Since the research behind the fuel cell system was not the focus of the PAC-Car II project, we chose to concentrate on the fuel cell's implementation and engineering. Several dissertations have already been written on fuel cell systems at ETH Zurich [44, 45]. These works served as the foundation for our understanding of the basic properties, and as such played a very important role in the success of the PAC-Car II project.

This chapter begins with a brief introduction to fuel cells, in which the basic equations for calculating such elements as current and voltage variations are explained. This information is essential in order to understand the system and the controllers implemented. Readers who desire a more in-depth discussion are referred to the following authors: Guzzella [1, 46], the CEA report [47] and Barbir [48].

After this brief introduction, the PAC-Car II's fuel cell system is presented. Since it is often difficult to distinguish between the fundamentals and the case-specific facts of the PAC-Car II's system, this section includes many details that apply to this kind of system in general, but were also of special importance for our system. The mechanical, pneumatic and hydraulic parts of our fuel cell system are each described in detail, and our choices for the various components are discussed. A entire sub-section is devoted to a discussion of PAC-Car II's electronics because the efficiency of this system is crucial to the vehicle's overall efficiency. The chapter concludes with a discussion of some of the software's structural elements.

10.1. Fuel cell fundamentals

10.1.1. What is a fuel cell system?

A fuel cell system (FCS) is a kind of electric generator. A classic generating set (thermal engine + generator) produces electricity from fuel in a multi-step energy

conversion process. An FCS, on the other hand, produces electricity in a single step (Figure 10-1), which is one of the reasons why it is more efficient.

The fuel used in a FCS can be pure hydrogen, methanol or natural gas, depending on its technology. Like combustion engines, FCSs consume oxygen in addition to fuel. However, if hydrogen is used as fuel, FCSs produce no carbon dioxide, one of the greenhouse gases suspected of causing climate change.

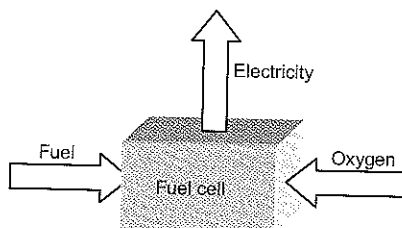


Figure 10-1: A fuel cell generates electricity from fuel and oxygen in one step.

In the PAC-Car II, we chose to use Proton Exchange Membrane (PEM) fuel cells, running on air and pure hydrogen. Our reasons for this choice are explained in Section 10.2.1. The following section presents the fundamentals for this type of FCS only.

10.1.2. PEM fuel cell system: stack and cell

A PEM FCS is composed of a reactor, inside of which components react and electricity is produced, and the system auxiliaries, whose main jobs are to properly supply the stack with fuel and oxygen and to collect the electricity produced.

Figure 10-2 shows the structure of a PEM FC reactor, also called a stack. As the name implies, a stack contains several stacked cells that are connected electrically in series. The cells are sandwiched between two end plates equipped with current collectors and terminals. Stacking is necessary because the output voltage of a single cell is too low for the majority of applications (about 0.7 V per cell).

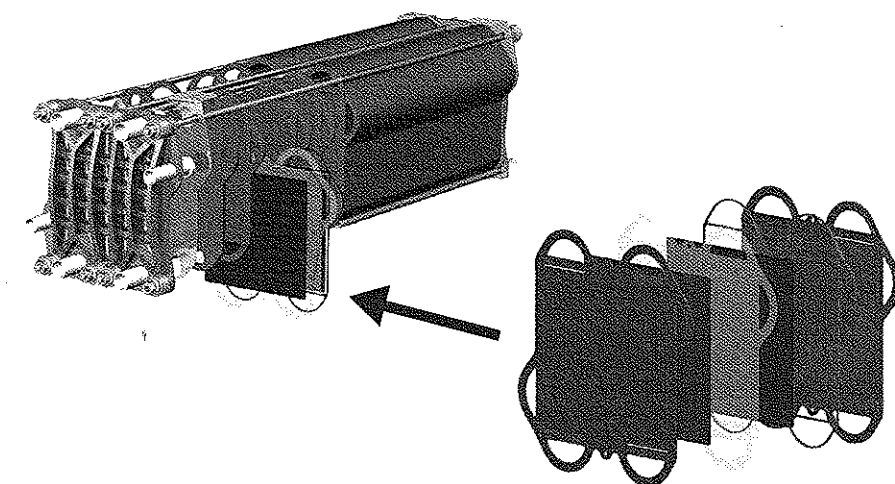


*Figure 10-2: Structure of a PEM FC stack [44].
(Courtesy of Paul Scherrer Institut)*

Each cell consists of two gas distributor plates separated by a Membrane Electrode Assembly (MEA) (Figure 10-3). These distributor plates are also called bipolar plates since they can be both cathode and anode, depending on the MEA that follows. The MEA contains at least three layers, including two porous electrodes and a polymer membrane. The membrane is ion conductive, but insulating and gastight. The distributor plates allow one side of the MEA to be in contact with hydrogen, while the other side is in contact with air. At the interface between the electrodes and the membrane, there are some catalyst particles, typically platinum.

Electrochemical reactions take place on the surface of the catalyst particles, with hydrogen splitting into protons and electrons. The protons travel through the membrane and the electrons travel through the outside circuit, where they perform useful work before coming back on the other side of the MEA. The catalyst makes the protons, electrons and oxygen react, creating water that must be evacuated from the MEA.

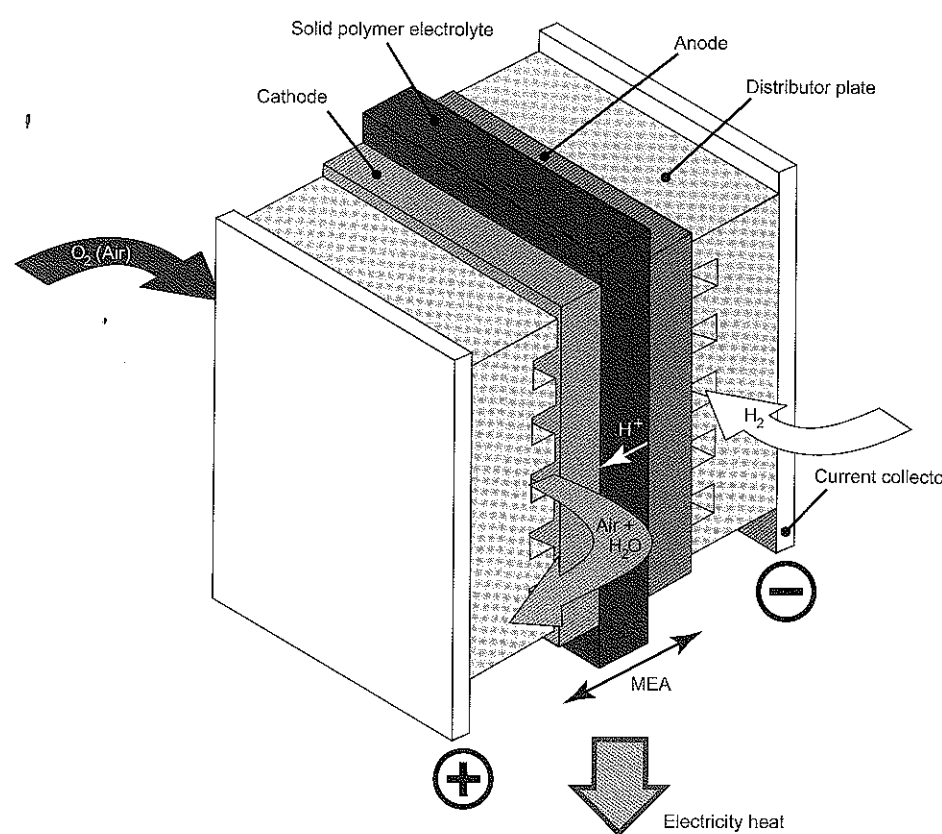


Figure 10-3: Operating principle of a basic PEM cell.

10.1.3. How does a fuel cell work?

The electrochemical reactions taking place in a single cell are basically:

- the splitting of the hydrogen molecule H_2 into protons H^+ and electrons e^- :



- the combining of these protons and electrons with oxygen O_2 :



These reactions only happen under certain temperature and pressure conditions and in presence of a catalyst, for example a precious metal, such as platinum. The

electrons produced in reaction (10.1) generate an electrical current that is available on the electrodes of a cell.

In a PEM FC, a membrane is used to separate the reactants. Only protons can move through the membrane, whereas electrons have to pass through the electric wiring. Thus, the membrane is an electric insulator, but also an ion conductor that is almost tight against gaseous hydrogen and oxygen. PEM FC use a thin layer of organic ion-conductive membrane (e.g., Nafion by Dupont) as an electrolyte. This membrane is coated with precious metal particles (mostly platinum) that serve as a catalyst. (The complete membrane-electrode-assembley (MEA) is available commercially.)

It is the mobility of the electrons through the electrical circuit that controls the reaction. If the circuit is open, no electron can move, and the reaction is stopped. Thus, no hydrogen is consumed. On the other hand, if short-circuited, the current reaches its maximum, but the reaction is limited by the mobility of the protons through the membrane and the presence of hydrogen and oxygen next to the catalyst. As long as hydrogen is used as a fuel, pure water (H_2O) is the only product of the reaction, which makes the fuel cell free of such emissions as carbon dioxide and nitrogen oxide.

Of course, in a real FC, this ideal approach is no longer strictly valid. Some of the problems that can arise will be discussed later in this chapter.

10.1.4. The quantity of reactants and products

This section provides the formulas and figures that allow the preliminary sizing of a FCS. In all these formulas and figures, the entry variable is current I or current density i , both these variables being bound by Equation (10.3). Current density is the current per unit area of the active surface S_{cell} of the MEA (more or less the surface that is in contact with the reactants). Current is set by the power demand, which can be controlled by the power electronics.

$$I_{cell} = i_{cell} S_{cell} \quad (10.3)$$

The above description is, of course, still the ideal cell operation. The amounts calculated below are both *ideal*, with all gas leaks, diffusions and purges being ignored, and *stoichiometric*, corresponding to the amount of products involved and not to the amount fed into the stack. (In reality, a stack runs with higher flows of air and hydrogen, resulting in what is called the over-stoichiometric operation.)

Hydrogen

By definition, the current I_c delivered by one cell is proportional to the number of generated electrons per time unit:

$$\dot{n}_{e,cell} = \frac{I_{cell}}{e^- N_A} = \frac{I_{cell}}{F} \quad (10.4)$$

where

$\dot{n}_{e,cell}$ is the electron flow, expressed in number of moles of electrons per second;

I_{cell} is the cell current [A];

e is the elementary electric charge (1.602×10^{-19} C);

N_A is the Avogadro number (6.022×10^{23}); and

F is the Faraday constant (equal to the product $e \times N_A$).

As one molecule of hydrogen produces two electrons, the volume of hydrogen [Sml] consumed per minute by a single cell $\dot{v}_{H_2,sto,cell}$ can be calculated as follows:

$$\dot{v}_{H_2,sto,cell} = \frac{60}{2} \dot{n}_{e,cell} V_M 10^3 \quad (10.5)$$

where V_M is the molar volume of a gas, under standard temperature and pressure conditions (273.15 K and 101.325 kPa), or in other words, 22.4 SI (standard liters) per mole.

Equations (10.4) and (10.5) yield:

$$\begin{aligned} \dot{v}_{H_2,sto,cell} &= \frac{60 V_M 10^3}{2 e N_A} I_{cell} = \frac{60}{2} \frac{22.4 \times 10^3}{1.602 \times 10^{-19} \times 6.022 \times 10^{23}} I_{cell} \\ \dot{v}_{H_2,sto,cell} &\approx 7 I_{cell} \end{aligned} \quad (10.6)$$

Obviously, this hydrogen flow is theoretical. In reality, it could be noticeably higher, especially for a FEV application in which the amount of hydrogen needed to drive the vehicle is low. That additional consumption of hydrogen is generated by:

- hydrogen leaks. The hydrogen molecule is so small that it can pass through any tiny gap, making connectors sources of leaks.

- hydrogen diffusion. Again due its small size, the hydrogen molecule migrates through all materials and sometime reacts with them. This is particularly true for the membrane, which is the thinnest barrier against hydrogen.
- hydrogen purges. Under certain conditions, it becomes necessary to purge the hydrogen circuit, which means evacuating a small amount of hydrogen. Temporarily increasing the hydrogen flow renews the molecules in contact with the membrane and removes the water droplets that might block the hydrogen channels in the distribution plates.

Please note that the stack current provides an easy way to estimate the instantaneous consumption of hydrogen. The current sensor used for the stack current is thus the starting point of the FCS control system (Section 10.3).

Oxygen

A similar calculation can be done for oxygen, taking into account that for every hydrogen molecule, half of an oxygen molecule is needed:

$$\dot{v}_{O_2,sto,cell} = \frac{\dot{v}_{H_2,sto,cell}}{2} \approx 3.5 I_{cell} \quad (10.7)$$

In cases in which air is used instead of pure oxygen, assuming that the air contains 20% of oxygen, a 1 A current delivered by one cell implies a stoichiometric consumption of 17.5 Sml of air per minute.

As mentioned earlier, a fuel cell core consists of a stack of cells, electrically connected in series in order to increase the voltage, but with a parallel supply of hydrogen and air. Therefore,

$$I_{cell} = I_{stack} \quad (10.8)$$

$$\dot{v}_{H_2,sto,stack} = N_{cell} \dot{v}_{H_2,sto,cell} \approx 7 N_{cell} I_{stack} \quad (10.9)$$

$$\dot{v}_{air,sto,stack} = N_{cell} \dot{v}_{air,sto,cell} \approx 17.5 N_{cell} I_{stack} \quad (10.10)$$

where N_{cell} is the number of cells in the stack and \dot{v} is expressed in Sml.

Water

The water discussed below is, with heat, the only byproduct of the reaction that takes place into the stack. Based on the electrochemical reactions expressed in

equations (10.1) and (10.2), the mass flow of water $\dot{m}_{H_2O,sto,stack}$, in grams per minute, produced by the stack is given by:

$$\dot{m}_{H_2O,sto,stack} = \frac{60}{2} \dot{n}_{e,cell} N_{cell} M_{M,H_2O} \quad (10.11)$$

where M_{M,H_2O} is the molecular mass of water (i.e., 18 g/mol). Therefore:

$$\begin{aligned} \dot{m}_{H_2O,sto,stack} &= \frac{60}{2} \frac{18}{1.602 \times 10^{-19} \times 6.022 \times 10^{23}} N_{cell} I_{stack} \\ \dot{m}_{H_2O,sto,stack} &= 5.6 \times 10^{-3} N_{cell} I_{stack} \end{aligned} \quad (10.12)$$

The membrane in the stack must be well humidified to be ion-conducting. In earlier FC, this was done using special humidifiers mounted upstream of the FC. We used a self-humidifying technique for the PAC-Car II's stack, thus eliminating the need for humidifiers. Part of the water produced is recycled internally. The humid outflowing air is guided to the other side of the membrane, where it humidifies the incoming air due to the water diffusing through the membrane. Hydrogen is humidified by reverse diffusion through the membrane. The amount of diffusion is a function of the difference in partial pressure of the water at the anode and cathode, respectively.

This internally-circulating water can be evacuated from the stack in either liquid or gaseous form. Excess water must be removed and is stored temporarily in a special water separator. Equation (10.12) can be used as datum point from which the water separator sizing may be conducted.

10.1.5. Cell potential

When working with FCSs, cell potential is key. In fact, cell efficiency (see section 10.1.7) is directly proportional to cell potential, which is itself strongly dependant on several parameters, such as current density, gas pressures, temperature, and stoichiometric hydrogen/oxygen ratios. Since the FCS output current depends on the torque demand at wheel, it is quite important to minimize the energy consumption of the entire propulsion system, in terms of track topology and the required minimal average velocity. The stack's cell potentials are also used to monitor FC functioning, mainly by comparing the potentials of the different cells in the stack. This comparison becomes the basis of a continual auto-diagnostic system.

Figure 10-4 shows the modeled polarization curve of a cell, which is the plot of cell potential versus current density. The curve represents the equilibrium potential and three kinds of losses: activation, ohmic and concentration. (The model's complete

development can be found in Barbir's paper [47]. For the actual measurements taken on the PAC-Car II's FCS, see section 10.4.)

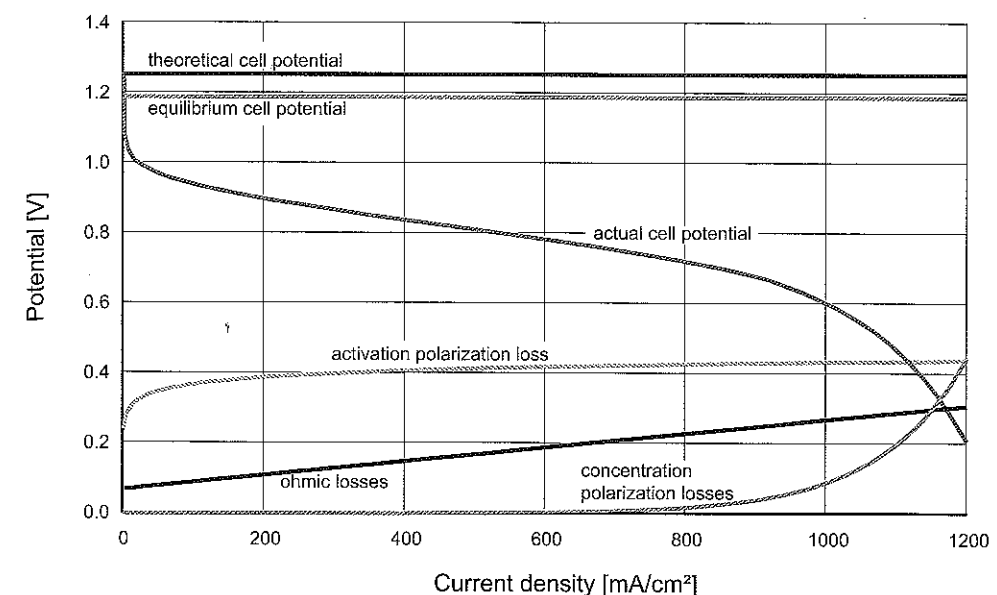


Figure 10-4: Cell potentials and polarization losses versus current density.

As can be seen in the figure above:

- The equilibrium potential is 1.189 V when hydrogen and air are used at 333°K under atmospheric pressure, which corresponds to the theoretical open circuit voltage.
- The activation polarization loss can be attributed to the difference in voltage from the equilibrium that is needed to get the electrochemical reaction going. This loss is associated with sluggish electrode kinetics.
- Ohmic losses stem from resistance to the ion flow through the MEA and resistance to the electron flow through the stack's electrically conductive components. These resistance losses are proportional to current density.
- Concentration polarization losses occur when a reactant (hydrogen or oxygen) is more rapidly consumed than supplied.

10.1.6. Cell power density

Power density is a product of cell potential and current density. Power density versus current density, as well as the polarization curve, is plotted Figure 10-5. As this figure demonstrates, a cell has a maximum power density. It does not make sense to operate beyond the level of maximum power density because the same power output can be obtained with a lower current and higher potential, which means higher efficiency (see section 10.1.7).

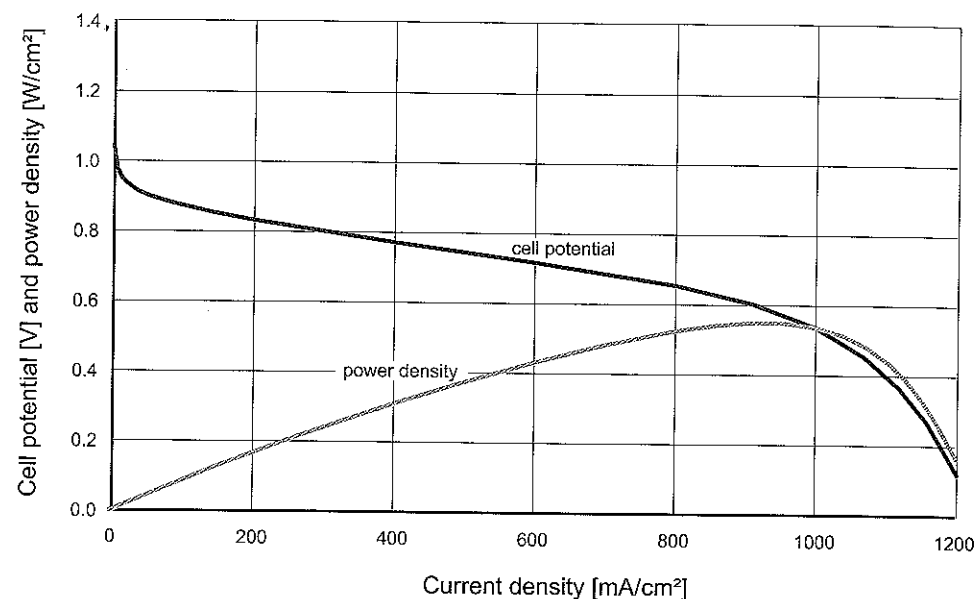


Figure 10-5: Cell power density versus current density.

10.1.7. Cell efficiency

The cell efficiency is defined as the ratio between energy input and useful energy output. In case of a fuel cell, it is also the ratio between cell output voltage and theoretical cell potential.

The theoretical cell potential is 1.254 V, which corresponds to the LHV of hydrogen (see Section 1.2.3) completely converted into electrical potential. Thus, cell voltage provides a direct image of cell efficiency (Figure 10-6).

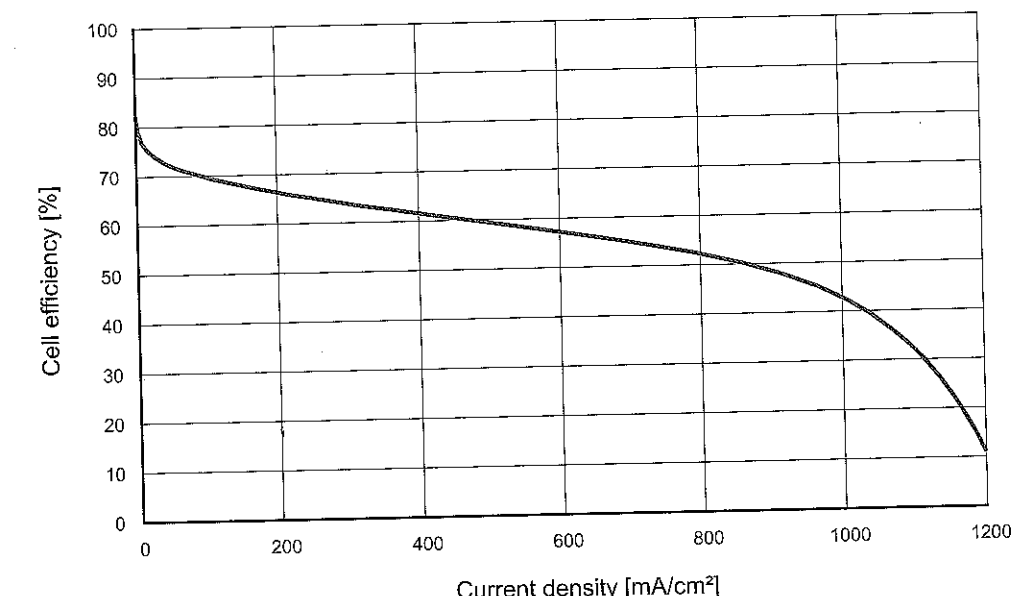


Figure 10-6: Cell efficiency versus current density.

10.1.8. Fuel cell system efficiency

A part of the electric energy produced by the stack is used to supply the auxiliaries, which lessens the useful energy output and thus the FCS efficiency. Some of these auxiliaries use constant energy; some, like the air compressor whose the energy consumption depends on stack current, do not.

In Figure 10-7, stack efficiency and FCS efficiency are plotted together versus current density. As the figure shows, an FCS has a maximum efficiency value. Unlike ICEs, which are quite inefficient under partial load conditions, the most efficient operating point of a FCS is reached at low power. In the fuel economy competitions, the goal is to operate the FCS at about this point, preferably around the values on the right-hand part of the curve, in order to avoid operating at the low current densities where FCS efficiency drops dramatically. Of course, this must be balanced against the efficiency ratings of the other parts of the power train, such as its power electronics and drive motor.

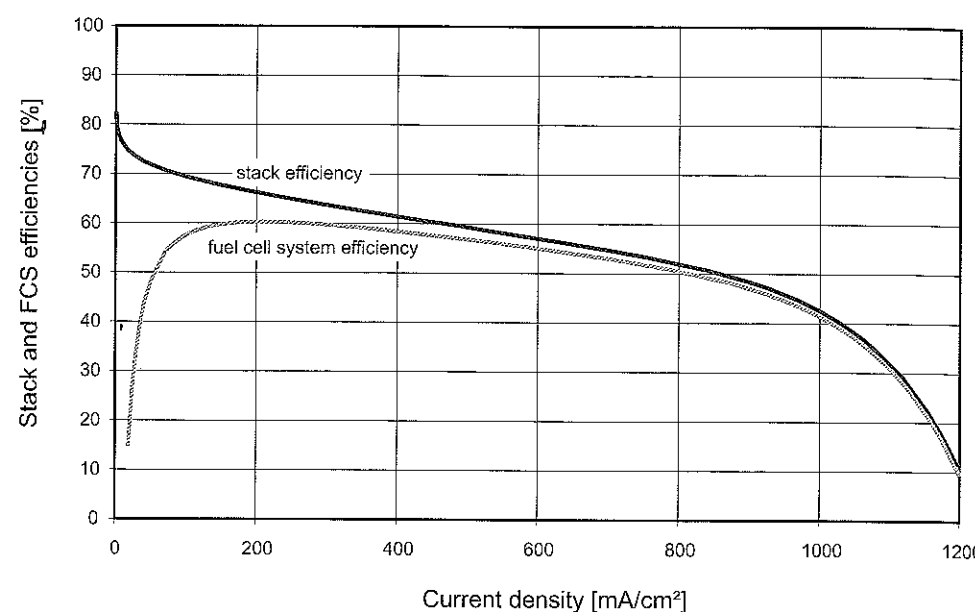


Figure 10-7: Stack and FCS efficiency versus current density.

10.1.9. Stack sizing

Electric power is calculated as the product of current and voltage. The maximal current of a fuel cell stack is proportional to the active membrane area of one cell, whereas its nominal voltage depends on the number of cells. Thus, a fuel cell stack is sized by determining the active area of the cell and the number of cells in the stack.

Several constraints have to be considered:

- the voltage is defined by usage, the drive motor in this case (even if a step-up converter can be used to increase voltage);
- the higher the number of cells in a stack, the lower its reliability and the higher the risk of leaks;
- the energy loss in an electric circuit is mainly due to the Joule effect, which is proportional to current;
- a FCS is most efficient, not at full power, but at about 1/3 power (section 10.1.8);

- operating at a very low current density is not advantageous since parasitic losses may be significant; and
- the cost and weight of a stack are hardly affected by the compromise between the area and number of the cells. In other words, for these two criteria, it doesn't matter whether a certain power is reached with a high current and low voltage, or vice versa. It is the total stack power that counts.

Obviously, stack size must be chosen by considering not only the stack itself, but also the entire electrical system, including the FCS and the drive motor with its power electronics, to name but a few elements. Of course, the drive motor choice depends on the speed and torque profiles, which themselves vary in accordance with the vehicle characteristics and track elevation profile. Thus, there is no systematic rule for sizing a stack; every stack must be created individually and optimized to meet the need of the intended application.

10.2. The fuel cell system of PAC-Car II

This section describes the FCS used in the PAC-Car II, including a discussion of the sizing of the important components and the distinctive features of the FCS. Since it is not possible to explain every detail, we made a somewhat arbitrary selection among the components to be presented. Some were left out because, though they might be important in other FCS, they were not crucial to the PAC-Car II.

10.2.1. Choosing a fuel cell technology for PAC-Car II

Choosing the fuel cell (FC) technology for the PAC-Car II was, in fact, a series of smaller choices. First, it was necessary to choose the FC type. There are a large variety of FC available: Proton Exchange Membrane FC (PEM FC), Direct Methanol FC (DMFC), Phosphoric Acid FC (PAFC), Alkaline FC (AFC), Molten Carbonate FC (MCFC) and Solid Oxide FC (SOFC). From these possibilities, we selected the ones that would fulfill the following requirements:

- viable at ambient or slightly higher temperatures;
- suitable for use in transportation applications;
- able to deliver the required range of power; and
- affordable and available on the market or from research laboratories.

Since the PEM FCs were the only ones that satisfied all the requirements, that is what we chose.

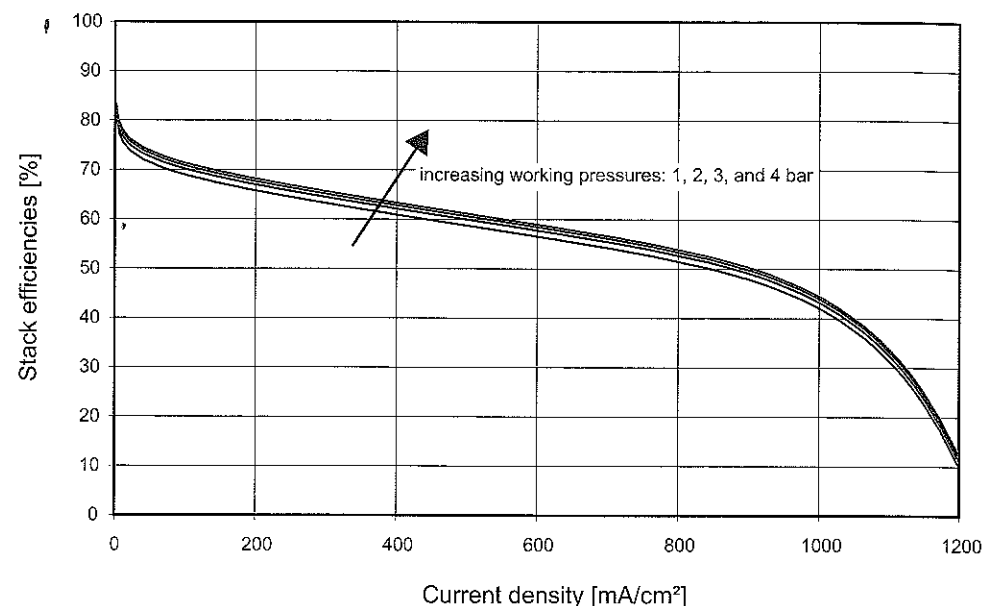


Figure 10-8: Cell efficiency versus current density for increasing working pressures (simulation).

Next, we had to choose the type of fuel that our FC would run on. Since the power density of PEM FCs running on methanol is approximately one fourth of hydrogen-powered FCs, hydrogen was the obvious choice. In addition, since the PEM FC must also be fed with oxygen, which can be drawn from the surrounding air or from a tank of pure oxygen, we needed to decide how the oxygen would be supplied. Using pure oxygen would have dramatically increased the tank-to-wheel efficiency of the system; however, to be fair to ICE vehicles, the use of pure oxygen is prohibited by the race regulations (Section 1.3). Therefore, the stack had to be supplied with oxygen from the surrounding air.

Then came the choice of the pressure level for the PEM FC. At atmospheric pressure, the air supply can be assured using a simple fan. However, the efficiency of the selected FC can be improved by raising fuel (i.e., hydrogen) and oxygen pressure to up to 3 bar (Figure 10-8). For the hydrogen, this increase is easy since hydrogen is always stored under pressure. The only draw-back is a reduced driving range per tank because the tank must be changed when it reaches a certain level, which depends on the pressure required. For the air, increasing the pressure requires a compressor.

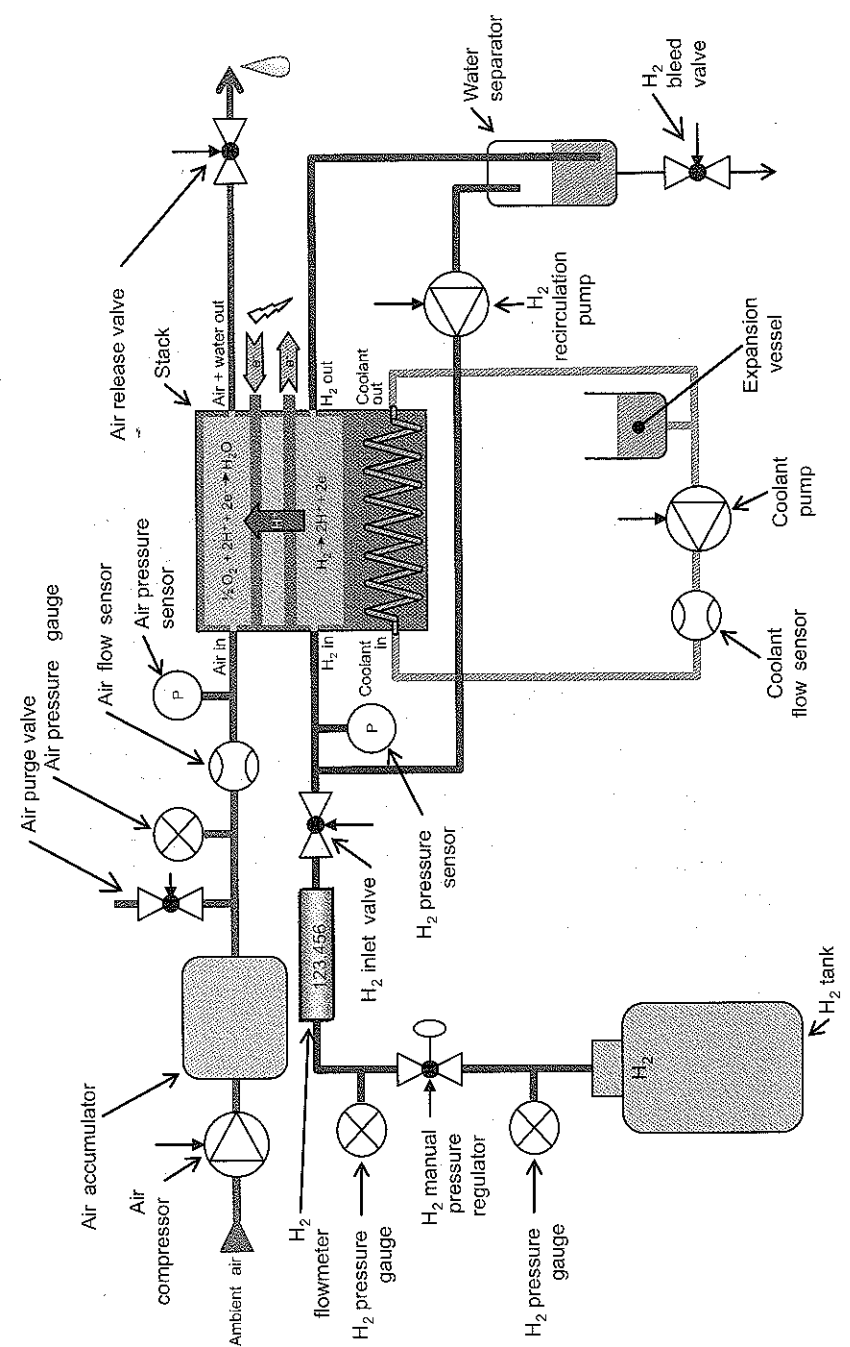


Figure 10-9: Schematic diagram of the PAC-Car II's fuel cell system, in which the hydrogen, air and coolant circuits are represented.

Clearly, working at higher pressures significantly increases the efficiency of the fuel cell core. But, this efficiency is achieved at the price of two major drawbacks: the system is more complex, and the energy savings is partially reversed by the energy consumption of the compressor.

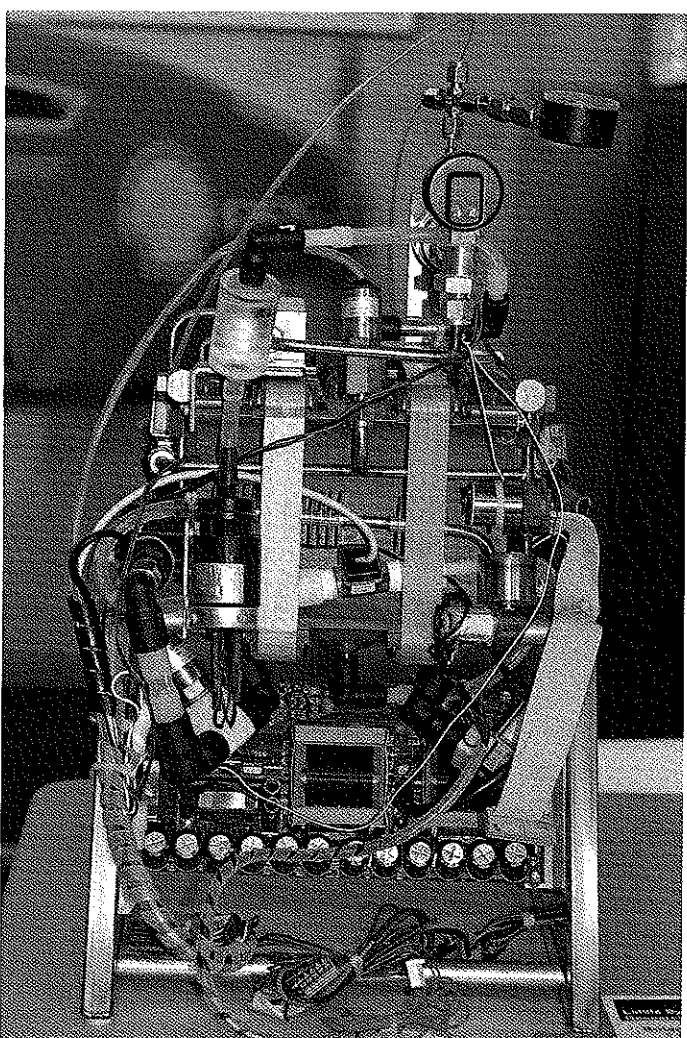


Figure 10-10: The PAC-Car II's fuel cell system in a test configuration.

In the end, we chose the pressurized technology for PAC-Car II, first for efficiency reasons, and second because it was a well-known system in ETH's Measurement and Control Laboratory (IMRT) and had been used on several occasions for such projects as HY.Power or PowerPac [49, 50].

The stack is only one part of the complete FCS. The components that supply hydrogen and air, the systems that evacuate water and heat, and the components needed for a variety of tasks (e.g., start-up, normal operations, shutdown, emergency operations etc.) are part of the FCS as well. In the paragraphs that follow, the FCS is described from a control point of view, focusing first on the components are detailed and later on how the sensor information must be processed in order to obtain the actuator settings. Figure 10-9 shows a schematic diagram of the main components of the PAC-Car II's FCS. Figure 10-10 shows the actual FCS, including electronics, during a test in the lab.

10.2.2. Sizing the stack

There are quite a number of FC and FCS manufacturers. If we had not had a lot of experience with FCS at ETH Zurich, we would most likely have chosen an off-the-shelf device. However, it was in fact our earlier experiences with FCS that pushed us to enter an FC powered vehicle in the fuel economy competitions. The Hy.Power and PowerPAC projects provided us with a sound foundation for implementing a small fuel cell in a vehicle. A preliminary trial was made with PAC-Car I, a vehicle that was built by the University of Valenciennes and equipped with a FC-electric powertrain at ETH Zurich. The FCS used in PAC-Car I was basically imported directly from the PowerPAC project since the power demands were actually quite similar. The system proved to be quite reliable, with no failures during any of the tests. The results for PAC-Car I were so promising that we decided to use this system in PAC-Car II.

The rated power of the FC in the PowerPAC and the PAC-Car I is approximately 1 kW, at a voltage of approximately 12 V. This power was judged much too high for PAC-Car II. Nevertheless, given the optimum FC efficiency at low partial-load power and the possibility of adjusting the auxiliaries to the new power demand, choosing the same FC was still reasonable. Though stack itself would still be able to deliver 1 kW, the rest of the system would not be able to support such power. In fact, the auxiliaries were resized for the much lower power demand of PAC-Car II – mainly to reduce their energy demands and the weight of the system – which meant that the PAC-Car II's FCS was unable to deliver the 1 kW because the supply of the reactants could no longer be maintained. As a result of this resizing, PAC-Car II is able to obtain a maximum power of approximately 300 W.

We decided to use the “old” cell design instead of designing a new one. Actually, changing the MEA area would have meant designing new distributor plates, which would have been an even longer and more difficult task since the goal was to reach high levels of efficiency and reliability.

The area of the chosen membrane is 136 cm², making currents of up to 100 A theoretically possible. The efficiency-optimal current of the system is, of course,

much lower and depends on the auxiliaries. This optimal current also depends on the operating conditions (i.e., pressure, humidity, air and hydrogen stoichiometric ratios, and temperature). In PAC-Car II, currents up to 15 A were used, thus maintaining the system at high efficiency levels. Still, the membrane and flow field made the FC over-dimensioned, which caused some of the problems we experienced (e.g., leakage, demand for purges).

The number of cells was defined so that the FCS would be able to provide, at its highest efficiency, the most frequently demanded power level, given the expected vehicle and drive motor characteristics. Once this number was defined, the nominal stack voltage was set and the drive motor and its power electronics could be chosen. Of course, the defined number of cells is not set in stone. For example, if no motors meeting the desired specifications can be found, the number might have to be redefined. The number of cells in the stack might also need to be changed due to the available space in the vehicle.

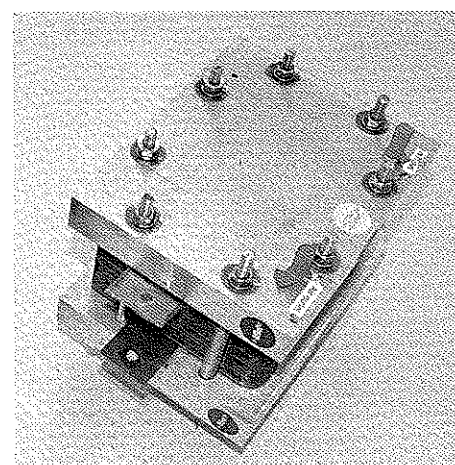
We found that all of the above constraints could be met by setting the number of cells to 20. Twenty cells are capable of providing supply voltages of approximately 15 V and higher, making reasonable speeds possible with 24 V motors.

The cell stack, including the MEA and the bipolar plates, was built at the PSI¹⁶. Their FC technology allowed them to build a self-humidifying system, incorporated in the stack itself, which made the FCS much simpler.

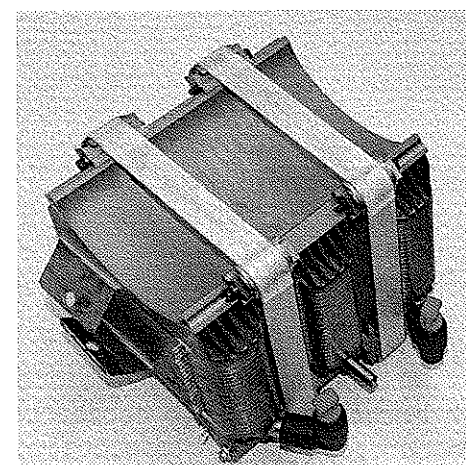
10.2.3. Constructing the stack

From the mechanical point of view, the PAC-Car II stack is composed of 20 cells stacked up and sandwiched between 2 end plates equipped with current collectors and terminals. The end plates hold the cells together with sufficient contact pressure to prevent leaking gas and to minimize the electrical contact resistance between the layers. Our main challenge was to make these end plates as light as possible. In the end, the classic solution involving two solid aluminum plates and several steel tie-rods as mechanical fasteners was replaced by two sandwiched plates made of reinforced glass-fiber plastic with an aluminum bow, and two glass-fiber straps used to hold them together. Figure 10-11 shows the two solutions, the first was used in PAC-Car I (a), the second in PAC-Car II (b). The modifications reduced the weight of the stack from 9 kg (a) to 4 kg (b), while keeping the number of cells and the cell construction basically the same. Figure 10-12 shows an exploded view of the PAC-Car II's stack, in which cell, end plates, straps and tensioners have been moved apart.

¹⁶ Paul Scherrer Institute, a research institute of the ETH domain. www.psi.ch



(a) classic solid aluminum end plates and
steel tie-rods
(PAC-Car I's stack)



(b) sandwiched end plates and straps used
to hold the stack together
(PAC-Car II's stack)

Figure 10-11: Old and new stacks of the PAC-Car projects (same scale).

The bipolar plates are manufactured as two half-plates, with the hydrogen and coolant flow-fields on each side of one half-plate and those of the coolant and air on each side of the other half-plate. These flow-fields are all milled. Because the bi-polar plates are made of graphite, they are electrically conductive. (A detailed description of the development of the bipolar-plates used can be found in Ruge's dissertation [44].) An MEA is situated between each of the bipolar plates. At both ends of the stack, the current is taken from gold-coated copper current collectors, equipped with terminals (Figure 10-13). The gold coating prevents the copper from oxidizing, thus guaranteeing an optimal electrical connection. Since high levels of current are common, these connectors had to be chosen very carefully.

The stack is held together and tightened with the endplates, connected to each other with pull-rods or similar devices. The main difficulty is that the pressure has to be applied evenly because an uneven distribution could damage the graphite bipolar plates, which are very delicate. If a bipolar-plate is damaged, the complete stack has to be disassembled and the defective plate has to be replaced.

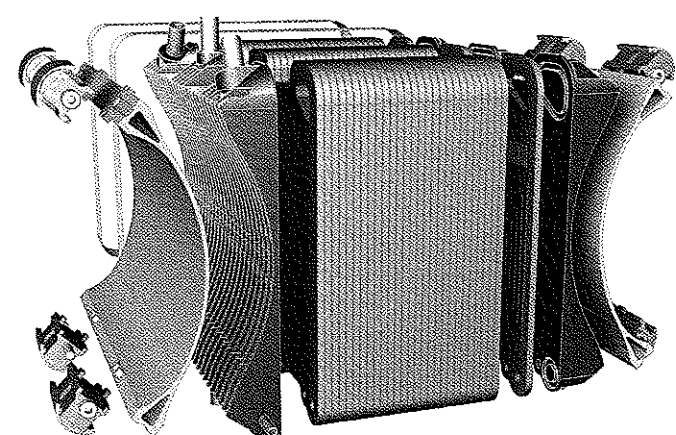


*Figure 10-12: Exploded view of the PAC-Car II's stack.
(Courtesy of Tribecraft AG, Zurich)*

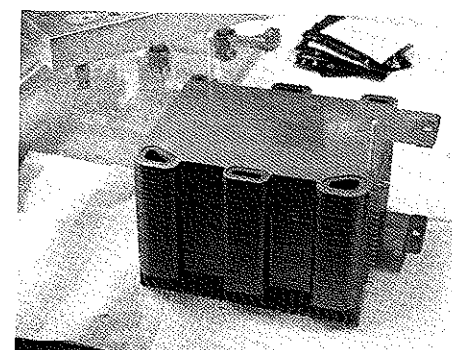


Figure 10-13: PAC-Car II's stack during assembly. The gold-coated copper current collector with terminal may be seen on top of the assembly. The two rods are used to properly position the stack elements between them.

Weight was an important issue for the stack design. A substantial amount of mass was saved by changing the endplates and the corresponding clamping construction. Previous versions of the stack had aluminum endplates with heavy steel rods. Ultimately, the PAC-Car II solution, with its reinforced glass-fiber plastic plates,

graphite endplates, and glass-fiber straps, did not compromise the efforts made to keep the other parts of the vehicle lightweight.

Lightweight fuel cell endplates

The PAC-Car II fuel cell stack is held together with a pressure of 30 bar, calculated based on the 3-bar normal operating pressure of this stack with a security factor of 10. This pressure produces a force of 35,000 N that must be distributed evenly over the contact surface between the stack and the end plates to prevent critical deformations of the brittle graphite plates of the stack.

The construction of the end plates used in the PAC-Car II is based on the D.Bow concept, patented by Tribecraft AG¹⁷. This D.Bow concept is a method for constructing ultra lightweight fuel cell endplates, in which a D-shaped bow is used to distribute the force of the screws holding the endplates together evenly over the contact surface between stack and end plates (Figure 10-14). This bowed shape allows the maximum strength of the bow material (aluminum) to be used, with tension at the top and compression on the rounded part, while removing the unstressed material in the center of the bow. A plastic rib construction transmits the forces from the bow to the stack.

The relatively small number of cells in the PAC-Car II stack makes it rather short, and the additional rigidity provided by the steel screws is not necessary. Thus, to make the PAC-Car II end plates even lighter than the already lightweight D.Bow end plates, the heavy steel screws that hold the end plates together were replaced by composite fiber straps, which are wrapped around the end plates and the stack. These straps also replace the tension section of the aluminum D.Bow, turning it into a kind of a "C.Bow," which reduces the weight even more (Figure 10-15). (Though "C.Bow" is used to facilitate references to this element, it is actually a derivative of the D.Bow concept.)

¹⁷ www.tribecraft.ch

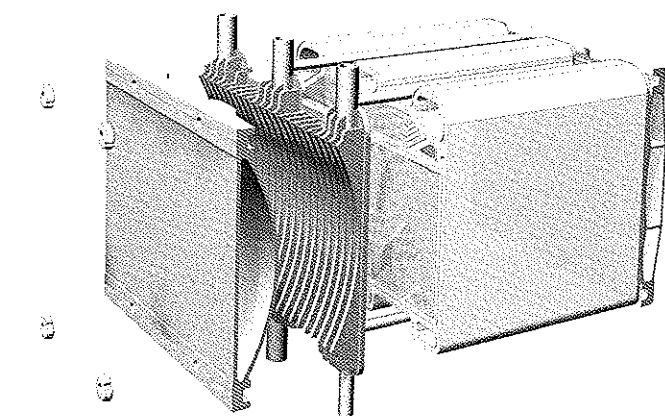


Figure 10-14: Exploded view of the PowerPAC stack. D.Bow end plates were used.
(Courtesy of Tribecraft AG, Zurich)

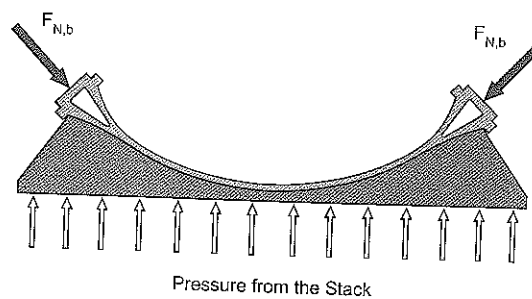


Figure 10-15: External forces applied to the "C.Bow" end plate assembly.

The endplates also serve to connect the supply tubes to the stack. The tubes for air, hydrogen and coolant are connected to the stack through the plastic parts of the end plates (Figure 10-16). Steel bushings with the same diameter as the connected tubes are glued onto the endplates (Figure 10-17), and the adjacent manifolds in the stack and the end plates are sealed with o-rings.

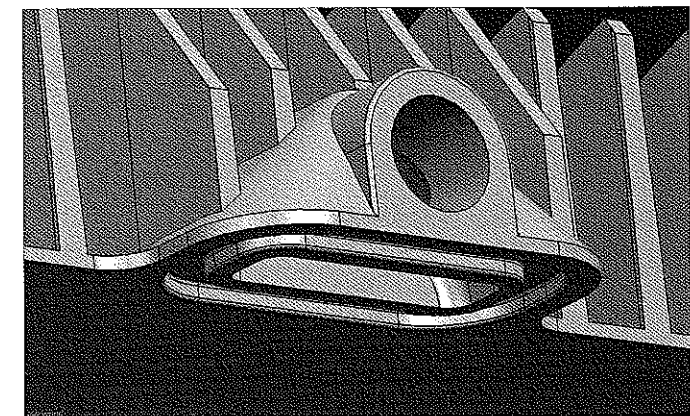


Figure 10-16: Air manifold milled in the glass-fiber reinforced plastic of the end plate.

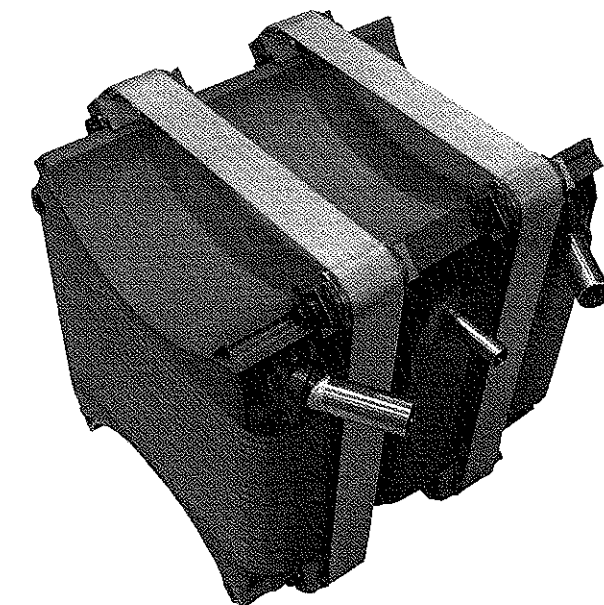


Figure 10-17: Photograph of the PAC-Car II stack. The steel bushings for air and coolant are glued onto the endplates. (Courtesy of Tribecraft AG, Zurich)

In PAC-Car II, the maximum height of the end plates was determined by the space available between the bulkhead and the rear wheel. Each endplate could be no higher than 46.5 mm, which was an additional challenge for the endplate designers.

Fuel cell straps and tensioners

The straps that make the design of the "C.Bow" possible apply force orthogonally to the bipolar plates. We chose a composite fiber strap construction for its low weight, but also its high strength and low rigidity. If the stack expands due to temperature increases, the forces have to remain as constant as possible so that the stack won't be overloaded or release the necessary tension. This constant force can be maintained by using a semi-flexible strap that is heavily pretensioned. To obtain the right balance between flexibility and rigidity, the strap was pre-stretched in order to stretch the composite material up to its material limit.

Manufacturing the straps was one of the most difficult parts of constructing the end plates. We chose to make the straps out of glass fibers since this material was thought to provide the best combination of high strength and low rigidity. To manufacture the straps, we used S2 glass fibers¹⁸ and an epoxy matrix in a winding technique, in which the strap was wound around an aluminum mold to give the strap the shape it would have on the stack. This was necessary because if such straps are not shaped during the manufacturing process, the epoxy will crack at the narrow corners of the strap. The strap was then compressed with a vacuum bag, hardened in an autoclave, and unmolded by shrinking the mold via deep-freezing. In order to obtain a straight and even edge, the strap was created too large and then cut to its final width with a diamond saw.

Since the bipolar distributor plates may creep, it must be possible to readjust the tension on the spot at the race. In the case of a defective cell, the stack must be disassembled and reassembled on the spot, which means that the mechanism for pre-stressing the strap also has to be dismountable and easy to use. A wedge construction on every corner allows the distance between the stack and the strap to be increased when any two of the wedges are screwed together (the fastening torque of the screw is linear to the force on the strap), thus facilitating a force-controlled pre-stretching of the strap.

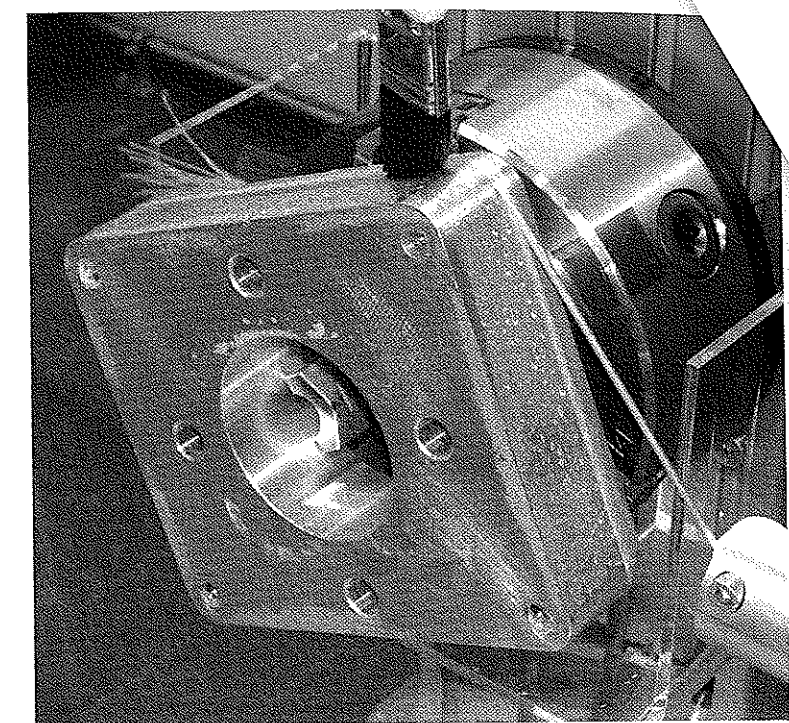
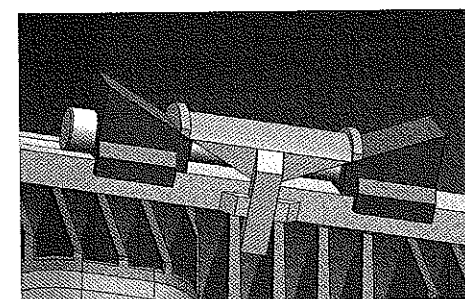
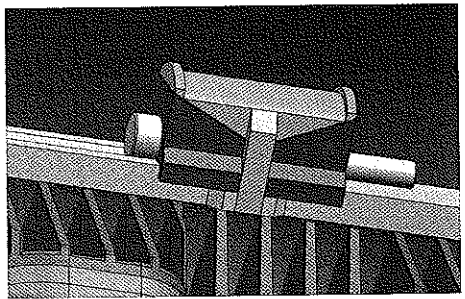


Figure 10-18: Manufacture of a glass fiber strap.



(a) wedges open



(b) wedges closed

Figure 10-19: CAD drawing of one strap tensioner.

¹⁸ www.agy.com

10.2.4. The hydrogen circuit

Figure 10-9 shows a schematic diagram of the complete FCS, including the hydrogen circuit (in red).

Hydrogen storage systems

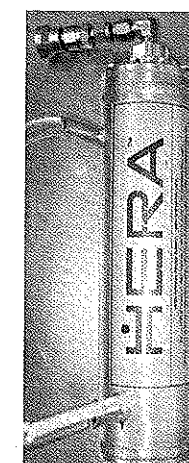
Like all the other components of the FCS, the hydrogen storage tank must be as small and lightweight as possible, which implies a minimal capacity. The tank's minimum capacity may be estimated from the targeted fuel consumption: 3,000 km/l of gasoline corresponds to approximately 2.5 g of hydrogen if the distance covered is 25 km, the average distance of a fuel economy competition run.

Two different storage systems were investigated during the PAC-Car projects: a metal hydride cartridge and a low pressure canister. Both systems have advantages and disadvantages, as described below.

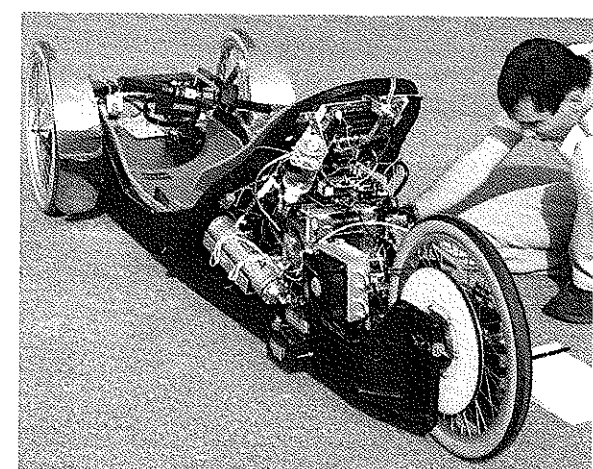
The main advantages of the metal hydride technology are a volume storage density comparable to liquid hydrogen and a high level of safety because damage to a metal hydride tank would not pose a fire hazard since the hydrogen would remain inside the metal structure. Its main drawbacks are more numerous, including a gravimetric storage density comparable to pressurized storage systems; a refilling time comparable to the time needed to recharge a battery; high sensitivity to certain gases, which might significantly reduce tank capacity after several charge-discharge cycles, implying the use of high-purity hydrogen (quality 5.0); the need to reheat the alloy to release hydrogen, which makes the stack's cooling system more complicated; and a hydrogen discharge flow rate that is limited by the desorption velocity.

This last disadvantage needs a bit more explanation. Assuming a vehicle tank-to-wheel efficiency of 50%, a power demand of 300 W at the wheel (requested during launching or ascent phases) implies a hydrogen flow rate of 0.3 g/min (or 3.4 SL/min). Unfortunately, the continuous maximum flow rate of a metal-hydride tank is bound to the quantity of alloy it contains and therefore to its capacity. This low maximal discharge flow rate, which is an advantage in the event that the tank breaks, becomes a disadvantage during regular use. To obtain a flow rate of 0.3 g/min usually means using a tank that has a hydrogen capacity of 5 g instead of the 2.5 g needed to cover the run distance.

Despite these disadvantages, this technology was used successfully in PAC-Car I. A photograph of the cartridge and its placement in the vehicle are shown in Figure 10-20. Table 10-1 provides the cartridge's main characteristics.



(a)



(b)

Figure 10-20: Metal hydride cartridge used in PAC-Car I.

Table 10-1: PAC-Car I's and PAC-Car II's hydrogen storage system comparison.

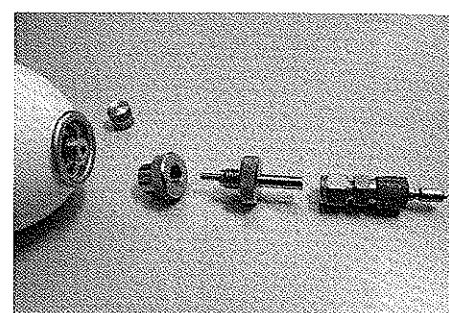
Vehicle	PAC-Car I	PAC-Car II
Technology	Metal hydride cartridge	Low pressure canister
Brand	Hera	Carbagas
Reference	SL 015C	Aerosol dispenser
Hydrogen content [g]	16	1
Output pressure [bar]	2 to 10	11 (full)
Weight [g] (without coupling)	1500	230

Despite the successful use of the first system in PAC-Car I, we chose to use the second system, a low pressure canister, in the PAC-Car II. The advantages of the low pressure canisters (about 10 bar) are mainly their low weight (230 g for a one liter canister) and the fact that, unlike high pressure canisters (usually 200 bar), no regulator is needed. (Since regulators are usually quite heavy, the need for a regulator would have increased the weight.) For safety reasons and to comply with race regulations, we used a canister available on the market and did not attempt to

manufacture it. For both runs, we chose to use the Carbagas¹⁹ aerosol dispensers distributed by Air Liquide, and shown in Figure 10-21(a). (Table 10-1 provides these canisters' vital statistics.) Each canister contains 1 g of hydrogen. A snap-on connector²⁰ (Figure 10-21-b) allows a fast exchange of the bottles between the runs.



(a) Two Carbagas canisters



(b) Close-up of the dismounted pipe fittings

Figure 10-21: Low pressure canister used in PAC-Car II.

Dead-end versus closed-loop hydrogen supply systems

Dead-end and closed-loop are two types of hydrogen supply systems (Figure 10-22).

The dead-end mode is the simplest way to supply hydrogen to a stack. Such a system requires only a regulator to reduce the pressure from the cylinder to the stack operating pressure. A bleed valve may be added at the stack's hydrogen outlet to eliminate the accumulation of inert gases, impurities and water. The opening of this valve may be programmed in relation to either stack voltage or time. Obviously, each time the valve is opened, a certain amount of hydrogen is discharged in the atmosphere, which reduces the efficiency of the system.

The closed-loop mode has a continuous flow of hydrogen through the stack from its inlet to its outlet. A recirculation pump is used to generate this flow, and a water separator to collect any liquid water present at the anode outlet. A bleed valve may still be useful to release the inert gases and impurities that may accumulate. Using a closed loop instead of the dead-end mode means that the bleed valve has to be

opened less often, increasing the efficiency of the stack. The main advantage of the closed-loop mode is due to the increased FCS efficiency, since the electrical energy needed to feed the recirculation pump may be lower than the additional electricity produced by the stack. This last point is discussed further in the next section. In order to benefit from this improved efficiency, we chose to use a closed-loop hydrogen supply system in the PAC-Car II.

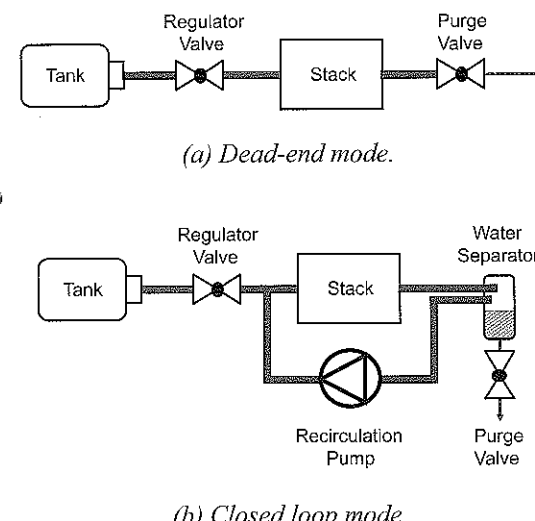


Figure 10-22: The two main hydrogen supply systems.

The recirculation pump

Experimentation has shown that the recirculation of 20% of the stoichiometric flow given by Equation (10.6) significantly improves stack efficiency. In this case, hydrogen is supplied in excess of the level stoichiometrically required, with a stoichiometric ratio of 1:2.

Since the stoichiometric flow is proportional to the stack current, the recirculation pump can be controlled from measured stack current in order to lessen the electric energy it consumes. However, since the pump behavior is strongly nonlinear, experiments must be carried out to determine an optimal control strategy that will maximize the FCS efficiency at any operating point.

¹⁹ www.carbagas.ch

²⁰ Miniature Quick-Connect QM Series from Swagelok, www.swageloc.com

The recirculation pump may be sized based on two main numbers: (1) 20% of the top hydrogen flow rate, calculated from the maximum required stack current; and (2) the pressure drop over the stack.

The pump used in the PAC-Car II is a NMP 015 M 12V from KNF²¹.

The inlet valve

As soon as hydrogen is consumed by the stack, the pressure inside the closed-loop system drops. Since the role of the inlet valve is to refill the closed-loop system in order to maintain a constant pressure, a proportional valve is used. Remember that a solenoid valve for gaseous media can be discrete or proportional. The first type has only two positions: fully closed or fully open. The second allows the valve to be opened gradually, which in turn allows the pressure to be slowly increased during the start-up mode (Section 10.3.2). The control of this valve is also discussed.

This valve must be chosen carefully. For the PAC-Car II, the major specifications were: gas type, orifice size, electrical specifications (i.e., AC/DC, voltage, electrical consumption) and opening response time. The other specifications that may influence the choice include weight, port type, operating pressure, operating temperature, leak rate, inductivity, reliability, and cycle life, but these are of secondary importance, either because they are always fulfilled (e.g., operating pressure and operating temperature), or they are not critical. Additionally, the valves have to be corrosion resistant and grease-free. Any foreign substance entering the stack may poison the catalytic surface of the MEA, thus reducing its efficiency and lifetime. This cleanliness specification is valid for the entire hydrogen circuit.

The maximum hydrogen flow rate may be calculated from the maximum requested stack current. With this maximum in mind, the valve's orifice size must be carefully chosen: too wide, the flow can be difficult to control; too narrow, the required maximum cannot be reached. Online tools²² are available to help with this choice.

After due consideration, we chose to use the hydrogen inlet valve, VSONC-3S25-VCF, from Pneutronics²³.

²¹ www.knf.com

²² For instance: www.ascovalve.com

²³ www.pneutronics.com

The manual pressure regulator and pressure gauge

Given an initial pressure of 11 bar in the hydrogen canister, the inlet valve should suffice to reduce the canister pressure to the stack operating pressure. Nonetheless, we installed a manual pressure regulator for system safety reasons: if for some reason the inlet valve stayed fully open, the cell membranes would be torn because of the sudden and/or important pressure gradient arriving on the air side from the hydrogen side. In addition, having a constant pressure upstream of the inlet valve during the entire operation time simplifies the design of the valve controller.

We chose to use an LG1 pressure regulator from GO²⁴, which reduces the pressure from the hydrogen bottle to 2 bar. Two pressure gauges display the pressure on both sides of the regulator. Upstream, one indicates the state of charge of the hydrogen tank; downstream, the other allows the delivered pressure to be adjusted.

The water separator

The water produced on the air side of the MEA is a normal by-product of the reaction. Small amounts of this water (about 1%) can migrate to the hydrogen side, due to the permeability of the MEA. However, since the hydrogen circuit is a closed loop, water can accumulate inside the stack and disrupt the circulation of hydrogen. The water separator collects this excess water in a small container outside the stack.

Usually, the water separator is a cylinder made of a material with good thermal conductivity (e.g., steel), inside of which the water vapor may condense. It is more efficient if it is located low in the hydrogen circuit and in a cool area. As shown in Figure 10-23, the water separator of the PAC-Car II's FCS is composed of a small container and a slightly-sloped finned pipe that follows the downward direction of the hydrogen flow.

²⁴ www.goreg.com

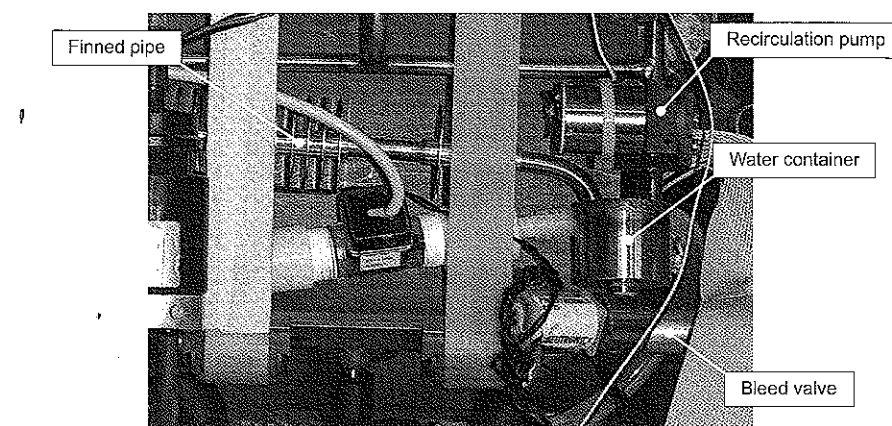


Figure 10-23: Close-up of the water separator in the hydrogen circuit of the PAC-Car II's fuel cell system.

The bleed valve

The bleed valve was added at the stack's hydrogen outlet to allow inert gases and impurities that may accumulate inside the closed-loop circuit to be eliminated, or purged. This valve can also be used to empty the circuit in the case of an emergency stop or system shutdown, or to purge the circuit after a long stop period.

We chose the 25-19-1-NV-12L50 bleed valve from Pneutronics for the PAC-Car II. As shown in Figure 10-23, this bleed valve is located under the water container, which allows the water in the container to be removed at each purge.

10.2.5. The air circuit

Figure 10-9 (section 1.3.2) shows a schematic diagram of the complete FCS, including the air circuit (in green).

The air circuit is designed to provide the necessary amount of air at the required pressure level. The air circuit pressure level defines the operative pressure level of the stack. As discussed in Section 10.2.1, this operative stack pressure is a parameter that must be optimized due to its influence on FCS efficiency. The stoichiometric amount of air that must be provided to the stack can be calculated using Equation (10.10). Just as in the hydrogen circuit, the air supplied must exceed the stoichiometrically required amount, with a stoichiometric ratio of 1.8:2.

The compressor

The compressor, which supplies pressurized air to the stack, is run by an electric motor that itself runs on electrical power from the stack. This makes the compressor the biggest parasitic load among the auxiliaries, and thus special attention must be paid to make it as efficient as possible.

The compressor used in the PAC-Car II's FCS is a derivative of a diaphragm compressor (ref. N828 from KNF²⁵). We replaced the compressor's original motor with a lighter, more efficient gear motor, and the housing was redesigned to make it lighter as well. Figure 10-24 shows the compressor, placed on a table.

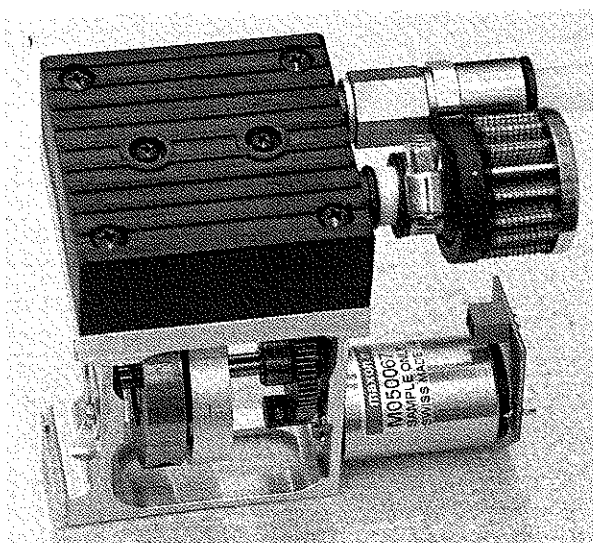


Figure 10-24: The air compressor of the PAC-Car II's FCS.

The air accumulator

Usually just a standard tank, the air accumulator stores pressurized air and acts as both a filter and a buffer. It acts to filter the pressure waves produced by the running compressor because such waves could weaken the mechanical properties of the MEA by repeated stress (i.e., fatigue) variations. It also acts as a buffer that

²⁵ www.knf.com

can supply air to the stack whether the compressor is switched on or off. The buffering action adds a degree of freedom to the system that allows the compressor:

- , to be used at its most efficient operating point, independently of stack current and thus of the drive power demand;
- to be switched on or off in order to shift the stack's operating point to an area in which it is more efficient (Figure 10-7); and
- to be downsized since both the accumulator and the compressor can work together to supply air to the stack when short bursts of full power to the wheel are necessary.

In addition, due to the buffer, the FCS remains pressurized in standby mode. It is therefore possible to move from the standby mode to the drive mode without any additional energy sources, such as a battery. A battery would have raised suspicions during the technical inspection because it would have been difficult to prove that the battery did not feed directly into the drive motor.

In the PAC-Car II, we tried to keep the air pressure as constant as possible, close to optimal operative stack pressure, while also maintaining a sufficient air supply in the stack for several minutes when the FCS is in standby mode (i.e., when no drive power is demanded at the wheel. See the “stop-and-go” driving strategy in Chapter 11). Thanks to the air accumulator, the stack remains pressurized, ready to deliver any requested power. Still, small amounts of hydrogen and air are still consumed as the stack continues to feed the auxiliaries. For this reason, the size of the accumulator tank depends on 3 parameters: (1) the power consumption of the auxiliaries in standby mode; (2) the requested duration of the standby mode; and (3) the acceptable pressure reduction in standby mode.

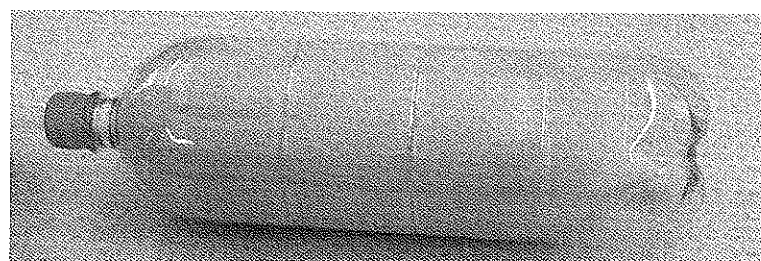


Figure 10-25: The air accumulator of PAC-Car II. The flexible envelope is visible inside the transparent protective bottle.

For the PAC-Car II's FCS specifications, the calculation suggests a 10-liter tank, which would have been impossible, due to lack of space inside the vehicle.

Consequently, we developed another type of accumulator specifically for PAC-Car II, one whose cylindrical envelope was flexible rather than rigid, being made of rubber. This envelope was placed inside a rigid tank, called a bottle, to protect it from perforation. The resulting pressure evolution law was, as a function of the air intake volume, partially equivalent to a tank that was twice the volume. Figure 10-26 shows a curve representing the behavior of a 2-liter accumulator. In addition to an important level of hysteresis, two zones can be distinguished on the curve: (1) from 0.2 to 1 Sl, the deformation of the envelope prevails, and the accumulator behaves rather like a larger rigid tank; and (2) from 1 to 1.8 Sl, the envelope comes in contact with the protective bottle, and the accumulator behaves rather like a 2-liter rigid tank. Still, the hysteresis indicates an energy loss in the envelope material, meaning that cycling the accumulator over its full volume range could lead to lower FCS efficiency ratings.

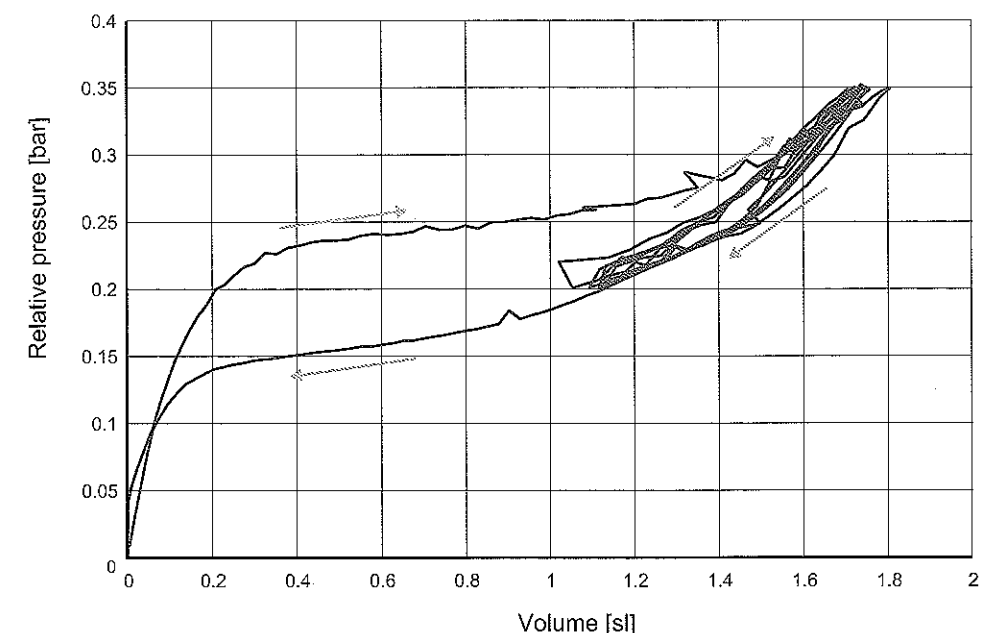


Figure 10-26: The curve of pressure versus air accumulator volume.

The pressure gauge

A pressure gauge helps to monitor the pressure in the FCS air circuit. It allows the pressure level in the air accumulator to be verified by the officials before and after a test run in order to guarantee that no stored pneumatic energy has been used.

The release valve

The release valve, mounted at the stack's outlet, controls the stack air flow. For this reason, it must be a proportional valve. It must also be corrosion resistant because the high degree of purity of the water produced makes the water highly aggressive.

In the PAC-Car II, we used two VSONC-6S11-ICF0 release valves from Pneutronics²⁶. The two valves, which were mounted in parallel, were chosen instead of one simply because they were lighter than the equivalent single valve available on the market.

10.2.6. The coolant circuit

Heat and water are the two by-products of any stack. The heat produced increases the temperature of the MEA, which increases the cell voltage and therefore its efficiency. Unfortunately, the MEA temperature must be kept under the limit – about 80 °C – imposed by the materials used. The role of the coolant circuit is to maintain the stack temperature just below this maximal temperature, at a temperature called the “optimal operating temperature”. Figure 10-27 shows the influence of the operating temperature on the polarization curve of the PAC-Car II stack. As the figure shows, the higher the operating temperature, the higher the stack voltage, and therefore the higher the stack efficiency.

In the PAC-Car II, the relatively low power demand and the high efficiency of the stack produces a maximum thermal power of about 100 W. Since the PAC-Car II's FCS operates intermittently, the average thermal power is even lower. Therefore, the heat dissipating from the stack via natural convection is sufficient to keep the FCS far under its optimal operating temperature. Nonetheless, the stack had to be insulated during the race.

Even so, the cell technology used in the stack of PAC-Car II required an external coolant circuit in order to avoid hot-spots on the MEA and to homogenize the temperature inside the stack. The coolant circuit is also used to warm the stack up to its optimal operating temperature, without having to run the FCS. This warming is carried out with the help of an electric heater embedded in the circuit and powered by a non-embedded battery. Since it is mainly used to heat the FCS, the term “coolant circuit” almost appears inappropriate. Nonetheless, that is what it is called!

²⁶ www.pneutronics.com

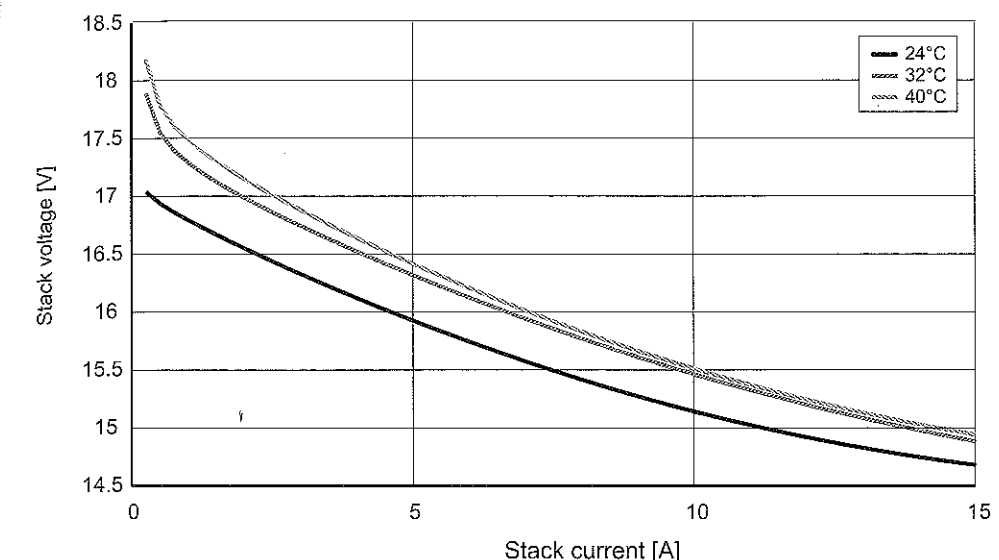


Figure 10-27: Polarization curve at three operating temperatures. From experiments carried out on the FCS of PAC-Car II. Temperature reported is the coolant temperature.

A pump, a Bosch windshield washer pump for automobiles (ref. 0392 010 008-12V), is used to circulate the coolant – demineralized water – in the circuit. This pump operates with a constant electric power that was set experimentally to the needed minimum value. A temperature sensor, submerged in the water, monitors the temperature, both taking measurements (Figure 10-27) and insuring safety. A water flow sensor (ref. 173931-C from Turboflow²⁷) monitors the flow, since any stop in the flow could damage the cells. A small expansion vessel was added to the circuit to compensate water loss due to evaporation and/or leaks.

10.2.7. The electronic systems

Power sources

The 2005 European Shell Eco-Marathon regulations allowed ICE vehicles to have some battery-fed auxiliaries, such as ignition devices, fuel injectors, starters, and Engine Control Units (ECU). The electrical energy drawn from this battery is not

²⁷ www.gemssensors.com

taken into account in calculating the vehicle's energy consumption and so does not affect its fuel efficiency rating. For reasons of fairness, certain FCS auxiliaries may also be battery-powered. In the PAC-Car II, for example, all of the sensors, the valves and the servos that mesh the drive train gears (Section 9.4.2) are battery-powered. All the other auxiliaries – the compressor, the hydrogen recirculation pump and the water pump – are powered by the stack.

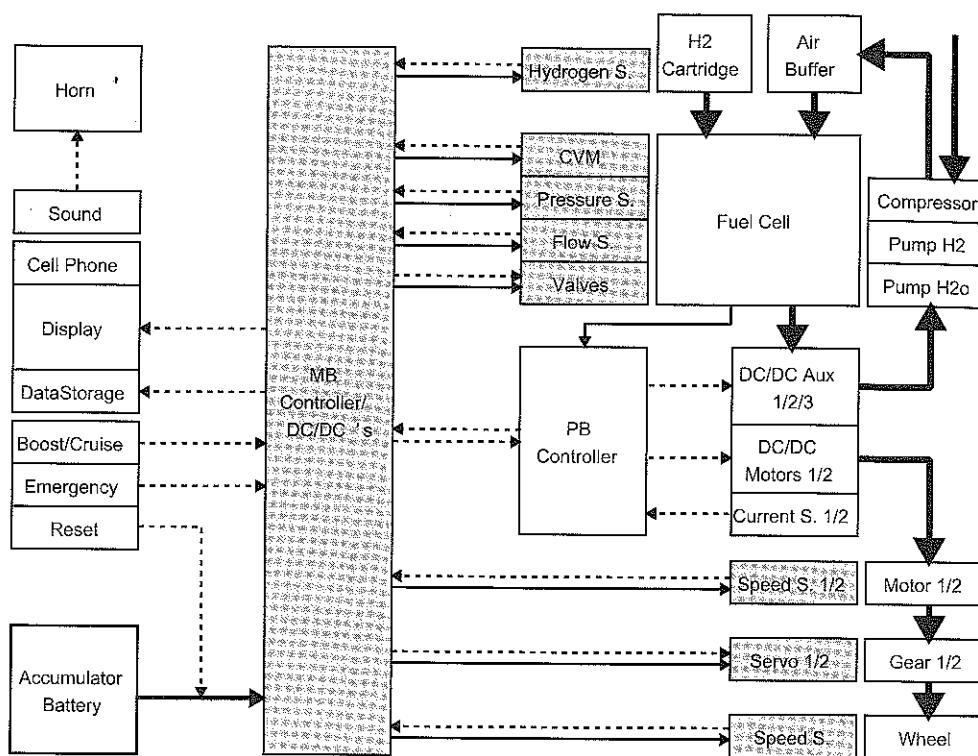


Figure 10-28: Energy, mass and information flows between the various PAC-Car II components.

The PAC-Car II electronics are distributed on two different boards: the mainboard and the powerboard. On the mainboard, there is a programmable high-level language processor that takes care of all the supervisory control. The powerboard handles the distribution of power from the stack to the auxiliaries and the drive motors. Since the current drawn by the drive motors has to be controlled, the powerboard also has a microprocessor. With this configuration, the mainboard can be considered as an ECU and can therefore be powered by an additional battery. The communication between mainboard and powerboard is via optical link, which

means that no power can be transferred from the mainboard battery to the drive motors.

The energy, mass and information flows are shown in Figure 10-28.

The compressor, the hydrogen recirculation pump, and the coolant recirculation pump are supplied by the stack via the powerboard. The sensors, valves and servos are supplied by the mainboard, and thus by the battery (i.e., a battery pack containing ten 1.5 V AA alkaline cells), which complies with the race regulations.

The mainboard

The mainboard (Figure 10-29) is the computer hardware that supervises the entire PAC-Car II powertrain (including the FCS, drive motors and servos). Based on the Phytec phyCORE-MPC555 Rapid Development Board PCM-001-220, the mainboard has a 32-bit PowerPC core running with 40 MHz and a 64-bit floating point unit. This core processor can be programmed using Matlab-Simulink, Realtime Workshop and Embedded Target for MPC555 Toolchain. The Simulink model is translated into target-specific C-Code. The usefulness of Matlab/Simulink for program development cannot be overestimated. We didn't have enough time to develop a complete control software in C or a similar programming language, but Matlab/Simulink made very fast program changes possible, including changes in the code for state transitions.

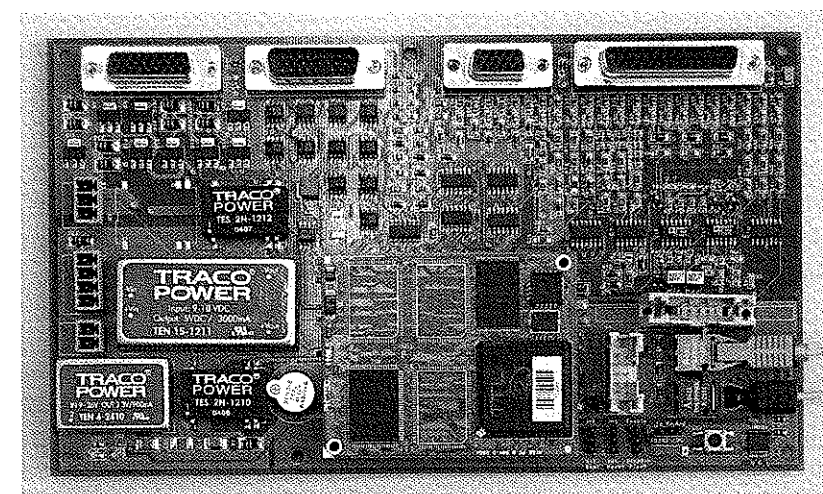


Figure 10-29: Mainboard of PAC-Car II.

In addition to the processor board, the mainboard houses customized hardware:

- low-pass filters for the sensor signals;
- pull-up and pull-down resistors for various inputs and outputs;
- inverters for outputs, if necessary;
- the optical link for serial communication with the powerboard;
- a hardware safety circuit for closing the hydrogen input valve in the event of a hydrogen leak;
- DC/DC converters for various supply voltages; and
- an alarm buzzer.

The powerboard

The powerboard (Figure 10-30) is the hardware that ensures the electrical interface between the power output of the stack and the electrical devices it feeds: the drive motors, compressor, water pump, and hydrogen recirculation pump. For each component, a DC/DC converter is used to reduce the stack voltage to the value requested by the mainboard. The powerboard is based on a MSP430-micro controller, chosen for its low energy consumption. This processor, programmed in C, is used for the digital control algorithms.

Many details of power board's power electronics had to be optimized to reach a very high level of efficiency:

- the MOS-FETs have an extremely low on-resistance;
- a 40 kHz switching frequency reduces the losses in the MOS-FETs and in the inductivities;
- free-wheeling diodes with synchronous switching MOS-FETs were chosen;
- the gate-pilot was optimized to guarantee the very fast shutdown of the MOS-FETs;
- a hardware adaptive shoot-through protection was implemented;
- the drive motor impedances have upright windings in order to minimize the proximity effect;
- connector cables with 8 mm² cross-section were used; and

- the current from the stack is distributed via solid copper bars.

As a result of these optimization efforts, the efficiency of the DC/DC converters for the drive motors is between 95% and 98%. Very accurate current sensors were needed to measure efficiency levels in this range!

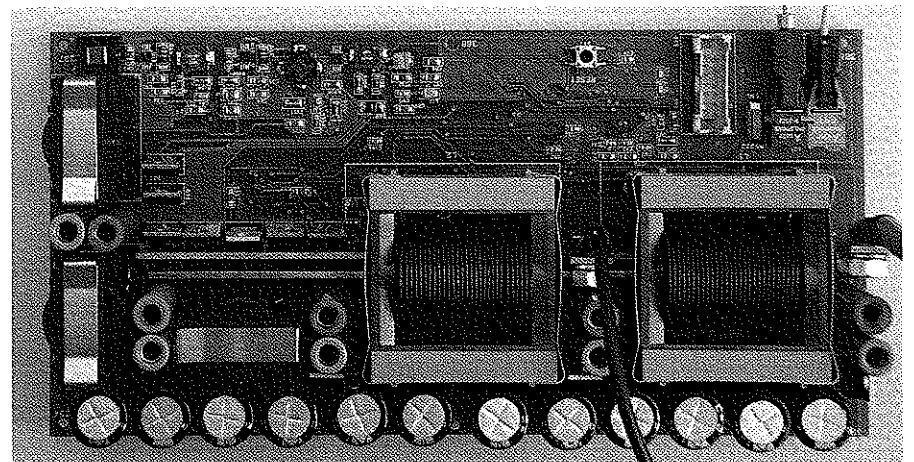


Figure 10-30: Powerboard of PAC-Car II.

Pilot Interface

The pilot interface is composed of all the devices that operate the information transfer from the pilot to the vehicle and vice versa. Part of the pilot interface has already been discussed in Sections 8.2 and 9.5, which deal with steering and braking, respectively. This section focuses on the interface between the driver and the powertrain. This pilot interface must be carefully designed so that the pilot receives only the relevant information that will allow him/her to keep the vehicle under control in all situations.

Let's begin with the systems that allow the driver to send information to the powertrain. One of the most important pieces of information is the torque set point. In a regular passenger vehicle, this information is conveyed by the pilot via the accelerator pedal. In the PAC-Car II, this pedal was replaced by 3-position toggle switch. This toggle switch is located on the same handle used to activate the hydraulic brakes. Holding this handle in her/his left hand, the pilot can boost, cruise, coast, or brake, while the right hand is used to steer the vehicle and to activate the mandatory horn. The pilot keeps all the vehicle controls continually in hand in order to face all driving situations.

We chose this 3-state system instead of a continuous one based on the results of an optimal driving strategy analysis (Chapter 11). In the middle position, no drive power is delivered and the FCS remains in the standby mode. The switch thus remains in the middle position until the pilot calls on drive power. The two other switch positions provide drive power: moving the toggle to the right, provides the maximal power and moving it to the left provides a constant low level of power.

In the PAC-Car II, only three drive modes were judged necessary to minimize the fuel consumption during a run:

- the coasting mode: no drive power is delivered but the powertrain is ready for duty. Everything is designed to minimize hydrogen consumption. For example, this mode is used when the vehicle glides down the hill;
- the boost mode: the maximal drive power is delivered. This mode is mainly used to launch the vehicle; and
- the cruising mode: the powertrain's control electronics maintain the vehicle velocity at a constant value selected by the pilot. This mode is the normal drive mode.

Two additional push-buttons are however accessible to the pilot: one to reset the mainboard and the other to send an emergency signal to the mainboard. The reset button may be used in case the software of the mainboard crashes. The emergency signal starts the emergency routine in the mainboard software. A second emergency switch is situated outside, at the rear of the vehicle, as required by the regulations.

The system that allows the driver to get information from the powertrain is contained in the dashboard. In PAC-Car II, the dashboard contains a LCD display. As a team, we had many discussions about how much information the pilot needed to have available. The answer came from the pilots themselves. Based on their experience in driving the PAC-Car I in 2004, they felt that, in order to let the pilot focusing on driving, the golden rule was "the simpler, the better". The information displayed includes:

- elapsed time;
- vehicle speed;
- distance traveled;
- fuel consumption in standard liters hydrogen; and
- stack temperature (used during the stack preheating process).

The display was a pocket organizer Qtek Pocket PC 9090, which could also serve as an emergency phone in the vehicle and a data-logging system. During a run, the relevant FCS information was transferred via a serial connection from the mainboard to the pocket organizer and saved on a SD-memory card. Thus, these data could be transferred easily to a computer for later analysis.

As mentioned above, the pocket organizer, with its built-in cellular phone, serves as an emergency phone. Compared to walkie-talkies, the Pocket PC has the clear dual advantage of unequivocal understanding and no other competitors on the same channel. Before the race, the phone was configured so that by pressing only one button, the pilot is immediately connected to the pit. Incoming calls are accepted automatically.

The cell voltage monitoring system (CVM)

The voltage distribution of each cell in the stack is a strong indicator of the health of the stack. A cell with a reduced voltage (in relation to the other cells) is probably a cell with a reactant supply problem. If no counteraction is taken, the voltage will continue to decrease until irreversible damage to the cell occurs. Since an individual bad reactant supply is most probably due to the accumulation of water in the supply lines, the most appropriate counteraction is usually a brief increase of the gas flow in order to remove the excess water. This gas flow increase can only be accomplished by opening either the air valve or the hydrogen purge valve. The cost in terms of fuel consumption of a hydrogen purge is much higher than flushing the supply line with air. Fortunately, the location of the problematic cell indicates which circuit – air or hydrogen – must be purged.

Each cell voltage is sent to the CVM device, which then sends to the mainboard the average cell voltage, the voltage of the cell that has the lowest voltage and the location of that cell in the stack. The stack is assumed to run properly if the following two conditions are fulfilled: (1) the difference between the average cell voltage and the lowest cell's voltage is less than 50 mV, and (2) the average cell voltage is higher than 550 mV. If these conditions are not fulfilled, purges are activated.

10.2.8. Other components

The following sensors are needed to monitor the various signals automatically and are all supplied by the mainboard battery:

- the pressure sensors in the hydrogen and air circuits;
- the air mass flow sensor that measures the amount of air flowing from the accumulator to the stack;

- the stack and coolant temperature sensors;
- the hydrogen leak sensor;
- the current sensors; and
- the speed sensors for the motors and the rear wheel (see Section 9.4.2).

The use of the information provided by these sensors will be discussed in the next section about FCS control tasks.

10.3. The control systems

The FCS control tasks can be divided into three categories:

- the control of the individual subsystems (e.g., air system, hydrogen system);
- the control of the FCS modes (e.g., shut-down, start-up, running); and
- the control of diagnostics and safety.

The first category, the control of the individual subsystems, is the most conventional type of control. Here, the required signal values are monitored by simple straight-forward controllers, such as PID-controllers or switch-type controllers. The second category, mode control, involves a state-machine control. Depending on the system mode, the values required by the individual controller may change. The third category, diagnostics and safety, required the continual scanning of the FCS for possible malfunctions so that, in critical situations, a shutdown procedure can be initiated automatically.

Due to the project's tight time schedule, the entire control software was developed with Matlab/Simulink using both Embedded Target for MPC555 and State-Flow toolboxes. For this reason, a micro-processor that could be programmed using Real-Time Workshop from Mathworks was chosen. A solution that would have required programming in C or a similar programming language would have been much less flexible.

The structure of the PAC-Car II control system is shown in Figure 10-31.

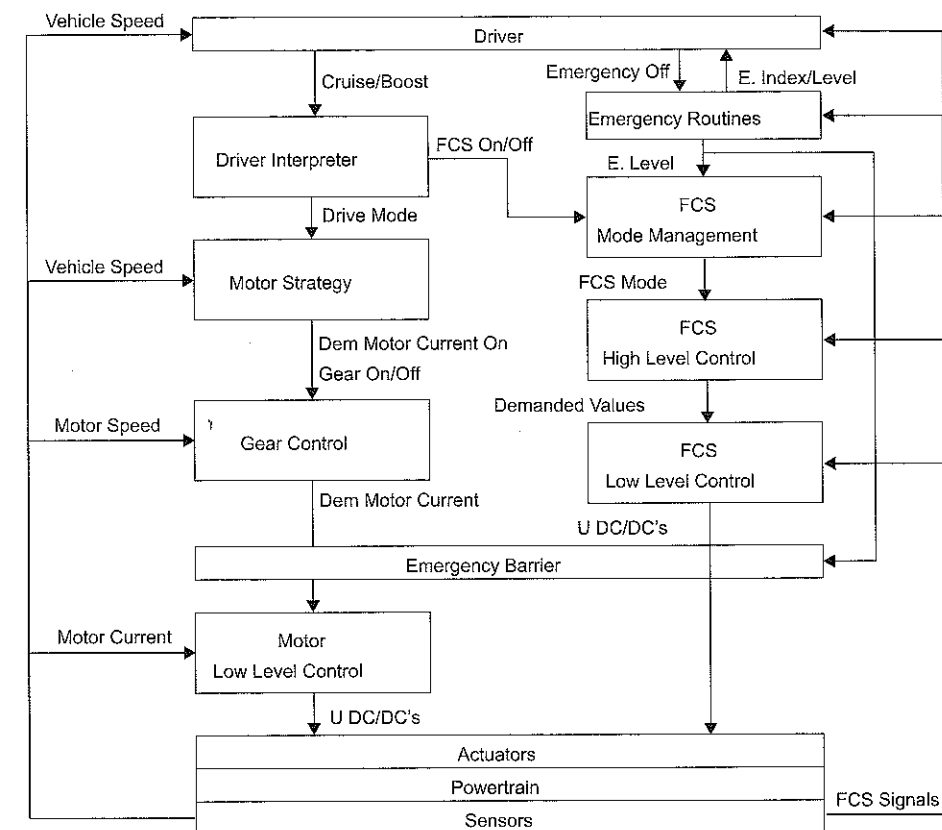


Figure 10-31: Control structure.

10.3.1. Subsystem control

Controlling the hydrogen circuit

The hydrogen pressure in the FCS is controlled with a PI-controller that drives the inlet valve (Section 10.2.4) in relation to the pressure in the air circuit (Figure 10-32). Choosing a high pressure allows the system to benefit from the higher partial hydrogen pressure, which increases stack voltage and therefore stack efficiency. However, the offset between air and hydrogen pressure is limited by the mechanical strength of the MEA. The inlet valve can be used to increase the hydrogen pressure in the stack, while the bleed valve can be used to decrease it. However, unlike the inlet valve, the bleed valve opening is not controlled by this control loop.

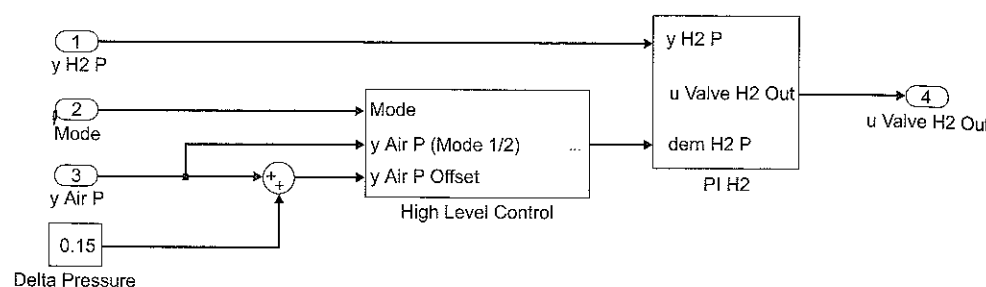


Figure 10-32: Flowchart of the hydrogen pressure control. A PI controller drives the hydrogen valve.

The bleed valve allows the water separator to be purged by introducing hydrogen pulses. Such pulses, resulting from a sudden opening of the valve, help to evacuate excess water [51]. Pulses of hydrogen or air are a common means of removing water droplets from the cells, thus improving stack operations.

The recirculation pump runs at a constant flow-rate, excepted at startup when it is slightly lowered.

Controlling the air circuit

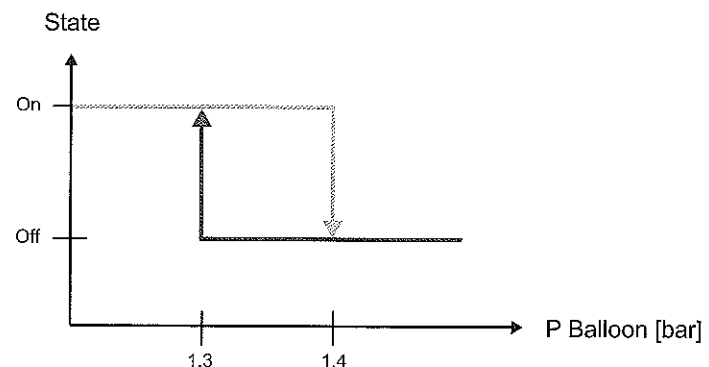


Figure 10-33: Flowchart of the compressor control.

Controlling the air circuit requires two control loops: one to control the pressure in the air accumulator and the other to control the air flow.

A switch-type controller with hysteresis is used to control the pressure level by switching the compressor on and off (Figure 10-33), thus making it operate at its most efficient operating points.

Controlling the stack's air mass flow is very important for maintaining proper operation conditions in the stack. Since the stack must respond dynamically to any power demand, a feedback-only structure would not be sufficiently rapid. Figure 10-34 shows the flowchart of the air mass flow control.

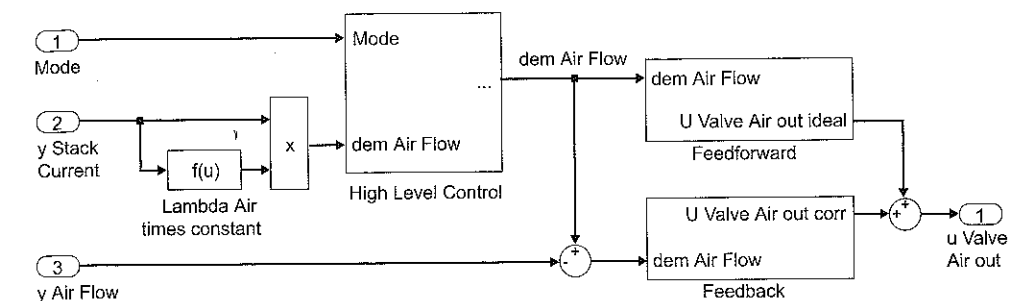


Figure 10-34: Flowchart for the control of the air path.

The current drawn from the stack is used to calculate the air flow set point, taking the stoichiometric ratio into account. This set point is used in a dynamic feed-forward controller and in a feedback controller. The output of the two controllers is then used to generate a pulse width modulated signal, which is the input signal for the two proportional release valves.

Note that the release valves are not only used to control the air mass flow, but, similarly to the process on the hydrogen side, also to purge the circuit and remove any excess water produced by reaction.

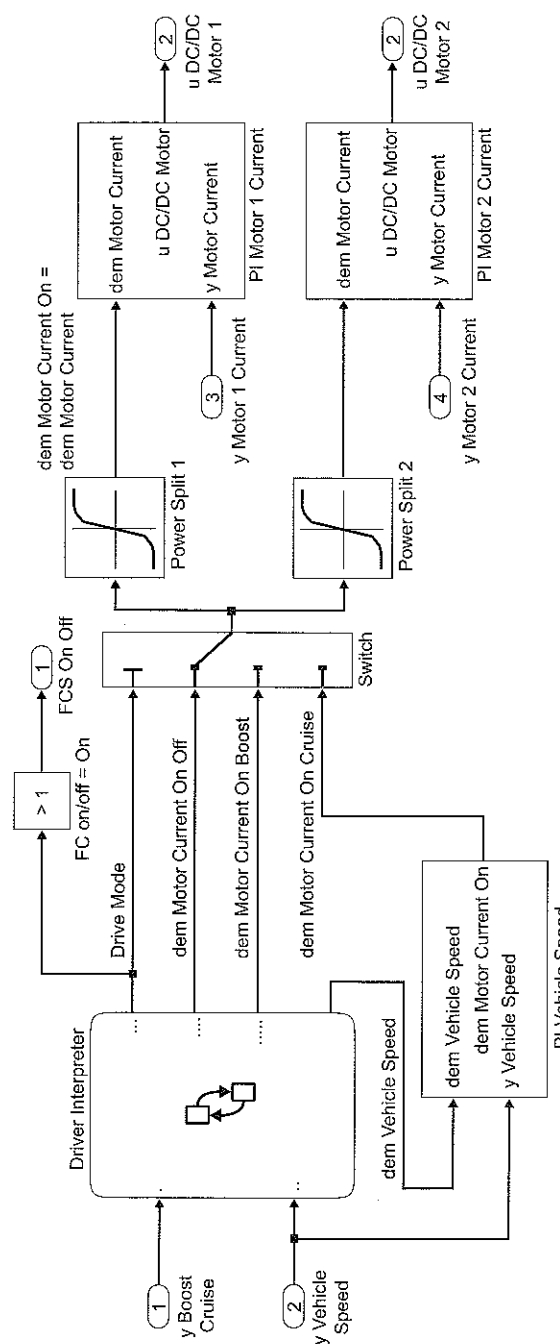


Figure 10-35: Flowchart of motor current control

Controlling the drive motor

The control of drive motors is carried out by the powerboard micro-processor.

In normal operating conditions, each motor is driven either with maximum current (boost mode) or at a constant speed (cruise mode). In both cases, the current control depicted in Figure 10-35 is used. To control the motor speed during the cruise mode or the synchronization phase needed prior to connecting the gear pairs (Section 9.4.2), an additional control loop is introduced, as shown in Figure 10-36.

Since the inertia of the motor is very different depending on whether it drives the vehicle (cruise mode) or not (synchronization phase), the speed control parameters have to be adjusted in consequence.

10.3.2. Mode control

So far, only the low-level controls of the FCS have been described. Low-level controls guarantee that the FCS will operate correctly under dynamic operating conditions. Because of the “stop and go” strategy (i.e., when the drive motors are switched on and off several times per lap), the start-up and shut-down procedures must be fast and reliable. To handle start-ups, shut-downs and emergencies correctly, a method of mode control that uses many state-machines was developed. For this kind of control, all possible states of the FCS must be included. We implemented the multi-level mode management method whose structure is depicted in Figure 10-37.

Six levels can be distinguished:

- Level 0: system off;
 - Level 1: Mainboard processor is working. Battery is plugged in;
 - Level 2: Air accumulator pressure allows the FC to be started;
 - Level 3: Powerboard is active and supplied by the FC; communication between mainboard and powerboard is established;
 - Level 4: Stack-voltage OK;
 - Level 5: Power supply to the auxiliaries from the FC is OK; and
 - Level 6: Motor current allowed.

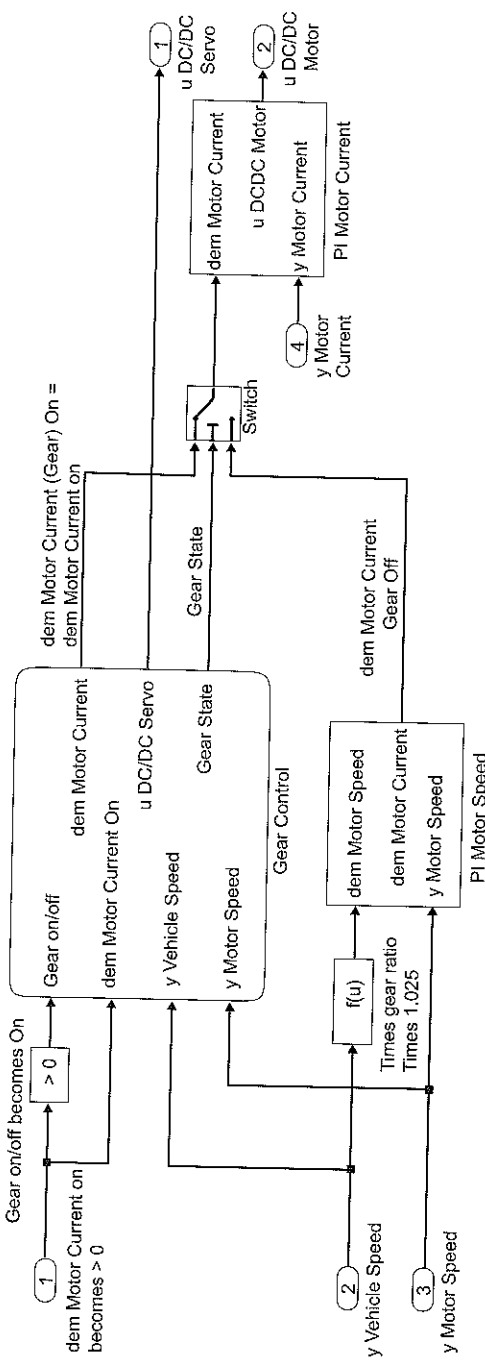


Figure 10-36: Flowchart speed control.

We felt that this rather sophisticated state-flow system was necessary for a couple of reasons. First, the better the system automation, the more reliable it would be in critical situations, including both failure situations and the time-critical situations at the start of a race. The pilot should be able to concentrate on completing a perfect race, rather than worrying about the FCS! Second, even with a FCS that is most efficient partially loaded, it would still be necessary to shut the motors on and off during the race, even during one lap. This would mean that the FCS would be idling, thus using hydrogen but not producing any drive power. Such a situation must be avoided at all costs, which justifies our inclusion of such a sophisticated state-flow system.

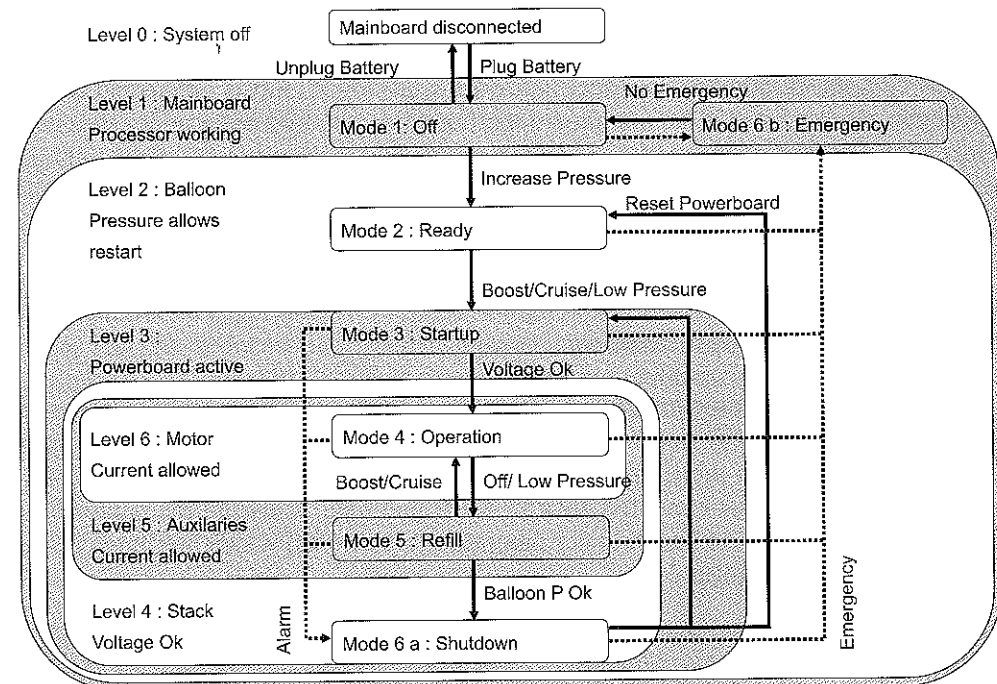


Figure 10-37: Mode management.

For these reasons, shutting the FCS off and turning it back on again must be fully automatic and fast. Shutting off the system requires refilling the air accumulator and then shutting off the coolant and hydrogen recirculation pumps. However, it is only possible to turn the system back on if the pressure in the air accumulator is high enough to supply the necessary air to the stack. If the power demand is null for a long time, the pressure in the air accumulator slowly drops due to a continuing air consumption that is needed to maintain the FCS at idle. In this case, when the air pressure goes under a certain level, the compressor automatically

begins to refill the air accumulator; otherwise, a restart of the system would no longer be possible.

10.3.3. Diagnostics and safety control

Several safety measures were included in the control design in order to avoid damaging the cell. For instance, all the sensor cables are equipped with pull-up or pull-down resistors, making it possible to detect a broken cable. The signals are continually verified to insure their plausibility and the proper functioning of the FCS. During such verifications, if minor errors arise, the system is put into shutdown mode. However, the stack remains under pressure so that the system will be able to start up again as soon as the error has been fixed. In the case of a serious system failure, the FCS is immediately shut-down by releasing the pressure in the supply circuits. In addition, a direct hardware shut-down loop is connected to the hydrogen sensor. Even if the mainboard malfunctions, the hydrogen inlet valve will close if the hydrogen concentration on top of the FCS compartment of the vehicle reaches 2.5% (a concentration of 4% of hydrogen in air is inflammable). This limit is higher than the corresponding software limit (1%) because a proper shutdown via software is preferred.

10.3.4. Operation optimization

Various operating parameters must be optimized for the entire vehicle in order to attain the most efficient performance. Since it would have been much too time consuming to perform these optimizations on the race track, the demanded power profile for the FCS was emulated with an electronic load, allowing the parameters to be optimized on a test bench under laboratory conditions, which are much more reproducible and comfortable.

Due to time restrictions, we were not able to complete a full grid optimization of the system. Therefore, the parameters were optimized sequentially according to their importance. A model-based optimization procedure would have been an excellent alternative, but unfortunately we did not have enough time to create a model detailed enough to reproduce all important effects.

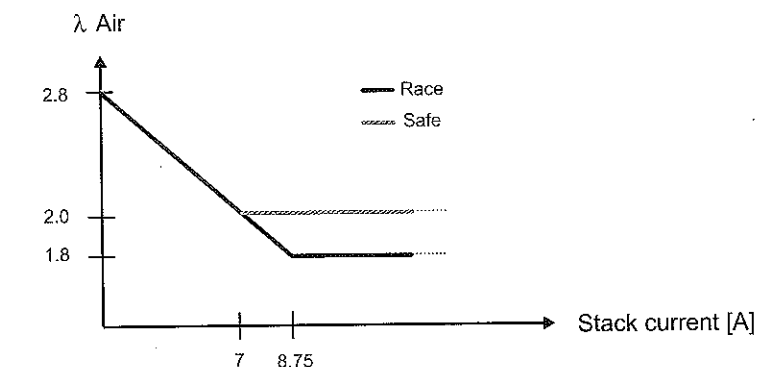


Figure 10-38: Air stoichiometry as a function of stack current.

The stoichiometry ratio

For a low power demand, an air stoichiometric ratio of 3 has been found to be optimal (i.e., the actual air mass flow is three times higher than the amount calculated with Equation (10.10)). For a high power demand, the air stoichiometric ratio can be reduced in order to lessen the consumption of energy by the compressor (Figure 10-38). For example, the stoichiometry ratio was reduced to 1.8 for competitions under full-power conditions, while a value of 2.0 was used during test runs.

The FCS pressure level

The pressure in the air circuit is the driving pressure of the FCS. The hydrogen circuit pressure is controlled according to the air circuit pressure. Generally, the higher the partial pressures of the hydrogen and the air-born oxygen, the more efficient the stack. The stack voltage and its efficiency thus change according to the Nernst equation:

$$E = E^0 + \frac{RT}{2F} \log \left(\frac{P_{H_2} P_{O_2}^{1/2}}{P_{H_2O}} \right) \quad (10.13)$$

Increasing the operative pressure of the stack is a way to increase partial pressures, but a higher air pressure leads to a higher energy consumption by the compressor. A compromise had to be found for the FCS in the PAC-Car II. Experimental results show that the optimum is attained at a value of 0.35 bar (relative pressure). The compressor in the PAC-Car II is therefore cycled around this level, as shown in Figure 10-26, with a hysteresis of 100 mbar.

Temperature

Figure 10-27 shows the dependency of the polarization curve on the temperature. Right before the race, the FC is conditioned in order to increase stack efficiency by heating the coolant to 50 °C with electrical heaters, which offsets ambient conditions by 16 °C. This offset allows the temperature to be kept high, but more or less constant. In fact, it dropped only slightly during the world-record race in Ladoux. Keeping the temperature more or less constant is very important because big temperature drops cause water condensation, which forces system purging. The losses incurred by purging are higher than the gain in efficiency due to a higher stack temperature.

Humidification

The moisture content of the MEA greatly affects stack efficiency: too dry, the cell efficiency drops; too wet, water droplets appear, which may disrupt gas flows leading to similar efficiency drops. In more powerful FCS, this issue is usually solved by adding auxiliaries to manage the moisture content of gases before they enter the stack.

In PAC-Car II, the stack cells have their own embedded passive humidifying system. On the air side, part of the water produced on the air side is recycled internally to humidify the intake air. Water droplets are removed from the MEA active area little by little, as long as the air flow is sufficient. If needed, pressure pulses generated by opening the release valve briefly (i.e., air purges) have proven to be an excellent means of removing the accumulated water. On the hydrogen side, the little amount of water that migrates from the air side to the hydrogen side through the MEA is enough to humidify the hydrogen. When the moisture content becomes too high, water vapor condenses inside the water separator. Under certain conditions, water vapor may condense inside the stack, which can lead to a drop in stack efficiency, as occurs on the air side. In this case, purging the hydrogen circuit by opening the bleed valve briefly is the only way to fix the problem (the hydrogen flow removes the water from the stack and deposits it in the water separator).

System purging

From the energy point of view, the air purges are “cheap” since the amount of air released each time is small, as is the amount of energy used to produce this quantity of air. On the other hand, hydrogen purges are much more “expensive” since each purge wastes a certain amount of hydrogen, compromising the overall efficiency of the FCS significantly. For this reason, the use of purges has to be reduced to the minimum, purging only the right circuit – air or hydrogen – and only when necessary.

Decreasing voltage in single cell is usually due to water condensation inside the channels of one of the two distributor plates in this cell. This unbalanced cell voltage distribution is detected by the CVM. Two typical cell voltage distributions are shown in Figure 10-39 and Figure 10-40. The first figure shows a situation that can be fixed with a hydrogen pulse, and the second one, a situation that can be corrected with an air pulse.

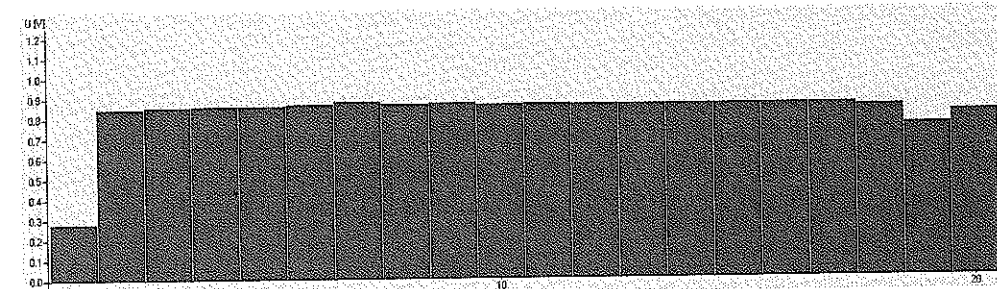


Figure 10-39: Typical voltage distribution in the stack cells due to hydrogen starvation in one cell.

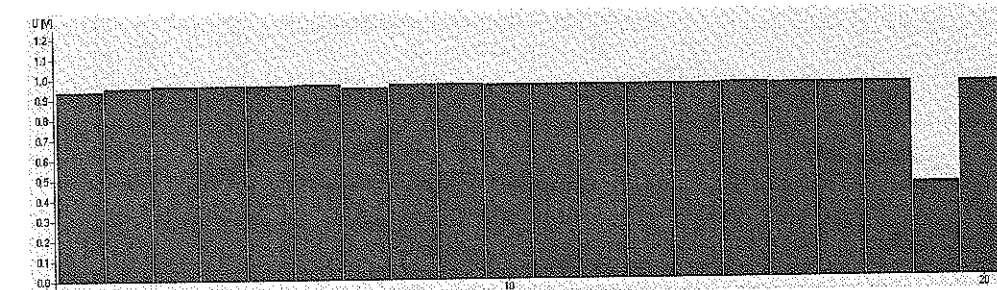


Figure 10-40: Typical voltage distribution in the stack cells due to air starvation in one cell.

The duration of a hydrogen purge is set to the minimum value that will achieve a positive effect. The purge should consist of several short pulses, which has been shown to be more effective than one longer pulse. Each of these short hydrogen pulses expends approximately 5 mg of hydrogen, meaning that if 20 pulses are needed (the initial value during our purge-strategy development phase), around 10% of the fuel “consumed” is wasted by the hydrogen purges.

At start-up, at least one air purge is necessary to remove the hydrogen that diffused through the MEA while the system was idling but pressurized. When this hydrogen arrives on the cathode side, it immediately reacts with the oxygen in the air, producing water. Practically speaking, water enrichment and oxygen starvation take place simultaneously at the cathode, and the water content of the air increases until it reaches 100% saturation. If the temperature of the saturated air drops even slightly, condensation occurs. A pulse of air is used to remove this water from the stack and to renew oxygen consumed at the cathode, which allows an immediate restart.

A good-quality stack has a low diffusion rate throughout the cell. It takes approximately 20 minutes for the stack voltage to drop to zero in the PAC-Car II, which indicates a high quality MEA. We observed that a hydrogen purge at start-up increased cell voltages and efficiency over the entire 20-minute period.

10.4. System results

In the following section, measurements from the world record race at Ladoux are given and explained. In this race, ten 2,068 m-long laps had to be covered at a minimum average speed of 30 km/h (Figure 10-41).

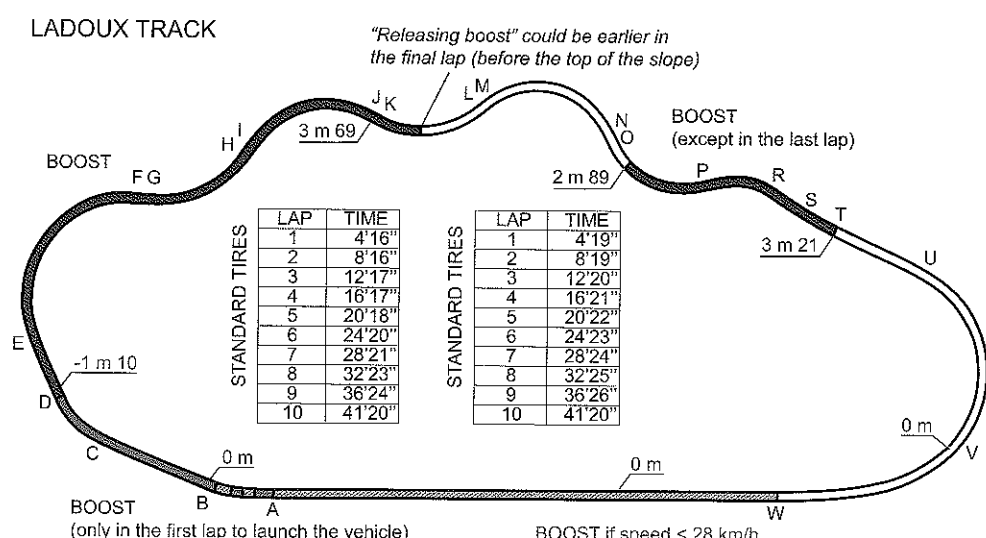


Figure 10-41: Schematic of the race track at Ladoux, with driving strategy indications for the pilot.

Theoretically, each lap requires only two boost phases, except for the first lap during which the vehicle launch requires extra power (Figure 10-42). The power-spikes before the second powerphase come from the torque limitation. The pilot tried to restart the system, but the motors were coupled off automatically, because the torque was too low for the motors to run efficiently. The measurement also shows that the concept of two independent motors was quite appropriate for the Ladoux track.

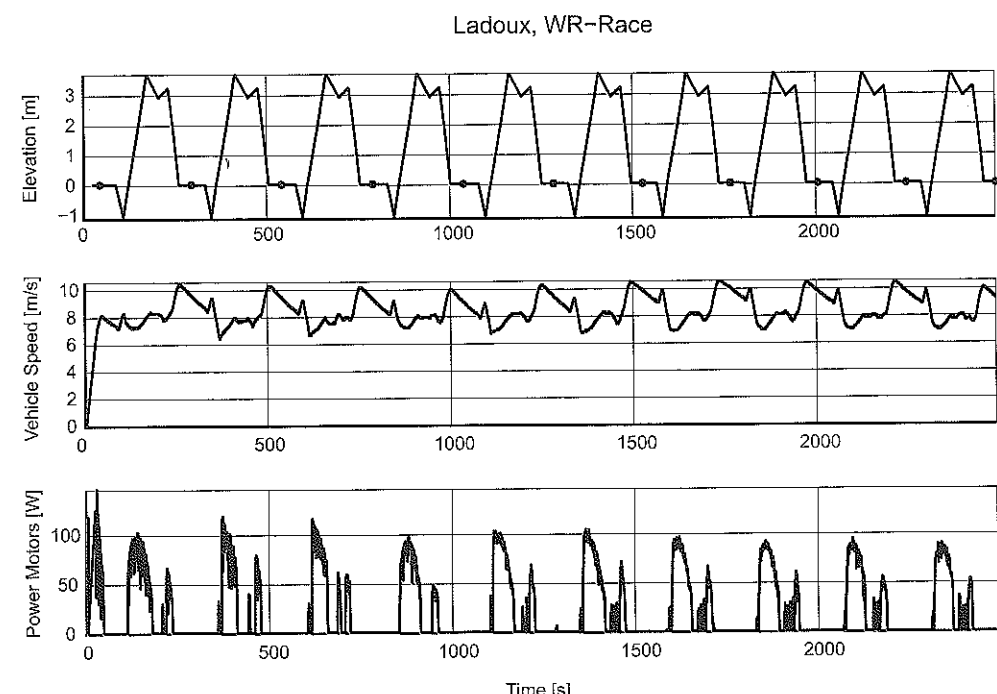


Figure 10-42: Measurements of the vehicle speed and the total power of the motors during the world record race in Ladoux.

Figure 10-43 shows the FCS measurements for a complete power phase. The lowest trace shows the compressor's duty-cycle and the short time for the compressor to refill the air accumulator at the end of the power phase. The hydrogen and coolant pumps work throughout the power phase. As soon as no more power is required from the FCS, shut-down is activated. The FCS voltage rises to a value over 19 V, which indicates a very good reactant supply and an easy restart.

Fuel Cell System

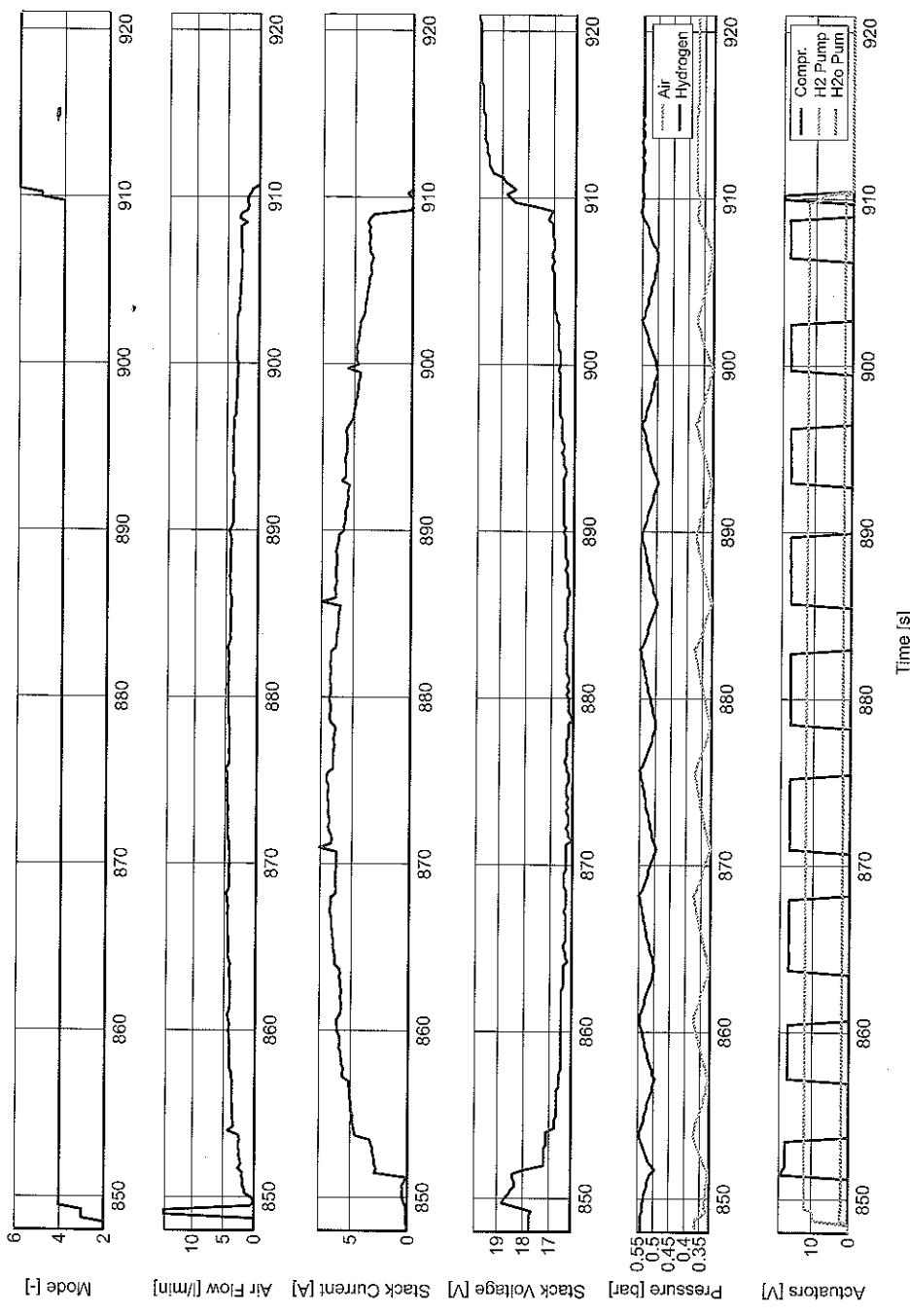


Figure 10-43: FCS measurements for a complete power phase.

Startup

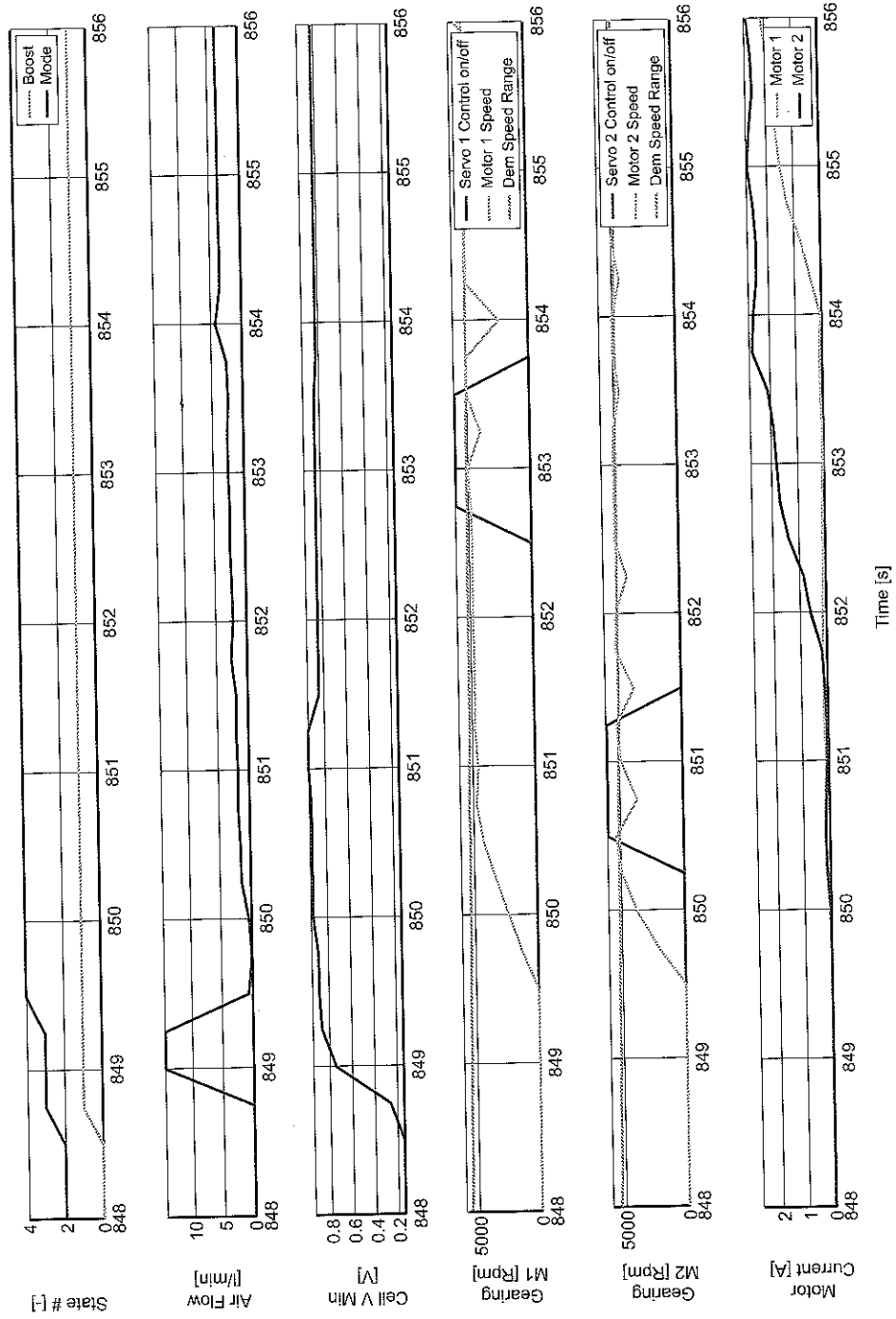


Figure 10-44: The FCS start-up after a coast phase during the race.

Figure 10-44 shows the FCS start-up and the motor coupling process. After a short air purge, the minimum voltage of the FCS rises very fast, insuring that the FCS is ready approximately 1 second after the pilot requests a boost phase. The motors begin to synchronize. Due to a problem in the synchronization, motor 2 engages later. While the motor is on, the optimal torque is applied (Motor 1, 2.5 A).

10.5. Conclusion

It is obvious that a well-designed, reliable FCS is essential. For the PAC-Car II, our stack choice was quite clear, given the experience we had already acquired on previous projects. The PAC-Car II stack is rather oversized, making it highly efficient, and the auxiliaries are dimensioned for a lower power demand. Still, the low flow rates led to water accumulation problems, which could only be solved by purging air and hydrogen. The need for duty cycling made reliable FCS shut-down and start-up procedures mandatory. Added to these requirements, the entire system had to run automatically, so that the pilot could concentrate on driving and did not have to worry about the FCS.

In the end, it was not the tuning of the PID-controllers that proved to be the most important factor in our system, but rather the well-structured and well-implemented mode management that handled all the control, diagnostic and failure management tasks correctly and reliably. Simulating the demanded power for the race in the lab proved to be an efficient way to finetune the many parameters of the FCS control system.

Chapter 11: Driving strategy

By Jérôme Bernard.

This driving strategies described in this chapter have been developed jointly with Chris Onder. The models and optimization methods used are taken from [1].

At the point where this chapter begins, the design of PAC-Car II is complete, and the vehicle has begun its trial runs. The aerodynamics are perfect, the mechanics are like a Swiss watch, the weight of the body has been minimized, and the powertrain efficiency (including the fuel cell system) has been maximized. The car has been optimized without any compromises and is able to attain enhanced fuel consumption performances. But, something remains to be done since even the most wonderful vehicle driven by the most talented pilot requires a good driving strategy.

What we call “driving strategy” refers the way the powertrain is used. The strategy used by many fuel economy competition teams is the stop-and-go tactic, which consists of either using the engine at full power or switching it off. In the case of our fuel cell powered electric vehicle, this strategy is not the best solution. By using mathematical optimization, we were able to reduce the PAC-Car II fuel consumption during the race by around 7% compared to this stop-and-go tactic. This hydrogen saving was also made possible by the driving skills of the two great pilots who tested the car and followed the instructions of the “driving strategy team” exactly.

This chapter presents our driving strategy development process, which was mainly based on simulations. First, we describe the model in detail and explain the overall methodology used to obtain it (Section 11.1). Then, the fuel consumption minimization problem is introduced and the mathematical optimization used to solve it is presented (Section 11.2). Finally, the race results that validate our strategy are reported and the “spirit” behind our strategy is explained (Section 11.3).

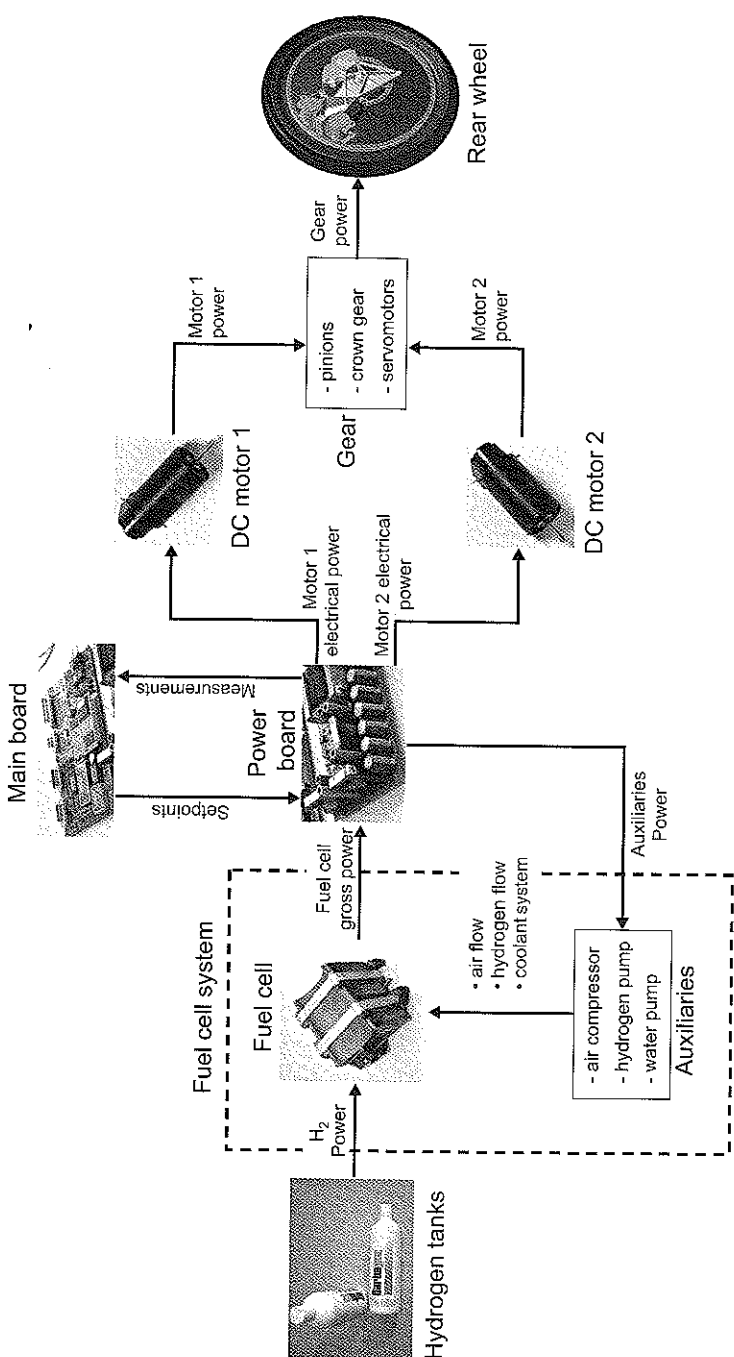


Figure 11-1: Powertrain scheme.

11.1. The PAC-Car II model

The vehicle is modeled to simulate the dynamic behavior of the vehicle and to provide an estimation of the fuel consumed. By definition, a model is “false” because it does not perfectly represent the reality, but rather only a part of the reality. This definition raises a critical question: how precise does the model need to be? On the one hand, if the model is too precise, it will be too complicated to use and will require too much time to simulate a seven-lap race. On the other hand, if it is too simple, it will not conform sufficiently to reality and thus will yield erroneous results leading to the wrong conclusions. Lots of assumptions were considered for the PAC-Car II model, but each simplification was chosen with care to insure the validity of the model.

The PAC-Car II model is divided into three sub-models: the powertrain model, the vehicle model, and the driving strategy model. The model was developed in the Matlab/Simulink software environment.

11.1.1. The powertrain Model

The powertrain is composed of all the components in the vehicle’s power path, from the fuel tank to the wheel (Figure 11-1): the hydrogen tanks, the fuel cell system, the power board, the two electric motors, the gears and the wheel.

The model used is an energy model, meaning that most of the dynamics have been neglected. This kind of model conforms closely enough to reality because the vehicle is fully electric, with the concomitant fast response times of the traction components.

The fuel tank

The fuel tank is composed of two 1-liter hydrogen canisters compressed at 11 bar, which corresponds to around 1 g of hydrogen (120 kJ). The canisters were not modeled, just the amount of hydrogen (2 g) available for the entire race was considered.

The fuel cell system

A fuel cell is a complex system mainly described by the laws of fluid dynamics and electrochemistry. These phenomena are well described in the literature [52] but are not suitable for our energetic model. Only maps were taken into account in the model [53]. Since a PEM fuel cell system is able to fulfill fast transient power demands, dynamics were neglected.

A fuel cell system (FCS) consists of two sub-systems:

- The fuel cell stack, which converts chemical power (hydrogen and oxygen) into electrical power. A stack is typically represented by its polarization curve for a given pressure, membrane humidity and gas stoichiometry (Figure 11-2). The PAC-Car II stack was derived from the "PowerPac" power unit developed by ETH and PSI [50, 54]. This unit has a maximal power dynamic of 10 kW/s.

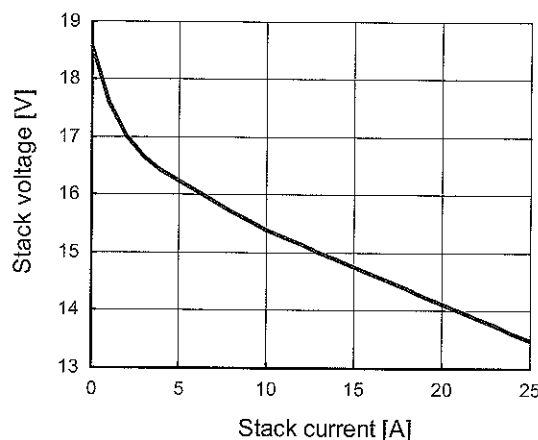


Figure 11-2: Polarisation curve of the fuel cell stack.

- The auxiliary components, which include the air compressor and the hydrogen pump that supply air and hydrogen to the stack, and the water pump cool down the system. These auxiliary circuits consume a part of the electrical energy produced by the stack (Figure 11-3).

The energetic performance of the system can be evaluated using the two maps above (i.e., the polarization curve and auxiliary power consumption curve), while the power delivered by the stack (called gross power) can be deduced from the polarization curve:

$$P_{fc}(I_{fc}) = U_{fc}(I_{fc}) I_{fc} \quad (11.1)$$

where I_{fc} is the stack current [A]; U_{fc} is the stack voltage [V]; and P_{fc} is the fuel cell stack power [W].

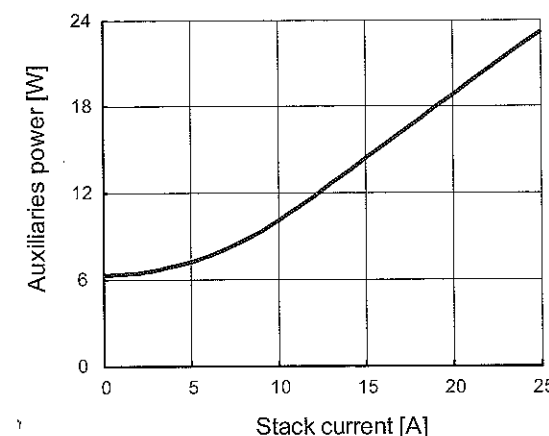


Figure 11-3: Power consumed by the auxiliary components.

The power delivered by the FCS (called net power) depends on the stack power and the auxiliary power, and corresponds to the real electrical power available:

$$P_{fcs}(I_{fc}) = P_{fc}(I_{fc}) - P_{aux}(I_{fc}) \quad (11.2)$$

where P_{fcs} is the FCS power [W] and P_{aux} is the auxiliary power [W].

The instantaneous hydrogen mass flow consumed by the electrochemical reaction is proportional to the stack current:

$$\dot{m}_{H_2} = \frac{N_{cell} M_{H_2}}{n_e F} I_{stack} \quad (11.3)$$

where

\dot{m}_{H_2} is the hydrogen mass flow consumed [g/s];

N_{cell} is the number of cells in the stack [-];

M_{H_2} is the hydrogen molar mass (2 g/mol);

n_e is the number of electrons in the oxidation-reduction reaction (2); and

F is the Faraday constant (96,487 Coulomb or s.A/mol).

Equation (11.3) provides a good evaluation of the hydrogen consumption, but does not take into account the losses due to small leaks in the stack, hydrogen diffusion through the membrane and hydrogen purges. For PAC-Car II, these losses were estimated to be about 5% of the fuel consumed.

Since both the fuel consumption and the net power of the system depend on the stack current (Equation (11.3) and Equation (11.2), respectively), the amount of hydrogen consumed $\dot{m}_{H_2}(P_{fcs})$ to produce the FCS power requested (Figure 11-4) can be calculated. This is the main map to take into consideration.

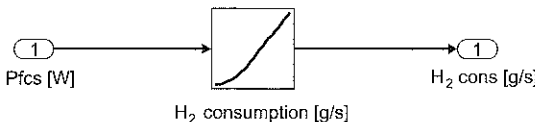


Figure 11-4: Hydrogen mass flow versus the net power of the FCS.

Based on Figure 11-4, the fuel cell system may be reduced to a single map in the Simulink model (Figure 11-5).

Figure 11-5 is a graphic representation of the fuel consumption calculation, but the calculations below are required to obtain the efficiency of the fuel cell system.

The hydrogen power used is deduced from the hydrogen mass flow:

$$P_{H_2}(I_{fc}) = \dot{m}_{H_2}(I_{fc}) LHV_{H_2} \quad (11.4)$$

Where P_{H_2} is the hydrogen power [W], and LHV_{H_2} is the lower heating value of hydrogen (120 MJ/kg).

The stack and FCS qualities can be deduced from the efficiency curves (Figure 11-6):

$$\eta_{stack}(I_{fc}) = \frac{P_{stack}(I_{fc})}{P_{H_2}(I_{fc})} \quad (11.5)$$

$$\eta_{fcs}(I_{fc}) = \frac{P_{fcs}(I_{fc})}{P_{H_2}(I_{fc})} \quad (11.6)$$

where η_{stack} is the stack efficiency, and η_{fcs} is the fuel cell system efficiency.

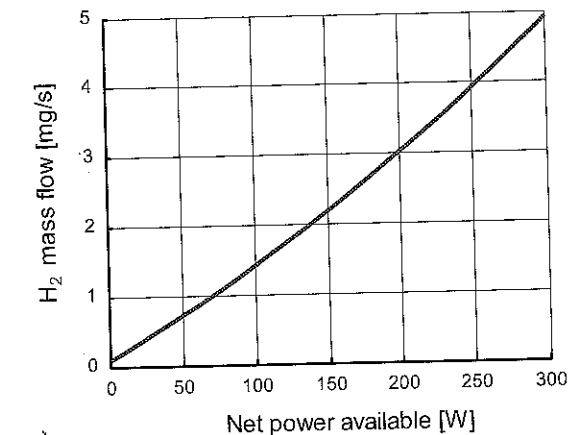


Figure 11-5: Simulink model of hydrogen consumption.

Figure 11-6 shows that the maximum efficiency of the fuel cell system is 59% for a current of 5 A.

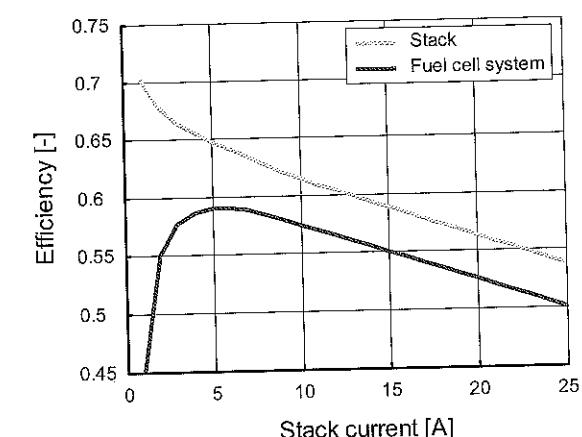


Figure 11-6: Stack and fuel cell system efficiency curves.

The DC/DC converters and electric motors

The two electric motors (Maxon Motors) are DC motors with permanent magnets. Their nominal power is 150 W each, thus providing a maximal available traction

power of 300 W. The maximum permanent current is 6 A, which corresponds to a torque of 180 mN.m with a motor constant $K\Phi$ of 30 mN.m/A.

The electrical equations for one such DC motor are:

$$U_{em}(t) = R_{em}I_{em}(t) + L_{em}\frac{dI_{em}(t)}{dt} + (K\Phi)\omega_{em}(t) \quad (11.7)$$

$$T_{em}(t) = (K\Phi)I_{em}(t) \quad (11.8)$$

Where:

U_{em} is the motor voltage [V];

I_{em} is the motor current [A];

ω_{em} is motor speed [rad/s];

T_{em} is the motor torque [N.m];

R_{em} is the internal resistor [ohm];

L_{em} is the inductivity [H]; and

$K\Phi$ is the motor constant [N.m/A or V/rad/s].

The two DC/DC converters and the two current regulators on the power board allow the two motors to be controlled by current. Since the torque is proportional to the current (Equation (11.8)), the motors can be considered as controllable torque generators. The torque response time is about 25 ms, making it possible to neglect the motor dynamics, just as the FCS dynamics were neglected.

The efficiency of the DC/DC converters and the motors was computed for the data obtained on a test bench, and the results are given below in Figure 11-7 and Figure 11-8.

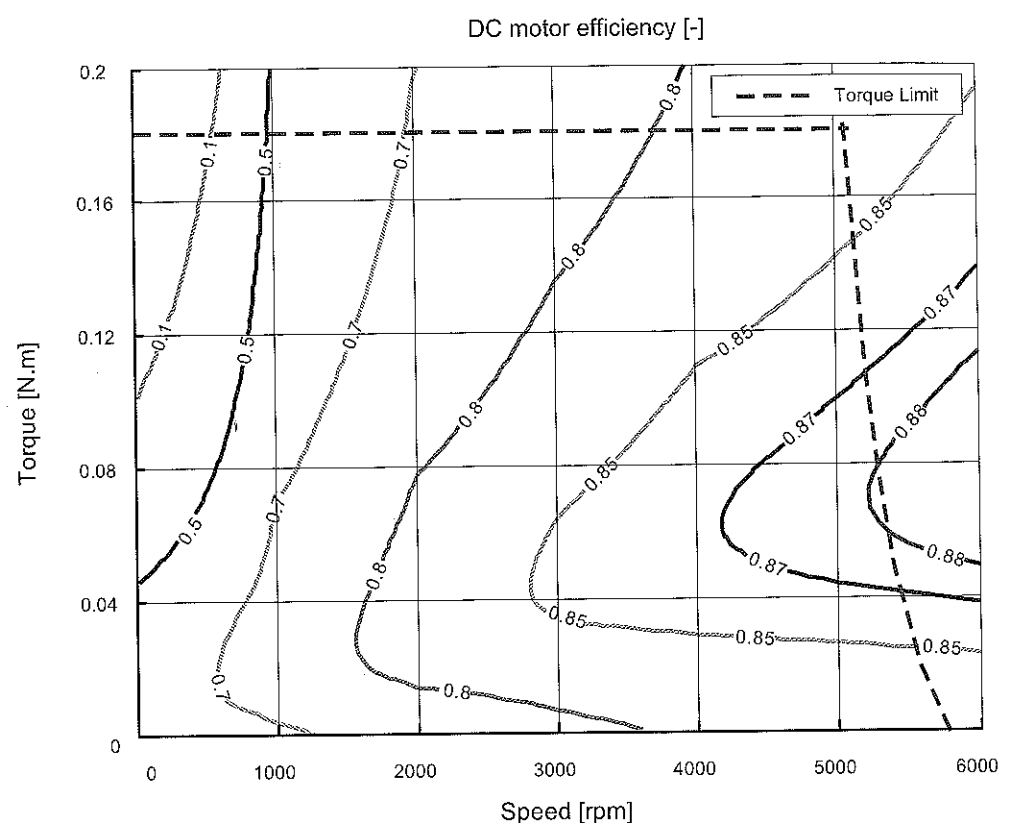


Figure 11-7: DC motor efficiency map.

Figure 11-7 clearly shows that there is a torque limitation. In PAC-Car II, this limitation is due to the maximum torque of the motor (180 mN.m) and the limited voltage supply from the FCS (see Figure 11-2). Please note that the maximum motor speed is partly limited by the size of fuel cell stack. The motor speed could have been increased by adding cells to the stack, which would have increased the fuel cell voltage.

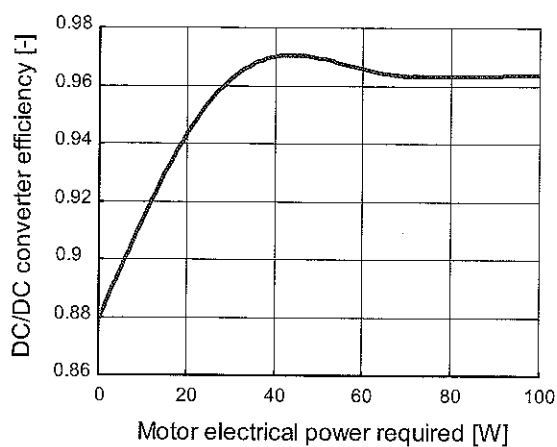


Figure 11-8: DC/DC converter efficiency map.

The Simulink model of one motor is shown in Figure 11-11. As mentioned, this model doesn't take motor dynamics into account. The output torque equals the torque setpoint.

The gears and the wheel

The gear model is quite simple (Figure 11-9), consisting of a gear ratio with a constant mechanical efficiency:

$$T_{wheel}(t) = (T_{em1} + T_{em2}) r_{gear} \eta_{gear} \quad (11.9)$$

$$\omega_{wheel} = \frac{\omega_{em}}{r_{gear}} \quad (11.10)$$

where

T_{wheel} is the torque of rear wheel [N.m];

ω_{wheel} is the speed of rear wheel [rad/s];

T_{em1} is the torque of motor 1 [N.m];

T_{em2} is the torque of motor 2 [N.m];

Ω_{em} is the speed of motor [rad/s];

R_{gear} is the gear ratio [-]; and

η_{gear} is the gear efficiency [-].

The losses induced by the coupling and uncoupling phases of each motor were neglected in the model, since synchronization is only needed 4 or 5 times per lap). Both motors are assumed to be continuously engaged, without any additional losses. In the end, the mechanical efficiency of the gear was estimated to be 95%.

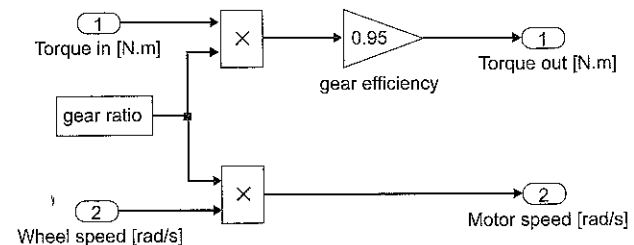


Figure 11-9: Simulink model of the gear.

The rear wheel converts the output gear torque into traction force. In the following equations, the slip of the tire has been neglected:

$$F_{traction} = \frac{T_{wheel}}{r_{wheel}} \quad (11.11)$$

$$V_{car} = \omega_{wheel} r_{wheel} \quad (11.12)$$

Where $F_{traction}$ is the traction force [N]; V_{car} is the vehicle velocity [m.s]; and r_{wheel} is the wheel radius [m].

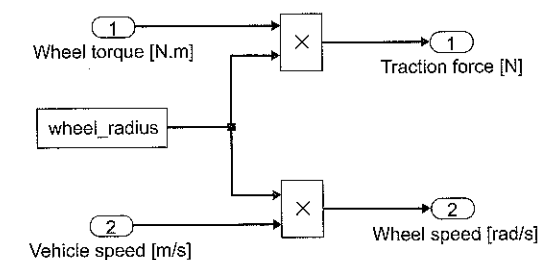


Figure 11-10: Simulink model of the wheel.

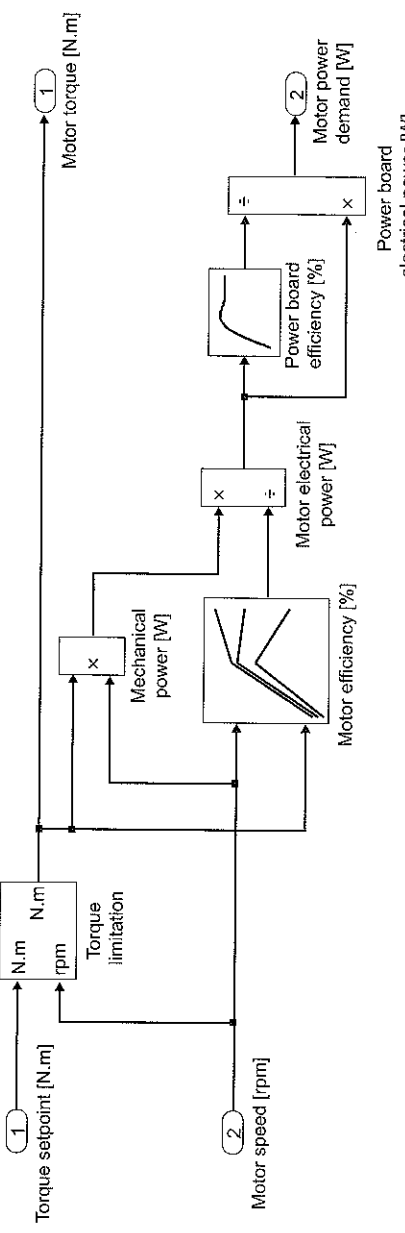


Figure 11-11: Simulink model of one motor.

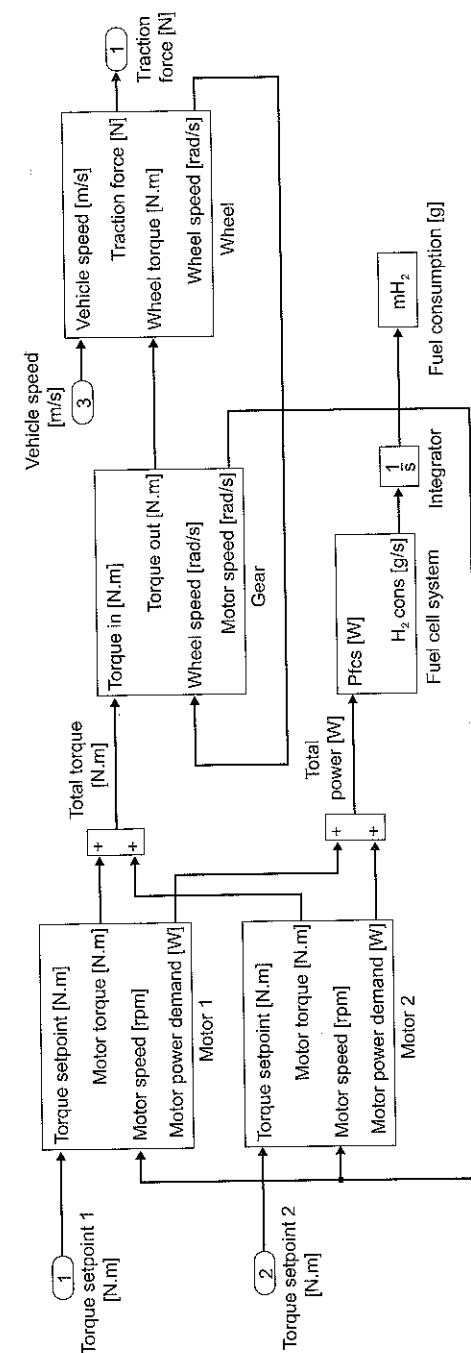


Figure 11-12: Simulink model of the powertrain.

The complete powertrain model

All the sub-models presented above were linked to create the powertrain model (Figure 11-12). The model inputs are the two motors' torque setpoints and the output is the traction force obtained. The vehicle speed is considered to be a reaction (i.e., a consequence) of the traction force applied to the vehicle.

11.1.2. The vehicle model

The vehicle has a very low dynamic response time, which is the reason why all the fast dynamics (i.e., of the FCS, DC/DC converters and motors) presented above could be neglected.

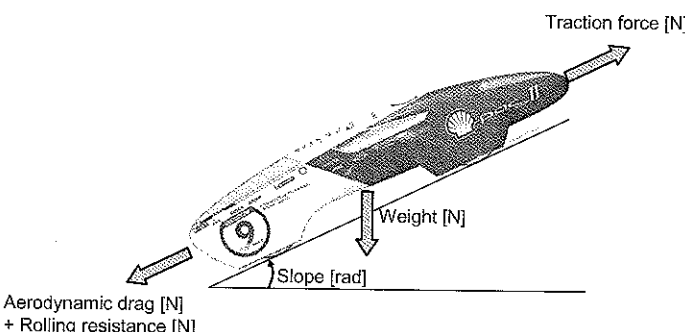


Figure 11-13: Forces acting on the vehicle.
(Drawing courtesy of Tribecraft AG, Zurich)

The fundamental dynamic principles characterizing the vehicle can be expressed as:

$$M_{car} \frac{dV_{car}(t)}{dt} = \sum_{i=1}^5 F_i(t) \quad (11.13)$$

The forces shown in Figure 11-13 can be expressed as:

$F_1 = F_{traction}(t)$ representing the traction force [N];

$F_2 = -\frac{1}{2} \rho_{air} A_f C_x V_{car}^2(t)$ representing the aerodynamic drag [N];

$F_3 = -M_{car} g \cos(\alpha_{track}(t)) C_r$ representing the rolling resistance [N];

$F_4 = F_{bearings}$ representing the bearing resistance [N]; and

$F_5 = -M_{car} g \sin(\alpha_{track}(t))$ representing the slope resistance [N].

where

M_{car} is the vehicle mass [kg];

ρ_{air} is the air density [kg/m³];

A_f is the frontal area [m²];

C_x is the aerodynamic drag coefficient [-];

g is the gravity constant [m/s²];

C_r is the rolling resistance coefficient [-]; and

α_{track} is the track slope [rad].

This model, shown in Figure 11-14, only considers the longitudinal behavior of the vehicle; the lateral behavior hasn't been considered. This model is a significant simplification because there are certainly many losses between the ground and the tires when cornering. A rolling resistance map depending on the steering angle should have been integrated to obtain a more accurate model, but was not due to lack of time.

11.1.3. The driving strategy model

At this point in the model development process, the driving strategy had not yet been defined. This strategy will be presented in the next section. Nonetheless, when developing the model, we knew that, to drive the car, the pilot would need to have access to three main data elements: the vehicle speed (in km/h); the track position (visual information); and the time elapsed (in minutes/seconds).

Furthermore, the pilot would need to be able to select the motors' torques. A basic accelerator was planned for moving the car forward, but as discussed in the following section, something more comfortable for the pilot was designed.

11.1.4. The complete model

The three sub-models described thus far (powertrain, vehicle and driving strategy) form the overall model shown in Figure 11-15.

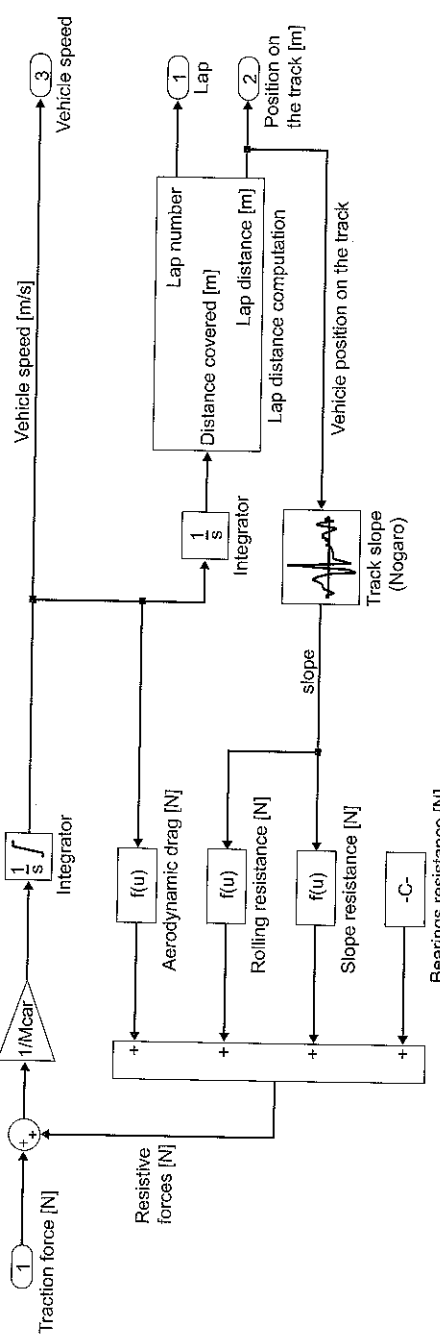


Figure 11-14: Simulink model of the vehicle.

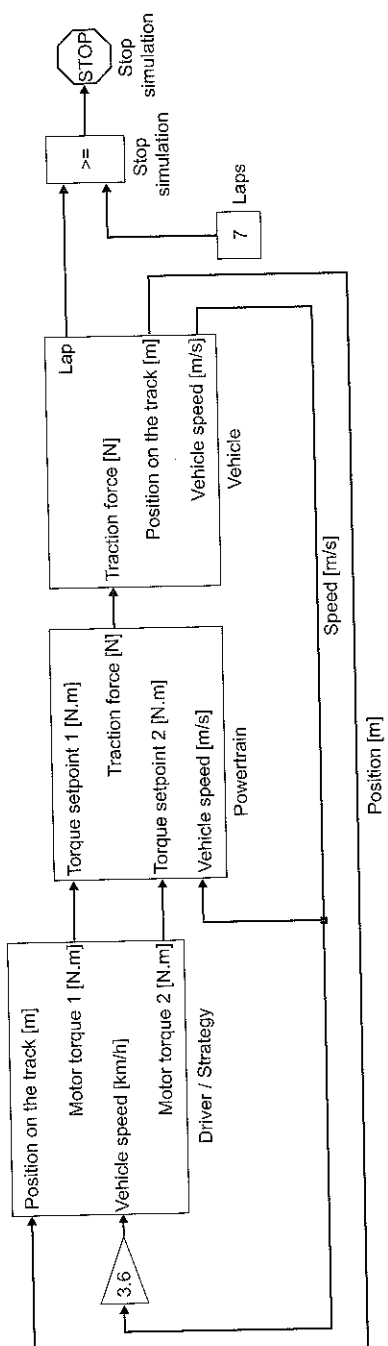


Figure 11-15: The final Simulink model of PAC-Car II.

In this model, the number of laps to be run can be selected. The energy model was mainly used to estimate the fuel consumption and to finetune the driving strategy presented in Section 11.2. The model allowed us to compare the fuel consumption of various driving strategies (Table 11-1).

11.2. The driving strategy problem

We formulated the following question as an optimization problem: how should the vehicle be driven in order to minimize the fuel consumption for the Nogaro and Ladoux races? This problem can be solved either by testing a lot of different strategies using the Simulink model, or by using mathematical approaches such as dynamic programming or optimal control theory.

This section presents an overview of the dynamic programming method we chose to use to formulate the problem.

11.2.1. Formulating the optimization problem

An optimization problem is described by the objective, the constraints, and the system. Obviously, the objective of a fuel economy race is to minimize fuel consumption:

$$J = \int_0^{t_f} \dot{m}_{H_2} (F_{traction}(u), V_{car}(u)) du \quad (11.14)$$

where t_f is the final race time [s], and \dot{m}_{H_2} is the instantaneous hydrogen mass flow [g/s].

The map of the hydrogen mass flow \dot{m}_{H_2} depends on the traction force $F_{traction}$ applied to the vehicle and on the vehicle speed V_{car} . This map is computed by using the efficiency maps of all the powertrain components, from the fuel cell system to the wheel. The hydrogen flow map for the Nogaro race was calculated for a gear ratio of 14.9 (Figure 11-16). As the motor torque was limited (Figure 11-7), the traction force was also limited, depending on the vehicle speed.

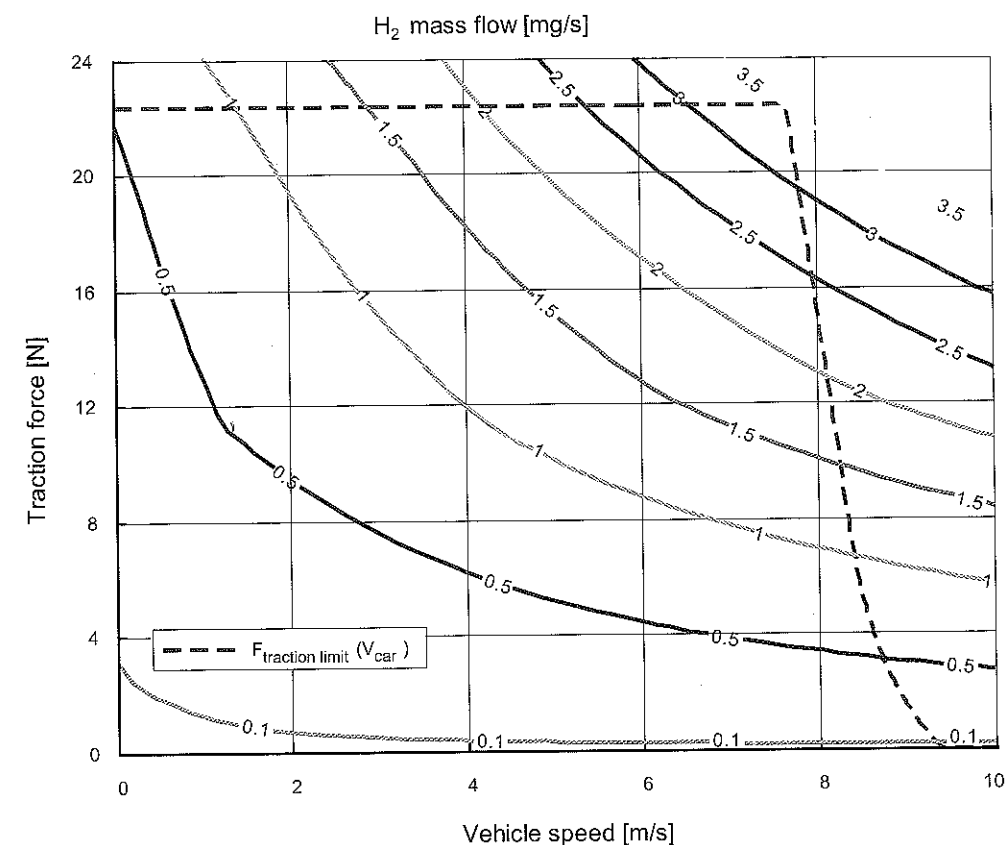


Figure 11-16: Hydrogen mass flow versus the traction force and the vehicle speed.

The main constraint in a fuel-economy race is the minimum average speed \bar{V}_{car}^{min} (30 km/h), which can be expressed as a time constraint:

$$t_f \leq t_f^{\max} \quad (11.15)$$

$$t_f^{\max} = \frac{N_{lap} d_{lap}}{\bar{V}_{car}^{min}} \quad (11.16)$$

where

t_f^{\max} is the time limit [s];

N_{lap} the number of laps [-];

d_{lap} the lap length [m]; and

\bar{V}_{car}^{min} the minimum average speed [m/s].

The second constraint is the limited traction force:

$$F_{traction} \leq F_{traction}^{\max}(V_{car}) \quad (11.17)$$

The system is described using the fundamental dynamic principles (already introduced in Equation (11.13)):

$$M_{car} \frac{dV_{car}(t)}{dt} = \sum_{i=1}^5 F_i(t) \quad (11.18)$$

The final element that must be determined is the control variable (i.e., the system input). For the PAC-Car II, we assumed that the traction force is the control variable and the vehicle speed is the output of the system (Figure 11-14).

The optimization problem may thus be stated as follows:

- Objective:

$$\min(J) = \min \left\{ \int_0^{t_f} \dot{m}_{H_2} (F_{traction}(u), V_{car}(u)) du \right\} \quad (11.19)$$

- Constraints:

$$t_f \leq t_f^{\max} \quad (11.20)$$

$$F_{traction}(t) \leq F_{traction}^{\max}(V_{car}(t)) \quad (11.21)$$

- System:

$$M_{car} \frac{dV_{car}(t)}{dt} = \sum_{i=1}^{n=5} F_i(t) \quad (11.22)$$

This problem formulation is expressed in continuous time. The equivalent formulation in discrete time is:

- Objective:

$$\min(J) = \min \sum_{k=0}^{N-1} \dot{m}_{H_2} (F_{traction}(k), V_{car}(k)) Ts \quad (11.23)$$

- Constraints:

$$k \leq N \quad (11.24)$$

$$F_{traction}(k) \leq F_{traction}^{\max}(V_{car}(k)) \quad (11.25)$$

- System (Euler first-order approximation):

$$M_{car} \frac{V_{car}(k) - V_{car}(k-1)}{Ts} = \sum_{i=1}^{n=5} F_i(k) \quad (11.26)$$

where T_s is the sampling time; k is the sample ($t = kT_s$); and N is the sample number ($t_f = NT_s$).

11.2.2. The dynamic programming algorithm

We applied an algorithm based on Bellman's optimization principle to the PAC-Car II optimization problem. This theory states that an optimal solution is composed of a series of optimal sub-solutions. The keys to using the algorithm are explained in the following paragraphs. (For a more detailed explanation, please refer to the literature [55]).

First of all, the distance covered by the vehicle is limited by a minimum and a maximum. In other words, once the final time constraint (11.15) is satisfied, the vehicle cannot be anywhere on the track. A vehicle starting at $t = 0$ s and going as fast as possible within the limits of the maximum traction force available would be sure to finish the race ahead of time, thus satisfying the minimum average speed requested. This situation corresponds to the first position limit.

Imagine now that the vehicle does not start at $t = 0$ s, but a few minutes later. If this vehicle now goes as fast as possible and crosses the finish line just in time, it will achieve an average speed of exactly 30 km/h. This situation corresponds to the second position limit. Figure 11-17 represents the two limits and the "state space" between those bounds.

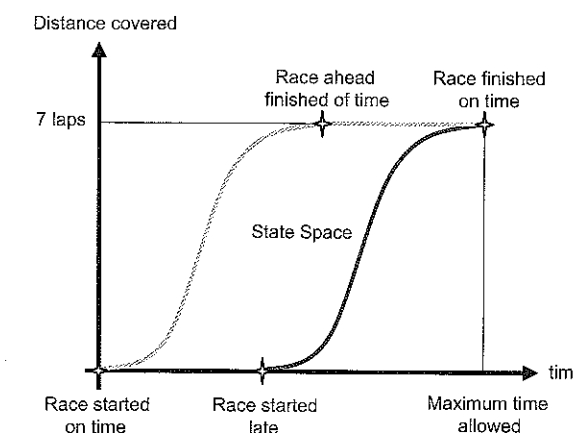


Figure 11-17: Position limits of the vehicle.

Then, the defined state space is sampled and the possible positions of the vehicle are represented by grid points (Figure 11-18).

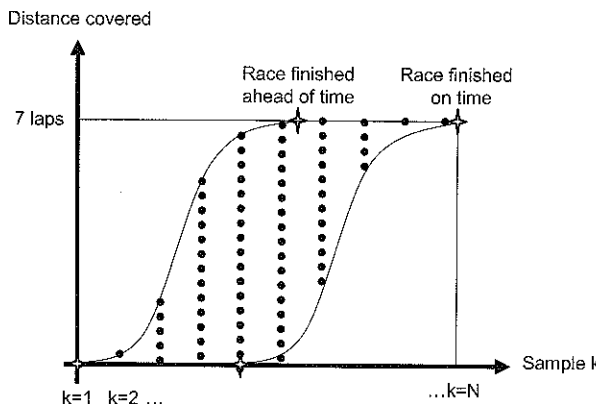
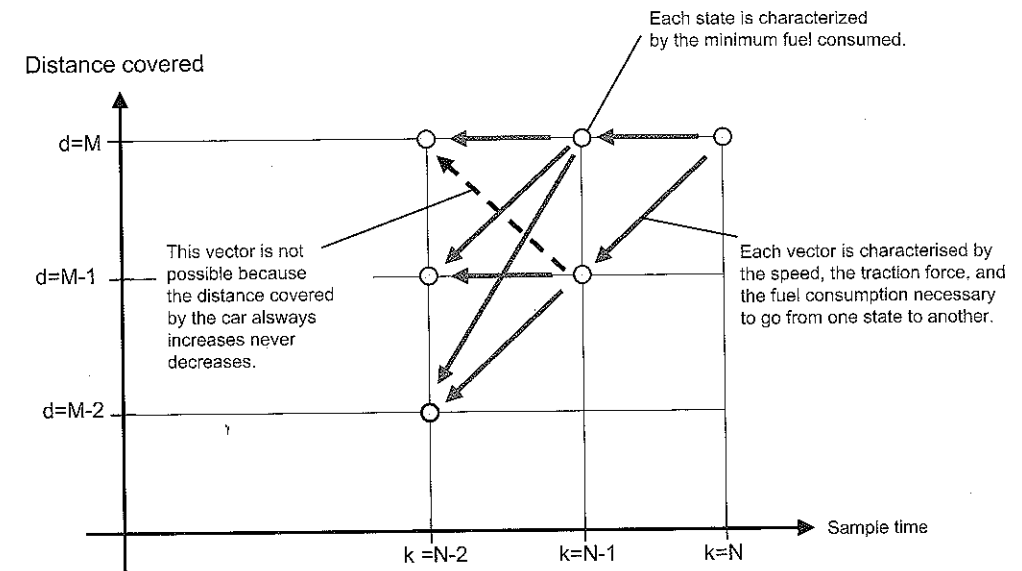


Figure 11-18: Sampled state space

The next step is determining the optimal points (called states) that should be crossed. This is done with the dynamic programming algorithm, a graphic representation of which is provided in Figure 11-19. The goal is to go from the state at $k = N$ to the state at $k = 1$ consuming as little hydrogen as possible.



Recurrence equation to evaluate the minimum hydrogen consumption:

$$m_{H_2}^{\min}(k, d) = \min_{i \in [0, M]} (m_{H_2}(k-1, i-1) + m_{H_2}\{(k-1, i-1) \rightarrow (k, i)\})$$

Recurrence equation for evaluating the minimum hydrogen consumption:

$$m_{H_2}^{\min}(k, d) = \min_{i \in [0, M]} (m_{H_2}(k-1, i-1) + m_{H_2}\{(k-1, i-1) \rightarrow (k, i)\})$$

Figure 11-19: Dynamic programming principle.

This algorithm is easy to program in a C language or in Matlab. The main problem is the time needed to calculate a solution. Though more states means more precise data, but the rise in computation time is exponential. Thus a compromise must be made between accuracy and computation time.

The solution provided by this algorithm for the Nogaro race is shown in Figure 11-20 and Figure 11-21.

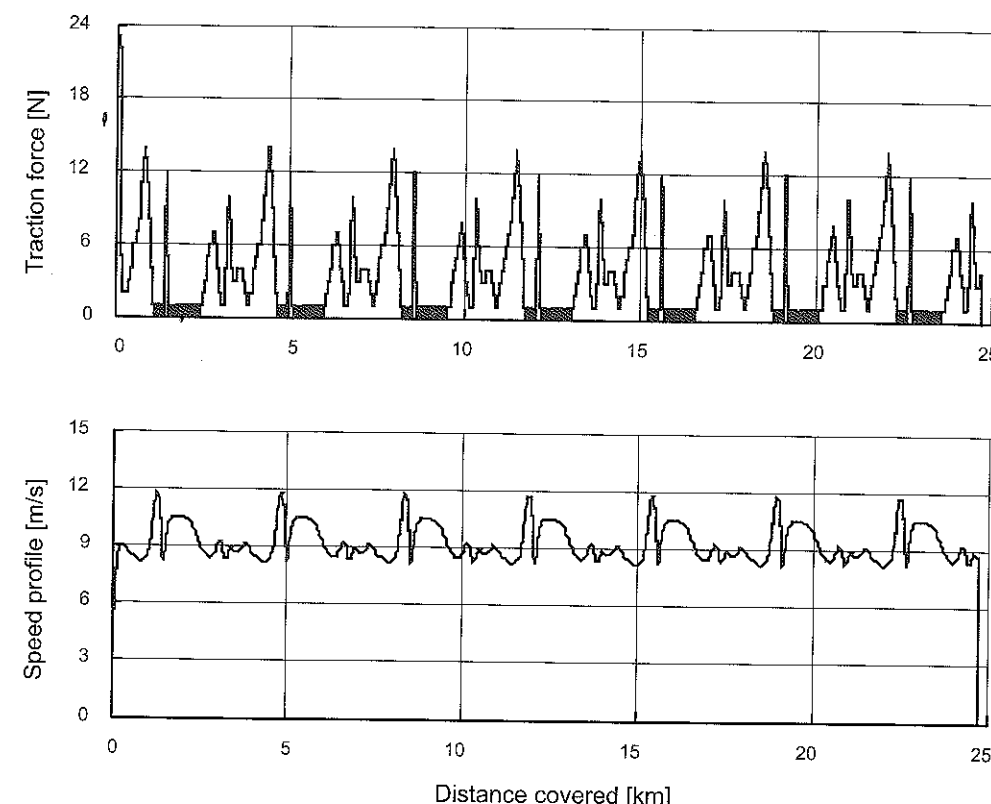


Figure 11-20: Optimization result for the Nogaro track (7 laps).

11.2.3. The driving strategy

The result of the optimization problem is an optimal traction force and an optimal speed profile. Though these results are optimal (or maybe slightly sub-optimal due to the simplifications made), the calculation was made without considering any disturbances, such as other cars present on the track or the wind. In other words, it is only an open-loop optimal control solution. This means that the results have to be analyzed to derive a real-time strategy that is easily understandable and pilot-friendly.

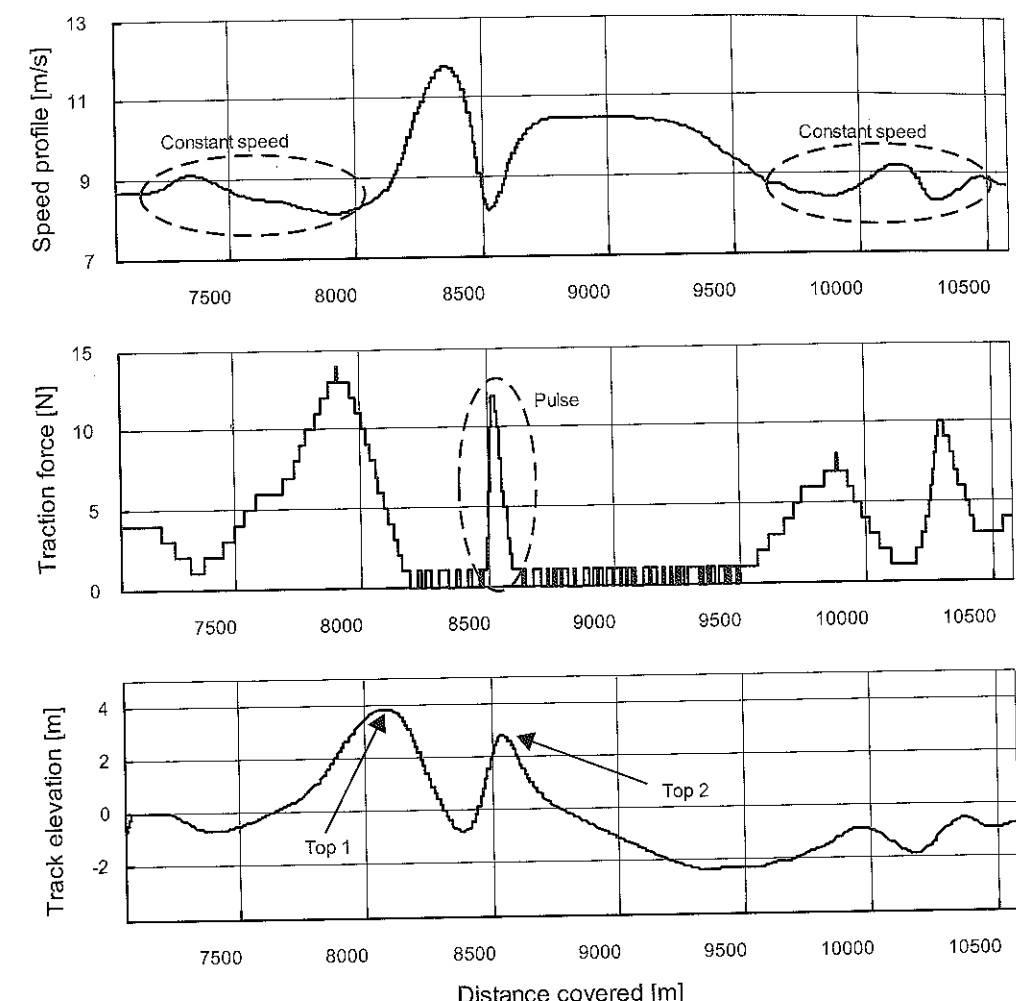


Figure 11-21: Optimization result for the Nogaro track (1 lap).

From the curves shown in Figure 11-21, certain information can be extracted:

- During the two big descents, the traction force is zero, meaning the car was running free. This is an obvious result, which simply confirms that it is not necessary to accelerate during a descent.

- The speed is almost constant and equals 9 m/s when torque was applied to the wheel. Moreover, the constant speed appears only on uphill sections or flat ground. This information is more interesting for the driving strategy.
- A short traction force pulse was needed to move up the second uphill section.

These observations can be confirmed with the minimum principle of optimal control theory. Indeed, the analytic solution of the simplified optimal control problem, where the efficiency of the powertrain is assumed to be time-invariant, shows that only maximum force, constant speed, or no force (vehicle in free-wheel mode) are possible candidates for an optimal solution [56].

Based on these reliable results, we designed a very simple accelerator, with a three-position switch (Figure 11-22):

- A boost position: In this position, the maximum traction force (full motor torque) is applied. The boost is supposed to be used during the first acceleration to launch the vehicle and briefly during the race if needed.
- A standby position: In this position, no power is transmitted to the motor; the vehicle is in free-wheel mode, and the fuel cell system is shut down. Standby is supposed to be used in descents.
- A cruise control position: In this position, the current speed of the vehicle is sustained, even if the slope is null or positive. Based on our optimization results, the driver is supposed to select cruise control as soon as the vehicle speed decreases to less than 9 m/s (31 to 32 km/h). The cruise controller is based on a digital PI controller.

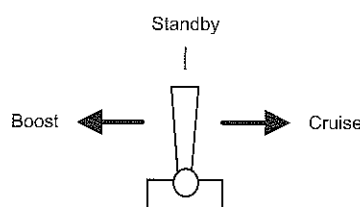


Figure 11-22: Powertrain control switch.

Figure 11-23 shows a driving strategy map, representing the Nogaro track and the sections where the “boost” and the “cruise” position must be used. This map was very helpful for the driver.

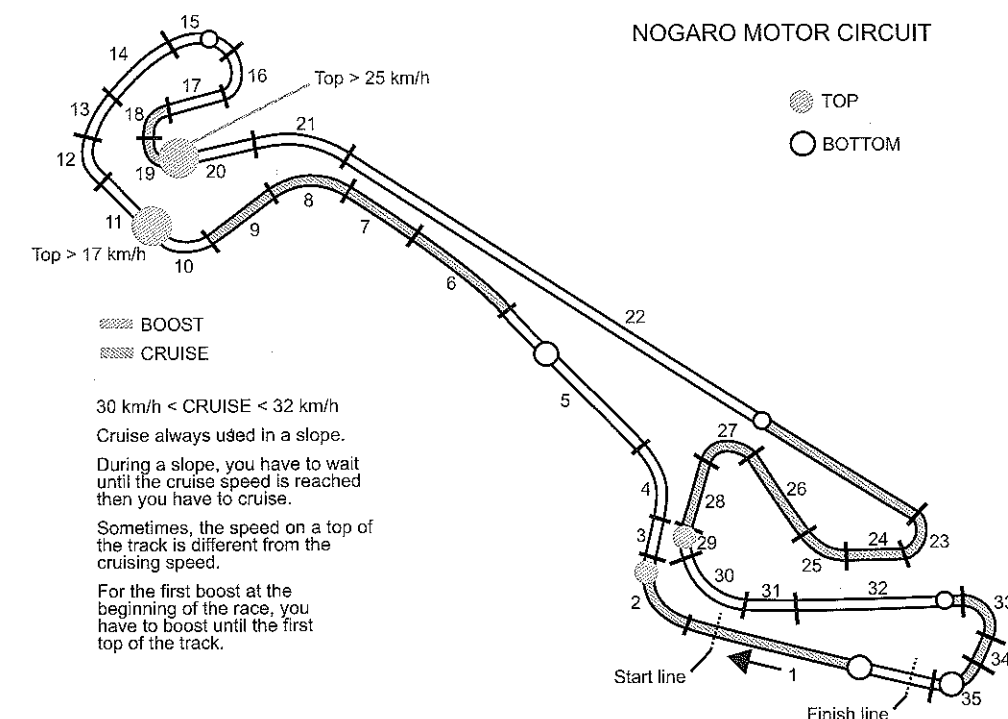


Figure 11-23: The driving strategy map provides information for the driver (NOGARO).

The same optimization approach was used for the Ladoux track. The map corresponding to the Ladoux track is shown in Figure 10-41.

11.3. Validating the strategy and race results

The race strategy was finetuned through simulations with the Simulink model to take the vehicle capabilities and the constraints into account.

For example, the risk of roll-over, not considered until now, was reduced by adjusting the speed (Figure 11-24) in the infamous critical curve at Nogaro (Figure 11-23, Sections 15 and 16). By lowering the speed, we reduced the final average speed (taking the risk to be unqualified), but this was not a real problem for two reasons: first the final average speed in the optimization was a little bit higher than 30 km/h, which gave a little time leeway; second, if the driver fell behind at any time during the race, the “boost” position could be used briefly to increase the speed. Of course, this modification made our strategy non-optimal compared to the optimization results, but the energy loss was negligible.

We could also have integrated various disturbances into the Simulink model (e.g., wind and ground temperatures, which influence rolling resistance), and analyzed the effect of each disturbance on the fuel consumption. However, lack of time forced us to forgo these possibilities with PAC-Car II.

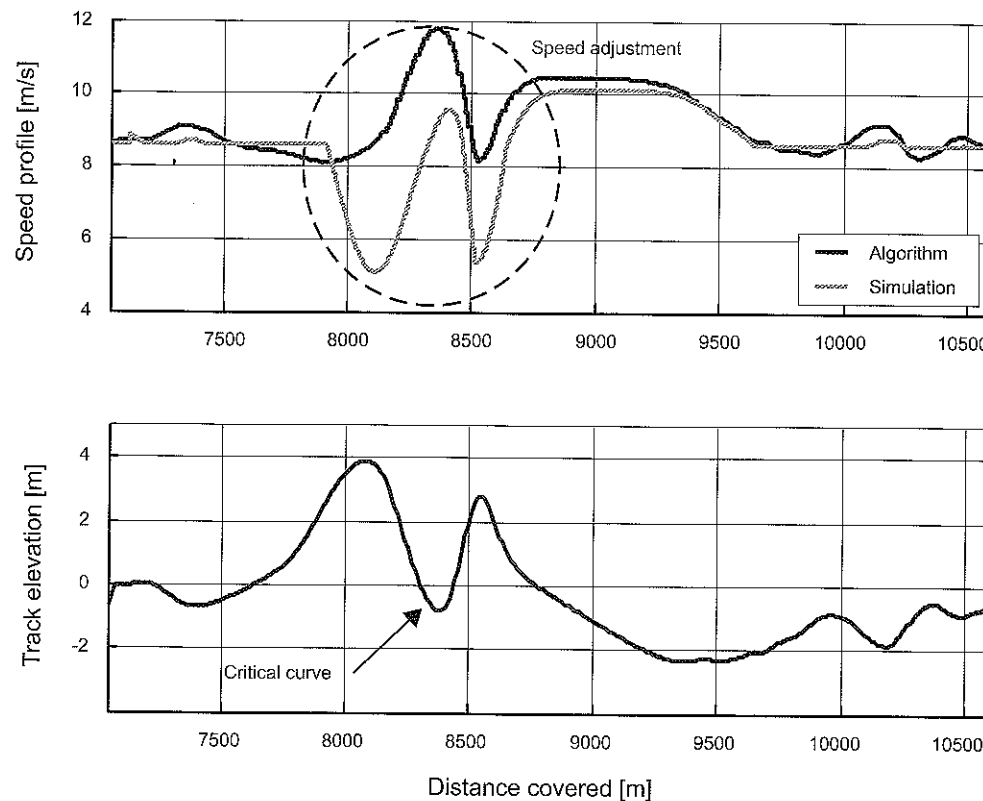


Figure 11-24: Strategy modifications.

During the Nogaro races (May 21-22, 2005), the pilots followed the defined strategy almost exactly. Figure 11-25 clearly shows that the simulated speed curve and the curve for the speed recorded during the race are very similar.

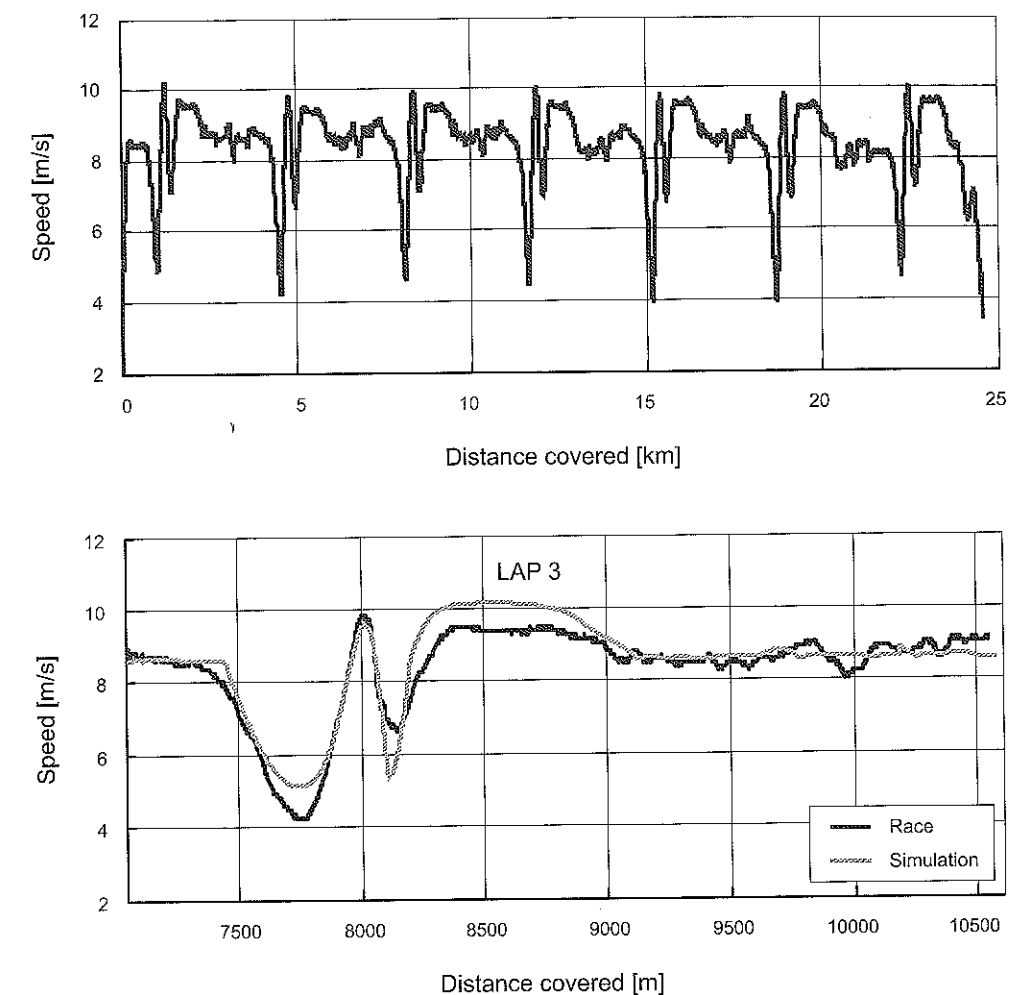


Figure 11-25: Simulated speed and real recorded speed.

Moreover, the fuel consumption measured by the race officials was close to our estimation (Table 11-1).

The “bad” stop-and-go strategy mentioned previously was also tested to highlight the importance of our optimization method. The stop-and-go strategy involved a simple thermostatic regulator: The maximum torque was applied to the wheel when the speed dropped below 25 km/h and the powertrain was shut down when the speed rose above 31 km/h. The simulated hydrogen consumption for these conditions was 7% higher than the fuel consumption with the strategy developed,

thus demonstrating the role and energy savings potential of our optimized driving strategy.

Table 11-1: Fuel consumption for the Nogaro race.

	H ₂ consumption [g]	Equivalent consumption [km/liter of gasoline]
Simulation	1.79	3,768
Real race	1.75	3,836
Stop-and-go strategy	1.92	3,514

11.4. Conclusion

The developed energy model appears to be precise enough to provide a good fuel consumption estimation. Moreover, based mainly on efficiency maps, this model is quite simple. The efficiency maps were computed with data extracted from test benches especially designed to test our components (e.g., fuel cell system, motors, power board). Computing these maps provided useful data and improved our technical skills for each fundamental part of the powertrain. This approach can be used for any fuel-economic vehicle, though it is important to remember that the torque response time of an ICE powertrain is generally on the order of one second different from a fuel cell system+electric motor dynamic and this difference may not be ignored.

We think that a good vehicle model is as important as the vehicle design itself. A model can easily simulate a hundred laps or more, thus saving time leading up to competitions. For example, during the two days before the Nogaro week-end races, the PAC-Car II pilots were able to focus on testing, analyzing, and adapting the driving strategy on the track.

This chapter presented our fuel consumption optimization process. This optimization process is not the only solution nor even perhaps the best solution to developing a winning driving strategy. We would just like to show that it is possible to formally express such an optimization problem and to use mathematical tools to solve them. Taking the time to develop a well-defined strategy improves the vehicle performance without necessitating any technical or mechanical modifications. At the very least, a model like our Simulink model can be used to test and to analyze the strengths and the weaknesses of various race tactics, which allows pilots to exploit the maximum capability of their vehicles.

Chapter 12: Conclusion and outlook

By Lino Guzzella.

While working on the PAC-Car I and II projects, all the people involved learned many technical and non-technical lessons. The technical aspects are described in detail in the previous chapters. Looking back, however, it seems that some of the most important lessons were non-technical. For example, we learned that:

- A good project is always slightly beyond the possibilities of the group working on it. If the objectives are much too ambitious or much too straightforward to achieve, the process is not satisfactory. Thus, choosing the right topic to work on is as important as how you solve the problem chosen.
- Participating in a competition, with clearly defined objectives and deadlines, is very helpful and rewarding in many ways. We learned about project organization, meeting deadlines, and having fun all at the same time. Maybe regular projects should be artificially organized along similar lines.
- If a group decides to accept a challenge, then it must be ready to focus all of its available resources on that project and try to achieve the objectives without any compromises. Still, such focused bursts can only come in waves. After an intensive period, in which the group works beyond its steady-state limits, a recovery phase must follow.
- Redundancy helps to avoid timing problems. Crucial parts (e.g., the fuel cell stack) or components with long delivery delays (e.g., the motors) must be made or ordered redundantly, even if this puts an extra strain on the budget.
- The management of such a project must be “essentially collegial,” meaning that the decisions should almost always be made after discussion and consensus seeking. However, in the few cases for which this approach doesn’t work, one person must be ready and able to assume the responsibility and to make controversial decisions. Fortunately, in the PAC-Car project, this happened only three times.
- The same person must also be willing and able to shield the project team from external pressures and to provide sufficient resources for the project. In

particular, in an academic environment, doing so requires a substantial amount of energy.

However, all of the above lessons pale in light of the fun we had working on and racing with PAC-Car I and II. This experience will form a foundation that will enable all of the team members to take up the next challenge in their professional careers.

Speaking of future challenges, many people have asked us: "And now, what impact will PAC-Car II have on real vehicles?" This is, of course, a very important, but also very difficult question.

Obviously, the roads won't be crowded with PAC-Cars anytime soon. PAC-Car II is not an automobile, but a vehicle built to excel in a well-defined fuel economy test. As such, no compromises with respect to such factors as comfort, safety, or performance had to be made when designing the vehicle. Consequently, a one-to-one transfer to automobiles is not possible.

However, there are three main ways in which PAC-Car II will have an impact on future automobile technology:

- Increased public awareness. The sheer fact that it is possible to drive 30 km in one hour with the energy contained in approximately 1 g of hydrogen defines a benchmark that cannot be ignored when discussing the fuel economy of passenger cars. PAC-Car II has been presented in many places all over the world, and such presentations have always provided a good opportunity to discuss future options for individual mobility. The media coverage, the publications and the web site of PAC-Car II have helped to increase public awareness about fuel economy issues.
- Technology transfers. There are details in the PAC-Car II design that have already been picked up by people in industry and academia and that will, eventually, find their way into commercial products.
- Knowledge transfers. The students and faculty members who worked on this project have learned many important lessons, and this knowledge will be carried with them to whatever projects these people work on in future.

The book you are holding in your hands is one example of the way this knowledge will filter through, and all of the authors hope that it will help other colleagues to further improve the fuel economy of experimental and every-day vehicles.

Indeed, such improvements are very much needed. The number of automobiles and the price of fossil fuels are increasing inexorably. To stretch the availability of fossil reserves and to prepare the transition to renewable fuels, efficient

automobiles must be developed. As PAC-Car II shows, there are essentially three approaches through which this objective can be achieved:

- More efficient conversions from fuel energy to mechanical energy. In the best case, modern cars can achieve average efficiencies near 20%. Increasing this figure to an average efficiency of close to 30% is possible within the next 10 to 15 years. Fuel cell or battery electric vehicles can reach substantially higher figures. However, these systems will only be able to make a substantial contribution if several open problems are solved first (e.g., poor energy density in batteries, hydrogen production, distribution, and storage, high system costs).
- Reduced consumption of the mechanical energy needed to drive a set distance. Improving aerodynamics and reducing rolling resistance are the obvious first steps, but cars must also be made much lighter without compromising safety or usefulness. The latter can be achieved through a combination of better materials (which, unfortunately, will be more expensive) and active safety devices.
- Improved mobility systems. Reducing the speed and acceleration capabilities of passenger cars would allow propulsion systems to be downsized, thus increasing their efficiency. Avoiding excessive speeds and reducing traffic jams is another option to save fuel. Finally, increasing the availability of public transportation systems, combining such systems appropriately with individual mobility systems, and avoiding urban sprawl will all lead to a substantially reduced demand for fuel.

We are optimistic that most of these objectives can be achieved, and we hope that the PAC-Car I and II projects contribute toward that goal.

Abbreviations

APU	Auxiliary Power Unit
CAD	Computer Aided Design
CFD	Computational Fluid Dynamics
CG	Center of Gravity
CNC	Computer Numerical Control
CVM	Cell Voltage Monitoring
DC	Direct Current
DT	Direction of Travel
ECU	Engine Control Unit
ETHZ	<i>Eidgenössische Technische Hochschule Zürich</i> (Swiss Federal Institute of Technology Zurich, Switzerland)
FC	Fuel Cell
FCPV	Fuel Cell Powered Vehicle
FCS	Fuel Cell System
FEM	Finite Element Method
GPS	Global Positioning System
GWR	Guinness World Records
H ₂	Hydrogen
IC/ICE	Internal Combustion/Internal Combustion Engine
IMRT	<i>Institut für Mess- und Regeltechnik</i> (Measurement and Control Laboratory, Zurich, Switzerland)
LHV	Lower Heating Value
LPG	Liquefied Petroleum Gas
MEA	Membrane Electrode Assembly
NLF	Natural Laminar Flow
PAC(-Car)	<i>Pile À Combustible</i> (“Fuel Cell” in French)
PCII	PAC-Car II
PEMFC	Proton Exchange Membrane Fuel Cell
PSI	<i>Paul Scherrer Institut</i> (Villigen, Switzerland)
RCAS	Road Contact Axis System
SEM	Shell Eco-marathon
SI	Standard liter
UVHC	<i>Université de Valenciennes et du Hainaut Cambrésis</i> (University of Valenciennes, France)
VER	Fuel Economy Race
VEV	Fuel Economy Vehicle
VFCS	Vehicle Fixed-Coordinate System

Bibliography

1. Guzzella, L. and A. Sciarretta, *Vehicle Propulsion Systems - Introduction to Modeling and Optimization*. 2005: Springer.
2. *Shell Eco-marathon Rules and Regulations*. 2006.
3. Bauer, H., *Automotive Handbook*. 5th edition ed. 2000: Robert Bosch GmbH.
4. Gross, A., K. Chester, and D. Malevicki, *L'aérodynamique des véhicules mus par la force musculaire*. Pour la Science, 1984. **76**: p. 66-74.
5. Riley, R.Q., <http://www.rqriley.com>.
6. *SKF General Catalogue*. 2003.
7. *The tyre. Rolling Resistance and Fuel Savings*, in *Michelin Technical Encyclopedia Entitled*. 2005, Michelin.
8. *Performance Testing of the Resco Steered Frame Freight Car Truck at the AAR Test Track, and Comparisons with Standard and Premium Three-Piece Trucks*. 2003, RESCO Engineering.
9. Taborek, J.-J., *Mechanics of Vehicles*. Machine Design, 1957.
10. French, T. *Construction and Behaviour Characteristics of Tyres*. in *Institution of Mechanical Engineers, Automobile Division*. 1980.
11. Janssen, M.L. and G.L. Hall, *Effect of Ambient Temperature on Radial Tire Rolling Resistance*. Society of Automotive Engineers, 1980. **800090**.
12. Nakane, H., <http://fancycarol.com>.
13. DeRaad, L.W. *The Influence of Road Surface Texture on Tire Rolling Resistance*. in *Tire Rolling Losses and Fuel Economy—An R&D Planning Workshop*. 1977.
14. Delvert, J.P., *A propos de pneumatiques*. La gazette du marathon Shell, 1993.

15. <http://eco-tires.webmichelin.com>.
16. Pacejka, H.B. and E. Bakker, *The magic formula tyre model, 1st colloquium on tyre models for vehicle analysis, 1991*. Vehicle System Dynamics, 1993. **suppl. 21**.
17. Gillespie, T.D., *Fundamentals of Vehicle Dynamics*. 1992: Society of Automotive Engineers.
18. Tamai, G., *The Leading Edge - Aerodynamic Design of Ultra-streamlined Land Vehicles*. 1999: Robert Bentley, Inc.
19. Hübner, C. and M. Lengg, *Windkanaltests am PAC-Car II*. 2004, Semester Thesis, ETH Zürich, Switzerland.
20. Carroll, D.R., *The Winning Solar Car - A Design Guide for Solar Race Car Teams*. 2003: SAE International.
21. Weidmann, N., S. von Bergen, and J.-J. Santin. *PAC-Car II – Aerodynamic Design of a Low Consumption Vehicle Using CFD*. in International Congress: *Fluid Dynamics Applications in Ground Transportation*. 2005. Lyon, France.
22. Delannoye, T.-P., *Roulements de Roues de PAC-Car II*. 2004, Workplace Training Report, SNFA, University of Valenciennes, France.
23. Riguetti, S., *Design of a Lightweight Rim*. 2003, Diploma Thesis Report, ETH Zürich, Switzerland.
24. Tew, G.S. and A.T. Sayers, *Aerodynamics of yawed racing cycle wheels*. Journal of Wind Engineering and Industrial Aerodynamics, 1999. **82**(1-3): p. 209-222.
25. Sayers, A.T. and P. Stanley, *Drag force on rotating cycle wheels*. Journal of Wind Engineering and Industrial Aerodynamics, 1994. **53**(3): p. 431-440.
26. Zdravkovich, M.M., *Aerodynamics of bicycle wheel and frame*. Journal of Wind Engineering and Industrial Aerodynamics, 1992. **40**(1): p. 55-70.
27. Kyle, C.R., *Aerodynamic wheels*. Bicycling, 1985.
28. Burke, E.R., *High Tech Cycling*. Human Kinetics, 1996.
29. Fackrell, J.E. and J.K. Harvey. *The Aerodynamics of an Isolated Road Wheel*. in second AIAA symposium on aerodynamics of sports & competition automobiles.

Bibliography

333

30. Abbott, A.V. and G.W. David, *Human-Powered Vehicles*. Human Kinetics, 1995.
31. Pacejka, H.B., *Tyre and Vehicle Dynamics*. 2nd edition ed. 2006: Butterworth-Heinemann.
32. Gruber, C. and W. Benoit, *Mécanique Générale*. 1998: Presse Polytechniques et Universitaires Romandes, 2nd edition.
33. Gates, *Manuel de détermination, courroies synchrones, Powergrip HTD, E1/20099*. 1999.
34. Henriot, G., *Engrenages : Conception - Fabrication - Mise en oeuvre*. 1999: Dunod.
35. Cross Morse, *Transmissions catalogue, CT95*. 1995.
36. <http://www.proteaux.fr/thermoplastiques-usuels/POM.php>.
37. mdmetric.com/or/propcgb.htm.
38. Ashby, M.F. and D. Cebon, *Materials selection in mechanical design*. Journal de Physique, 1993. **IV**, sup. **III**(3): p. 1-9.
39. Niflor : *Revêtement Technique Composé Nickel & PTFE – Lubrification & Frottement à Sec*. Rechim SA.
40. <http://www.manufacturingtalk.com/news/krs100.html>.
41. <http://www.bekaert.com/bac/Products/Diamond-like%20coatings/Racing%20Engine%20Parts.htm>.
42. *Les Revêtements Couche Mince TiN, TiCN, Cavidur® et Cavigliss®*. Sorevi.
43. NF E 23-015: *Engrenages : détermination de la capacité de charge des engrenages cylindriques extérieurs de mécanique générale*. 1982, Afnor, Paris.
44. Ruge, M., *Entwicklung eines flüssigkeitsgekühlten Polymer-Elektrolyt-Membran-Brennstoffzellenstapels mit einer Leistung von 6,5 kW*. 2003, Diss. ETH Nr. 14901, Zürich, 2003.
45. Rodatz, P.H., *Dynamics of the Polymer Electrolyte Fuel Cell*. 2003, Diss. ETH Nr. 15320, ETH Zürich, Switzerland.

46. Guzzella, L. and C.H. Onder, *Introduction to Modeling and Control of Internal Combustion Engine Systems*. 2004: Springer.
47. L'hydrogène, les nouvelles technologies de l'énergie. Clefs CEA, 2004-2005. **50/51**.
48. Barbir, f., *PEM Fuel Cells, Theory and Practice*. 2005: Elsevier Academic Press.
49. Rodatz, P.H., et al., *Performance and operational characteristics of a hybrid vehicle powered by fuel cells and supercapacitors*. 2003.
50. <http://www.powerpac.ethz.ch>.
51. Rodatz, P.H., et al. *Efficiency improvements by pulsed hydrogen supply in PEM fuel cell systems*. in *15th IFAC Triennial World Congress*. 2002.
52. Pukrushpan, J.T., S. A.G., and H. Peng, *Control of Fuel Cell Power Systems, Advance in Industrial Control*. 2004: Springer.
53. Boettner, D.D., et al. *Proton Exchange Membrane Fuel Cell System for Automotive Vehicle Simulation and Control*. in *ASME International Mechanical Engineering Congress and Exposition*. 2001. New York, New York.
54. Santis, M., et al., "PowerPac", a Portable 1 kW Fuel Cell System. 2004, Paul Scherrer Institut, Switzerland.
55. Bergounioux, M., *Optimisation et contrôle des systèmes linéaires*. Collection Cours 2e cycle Ecoles d'Ingénieur. 2001: Dunod.
56. Guzzella, L. and C.H. Onder, *Past, Present and Future of Automotive Control*. Control and Information Sciences, 2006. **329**: p. 163-182.

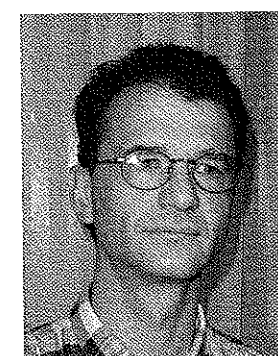
About the Authors

Dr. Jean-Jacques Santin

Jean-Jacques Santin, born in 1966 in Valenciennes (France), is lecturer at the UVHC (*Université de Valenciennes et du Hainaut-Cambrésis*), where he mainly teaches mechanical engineering. He defended his doctoral dissertation dealing with drive components for thermal-electric hybrid vehicles, sponsored by PSA Peugeot-Citroën, earning his *thèse de doctorat en génie mécanique* (PhD in mechanical engineering) in 2001. He is a member of the research laboratory LAMIH-UMR CNRS 8530. He began participating in fuel economy competitions in 1994 and managed the PAC-Car II project for ETH Zurich. He has been on staff with the European Shell Eco-marathon since 2007, lending his expertise in fuel cell powered vehicles during the technical inspections. He was the managing editor for this book.



Dr. Christopher H. Onder



Christopher H. Onder was born in Fostoria (OH, USA) in 1961. He received his *Diplom als Maschineningenieur* (diploma in mechanical engineering) with honors in 1985 and became *Doktor der technischen Wissenschaften* (doctor of technical sciences) in 1993 from the ETH Zurich. For his doctoral thesis, he received the BMW Scientific Award. He is currently senior scientist and lecturer at the Measurement and Control laboratory, ETH Zurich. He supervises many of the laboratory's engine systems projects, focusing on optimizing fuel consumption and reducing emissions. His research interests are modeling and control of automotive systems, highly dynamic test bench equipment, and model-based robust control and optimization.

Jérôme Bernard

Jérôme Bernard was born in Saint-Omer (France) in 1981. He is an engineer in automation and industrial computer science from the ENSIAME, (Valenciennes, France). He is currently preparing a PhD in modeling and control at the UVHC (*Université de Valenciennes et du Hainaut-Cambrésis*) within the research laboratory LAMIH-UMR CNRS 8530. His primary interests are electric cars, hybrid cars and fuel cell systems. His research focuses on powertrain sizing, powertrain control and power management strategies for fuel cell hybrid vehicles. He would like one day to design an electric race car for challenging competitions.



Dominik Isler



Born in Baar, canton of Zug (Switzerland) in 1980, Dominik Isler received his *Diplom als Maschineningenieur* (diploma in mechanical engineering) from ETH Zurich in 2006. During his studies, he focused on mechanical design, completing several industrial internships related to mechanical design and participating in several design and engineering student projects. Of these projects, the PAC-Car project was the most outstanding, with PAC-Car II being the subject of his *Projektorientierte Vertiefung* (project-oriented major). Project coordinator at ETHZ's Centre of Structure Technologies since May 2006, he is especially interested in managing R&D projects and sees his future in this field.

About the Authors

Pius Kobler

Born in 1979 in Rapperswil (Switzerland), Pius Kobler was also one of the four students who chose to do their *Projektorientierte Vertiefung* (project-oriented major) studies on the PAC-Car II project. He was responsible for the lightweight construction of the body shell and the fuel cell end plates. Following his *Diplomarbeit* (Diploma thesis) from ETH Zurich in the field of Aeroelastic Tailoring (fluid-structure-coupling) of airplane wings, he went to work as a product developer at Tribecraft AG in Zurich, where he still works.



Florian Kolb



Florian Kolb was born in Zurich (Switzerland) in 1980 and grew up in Trüllikon, a small village in the north of Switzerland. His fascination with dynamic systems, Chaos Theory and higher mathematics led him to study mechanical engineering with a focus on control at the ETH in Zurich. Within the PAC-Car team, he worked primarily on optimizing the fuel cell system and its system of control, beginning by collecting data and finally developing a general control strategy for PAC-Car II. This project was a great opportunity to put newly acquired knowledge directly into practice and learn a lot about teamwork and project management. His *Diplomarbeit* (Diploma thesis) in the hybrid powertrain system development department at Robert Bosch GmbH deepened his knowledge in sustainable mobility, leading to his *Diplom als Maschineningenieur* (diploma in mechanical engineering) from ETH Zurich in 2006.

Nicolas Weidmann

Nicolas Weidmann was born in Basel (Switzerland) in 1979. In October 2006, he finished his *Diplom als Maschineningenieur* (diploma in mechanical engineering) from ETH Zurich. From 2003 to 2006, he worked on the PAC-Car project, where he was responsible for the aerodynamic design of PAC-Car II and the manufacturing of its carbon-fiber-reinforced plastic wheels. Nicolas Weidmann also worked in project management. Since January 2007, he has been a consultant to the project organization team of the MIT Vehicle Design Summit. Nicolas Weidmann's main interests span the entire field of energy efficient solutions.



Professor Dr. Lino Guzzella



Born in Zurich in 1957, he received his *Diplom als Maschineningenieur* (diploma in mechanical engineering) from ETH Zurich in 1981. During his doctoral studies, he focused on nonlinear control methods. Following his dissertation in 1986, Prof. Guzzella held various R&D positions in industry, and was hired as an assistant professor of engine electronics at ETH Zurich in 1993. Lino Guzzella has been a full professor of thermotronics since 1999. His current research interests include the modeling, control, and model-based optimization of mechatronic and energy systems. The primary aim of his Engine Systems Group within the ETH Zurich Laboratory is to help reduce fuel consumption and engine emissions levels. As a teacher, Prof. Guzzella is especially interested in fostering cooperative, project-oriented learning techniques.

Awards

Amongst others, the PAC-Car team received for the PAC-Car II the following national and international awards:

2007, January:

Watt d'Or 2007, category "Energy Efficient Mobility", from the *Bundesamt für Energie* (BfE – Swiss Federal Office of Energy), www.bfe.admin.ch

2006, March:

Energy Globe Award 2005, category "Youth", from the Energy Globe – The world award for sustainability, www.energyglobe.org

2005, June:

Guinness World Record in fuel efficiency (5,385 km/l of gasoline equivalent), from the Guinness World Records, www.guinnessworldrecords.com

2005, May:

First prize at the European Shell Eco-marathon 2005 (3,836 km/l of gasoline equivalent), European Shell Eco-marathon, Nogaro, France, www.shell.com/eco-marathon



Eidgenössische Technische Hochschule Zürich
Swiss Federal Institute of Technology Zurich



Schweizerische Eidgenossenschaft
Confédération suisse
Confederazione Svizzera
Confederaziun svizra

Bundesamt für Energie BFE
Office fédéral de l'énergie OFEN
Ufficio federale dell'energia UFE
Uffizi federali d'energia UFE

The goal of the PAC-Car project, a joint undertaking of ETH Zurich and its partners, was to build a vehicle powered by a hydrogen fuel cell system that uses as little fuel as possible. PAC-Car II set a new world record in fuel efficient driving (the equivalent of 5,385 km per liter of gasoline) during the Shell Eco-marathon in Ladoix (France) on June 26, 2005.

This book, addressed to graduate students, engineering professors and others interested in fuel economy contests, is the first to summarize the issues involved when designing and constructing a vehicle for fuel economy competitions. It describes the adventure of developing the PAC-Car II and offers some specific technical advice for anyone who wants to design an ultra-lightweight land vehicle, whatever its energy source.

PAC-Car Team

ETH Zurich
Institut für Mess- und Regeltechnik
Soneggstr. 3
CH-8092 Zurich
Switzerland
Email: paccar@ethz.ch
www.paccar.ch

FUEL EFFICIENCY
WORLD RECORD
5385 kilometers per liter
[12'666 mpg (US)]
Ladoix, France
2005. 06. 26. 12am



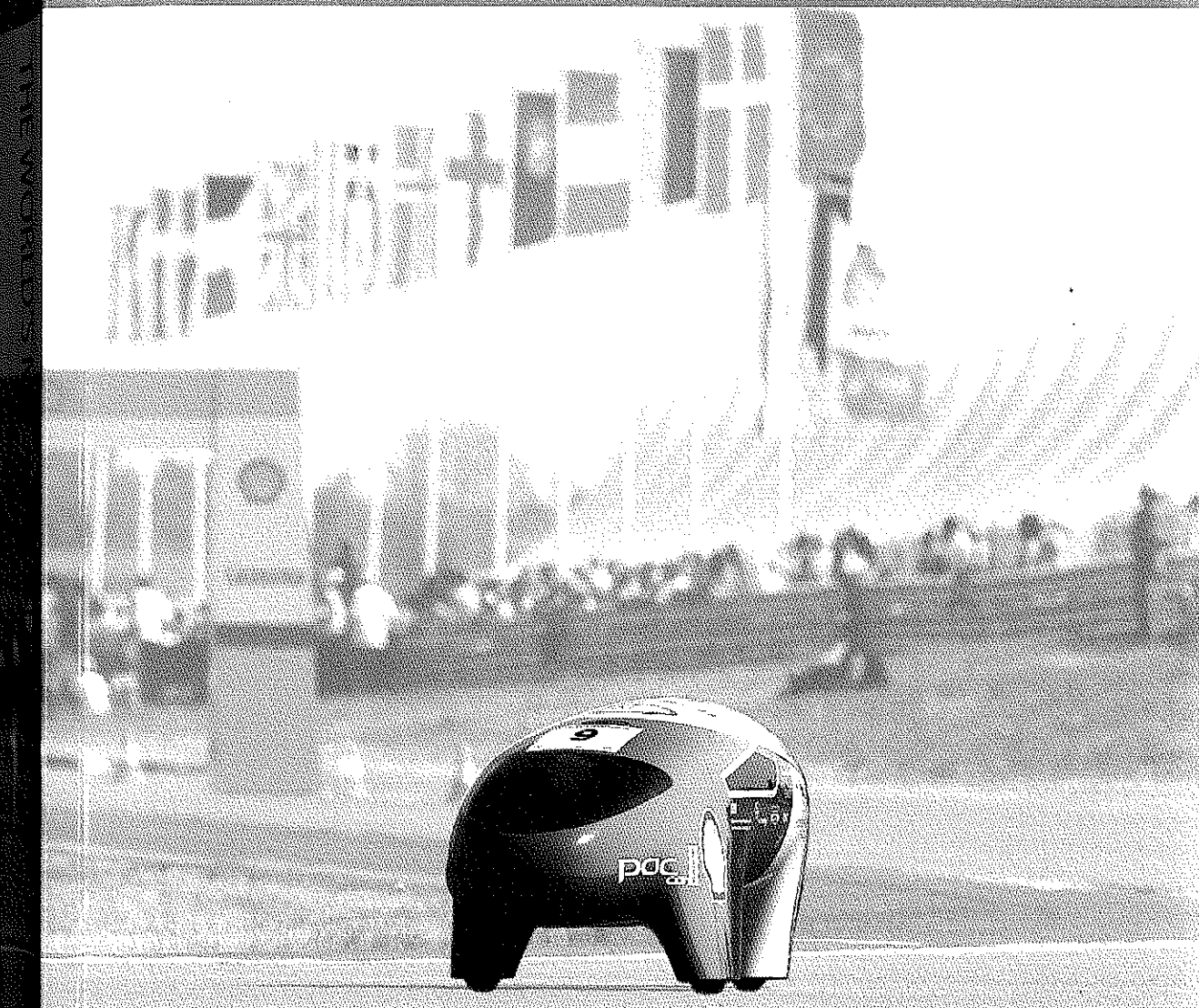
9 783728 131348

ISBN 978-3-7281-3134-8

vdf www.vdf.ethz.ch
verlag@vdf.ethz.ch

THE WORLD'S MOST FUEL EFFICIENT VEHICLE

DESIGN AND DEVELOPMENT OF **pac_{car} II**



J.J. Santin, C.H. Onder, J. Bernard, D. Isler,
P. Kobler, F. Kolb, N. Weidmann, L. Guzzella

vdf